Author:
Malmierca Vallet, Irene

Title:
Modelling Last Interglacial Stable Water Isotopes in Greenland Ice Cores

University of Bristol

&

The British Antarctic Survey

Modelling Last Interglacial Stable Water Isotopes in Greenland Ice Cores

Irene Malmierca Vallet

A dissertation submitted to the University of Bristol in accordance with the requirements for award of the degree of Doctor of Philosophy in the Faculty of Science

School of Geographical Sciences

September 2020

Word Count: 58,008

Abstract

In this thesis, paleoclimate records are compared with isotope-enabled model simulations. We concentrate on the Last Interglacial (LIG), the most recent period when global temperatures were similar to the low-end 21^{st} Century projections (1.5-2°C warmer).

A relevant outcome of the thesis focusses on explaining the LIG Greenland $\delta^{18}O$ maximum. Chapters 3 to 6 examine how Greenland ice core $\delta^{18}O$ responds to variations in Arctic sea ice extent, Greenland Ice Sheet (GIS) morphology and freshwater forcing from the retreating GIS. Chapter 3 demonstrates that Arctic sea ice changes need to be accounted for to ensure an optimised model-data solution. Chapter 4 highlights that, if more certain records at Camp Century and DYE3 ice core sites were available, this would be in agreement with LIG GIS morphologies with lower elevations in the south and a likely two-dome structure of the GIS. In addition, Chapter 6 shows freshwater forcing from the retreating GIS is an important player on the LIG Greenland $\delta^{18}O$ change.

Another important contribution of the thesis concentrates on examining how Greenland ice core $\delta^{18}O$ depends on the magnitude and sign of GIS elevation changes. Chapter 5 shows a non-linearity for $\delta^{18}O$ changes over Greenland; $\delta^{18}O$ changes are weaker for increases in GIS elevation than for decreases. This results in a non-linearity isotopic lapse rate. In particular, winter sea ice changes may significantly influence isotopic-elevation gradients. This has important implications for paleoclimate studies, in which stationary lapse rates are assumed and normally based on present-day observations.

Future steps are to: obtain additional (DYE3 and Camp Century) data; consider sea ice and ice changes in a joint framework following a Gaussian Process emulation approach and take also account of isostatic change.

Acknowledgements

Firstly, thank you to my supervisor Louise Sime for all the good advice and encouragement she has given me over the last four years. I have very much enjoyed our discussions at our weekly meetings. I must also thank my co-supervisors Paul Valdes and Julia Tindall, for their enthusiasm and for ensuring continued progress of the thesis. This thesis was funded by a NERC studentship.

I'd like to present my sincere thankfulness to my dear father for his great role in my life and for encouraging me to finish this piece of work.

A special thanks goes to my husband, whose sense of humour, company and unconditional help in all aspects of life helped me immensely throughout my PhD.

Finally, thanks go to my cute little daughter, Teresa for keeping my spirit up with all her innocence. Teresa, you have made me stronger, better and more fulfilled than I could have ever imagined.

Irene Malmierca Vallet

PORQUE TÚ LO VALES PEQUEÑA

This dissertation is dedicated to the memory of my mum:
Teresa Vallet Monge, 10th June 1949 - 8th January 2017.

For her continuous support and advice, for her patience, because she always understood. This is for her.

Declaration of Authorship

I declare that the work in this dissertation was carried out in accordance with the requirements of the University's Regulations and Code of Practice for Research Degree Programmes and that it has not been submitted for any other academic award. Except where indicated by specific reference in the text, the work is the candidate's own work. Work done in collaboration with, or with the assistance of, others, is indicated as such. Any views expressed in the dissertation are those of the author.

Irene Malmierca Vallet

Signed: _____

Date: _____

Contents

Abstract iii

Acknowledgements iv

Declaration of Authorship vi

List of Figures xiii

List of Tables xxi

Abbreviations xxiii

1 Introduction 1

1.1 Significance . . . 1

1.2 Isotopes in the climate system . . . 2

1.3 An introduction to the Last Interglacial period . . . 5

1.3.1 Arctic sea ice changes during the LIG . . . 6

1.3.2 GIS changes during the LIG . . . 7

1.3.3 North Atlantic response to freshwater fluxes . . . 9

1.3.4 Previous isotopic climate simulations of the LIG . . . 10

1.4 Outline of the thesis . . . 11

1.4.1 Objectives . . . 11

1.4.2 Thesis structure . . . 11

1.4.2.1 Contribution of this PhD to published literature . . . 12

2 Methodology 15

2.1 The isotope-enabled HadCM3 . . . 15

2.1.1 Atmosphere . . . 16

2.1.2 Ocean . . . 19

2.1.3 Sea ice model 19
2.1.4 Isotopes 20

3 Simulating the LIG Greenland stable water isotope peak: The role of Arctic sea ice changes 23
3.1 Abstract 24
3.2 Introduction 24
3.3 Methods 28
3.3.1 Model description 28
3.3.2 Experimental setup - isotopic simulations 28
3.3.3 Model-data comparison 29
3.3.3.1 Greenland ice core data 29
3.3.3.2 Sea surface temperature observations 31
3.4 Isotopic simulation results 32
3.4.1 Model performance 33
3.4.2 Sea ice extent 33
3.4.3 Sea surface and surface air temperatures 36
3.4.4 Response of the hydrological cycle to the sea ice retreat 38
3.4.5 Decomposition of $\delta^{18}O$ changes 40
3.4.6 Mean annual $\delta^{18}O$ changes at the NEEM deposition site . . . 42
3.4.7 Mean annual $\delta^{18}O$ changes at other Greenland ice core sites . 43
3.5 Discussion 47
3.5.1 Estimating the Arctic LIG sea ice retreat from Greenland ice core $\delta^{18}O$ 47
3.5.2 What caused this LIG Arctic sea ice retreat? 48
3.5.3 Uncertainties on LIG $\delta^{18}O$ from Greenland ice cores 49
3.5.4 Ice sheet, temperature, and wider atmospheric circulation changes 50
3.6 Conclusions 51
3.7 Supplementary information 52
3.7.1 Model evaluation 52
3.7.2 Modelled uncertainty on $\delta^{18}O$ 53
3.7.3 Annual deuterium excess changes 56

4 Using ice cores and Gaussian Process emulation to recover changes in the GIS during the LIG 65
4.1 Abstract 66
4.2 Introduction 66

4.3 Data . . . 70
4.4 Methods . . . 71
4.4.1 Parameterising the Set of Ice-Sheet Morphologies . . . 72
4.4.2 Choosing Morphologies for the $\delta^{18}O$ Simulations . . . 76
4.4.3 HadCM3 Simulation Runs . . . 78
4.4.4 The Emulator . . . 79
4.4.4.1 General Setting . . . 80
4.4.4.2 Choosing the Mean and Covariance Functions . . . 82
4.4.4.3 Estimation of Correlation Lengths and Nugget Term 83
4.4.5 Data-Model Comparison . . . 85
4.5 Results . . . 87
4.5.1 Fit of the Emulator . . . 87
4.5.2 Comparison Between Emulator Predictions and Ice Core Records 89
4.5.3 Shape and Uncertainty of Record-Compatible Morphologies . 92
4.5.4 Record Compatibility in the Wider Sense . . . 93
4.6 Conclusions . . . 95
4.7 Supplementary information . . . 97
4.7.1 Ice-core Data . . . 97
4.7.2 The Selection of Greenland Ice Sheet Morphologies . . . 99
4.7.3 The $\delta^{18}O$ Climate Simulator . . . 100
4.8 Weighted Principal Component Analysis . . . 101
4.9 Mask Generation for Synthetic Morphologies . . . 104

5 Sea-ice feedbacks influence the isotopic signature of GIS elevation changes: LIG HadCM3 simulations 107
5.1 Abstract . . . 107
5.2 Introduction . . . 108
5.3 Methods . . . 110
5.3.1 Experimental setup . . . 110
5.4 Isotopic simulation results . . . 111
5.4.1 GIS elevation change scenarios . . . 112
5.4.1.1 Mean annual $\delta^{18}O$ changes at ice core sites . . . 112
5.4.1.2 Surface air temperatures . . . 114
5.4.1.3 Atmospheric circulation . . . 114
5.4.1.4 Changes in precipitation pattern . . . 117
5.4.1.5 Changes in sea ice . . . 121

5.4.2 The response of the isotopic lapse rate to changes in the background climate state . . . 122
5.5 Discussion . . . 125
5.5.1 Response of Arctic sea ice and atmospheric circulation to GIS elevation changes . . . 125
5.5.2 Lapse rates in response to GIS elevation changes . . . 126
5.5.3 The response of the isotopic lapse rate to the background climate state . . . 127
5.6 Conclusions . . . 128
5.7 Supplementary information . . . 129

6 The role of Greenland iceberg discharge on the ice $\delta^{18}O$ signal across Greenland: LIG HadCM3 simulations 139
6.1 Introduction . . . 139
6.2 Methods . . . 141
6.2.1 Model Description . . . 141
6.2.1.1 Water conservation in HadCM3 . . . 141
6.2.2 Experimental Setup . . . 142
6.3 Results . . . 143
6.3.1 Model performance . . . 143
6.3.2 Climate response to variations in Greenland iceberg discharge 144
6.3.3 Overturning circulation . . . 147
6.3.4 Constraints on LIG Greenland iceberg fluxes . . . 148
6.3.5 Model-Data comparisons . . . 150
6.3.5.1 $\delta^{18}O$ changes over Greenland . . . 150
6.3.5.2 Sea surface temperatures changes . . . 150
6.4 Discussion . . . 153
6.4.0.1 $\delta^{18}O$ response to variations in Greenland iceberg discharge . . . 153
6.4.0.2 Estimating LIG Greenland iceberg discharge rates . . 153
6.5 Conclusions . . . 155
6.6 Supplementary Information . . . 156

7 Conclusions 157
7.1 Summary of principal findings . . . 157
7.1.1 Simulating the LIG Greenland stable isotope peak: The role of Arctic sea ice changes . . . 157

7.1.2 Using ice cores and GP emulation to recover changes in the GIS during the LIG 158
7.1.3 Sea-ice feedbacks influence the isotopic signature of GIS elevation changes: LIG HadCM3 simulations 159
7.1.4 The role of Greenland iceberg discharge on the ice $\delta^{18}O$ signal across Greenland: LIG HadCM3 simulations 160
7.2 Future work 161

A Meetings, Presentations and Courses **193**
A.1 Scientific Presentations 193
A.2 Courses 194

B Published and Submitted Work **197**
B.1 Collaborative Publications 197

List of Figures

1.1 Map of the Arctic Ocean showing the position of observations of sea ice change based on subpolar foraminifers (yellow circles), mollusc and ostracode faunas (orange circles), biomarker proxy IP25 (red circles) and dinocysts data (green circles). Also indicated are key regions: Morris Jesup Rise (MJR), Mendeleyev Ridage (MR) and Lomonosov Ridge (LR). Also shown are Greenland ice core records (yellow stars) which contain LIG ice; these are from north to south: Camp Century (77.2°N 61.1°W), NEEM (77.5°N, 51.1°W), NGRIP (75.1°N, 42.3°W), GRIP (72.6°N, 37.6°W), GISP2 (72.6°N, 38.5°W), Renland (71.3°N, 26.7°W), DYE3 (65.2°N, 43.8°W). 8

2.1 Schematic representation of the land surface scheme MOSES 2.1 (adapted from Cox *et al.* (1999)). Evaporation fluxes are marked in blue, variables in red refer to how precipitation is dealt with and melt from snow is represented by variables in green. 18

3.1 Comparison of the PI simulation to gridded observational sea ice data. Observational data for: (a) winter (March) and (d) summer (September) sea ice concentration (Meier *et al.*, 2017; Peng *et al.*, 2013). In particular, we use the Goddard Merged sea ice record from 1979 to 1989 (see Meier *et al.* (2017); Peng *et al.* (2013) for more information about the sea ice data). Simulated sea ice concentration for: (b) winter (March) and (e) summer (September) under PI conditions. (c) and (f) show anomalies (PI minus observations) for winter and summer respectively. 34

3.2 Mean sea ice concentrations (sic - %) for September (first row) and March (second row) for the experiments: 125-ka control (a and e), WSIR-7 (b and f), WSIR-35 (c and g) and WSIR-94 (d and h). . . . 34

3.3 The 125 ka data-based time slice (dots) provided by Capron *et al.* (2014) superimposed onto modelled summer (JAS) SST anomalies relative to the PI simulation for: (a) 125ka-control (RMSE = 3.0), (b) WSIR-7 (RMSE = 3.0), (c) WSIR-35 (RMSE = 3.2) and (d) WSIR-94 (RMSE = 3.2). 38

3.4 The 125 ka data-based time slice (dots) provided by Hoffman *et al.* (2017) superimposed onto modelled summer (JAS) SST anomalies relative to PI simulation for: (a) 125ka-control (RMSE = 2.3), (b) WSIR-7 (RMSE = 1.9), (c) WSIR-35 (RMSE = 1.5) and (d) WSIR-94 (RMSE = 1.4). Due to its coastal proximity we exclude MD95-2040 site from our model-data analysis. See Hoffman *et al.* (2017) for additional information. 39

3.5 The 125 ka data-based time slice (dots) provided by Hoffman *et al.* (2017) superimposed onto modelled annual SST anomalies relative to PI simulation for: (a) 125ka-control (RMSE = 1.9), (b) WSIR-7 (RMSE = 1.5), (c) WSIR-35 (RMSE = 1.5) and (d) WSIR-94 (RMSE = 1.4). Due to its coastal proximity we exclude MD95-2040 site from our model-data analysis. See Hoffman *et al.* (2017) for additional information. 40

3.6 Modelled annual (ann), summer (JJA) and winter (DJF) evaporation anomalies for the 125ka-control simulation (a to c), WSIR-7 (d to f), WSIR-35 (g to i) and WSIR-94 (j to l) compared to the PI simulation. Only the anomalies statistically significant at the 95% confidence level are displayed. 41

3.7 Decomposition of $\delta^{18}O$ changes from 125 ka sea ice retreat experiments. (a,d,g) WSIR-7; (b,e,h) WSIR-35; (c,f,i) WSIR-94. (a-c) The total change in $\delta^{18}O$ ($\Delta\delta^{18}O$). (d-f) The change due to variations in the seasonality of precipitation (ΔP_{seas}). (g-i) The change caused by variations in the $\delta^{18}O$ of precipitation ($\Delta\delta$). Anomalies are calculated compared to the 125 ka control simulation with no additional sea ice forcing. 43

3.8 Observed $\delta^{18}O$ anomalies at seven Greenland ice core sites (dots) Johnsen and Vinther (2007); NEEM community members (2013) superimposed onto simulated annual mean precipitation-weighted $\delta^{18}O$ anomalies for: (a) 125ka-control, (b) WSIR-7, (c) WSIR-35 and (d) WSIR-94 compared to the PI simulation. 45

3.9 Simulated $\delta^{18}O$ anomalies as a function of winter (March) sea ice retreat. Ice core sites shown: (a) NEEM, (b) NGRIP, (c) GRIP, (d) Renland, (e) Camp Century, (f) DYE3, (g) GISP2. The retreat of sea ice is calculated as the percentage change in winter (March) sea ice extent compared to the PI experiment. Results for each of the 21 sea ice sensitivity experiments are represented by triangles. Solid lines signify best fit lines (fit = b * (log(x) – a)). Also shown 1σ (lines with dashes) and 3σ uncertainty (shade envelopes) on the best fit curve. The observed $\delta^{18}O$ anomalies at each ice core site are marked with a black horizontal line with dashes. Black vertical lines with dashes represent the intersections with best fit line and 1σ uncertainty lines. 46

3.10 Present-day observations of $\delta^{18}O$ and temperature (Vinther *et al.*, 2010; Sjolte *et al.*, 2011) superimposed onto modelled present-day (1950-2000) values. (a) Annual $\delta^{18}O$ (‰) and (b) annual surface temperatures (°C). Seven transient present-day simulations covering the period 1850-2004 are considered for this analysis. In particular, the shading on each plot shows the mean of these seven present-day simulations for the period 1950-2000. 53
3.11 Variability of annual mean $\delta^{18}O$p for a low (a-c), medium (d-f) and high (g-i) sea ice forcing, at 50-year average (a, d, g), decadal (b, e, h) and annual (c, f, i) time scales. The shading in each plot shows the standard deviation calculated using sea ice retreat experiments with a low (between 7% and 19%), medium (between 21% and 65%) and high (between 72% and 100%) winter sea ice loss compared to the PI simulation. 55
3.12 Variability of annual mean $\delta^{18}O$p for a present-day scenario at (a) 50-year average, (b) decadal and (c) annual time scales. The shading in each plot shows the standard deviation calculated using seven present-day experiments covering the period 1850-2000. 56
3.13 The d-excess data compiled by Landais *et al.* (2016) superimposed onto modelled annual d-excess anomalies relative to the PI simulation for: (a) 125ka control (RMSE = 1.1‰), (b) WSIR-7 (RMSE = 1.0‰), (c) WSIR-35 (RMSE = 1.1‰) and (d) WSIR-94 (RMSE = 3.4‰). . . . 57
3.14 Change in the seasonal cycle of (a) temperature (°C), (b) $\delta^{18}O$ (‰), and (c) precipitation (mm/month) at the NEEM deposition site. Anomalies are calculated between the 125 ka simulations using heat fluxes of 0 W m-2 (125ka-control, dark blue), 15 W m-2 (WSIR-7, green), 100 W m-2 (WSIR-35, red) and 200 W m-2 (WSIR-94, cyan) compared to the PI simulation. Also shown the annual cycle of Arctic sea ice extent (SIE – 10^6 km^2) in the LIG simulations. 60
3.15 Modelled annual (ann), summer (JJA) and winter (DJF) surface air temperature anomalies for the 125ka-control simulation (a to c), WSIR-7 (d to f), WSIR-35 (g to i) and WSIR-94 (j to l) compared to the PI simulation. Only the anomalies statistically significant at the 95% confidence level are displayed. 61
3.16 Modelled annual (ann), summer (JJA) and winter (DJF) precipitation anomalies for the 125ka-control simulation (a to c), WSIR-7 (d to f), WSIR-35 (g to i) and WSIR-94 (j to l) compared to the PI simulation. Only the anomalies statistically significant at the 95% confidence level are displayed. 62
3.17 Modelled winter sea level pressure anomalies (Pa) for: a) 125ka-control, b) WSIR-7, c) WSIR-35 and d) WSIR-94 compared to the PI simulation. Only the anomalies statistically significant at the 95% confidence level are displayed. 63

4.1 Summary of the data used. (a) $\delta^{18}O$ records from: NEEM (red line, NEEM community members (2013)) and NGRIP (grey line, NGRIP Project Members (2004)), both displayed on the AICC2012 chronology (Govin *et al.* (2015); Bazin *et al.* (2013); Veres *et al.* (2013); E. Capron, personal communication); GRIP (blue squares, dated by Landais *et al.* (2003)); GISP2 (green squares dated by Suwa and Bender (2008) and green circles dated by Yau *et al.* (2016)). (b) Camp Century, $\delta^{18}O$ on a depth scale (Johnsen *et al.*, 2001). (c) DYE3, $\delta^{18}O$ on a depth scale (Johnsen *et al.*, 2001). Panels (a) to (c): present-day $\delta^{18}O$ values are indicated with horizontal dashed lines. (d) Locations of Greenland ice cores: NEEM (77.45°N, 51.06°W), NGRIP (75.1°N, 42.3°W), GRIP (72.6°N, 37.6°W), GISP2 (72.6°N, 38.5°W), Camp Century (77.2°N, 61.1°W), DYE3 (65.2°N, 43.8°W). 69

4.2 The surface height (meters) of LIG GIS morphologies used in this study. Panels contain data from: (a) Born and Nisancioglu (2012); (b) Calov *et al.* (2015) at 121.3 ka; (c) Calov *et al.* (2015) at 122.1 ka; (d) Calov *et al.* (2015) at 123.3 ka; (e) Helsen *et al.* (2013); (f) Langebroek and Nisancioglu (2016) (minimum GIS for temperature lapse rate of 6.5°C/km); (g) Langebroek and Nisancioglu (2016) (minimum GIS for temperature lapse rate of 8°C/km); (h) Quiquet *et al.* (2013) (CNRM anomaly experiment); (i) Quiquet *et al.* (2013) (IPSL anomaly experiment); (j) Robinson *et al.* (2011) (strongly retreated GIS); (k) Robinson *et al.* (2011) (moderately retreated GIS); (l) Robinson *et al.* (2011) (weakly retreated GIS);(m) Stone *et al.* (2013) (GIS extent for the maximum contribution to sea level rise, +3.8m); and (n) Stone *et al.* (2013) (GIS extent for the most likely contribution to sea level rise, +1.5m). 74

4.3 Plots of the PCs used to generate new synthetic morphologies in equation (4.1). Within each PC, areas of opposite sign yield opposite contributions to the surface height of the generated morphology. The values in the colour bar do not have a physical meaning: the PCs have norm equal to one with respect to the scalar product used to carry out the PCA. 75

4.4 Simulated per-mille $\delta^{18}O$ anomalies for the design morphologies. Results are shown for pairs of locations. Shaded bands in red correspond to the ranges reconstructed using ice core records, using the minimum/-maximum values shown in Table 4.1. 79

4.5 Cross-Validated residuals of the emulators at the different sites. Each red dot in a panel corresponds to one of the 69 simulations: the x component shows the simulator output; the y component shows the difference between the emulator prediction and the simulator output, measured in multiples of the standard deviation associated with the emulator prediction. The shaded bands highlight y values between -2 and 2, where around 95% of the standardised predictions are expected to lie. This is the case for all the six emulators used in this work. . . 88

4.6 Two-dimensional sections of the space of PC scores, for the first three PCs. On the diagonal, illustration of the PCs. The shaded grey background in the off-diagonal plots represents the density of the prior Gaussian distribution on the morphologies. The contour lines represent contours of the posterior densities of RC morphologies, in the case of the loose (blue) and tight (red) scenarios. Labels indicate the percentage of morphologies that are compatible with the records along the specified contour. Different contours are shown in symmetric plots. . 91

4.7 Plots represent the cell-wise standard deviation (top part) and average (bottom part) of the surface height of different sets of morphologies. $N = 10^7$ morphologies sampled from the prior distribution are used in the plots on the left; only RC morphologies are used for the posterior in the three scenarios on the right. To ease visual interpretation, in the bottom-right plots we show the difference between the posterior and prior mean. The "Loose" scenario corresponds to the best current data, the "Middle" and "Tight" scenarios illustrate results which could be achieved, if better constraints for DYE3 and Camp Century were available. 94

4.8 Masks associated with the reconstructed GIS morphologies of the studies listed below. In each panel: on the left the original mask provided by the corresponding study; on the right, the mask generated through the procedure described in Section 4.9, starting solely from the morphology surface height. It can be appreciated that differences are mostly negligible, supporting the validity of the mask-generation procedure employed. Panels show data from: (a) Born and Nisancioglu (2012); (b) Calov *et al.* (2015) at 121.3 ka; (c) Calov *et al.* (2015) at 122.1 ka; (d) Calov *et al.* (2015) at 123.3 ka; (e) Helsen *et al.* (2013); (f) Langebroek and Nisancioglu (2016) (minimum GIS for temperature lapse rate of 6.5°C/km); (g) Langebroek and Nisancioglu (2016) (minimum GIS for temperature lapse rate of 8°C/km); and (h) Quiquet *et al.* (2013) (CNRM anomaly experiment). 105

4.9 Continued from Figure 4.8, with data from the following studies: (a) Quiquet *et al.* (2013) (IPSL anomaly experiment); (b) Robinson *et al.* (2011) (strongly retreated GIS); (c) Robinson *et al.* (2011) (moderately retreated GIS); (d) Robinson *et al.* (2011) (weakly retreated GIS); (e) Stone *et al.* (2013) (GIS extent for the maximum contribution to sea level rise, +3.8m); and (f) Stone *et al.* (2013) (GIS extent for the most likely contribution to sea level rise, +1.5m). 106

5.1 Change in $\delta^{18}O$p, temperature, precipitation flux and winter (March) sea ice extent as a function of GIS elevation changes (m - absolute change in meters compared to 125 ka control at each ice core site location). Changes are calculated as anomalies compared to 125 ka control experiment. Ice core sites displayed: (a-d) NEEM, (e-h) NGRIP, (i-l) GRIP, (m-p) GISP2, (q-t) DYE3, (u-x) Camp Century. Results for each of the 16 GIS elevation change scenarios are represented by red dots. Solid lines signify best fit curves (y = ax). Also shown ±3 Stdev (lines with dashes) on the best fit lines. 113

5.2 Modelled annual (ANN), winter (DJF) and summer (JJA) surface air temperature anomalies for m900 (d to f), and p900 (g to i) compared to the 125Control simulation. Also shown temperature anomalies for the 125Control compared to the PI simulation (a to c). Only the anomalies statistically significant at the 95% confidence level are displayed. . . . 115
5.3 ANN, DJF and JJA mean sea level pressure anomalies (Pa) for: m900 (d to f) and p900 (g to i) compared to the 125Control simulation. Also shown sea level pressure anomalies for the 125Control compared to the PI simulation (a to c). Only the anomalies statistically significant at the 95% confidence level are displayed. 116
5.4 Absolute DJF and JJA low-level winds (at 850hPa) for PI (a-b), 125Control (c-d), m900 (e-f) and p900 (g-h). Shading displays wind speed (m/s).118
5.5 Sea ice concentration anomalies (%) for summer (September) and winter (March) for the scenarios m900 (a and d) and p900 (c and f) compared to the 125Control simulation. Also shown absolute sea ice concentration for the 125Control simulation for summer (b) and winter (e). Only the anomalies statistically significant at the 95% confidence level are displayed. 119
5.6 Annual (ANN), Winter (DJF) and summer (JJA) precipitation anomalies for m900 (d to f) and p900 (g to i) compared to the 125Control simulation. Also shown precipitation anomalies for the 125Control compared to the PI simulation (a to c). Only the anomalies statistically significant at the 95% confidence level are displayed. 120
5.7 $\delta^{18}O$p anomalies as a function of ice core site elevation change (m) relative to PI (first column) and 125Control (second column). Also shown sea-ice-corrected $\delta^{18}O$p anomalies compared to 125Control (third row). Ice core sites displayed: NEEM (first row), NGRIP (second row), GRIP (third row), GISP2 (fourth row), DYE3 (fifth row) and Camp Century (sixth row). Triangles represent results for the 16 elevation change experiments. Dots represent results for the 32 simulations that examine the joined impact of Arctic sea ice retreat and modified GIS shape. Solid lines signify best fit curves (first column, y = a + bx; second and third columns, y = ax) and shade envelopes represent ±3s uncertainty on the best fit lines. 123
5.8 Surface elevation (meters) of LIG GIS morphologies used in the 32 simulations that examine the joint impact of modified Arctic sea ice retreat and modified GIS morphology. See Table. 5.1 for more details. 133
5.9 Winter (DJF) and summer (JJA) low-level winds (at 850 hPa) anomalies for m900 (c-d) and p900 (e-f) compared to the 125Control simulation. Also shown low-level wind anomalies for the 125Control compared to the PI simulation (a-b). Only the anomalies statistically significant at the 95% confidence level are displayed. Shading displays wind speed (m/s). 134
5.10 Annual salinity (PSU; averaged over the top 535 m) anomalies for m900 (a) and p900 (b) compared to 125Control simulation. Only the anomalies statistically significant at the 95% confidence level are displayed. Shading displays wind speed (m/s). 135

5.11 Change in 10 m winter (DJF) wind speed (in m/s) for (a) m900 and (b) p900 compared to 125Control. Only the anomalies statistically significant at the 95% confidence level are displayed. 135
5.12 Simulated $\delta^{18}O$p anomalies as a function of winter (March) sea ice retreat. The retreat of sea ice is calculated as the percentage change in winter sea ice extent compared to the 125 ka control simulation. Ice core sites shown: (a) NEEM, (b) NGRIP, (c) GRIP, (d) GISP2, (e) Camp Century, (f) DYE3. Triangles represent results from the sea ice sensitivity experiments performed by Malmierca-Vallet et al. (2018). Solid lines signify best fit lines (fit = b*(log(x) – a)). Also shown 1σ (lines with dashes) and 3σ uncertainty (shade envelopes) on the best fit curve. We assume a straight line regression (fit = a+bx) for winter sea ice losses between 0% and 9% and increases up to −4.5%. This figure is an adaptation of figure 10 shown in Malmierca-Vallet et al. (2018). 136
5.13 $\delta^{18}O$p anomalies as a function of the ice core site elevation change (m) relative to (1) PI (red), and (2) 125Control (blue). Also shown sea-ice-corrected $\delta^{18}O$p anomalies relative to 125Control (purple). Ice core sites shown: (a) NEEM, (b) NGRIP, (c) GRIP, (d) GISP2, (e) Camp Century, (f) DYE3. Solid lines signify best fit curves and shade envelopes represent ±3 Stdev on the best fit lines. 137

6.1 Mean climatologies for 125-Cnt (a-b) and anomalies for FWred80 (c-d) and FWinc80 (e-f) relative to 125-Cnt for winter (December-January-February) SATs and SSTs. Only anomalies considered 95% confident are displayed. 145
6.2 Mean climatologies for 125-Cnt (a-b) and anomalies for FWred80 (c-d) and FWinc80 (e-f) relative to 125-Cnt for March sea ice concentration (SIC) and annual salinity. Only anomalies considered 95% confident are displayed. 145
6.3 Mean climatologies for 125-Cnt (a-b) and anomalies for FWred80 (c-d) and FWinc80 (e-f) relative to 125-Cnt for DJF Mixed Layer Depth (MLD) and AMOC. Only anomalies considered 95% confident are displayed. 146
6.4 Change in the maximum AMOC strength (Sv) as a function of Greenland iceberg flux changes (Sv). Changes are calculated as anomalies compared to 125-Cnt. Results for each of the 14 sensitivity simulations are represented by blue triangles. Solid lines signify best fit curves (y = bx). Also shown ± 1 Stdev (lines with dashes) on the best fit lines. 148

6.5 Percentage reduction (%) in cumulative mass balance over the whole Greenland area as a function of NEEM ice core site elevation change (m) relative to PI. Triangles represent results for the 32 simulations with different LIG GIS shapes previously examined in Chapter 5 (Malmierca-Vallet *et al.*, 2020). Solid lines signify best fit curves (y = a + bx) and dash lines represent ±1s uncertainty on the best fit lines. Note: To estimate cumulative mass balance over Greenland, we calculate snow depth changes over 10 year non-overlapping periods during the course of each run. That is snow depth at the end of 10 years minus snow depth at the beginning of the 10 years. We then average the last 3 estimates (last 30 years of each run) to give a most definitive estimate for each run. In the model the net snow accumulation can be seen somehow as a result of doing the surface mass balance (SMB) at the scale of the GCM grid box. Note, these numbers are not used in this paper as a true SMB values because we know that true snow melt happens in a much narrow region associated with the elevation and this is not well represented at the HadCM3 grid. 149

6.6 Modelled annual $\delta^{18}O$ (first row), annual SSTs (second row) and summer (JAS) SSTs (third row) anomalies compared to PI for: 125-Cnt (first column), FWred40 (second column) and FWred50 (third column). Model results are compared to: (a-c) the Domingo *et al.* (2020) compilation of LIG stable water isotopic information ($\delta^{18}O$), (d-f) the 125 ka data-based time slice provided by Hoffman *et al.* (2017), and (g-i) the 125 ka data-based time slice provided by Capron *et al.* (2014). 151

6.7 Change in $\delta^{18}O$p as a function of Greenland iceberg flux changes (Sv). Changes are calculated as anomalies compared to 125-Cnt. Ice core sites displayed: (a) NEEM, (b) NGRIP, (c) GRIP, (d) GISP2, (e) DYE3 and, (f) Camp Century. Results for each of the 14 sensitivity simulations are represented by blue triangles. Solid lines signify best fit curves (y = bx). Also shown ±3 Stdev (lines with dashes) on the best fit lines. 152

List of Tables

3.1 Modelled annual mean precipitation-weighted $\delta^{18}O$ anomalies (‰) at seven ice core sites (NEEM, NGRIP, GRIP, Renland Camp Century, DYE3 and GISP2) for selected LIG simulations. 30

3.2 Monthly and annual mean sea ice extent and amplitude of sea ice extent (maximum minus minimum annual sea ice extent) for the PI and selected LIG simulations. Values expressed in $10^6 km^2$. 35

3.3 Modelled annual means of precipitation-weighted $\delta^{18}O$, precipitation-weighted SAT and non-weighted SAT anomalies compared to the PI simulation at the NEEM deposition site. Anomalies are listed for each of the 125 ka simulations. The experiments marked in red are the ones mainly discussed in the text. 44

3.4 Modelled variability of annual mean $\delta^{18}O$p at seven ice cores sites at 50-year average, decadal and annual time scales. We list standard deviations (‰) for the sea ice retreat experiments ensemble and a present-day scenario. For the present-day scenario, the standard deviation between seven present-day experiments covering the period 1850-2000 is presented. 54

3.5 Compilation of observations of NH sea ice changes for the LIG. 58

3.6 Full list of simulations. The experiments marked in red are those focussed upon in the text. 59

4.1 Stable water isotopic ($\delta^{18}O$) information from six Greenland deep ice cores: NEEM, NGRIP, GRIP, GISP2, Camp Century and DYE3. Most likely, maximum, and minimum values between 120 and 126 ka. All values are anomalies with respect to the present day. See Section 1 of the Supporting Information for full details. 71

4.2 Standard deviations σ_i associated with the Principal Components through PCA (first row), and corresponding percentages of variance explained (second and third row). 73

4.3 Location by location, the values of the correlation length (d) and the nugget term (μ) which are used to build the corresponding emulator. The estimation is carried out through the cross-validation procedure explained in Section 4.4.4.3. Higher values of d denote a stronger correlation between the $\delta^{18}O$ outputs associated with different morphologies. For a given d, higher values of μ indicate higher variance of the emulator predictions at the design points, alongside a generally smoother mean prediction. 87

5.1 Full list of scenarios. Third and fourth columns show the sea ice forcing (SIF) implemented and the winter sea ice extent (SIE) respectively. The simulations highlighted in blue are the ones primarily discussed in the text. All LIG simulations are performed with greenhouse-gas and orbital forcing centred at 125ka (Eccentricity - 0.04001; Obliquity - 23.80°; Perihelion - 201.3 day of yr; CO_2 - 276 ppmv; CH_4 - 640 ppbv; N_2O - 263 ppbv). The boundary conditions for the PI simulation are the following: Eccentricity - 0.0167; Obliquity - 23.45°; Perihelion - 1.7 day of yr; CO_2 - 280 ppmv; CH_4 - 760 ppbv; N_2O - 270 ppbv. Note (*): To account for the modelled climate variability for a 125 ka control scenario, we use an average of three 125 ka simulations which feature very minor GIS elevation changes between them (maximum scaling percentage of ±1.8 in Eq. 1) as our 125 ka control. 130

6.1 Full list of scenarios. First column shows percentage changes in the Greenland iceberg freshwater flux (W in Eq. 1) for each sensitivity experiment relative to PI. Second column displays Greenland iceberg discharge rates between latitudes 85-40°N and longitudes 80°W–0°E. . 156

Abbreviations

AIS	Antarctic Ice Sheet
AMOC	Atlantic Meridional Overturning Circulation
AOGCM	Atmosphere Ocean General Circulation Model
GCM	General Circulation Model
GHG	Greenhouse Gas
GIS	Greenland Ice Sheet
GNIP	Global Network of Isotopes in Precipitation
HadAM3	Hadley Centre Atmosphere Model
HadCM3	Hadley Centre coupled Model
HadOM3	Hadley Centre Ocean Model
IPCC	Intergovernmental Panel on Climate Change
ka	thousand years before present
LIG	Last Interglacial
MOSES	Met Office Surface Exchange Scheme
NADW	North Atlantic Deep Water
NH	Northern Hemisphere
SAT	Surface Air Temperature
SMOW	Standard Mean Ocean Water
SST	Sea Surface Temperature
WAIS	West Antarctic Ice Sheet

Chapter 1

Introduction

1.1 Significance

In light of current rates of climate change, which are unprecedented for at least the last millennium (Smith *et al.*, 2015), advancing our understanding of how the climate has changed before the instrumental record can aid in informing future projections (e.g., Braconnot *et al.*, 2012). Knowledge of how climate system components have reacted to past forcing, such as sea level rise, ice sheet stability, weather extremes and climate variability, is important to foresee future risk levels and inform policy (Hansen *et al.*, 2016; IPCC, 2013).

The Last Interglacial (LIG - between about 130 and 116 thousand years ago (ka)), is a particularly interesting time period to investigate and will be the focus of this thesis. It is believed to be the last time in Earth's history when global mean sea-level was likely at least 5 m higher than today (e.g., Kopp *et al.*, 2009) and the Arctic experienced significantly warmer temperatures (CAPE Last Interglacial Project Members, 2006; NEEM community members, 2013; Hoffman *et al.*, 2017). The LIG is thus an excellent test bed to investigate processes of high-latitude amplification in a warmer-than-present-day climate. Improving our knowledge of the climate processes and feedbacks taking place at northern high (NH) latitudes is extremely important for predicting future responses of the Arctic region to rising atmospheric CO_2 emissions. It is also a time period where sufficient data is available for model-data evaluation.

Stable water isotopes ($\delta^{18}O$ and δD) have been widely used to infer a wide range of properties of past climates. In particular, the isotopic composition of both Greenland and Antarctica deep ice cores, have been commonly used to infer surface temperature records covering hundreds of thousands of years (e.g., Jouzel *et al.*, 2007; NEEM community members, 2013). Due to the fact that water isotopes are affected by several climate factors such as atmospheric circulation, vapour source conditions, ambient temperature, local precipitation and sea ice variations (Hoffman *et al.*, 2000; Werner *et al.*, 2001; Werner and Heimann, 2002; Stenni *et al.*, 2003; Masson-Delmotte *et al.*, 2008; Sime *et al.*, 2013), it is agreed that the interpretation of a simple single parameter could be too simplistic. The incorporation of water isotope physics into a General Circulation Model (GCM) permits a fuller approach to understanding mechanisms in the hydrological cycle and has yielded significant knowledge of both our present and past climates (e.g., Xi, 2014).

This thesis focuses on the Arctic climate of the LIG. Several paleoclimate questions are addressed using the isotope-enabled HadCM3 climate model and comparing the model output with Greenland ice core records and other proxy data. The current Chapter 1 reviews the literature in the context of the basics of stable water isotopes and their connection with climate. The main forcings and features of climate change during the LIG period are introduced. Finally, aims and the structure of thesis are outlined.

1.2 Isotopes in the climate system

Stable water isotopologues, $H_2^{18}O$, $HD^{16}O$ and $H_2^{16}O$ vary in mass and consequently behave differently during phase changes; lighter molecules tend to evaporate while heavier molecules preferentially remain in liquid or solid phases (Dansgaard, 1964; Clark and Fritz, 1997). Phase changes result in a modification in the ratio of heavy to light isotopologues, between related vapour and condensate; this is known as isotopic fractionation (Merlivat and Jouzel, 1979; Cappa *et al.*, 2003). Recurrent fractionation has a cumulative impact on the air-mass isotopic composition, leaving a mark of its history (e.g., Merlivat and Jouzel, 1979; Johnsen *et al.*, 1989).

Most of the water in the atmosphere comes from the ocean surfaces, with an almost uniform relative abundance of $H_2^{18}O$, $HD^{16}O$ and $H_2^{16}O$ of $0.0020 : 0.0003 : 0.997$ (Cuffey and Paterson, 2010). The isotopic composition is determined as a deviation from the Standard Mean Ocean Water (SMOW) in units of parts per mill (‰) and using the delta notation. For instance, for oxygen-18:

$$\delta^{18}O = (R_{sample}/R_{SMOW} - 1) * 1000 \tag{1.1}$$

Where R is the ratio of concentrations of heavy to light isotopologues ($[H_2^{18}O]/[H_2^{16}O]$). For deuterium ($HD^{16}O$), the same notation is used to determine δD.

In the 1950s, Willi Dansgaard first discovered the link between the cloud condensation temperature and the abundance of oxygen-18 in precipitation (Dansgaard, 1953). With this interpretation, atmospheric vapour transport is seen as a destillation system through which masses of air at high altitudes and high latitudes are depleted in heavy isotopes as a result of continuous rainout during transport and cooling (Dansgaard, 1964; Cuffey and Paterson, 2010). With the Camp Century ice core drilling on Greenland, Willi Dansgaard illustrated how the isotope thermometer could be used in connection with paleoclimate; this led to the first glacial climate record inferred from an ice core (Dansgaard *et al.*, 1968).

Since then, measurements of $\delta^{18}O$ in polar ice cores have been commonly translated into temperature (T) making use of a linear relation (e.g., Dansgaard, 1964):

$$\delta^{18}O = a * T + b \tag{1.2}$$

Where a ($\Delta\delta/\Delta T$) and b are constant coefficients.

The present-day spatial pattern of annual $\delta^{18}O$ and temperature at high latitudes indicates a variation of $\delta^{18}O$ with temperature of about 0.7 ‰ per °C (Dansgaard, 1964; Cuffey and Paterson, 2010). Such spatially derived relations, obtained from present-day data, have been applied to Greenland and Antarctic ice core records to

reconstruct past temperature changes on glacial-interglacial timescales (e.g., Jouzel *et al.*, 2007; NEEM community members, 2013).

With greater knowledge and more data, it is recognised now that this single parameter interpretation is too simplistic; any variation in local or remote climate can modify the process of recurrent fractionation which will modify the local isotopic composition (Noone and Simmonds, 1998; Masson-Delmotte *et al.*, 2008; Sturm *et al.*, 2010). The isotopic composition of precipitation is affected by the (1) temperature, (2) altitude, (3) amount, (4) continental effects (e.g., Dansgaard, 1964; Rozanski *et al.*, 1993). There is an increasing depletion of $\delta^{18}O$ in atmospheric vapour as:

1. Temperature decreases because of the temperature dependence of equilibrium fractionation among condensate and vapor (Lachniet, 2009).

2. During rainout as a result of the removal of moisture fractions from specific air masses (e.g., Rozanski *et al.*, 1993).

3. Elevation increases because of rainout and condensation by way of air masses ascending and cooling (Gonantine *et al.*, 2001).

4. Distance inland increases as a result of heavier isotopes being preferentially removed and not replaced by a local evaporation source (e.g., Winnick *et al.*, 2014).

In the past, different boundary conditions, such as the spatial distribution of the incoming solar radiation, ice volume and greenhouse gases, may have led to temporal relationships between $\delta^{18}O$ and temperature significantly different from the spatial relationship derived from present-day precipitation. Certainly, independent estimates of temperature, for example, borehole and gas-phase isotope techniques, show the imperfect correlation between temperature and isotopic records from ice cores during past periods of climate change (Grachev and Severinghaus, 2005; Landais *et al.*, 2004b). Hence, the use of a present-day relation can lead to inaccurate past temperature reconstructions. Although water isotope records are very valuable past climate indicators, the array of influences on these records needs cautious interpretation.

1.3 An introduction to the Last Interglacial period

The LIG, also known as the Eemian, is believed to be the last significantly warm climate period preceding the current interglacial. The LIG is one of many warm periods taking place around every 100 thousand years for the past one million years. The common view is that global oscillations between warm interglacial and cold glacial climate states can be initiated by variations in Earth's rotational and orbital parameters (Berger and Loutre, 1991). The process behind deglaciation is that the initial insolation forcing is amplified by several feedback mechanisms such as the ice-albedo feedback (Hall, 2014), the water vapour feedback (Dessler *et al.*, 2008), inter-hemispheric coupling (Govin *et al.*, 2015; WAIS Divide Project Members, 2015) and the release of CO_2 from the ocean because of increased ocean temperatures (Monnin *et al.*, 2001). In connection with the LIG, vegetation feedbacks are thought to have been important: palaeo-proxies suggest the spreading of shrubs and boreal forests into regions such as Alaska, Greenland and Siberia (CAPE Last Interglacial Project Members, 2006)). This led to a reduction in albedo over the norther latitudes (CAPE Last Interglacial Project Members, 2006).

Whereas orbital insolation was clearly different during the LIG relative to present-day (Laskar *et al.*, 2004), atmospheric CO_2 concentration values were close to pre-industrial (PI) levels (Lüthi *et al.*, 2008). LIG global annual sea surface temperature (SST) is believed to have been 0.7 ± 0.6°C warmer and global mean annual surface temperatures (SATs) 1 to 2°C warmer than during the PI period (Turney and Jones, 2010; McKay *et al.*, 2011), with the limitation that these two data compilations assume the warmest phases in both hemispheres were globally coincident. These numbers are mostly confirmed by more recent data synthesis which solves the temporal temperature evolution (Capron *et al.*, 2014; Hoffman *et al.*, 2017). Surfaces temperatures at high latitudes, averaged across several thousand years, are thought to have been at least 2°C warmer that today (IPCC, 2013) and up to 5°C warmer over the ice sheets (EPICA community members, 2004; Masson-Delmotte *et al.*, 2015). The NEEM ice core data also indicates a warming of 8 ± 4°C compared to the last millennium (NEEM community members, 2013). These increased temperatures severely

affect the ice sheets evolution during the LIG period as evidenced by large sea level changes (e.g., Grant *et al.*, 2012).

Although the LIG was analysed in the First Assessment Report of the Intergovernmental Panel on Climate Change (Folland *et al.*, 1990), it obtained more relevance in the Fourth and Fifth Assessment Reports (AR4 and AR5) due to evidence emphasizing that there was a rise in global mean sea level of at least 5 m (but possibly no higher than 10 m) relative to present day (IPCC, 2007, 2013; Dutton *et al.*, 2015). Recent climate and ice-sheet model simulations suggest an important retreat of the West Antarctic Ice sheet (WAIS) and possibly parts of East Antarctica during the Last Interglacial (Sutter *et al.*, 2016; DeConto and Pollard, 2016) although there is still a lack of observational evidence. The contribution from the Greenland Ice Sheet (GIS) to the LIG sea-level highstand remains unclear with previous studies showing highly variable results: the GIS contribution may have been anywhere between +0.3 to +5.5 m to global mean sea level (Cuffey and Marshall, 2000; Tarasov and Peltier, 2003; Otto-Bliesner *et al.*, 2006; Born and Nisancioglu, 2012; Quiquet *et al.*, 2013; Helsen *et al.*, 2013; NEEM community members, 2013; Yau *et al.*, 2016).

Past warm climates like the LIG period, represent ideal case studies to evaluate polar amplification feedbacks in a variety of temperature changes comparable to expected future changes (Otto-Bliesner *et al.*, 2013). The LIG is also known as a relevant period for testing our understanding of interactions between the climate and ice sheets during a warm climate state. Nevertheless, the LIG should not be seen as a straight analog to future climate change because the antropogenic forcing of the near future fundamentally differs from the orbital forcing representative of the LIG.

1.3.1 Arctic sea ice changes during the LIG

Our knowledge of the concentration or extent of Arctic sea ice during the LIG period is limited. Fig. 1.1 shows the scarce set of available observations of LIG Arctic sea ice changes. New data compilations (Capron *et al.*, 2014, 2017; Hoffman *et al.*, 2017) indicate that high-latitude sea surface and surface air temperatures (SSTs and SATs) were warmer during the LIG, suggesting lower summer and winter sea ice cover

relative to today. Additionally, marine cores located in the central part of the Arctic Ocean (Fig. 1.1: GreenICE and HLY0503-8JPC cores) point to a perhaps LIG Arctic Ocean free of summer ice cover, as planktonic foraminifers representative of subpolar, seasonally open waters lived at these sites during the LIG (Adler *et al.*, 2009). This is supported by the recovery of microfauna in LIG marine sediments along the Beaufort Sea Shelf, which indicate that possibly more saline Atlantic water was present along the Beaufort Shelf, an indication of a lack of perennial Arctic sea ice cover for some time during the LIG (Brigham-Grette and Hopkins, 1995). Moreover, the ostracode sea ice proxy of Cronin *et al.* (2010) shows minimum sea ice cover during the peak of the LIG on the Lomonosov and Mendeleyev Ridges and Morris Jesup Rise (Fig. 1.1: NP26-5/32, Oden96/12-1pc and PS2200-5 cores). In addition, estimates of sea ice cover from dinoflagellate cysts (dinocysts) point to LIG ice-free conditions south of 78°N (Fig. 1.1).

In a more recent study, Stein *et al.* (2017) document that a substantial retreat of LIG sea ice occurred along the Barents Sea continental margin (Fig. 1.1: PS2138-2 core) influenced by Atlantic Water inflow, while the central LIG Arctic Ocean remained ice covered throughout the summer (Fig. 1.1: PS2200-5, PS51/038-3 and PS2757-8 cores). Thus, there is currently a lack of consensus among the marine core literature regarding the presence of seasonal or perennial sea ice coverage over the central Arctic Ocean during the LIG.

1.3.2 GIS changes during the LIG

The extent of the GIS and its likely contribution to the LIG sea-level highstand remains uncertain. LIG ice sections have been retrieved, close to the bed, at seven Greenland ice core sites: Camp Century, NEEM, NGRIP, GRIP, GISP2, Renland and DYE3 (see Fig. 1.1 for the location of the ice core sites). The suggestion of the presence of LIG ice at each one of these cores relies on the high measurements of stable water isotopes ($\delta^{18}O$) in the deepest part of each ice core. Hence, this suggests a modest retreat of the GIS during the LIG. Nevertheless, complex flow and basal melting interfering with age-depth modelling causes ice dating to be very challenging

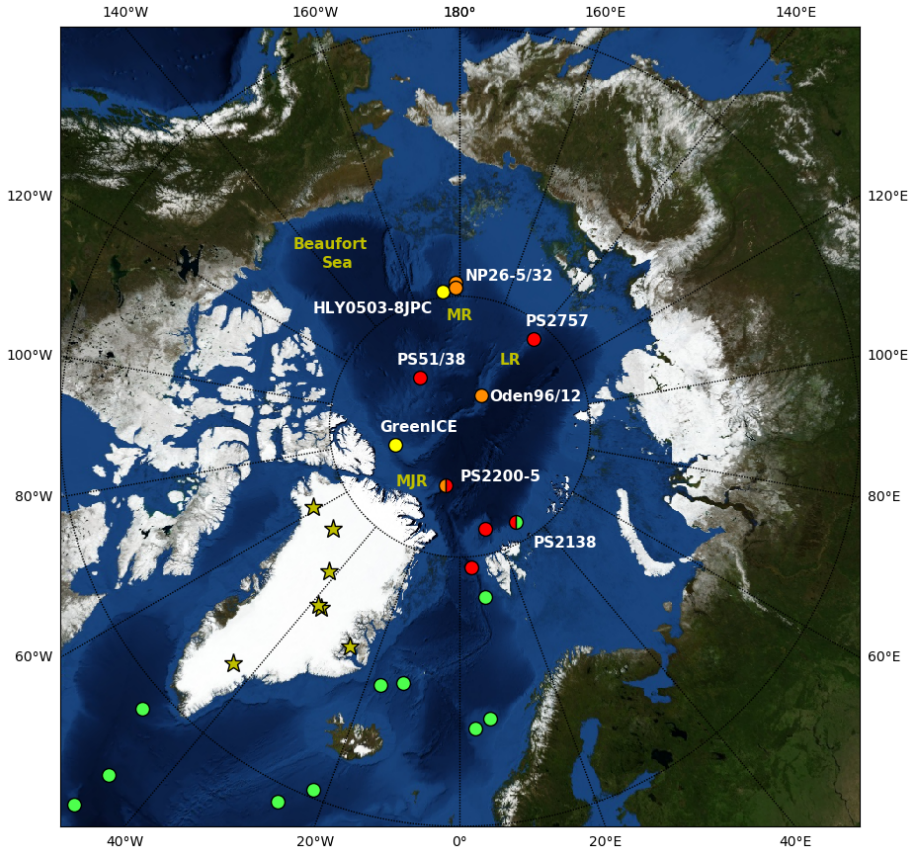

FIGURE 1.1: Map of the Arctic Ocean showing the position of observations of sea ice change based on subpolar foraminifers (yellow circles), mollusc and ostracode faunas (orange circles), biomarker proxy IP25 (red circles) and dinocysts data (green circles). Also indicated are key regions: Morris Jesup Rise (MJR), Mendeleyev Ridage (MR) and Lomonosov Ridge (LR). Also shown are Greenland ice core records (yellow stars) which contain LIG ice; these are from north to south: Camp Century (77.2°N 61.1°W), NEEM (77.5°N, 51.1°W), NGRIP (75.1°N, 42.3°W), GRIP (72.6°N, 37.6°W), GISP2 (72.6°N, 38.5°W), Renland (71.3°N, 26.7°W), DYE3 (65.2°N, 43.8°W).

at several of these sites (NGRIP Project Members, 2004; NEEM community members, 2013; Landais *et al.*, 2003).

This uncertainty on LIG-age contributes to a broad range of possible GIS scenarios for the LIG. Some studies propose strong melting in southern Greenland (e.g., Otto-Bliesner *et al.*, 2006; Tarasov and Peltier, 2003), some in northern Greenland (e.g., Quiquet *et al.*, 2013; Stone *et al.*, 2013), and others imply melting in both (e.g., Born and Nisancioglu, 2012; Calov *et al.*, 2015; Helsen *et al.*, 2013; Robinson *et al.*, 2011). Some studies even suggest a two-dome GIS structure (e.g., Calov *et al.*, 2015; Robinson *et al.*, 2011).

Interestingly though, total air content measurements suggest elevation over central Greenland was very close to present-day (Raynaud *et al.*, 1977) and the NEEM air content record have also been shown as indicative of a very modest lowering of the elevation of -130 ± 300 m compared to present-day (NEEM community members, 2013).

1.3.3 North Atlantic response to freshwater fluxes

During the penultimate deglaciation, the increased insolation forcing over the Northern Hemisphere (NH) led to rapid ice sheet retreat and enhanced freshwater input in the North Atlantic. This resulted in suppression of the Atlantic Meridional Overturning Circulation (AMOC) close to the end of the deglaciation (Carlson, 2008), and reduced North Atlantic Deep Water (NADW) formation compared to present-day (Oppo *et al.*, 1997; Lototskaya and Ganssen, 1999; Böhm *et al.*, 2015).

Previous studies with climate models of intermediate complexity present a slowdown of the AMOC due to freshwater fluxes injected into the North Atlantic (Ritz *et al.*, 2011; Loutre *et al.*, 2014; Goelzer *et al.*, 2016). Govin *et al.* (2012) investigated the melting of the GIS and its impact on NADW formation and surface temperatures at 126 ka and showed a reduction of the AMOC strength along with cooler SSTs over the North Atlantic. Similar work carried out by Otto-Bliesner *et al.* (2006) and Bakker *et al.* (2012) showed that melting of the GIS led to cooling conditions around the Labrador Sea and a decrease in the AMOC strength. Goelzer *et al.* (2016) indicated that freshwater from the Laurentide Ice Sheet (LIS) during Termination II led to a slowdown of the AMOC and increased Southern Ocean temperatures, while freshwater fluxes from the Antarctic Ice Sheet (AIS) resulted in cooling conditions in the same region. Stone *et al.* (2016) showed that freshwater fluxes injected into the North Atlantic could reproduce the reconstructed early LIG temperature patter of Capron *et al.* (2014), via a bipolar seesaw response.

Note that processes other than freshwater forcing have been proposed to cause millennial-scale changes in climate through variations in AMOC behaviour. These include wind stresses along the subpolar gyre linked to variations in the LIS shape (Zhang *et al.*,

2014) and a salt oscillator over the North Atlantic (Peltier and Vettoretti, 2014). In addition, climates at high latitudes are influenced by variations in the atmospheric circulation mode (e.g., Kleppin *et al.*, 2015).

1.3.4 Previous isotopic climate simulations of the LIG

LIG stable water isotope values ($\delta^{18}O$) measured in NGRIP and NEEM deep ice cores, and in the disturbed bottom layers at Summit, are around 3‰ higher compared to present-day (Landais *et al.*, 2004a; Suwa *et al.*, 2006a; Masson-Delmotte *et al.*, 2010; NEEM community members, 2013).

Previous simulations of the LIG, forced only by orbital forcing, using an ocean-atmosphere GCM (IPSL-CM4) with stable water isotope diagnostics, show very small increases in $\delta^{18}O$ over Greenland, accounting for less than 20% of the observed LIG-present-day isotopic anomaly (Masson-Delmotte *et al.*, 2011). Similar orbitally-driven LIG simulations carried out by Sjolte *et al.* (2014), show also limited increases in $\delta^{18}O$ across Greenland.

Since the orbital approach fails to reproduce the correct LIG-present-day $\delta^{18}O$ anomaly over Greenland, other studies (Masson-Delmotte *et al.*, 2011; Sime *et al.*, 2013) use greenhouse gas (GHG) driven model simulations (forced with 4xCO2 and 2xCO2 compared to PI values) as an approach to investigate the isotopic response to sea ice changes and sea surface warming (Sime *et al.*, 2013). Following this approach, Sime *et al.* (2013) show that if sea ice is reduced, and seas around northern Greenland warm by about +4 to +6 °C, $\delta^{18}O$ rises of around 3‰ can be simulated over central Greenland. Nevertheless, using GHG-driven simulations as analogues to the LIG climate could be problematic; the climate response to variations in the orbital parameters is very different to the climate response to variations in GHG values (Masson-Delmotte *et al.*, 2011).

Simulations considering the melting of the GIS at 126 ka, show a reduced AMOC and limited precipitation weighted $\delta^{18}O$ anomalies of 0.13 ‰ over central Greenland (Masson-Delmotte *et al.*, 2011).

1.4 Outline of the thesis

1.4.1 Objectives

As discussed in Section 1.3.4, previous isotopic climate simulations of the LIG forced only by orbital forcing have failed to reproduce the observed LIG-present-day $\delta^{18}O$ anomalies over Greenland. This together with the uncertainty on the contribution of the GIS to the LIG sea level highstand (e.g., Robinson *et al.*, 2011; Quiquet *et al.*, 2013; Helsen *et al.*, 2013) motives further research of the mechanism behind the LIG Greenland isotope peak. Thus, this research project examines how Greenland ice core $\delta^{18}O$ responds to several high-latitude feedback process which likely operated during the LIG; reduced Arctic sea ice extent, GIS changes and Northern Hemisphere freshwater forcing.

The specific objectives of this thesis are the following:

1. Investigate the potential significance of NH sea ice changes on the LIG Greenland isotopic maximum.
2. Investigate whether we can recover LIG GIS changes, and associated uncertainties, using stable water isotopic information from ice cores.
3. Study the $\delta^{18}O$ dependence on the magnitude and sign of LIG GIS elevation changes and assess how the response is altered by NH sea ice changes.
4. Isolate the isotopic signature of changes in Greenland iceberg discharge during the LIG.

1.4.2 Thesis structure

The following outlines the thesis structure followed by a summary of the contribution of this doctoral research to the published literature.

Chapter 3: This chapter investigates whether a NH sea ice retreat could have been responsible for the Greenland isotopic maximum. The HadCM3 climate model is

used to simulate the isotopic response to different Arctic sea ice retreat experiments. Model output is validated against Greenland ice core data ($\delta^{18}O$) and sea ice proxies.

Chapter 4: This chapter investigates the response of Greenland ice core $\delta^{18}O$ to variations in the morphology of the LIG GIS. Chapter 4 combines a synthesis of $\delta^{18}O$ data from deep Greenland ice cores, with simulations from HadCM3, and follows a Gaussian Process (GP) emulation approach to investigate the properties of the GIS morphologies that are compatible with the LIG $\delta^{18}O$ record.

Chapter 5: The HadCM3 climate model is used to simulate a set of LIG idealised GIS elevation change scenarios. This chapter investigates how $\delta^{18}O$ depends on the sing and magnitude of GIS elevation changes and test to which extent changes in Arctic sea ice may influence isotopic lapse rate values.

Chapter 6: Since Greenland iceberg calving fluxes in HadCM3 are tuned with regard to a present-day ice sheet distribution, they may not remain adequate for simulating past climates like the LIG, characterised by a reduced GIS (e.g., Robinson *et al.*, 2011; Quiquet *et al.*, 2013; Helsen *et al.*, 2013). This chapter explores the isotopic response to different LIG Greenland iceberg discharge scenarios.

1.4.2.1 Contribution of this PhD to published literature

Chapter 3 and 4 are published in Quaternary Science Reviews and Journal of Geophysical Research respectively. Chapters 5 is in review in Climate of the Past. Work during this thesis has also contributed to a number of collaborative projects, including:

1. **In revision scientific paper in Nature Climate Change** - Guarino, M.V., Sime, L.C., Schroeder, D., Malmierca-Vallet, I., Rosenblum, E., Ringer, M., Ridley, J., Feltham, D., Bitz, C., Steig, E.j., Wolff, E., Stroeve, J., and Sellar, A. (in revision). A sea ice-free Arctic during the Last Interglacial supports fast future loss. Nature Climate Change.

2. **In revision scientific paper in Climate of the Past** - Kageyama, M., Sime, L.C., Sicard, M., Guarino, M.V., de Vernal, A., Schroeder, D., Stein,

R., Malmierca-Vallet, I., Abe-Ouchi, A., Braconnot, P., Chamberlain, M.A., Lohmann, G., Menviel, L., Morozova, P., Nisancioglu, K., Otto-Bliesner, B., O'ishi, R., Sherriff-Tadano, S., Shi, X., Sun, B., Volodin, E., Yeung, N., Zhang, Q., Feltham, D., Bitz, C., Stroeve, J., and Ziehn, T. (in revision). A multi-model CMIP6 study of Arctic sea ice at 127 ka: Sea ice data compilation and model differences. Climate of the Past.

3. **In revision scientific paper in Climate of the Past** - Williams, C.J.R., Guarino, M.V., Capron, E., Malmierca-Vallet, I., Singarayer, J.S., Sime, L.C., Lunt D.J. and Valdes, P.J. (in revision). The UK contribution to CMIP6/PMIP4: mid-Holocene and Last Interglacial experiments with HadGEM3, and comparison to the pre-industrial era and proxy data. Climate of the Past.

Chapter 2

Methodology

2.1 The isotope-enabled HadCM3

This chapter describes the isotope-enabled coupled atmosphere-ocean HadCM3 model. This climate model was chosen for this PhD work because of its inclusion of stable water isotopes and its computational efficiency (permitting the completion of simulations of the order of hundreds of years).

HadCM3 was developed in 1998, is the third version of the UK Hadley Centre Coupled Model and the simulated climate has broadly been validated by previous studies (Cox *et al.*, 1999; Gordon *et al.*, 2000; Pope *et al.*, 2000; Pardaens *et al.*, 2003; Tett *et al.*, 2007). Previous literature has examined the models's atmosphere-ocean coupling (Gordon *et al.*, 2000), land surface scheme (Cox *et al.*, 1999), freshwater budgets (Pardaens *et al.*, 2003), atmospheric parameterizations (Pope *et al.*, 2000), transient response to GHG forcing (Tett *et al.*, 2007) and the performance of the model in the North Atlantic (e.g., Dong and Sutton, 2002) and at high northern latitudes (e.g., Stone and Lunt, 2013). HadCM3 presents a realistic and stable climatology in both the atmosphere and the ocean (Gordon *et al.*, 2000; Sime *et al.*, 2006), represents a realistic global hydrological cycle (Pardaens *et al.*, 2003), simulates observed estimates of both oceanic and atmospheric heat transport (Dong and Sutton, 2002; Cooper and Gordon, 2002) and has the ability to reproduce many observed features of climate

variability (Cooper and Gordon, 2002). HadCM3 model results have formed part of the Third, Fourth and Fifth Assessment Reports (AR) of the IPCC (IPCC, 2001, 2007, 2013).

A validation of the isotope output has also been carried out for the atmosphere only (HadAM3; Sime *et al.* (2008)) as well as for the coupled ocean-atmosphere model (Tindall *et al.*, 2009, 2010; Xinping *et al.*, 2012). HadCM3 is able to reproduce the large-scale features of $\delta^{18}O$ in precipitation, covering altitude, latitude, amount and continental effects (Tindall *et al.*, 2009). The observational dataset of Global Network of Isotopes in Precipitation (GNIP) has been used to validate the modelled $\delta^{18}O$ (Tindall *et al.*, 2009; Xinping *et al.*, 2012). In addition, simulated $\delta^{18}O$ has been compared against planktic foraminifera calcite $\delta^{18}O$ from ocean sediments (Holloway *et al.*, 2016b; Tindall *et al.*, 2010; Waelbroeck *et al.*, 2005) and modelled annual mean isotopic values of the precipitation over Greenland has been compared with observations compiled by Vinther *et al.* (2010) and Sjolte *et al.* (2011) (Sime *et al.*, 2013; Malmierca-Vallet *et al.*, 2018). HadCM3 presents a realistic representation of the geographical pattern of $\delta^{18}O$ in Greenland accumulation (Sime *et al.*, 2013), captures the variability observed in Antarctic ice cores (Tindall *et al.*, 2009), and presents good agreement with seawater $\delta^{18}O$ observations (Tindall *et al.*, 2009). The isotope-enabled HadCM3 has been used to study several paleoclimate periods such as the Eocene (Tindall *et al.*, 2010), the LIG (Sime *et al.*, 2009, 2013), the Pliocene (Tindall and Haywood, 2015) and the 8.2 ka abrupt climate change event (Tindall and Valdes, 2011).

2.1.1 Atmosphere

The HadCM3 atmosphere component is a global hydrostatic primitive equation model with a horizontal grid spacing of 2.5° (latitude) by 3.75° (longitude) (73 x 96 grid points), nineteen vertical levels and the time step is 30 minutes (Gordon *et al.*, 2000). Pope *et al.* (2000) examined the performance of the atmosphere component by forcing HadAM3 with observed SSTs. The model reproduces well the observations.

The radiation scheme included is that described in Edwards and Slingo (1996); it includes eight and six spectral bands in the longwave and shortwave respectively. The convective scheme used is that of Gregory and Rowntree (1190). The cloud scheme included is a prognostic scheme which diagnoses cloud ice and water and cloud amounts on the basis of potential temperature of liquid water and total moisture.

The land surface scheme chosen for this PhD work is MOSES 2 (Met Office Surface Exchange Scheme) (Cox *et al.*, 1999; Essery *et al.*, 2001); it includes a representation of the melting and freezing of soil moisture, and the stomatal resistance dependence on temperature, CO_2 and vapour pressure is included in the formulation of evaporation. Ice-sheets are fixed in MOSES 2. This scheme recognises nine surface types: needleleaf and broadleaf trees, temperate (C3) and tropical (C4) grasses, shrubs as well as land ice, bare soil, urban and inland water (Cox *et al.*, 1999; Essery *et al.*, 2001).

The land surface state is determined by the canopy water and temperature, amount of lying snow and moisture content of the different soil layers as displayed in Fig. 2.1. Precipitation is divided into canopy interception (C, available for evaporation), run-off (Y), throughfall (Tf), and infiltration into the ground (Cox *et al.*, 1999; Essery *et al.*, 2001). Water reaching the soil surface is lost through surface run-off and/or infiltration into the ground (Fig. 2.1). The overall moisture flux over a land gridbox is defined by four different evaporative fluxes: evaporation from wet canopy (Ec), evaporation via transpiration (Ev), evaporation from bare soil (Eb) and sublimation from a snow surface (Es) (Cox *et al.*, 1999; Essery *et al.*, 2001) (Fig. 2.1). For a full description of MOSES 2.1, the reader is referred to Cox *et al.* (1999); Essery *et al.* (2001).

The performance of HadCM3-MOSES 2 at high northern latitudes (over Greenland) is described in Stone and Lunt (2013). HadCM3 MOSES 2 is shown to be an appropriate model for studies over Greenland.

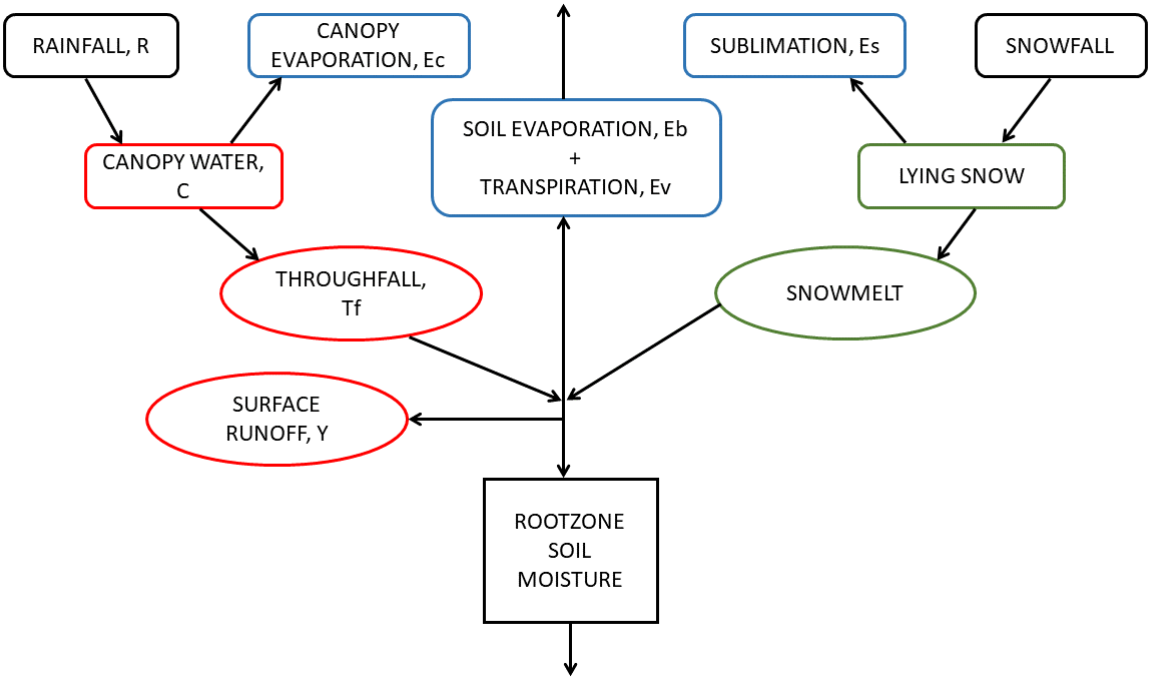

FIGURE 2.1: Schematic representation of the land surface scheme MOSES 2.1 (adapted from Cox *et al.* (1999)). Evaporation fluxes are marked in blue, variables in red refer to how precipitation is dealt with and melt from snow is represented by variables in green.

2.1.2 Ocean

The HadCM3 ocean component (HadOM3) has 20 vertical levels and a 1.25° by 1.25° latitude-longitude grid; it is a rigid lid model (Cox, 1984). For every atmosphere grid box, there are six ocean grid boxes with the potential to have partial sea ice cover. The time step is 60 minutes and the coupling with the atmosphere is once per day. The design of the vertical levels is such that resolution near the ocean surface is enhanced.

The spatial resolution is adequate to capture the key oceanic current structures (Gordon *et al.*, 2000). Due to the rigid lid model, no variation in ocean volume happens in response to fluxes of freshwater at the surface. HadCM3 does not require heat flux corrections. Nevertheless, as the iceberg calving process is not modelled in HadCM3, a small freshwater flux is prescribed into the ocean in order to balance the net snow accumulation over the ice-sheets and close the hydrological budget (Gordon *et al.*, 2000). This parameterisation will be described in more detail in Chapter 6.

2.1.3 Sea ice model

The sea ice model includes the parameterisation of ice drifts and leads (Cattle and Crossley, 1995) and a simple thermodynamic scheme derived from the zero-layer model of Semtner (1976). In the Arctic, the concentration of ice cannot surpass 0.995 since a totally unbroken ice coverage is infrequently seen in pack-ice. Water freezing in the leads results in ice formation and the removal of ice happens (1) during the year by melting at the base, and (2) during the summer months by melting at the surface. The formation of "white" ice can increase the sea ice depth (Gordon *et al.*, 2000).

Variations in ocean salinity due to the formation of sea ice are accounted for by considering a salinity constant of 0.6 ‰ for the sea ice. While ocean salinity increases due to sublimation processes, it decreases when white ice is formed. It is assumed that all rainfall reach the ocean surface though leads.

For temperatures below -10°C, the sea ice surface albedo is 0.8 and descends linearly to 0.5 for temperatures between -10°C and 0°C. This accounts for the formation of melt ponds, snow ageing and the rather low albedo of bare ice. In section 3.4.1, the model sea ice output over the Arctic Ocean is reviewed and compared against the observational sea ice data of Meier *et al.* (2017) and Peng *et al.* (2013).

2.1.4 Isotopes

Tindall *et al.* (2009) describe the inclusion of $\delta^{18}O$ into HadCM3. Because of the different structure of the ocean and atmosphere components of HadCM3, isotopes are incorporated in each component using distinct techniques (Tindall *et al.*, 2009). Since water is modelled explicitly in HadAM3, two water species are added: $H_2^{18}O$ and $HD^{16}O$. The advection of the water vapour and associated isotopes is thus a function of their spatial gradients (Tindall *et al.*, 2009). The ocean component, HadOM3, is a rigid lid model which assumes a fixed volume of water for each grid box. Consequently, the isotopes are included as tracers, so that each isotope species comprises a fraction of each grid box. The technique used to incorporate isotopes in HadCM3 is thus a tracer advection scheme, similar to those already included in the model (e.g. salinity and temperature) (Tindall *et al.*, 2009). In terms of the schemes of advection and convection, there is no distinction between "normal" water and isotopic tracers. Nevertheless, if the scheme of advection leads to physically unrealistic changes in $\delta^{18}O$, a scheme of "water-filling" is included which redistributes some $\delta^{18}O$ between nearby grid boxes after the step of advection to correct this (Tindall *et al.*, 2009).

The technique used for the conservation of isotopes is the same to that used for salinity; a flux correction field is necessary for salinity to represent the iceberg calving process, one is also implemented for isotopes to account for the reintroduction into the ocean of $H_2^{18}O$. $H_2^{16}O$ and $H_2^{18}O$ in precipitation, runoff and evaporation, lead to water and isotope fluxes into the ocean, which are transformed into a virtual isotope flux. This is similar to the virtual salinity flux and modifies the ratio of $H_2^{18}O/H_2^{16}O$ at the ocean top level by an amount in accordance with the fluxes of water and isotope

from the atmosphere and land surface (Tindall *et al.*, 2009). HadCM3 imposes a limit on salinity of between 0 to 40 psu, comparable limits are implemented for $\delta^{18}O$; -10 and +10 ‰ for the lower and upper values of $\delta^{18}O$. Thus, in relation to conservation, isotopes do not require any extra parametrization compared to salinity. Using exactly the same method as for $\delta^{18}O$, deuterium is also included in HadCM3.

Chapter 3

Simulating the LIG Greenland stable water isotope peak: The role of Arctic sea ice changes

This chapter is published in Quaternary Science Reviews as; Malmierca-Vallet, I., Sime, L.C., Tindall, J.C., Capron, E., Valdes, P.J. Vinther, B.M., and Holloway, M.D. 2018. Simulating the Last Interglacial Greenland stable water isotope peak: The role of Arctic sea ice changes. Quaternary Science Reviews 198, 1-14, doi:10.1016/j.quascirev.2018.07.027.

I.M.V. performed the isotope-enabled climate model experiments, carried out the analysis and wrote the article. L.C.S. provided feedback throughout the writing and analysis and L.C.S. also provided the initial motivation. P.J.V., J.C.T. and M.D.H. provided technical advice about how to perform and interpret the climate model simulations. E.C. and B.M.V. provided additional advice related to interpreting $\delta^{18}O$ ice core records. All authors discussed the model results and commented on the manuscript.

3.1 Abstract

Last Interglacial (LIG), stable water isotope values ($\delta^{18}O$) measured in Greenland deep ice cores are at least 2.5‰ higher compared to the present day. Previous isotopic climate simulations of the LIG do not capture the observed Greenland $\delta^{18}O$ increases. Here, we use the isotope-enabled HadCM3 (UK Met Office coupled atmosphere-ocean general circulation model) to investigate whether a retreat of Northern Hemisphere sea ice was responsible for this model-data disagreement. Our results highlight the potential significance of sea ice changes on the LIG Greenland isotopic maximum. Sea ice loss in combination with increased sea surface temperatures, over the Arctic, affect $\delta^{18}O$: water vapour enriched in heavy isotopes and a shorter distillation path may both increase $\delta^{18}O$ values over Greenland. We show, for the first time, that simulations of the response to Arctic sea ice reduction are capable of producing the likely magnitude of LIG $\delta^{18}O$ increases at NEEM, NGRIP, GIPS2 and Camp Century ice core sites. However, we may underestimate $\delta^{18}O$ changes at the Renland, DYE3 and GRIP ice core locations. Accounting for possible ice sheet changes is likely to be required to produce a better fit to the LIG ice core $\delta^{18}O$ values.

3.2 Introduction

Polar Regions are especially sensitive to variations in radiative forcing; they can act as amplifiers of climate change via albedo feedbacks (e.g., IPCC, 2013). Studying these climate feedback processes is fundamental for better understanding future high-latitude responses to increasing greenhouse gas (GHG) emissions. Past warm periods like the Last Interglacial (LIG, approximately 129-116 thousand of years BP, hereafter ka) provide an ideal case study to evaluate the capability of climate models to appropriately capture processes involved in polar amplification (e.g., Otto-Bliesner *et al.*, 2013; Schmidt *et al.*, 2014).

During the LIG, large parts of the Earth showed warmer conditions compared to present day (e.g., CAPE Last Interglacial Project Members, 2006; Turney and Jones, 2010). The increase in summertime insolation at northern high latitudes contributed

to a warmer-than-present-day Arctic region (CAPE Last Interglacial Project Members, 2006; IPCC, 2013), and maximum global sea level reached 6 to 9 m above present level (e.g., Dutton *et al.*, 2015; Kopp *et al.*, 2009).

Little is known about the precise extent or concentration of Northern Hemisphere (NH) sea ice during the LIG. Figure 1.1 and Supplementary Table 3.5 show the sparse set of available observations of NH sea ice changes for the LIG. As recent data compilations show that high northern latitude surface air temperatures (SATs) and sea surface temperatures (SSTs) were warmer in the LIG (Capron *et al.*, 2014, 2017; Hoffman *et al.*, 2017), it is probable that there was both reduced winter and summer sea ice extent compared to today. This is supported by marine cores located in the Arctic Ocean (Fig. 1.1: GreenICE and HLY0503-8JPC cores) which show planktonic foraminifers characteristic of subpolar, seasonally open waters were present at these sites during the LIG, possibly reflecting ice free summer conditions in the central LIG Arctic Ocean.

In addition, LIG deposits on the Chukchi Sea coast include fossils of species presently known to be limited to the warmer northwest Pacific, while intertidal snails retrieved close to Nome suggest annually ice-free conditions around the coast south of the currently seasonally ice covered Bering Strait (Brigham-Grette and Hopkins, 1995; Brigham-Grette *et al.*, 2001). Deposits close to Barrow contain some ostracode species that are only found today in the North Atlantic and deposits on the Alaskan Coastal Plain indicate that several mollusc species expanded their range well into the Beaufort Sea (Brigham-Grette and Hopkins, 1995). The nature of marine faunas at St. Lawrence Island, Beaufort Sea shelf and Nome suggests that winter sea ice did not expand south of Bering Strait, and that the Bering Sea was annually ice-free (Brigham-Grette and Hopkins, 1995) (Fig. 1.1 and Supplementary Table 3.5). Additionally, the ostracode sea ice proxy of Cronin *et al.* (2010) (Fig. 1.1: NP26-5/32, Oden96/12-1pc and PS2200-5 cores) agree with the idea of sea ice glacial-interglacial variability, with sea ice maximum on the Morris Jesup Rise and the Lomonosov and Mendeleyev Ridges during interglacial-to-glacial transitions and minimum coverage during peak interglacial periods (e.g. MIS 5e) (Supplementary Table 3.5).

In a recent study, a more direct sea ice proxy named "IP25" is used in combination with terrestrial and open-water phytoplankton biomarkers to reconstruct the Arctic sea ice distribution during the LIG (Stein *et al.*, 2017). The authors propose relatively closed sea ice cover conditions over PS2757-8 core (Fig. 1.1 and Supplementary Table 3.5), possibly ice-free conditions in the direction of the East Siberian shelf and significantly reduced sea ice cover over the Barents Sea continental margin (Fig. 1.1: PS2138-2 core). In contrast to previous studies (e.g., Adler *et al.*, 2009), that point to an Arctic Ocean perhaps free of summer sea ice, Stein *et al.* (2017) indicate the presence of perennial sea ice in two cores from central Arctic Ocean during MIS 5e (Fig. 1.1: PS2200-5 and PS51/038-3 cores). Note, however, planktonic foraminifers were also present at these two sites (PS2200-5 and PS51/038-3) during the LIG, possibly reflecting phases of summer open-water conditions to allow foraminifers to reproduce (Spielhagen *et al.*, 2004).

Measurements of stable water isotopes, $\delta^{18}O$ and δD, in ice cores yield useful information on past temperature changes. High latitude local temperature is a principal control on the distribution of $\delta^{18}O$ and δD in preserved Greenland ice (Dansgaard, 1964). Originally, $\delta^{18}O$ measurements have been translated into temperature making use of a linear relationship ($\delta^{18}O$ = aT + b, T being surface temperature) obtained from spatial information (e.g., Dansgaard, 1964; Jouzel *et al.*, 1994, 1997). However, over the last decades, it has become evident that this isotope-temperature relationship is affected by atmospheric transport, evaporation conditions and precipitation intermittency, and therefore varies in both space and time (e.g., Jouzel *et al.*, 1994, 1997; Masson-Delmotte *et al.*, 2011). By influencing these key aspects, sea ice condition changes have been proposed to exert significant control over the distribution of isotopes in polar ice (e.g., Holloway *et al.*, 2016a, 2017; Rehfeld *et al.*, 2018; Sime *et al.*, 2013).

LIG ice layers have been found in numerous Greenland deep ice cores (Fig. 1.1) (e.g., NGRIP Project Members, 2004; NEEM community members, 2013; Landais *et al.*, 2016). The LIG $\delta^{18}O$ anomaly estimated at the initial snowfall NEEM deposition site (value of 3.6‰ at 126 ka) was translated into precipitation-weighted surface temperatures 7.5 ± 1.8 °C warmer compared to the last millennium and +8 ± 4

°C when accounting for Greenland ice sheet elevation changes and upstream effects (NEEM community members, 2013). LIG climate simulations in response to GHG and orbital forcing alone fail to capture these anomalies for both $\delta^{18}O$ and temperature (e.g., Lunt *et al.*, 2013; IPCC, 2013; Otto-Bliesner *et al.*, 2013; Sjolte *et al.*, 2014). Recent sensitivity studies show that changes in the GIS topography and sea ice retreat in the Nordic Seas can lead to enhanced surface warming (up to 5 °C) in northwest Greenland, reducing the mismatch between models and data (Merz *et al.*, 2014a, 2016).

Whereas the temperature profile measured in the borehole can be used to calibrate the Holocene isotope-temperature slope (Vinther *et al.*, 2009), this is not possible for the LIG as palaeotemperatures for this period are not conserved in the ice sheet. This means that, the use of isotopically enabled General Circulation Models (GCMs) is probably the best available method to constrain the LIG isotope-temperature slope (e.g., Sime *et al.*, 2013; Sjolte *et al.*, 2014). Previous isotopic climate simulations of the LIG underestimate the $\delta^{18}O$ anomalies of $+3‰$ observed in Greenland ice cores (Masson-Delmotte *et al.*, 2011; Sjolte *et al.*, 2014). An exception is the study carried out by Sime *et al.* (2013) where Greenland $\delta^{18}O$ anomalies of $> 3‰$ are simulated over central Greenland. Note, however, that Sime *et al.* (2013) use GHG forced simulations as analogies for the LIG climate which could be problematic because the climate response to the anthropogenic forcing projected for the near future is essentially different from the climate response to the orbital forcing characteristic of the LIG warmth.

Here we therefore aim to better understand the processes behind the LIG Greenland isotope peak. In particular,we investigate whether a retreat of NH sea ice could have been responsible for the Greenland isotopic maximum. Thus, we design a set of LIG sea ice sensitivity experiments that complement previous modelling studies with the detailed investigation of the role of NH sea ice changes on LIG isotopic simulations.

In overview, we first describe the isotopic model and explain the design of the LIG sea ice sensitivity experiments. Secondly, we summarise existing Greenland water isotopic as well as Arctic and Atlantic sea surface information across the LIG. Third, we analyse the modelled NH anomalies for $\delta^{18}O$ and temperature and discuss the

response of the hydrological cycle to sea ice retreat. Finally, we summarise our findings and draw together some conclusions.

3.3 Methods

3.3.1 Model description

In order to investigate the isotopic response to a retreat of NH sea ice, we use the isotope-enabled HadCM3 (Hadley Centre Coupled Model Version 3); a UK Met Office coupled atmosphere ocean GCM. The horizontal grid spacing of the atmosphere component is 2.5° (latitude) by 3.75° (longitude) with 19 vertical levels (Gordon *et al.*, 2000). The ocean component has a horizontal grid resolution of 1.25° by 1.25° and has 20 vertical levels (Gordon *et al.*, 2000). In addition to the ocean and atmosphere components, HadCM3 also includes sea ice and vegetation components (Gordon *et al.*, 2000). We use the TRIFFID (Top-down Representation of Interactive Foliage and Flora Including Dynamics) dynamic global vegetation model and the MOSES 2.1 land surface scheme where energy and water fluxes between the surface and the atmosphere are calculated.

HadCM3 has been used to investigate the Last Glacial Maximum (Holloway *et al.*, 2016b), past warm intervals (Holloway *et al.*, 2016a; Tindall and Haywood, 2015), as well as present day (Tindall *et al.*, 2009). The representation of the distribution of isotopes in the atmosphere and ocean shown by the model is reasonable (Tindall *et al.*, 2009, 2010) (see Supplementary information, section 3.7.1 for a more detailed description of how HadCM3 performs across Greenland).

3.3.2 Experimental setup - isotopic simulations

HadCM3 is used to simulate the isotopic response to different sea ice retreat scenarios. We perform snapshot simulations, representative of 125 ka conditions. All LIG climate model simulations are driven with greenhouse gas concentrations and

orbital parameters for 125 ka and compared to a pre-industrial (PI) control experiment, driven with greenhouse gas values and orbital parameters for 1850-years before present (BP). All experiments are run with a pre-industrial ice-sheet distribution (US Navy 100 dataset - see unified model documentation No 70 by Jones (1995)). Each of the 70-year long LIG sea ice sensitivity experiments are continued from a 200-year long spin-up of a 125 ka control simulation. The 200-year long spin up ensures quasi equilibrium conditions between the atmosphere and the upper ocean.

To test whether NH sea ice retreat was responsible for the Greenland LIG isotope peak, we perform a suite of experiments each with a different reduction in Arctic sea ice extent. To generate the sea ice retreats, we apply the same method previously used by Holloway *et al.* (2016a) and implement heat fluxes (from 0 Wm^{-2} up to 300 Wm^{-2}) to the bottom of the NH sea ice. No other effects are applied to the model physics. That is, the sea ice specific heat flux forcing is kept constant during the whole annual cycle, so the seasonal cycle of sea ice decay and growth is still calculated by the model. The atmosphere and ocean components respond to sea ice variations and sea ice thus changes over time with the coupled model. A full list of experiments is shown in Supplementary Table 3.6. A total of 22 experiments have been conducted with different sea ice scenarios each forced by a sea ice heat flux from between 0 and 300 Wm^{-2}. This approach explores the impact of forced Arctic sea ice changes on the ice $\delta^{18}O$ signal across Greenland.

3.3.3 Model-data comparison

3.3.3.1 Greenland ice core data

To evaluate the impact of different sea ice configurations on the $\delta^{18}O$ ice core record, the model results are compared to the $\delta^{18}O$ values in LIG ice layers. These layers have been identified near the bedrock of seven Greenland deep ice cores: NEEM (NEEM community members, 2013), NGRIP (NGRIP Project Members, 2004), GISP2 (Grootes *et al.*, 1993), GRIP (GRIP members, 1193), Camp Century (Dansgaard *et al.*, 1969), Renland (Johnsen *et al.*, 2001) and DYE-3 (Dansgaard *et al.*, 1982) (NEEM community members, 2013; Johnsen and Vinther, 2007) (Fig. 1.1 and Table 3.1).

TABLE 3.1: Modelled annual mean precipitation-weighted $\delta^{18}O$ anomalies (‰) at seven ice core sites (NEEM, NGRIP, GRIP, Renland Camp Century, DYE3 and GISP2) for selected LIG simulations.

	NEEM	**NGRIP**	**GRIP**	**Renland**	**Camp Century**	**DYE3**	**GISP2**
	Observed δ^{18}O anomalies (‰)						
	3.6	**3.1**	**3.5**	**3.5**	**2.5**	**4.7**	**2.7**
Exp ID	**Modelled δ^{18}O anomalies (‰)**						
125-ka control	1.7	1.4	1.1	0.2	0.5	-0.3	1.1
WSIR-7	2.6	2.2	1.6	0.6	1.6	-0.1	1.6
WSIR-35	3.6	3.2	2.8	1.8	3.6	0.9	2.8
WSIR-94	3.7	3.2	2.7	1.4	3.7	1.1	2.7

The bottom of the DYE-3, Camp Century, Renland, GRIP and GISP2 ice cores is affected by stratigraphic disturbances and cannot be unambiguously datable (e.g., Johnsen *et al.*, 2001; Grootes *et al.*, 1993; Landais *et al.*, 2003). It is possible that the NGRIP core does not cover the entire LIG, however, its stratigraphy is well preserved all the way down to bedrock (NGRIP Project Members, 2004). Peak NGRIP LIG $\delta^{18}O$ ice values were 3.1‰ higher than present day (Johnsen and Vinther, 2007).

The recent deep drilling at NEEM yielded an 80 m section of ice in stratigraphic order, in between disturbed layers. It extends the Greenland $\delta^{18}O$ record back to 128.5 ka (NEEM community members, 2013). At 126 ka, $\delta^{18}O$ ice values were estimated to be 3.6‰ higher than preindustrial local values at the NEEM deposition site (around 205 ± 20 km upstream of the NEEM drilling site) (NEEM community members, 2013). The NEEM community members (2013) used the Holocene isotope-temperature relationship of 0.5‰/°C (calibrated using borehole temperature data from other Greenland ice cores; Vinther *et al.* (2009)) to translate the 3.6‰ anomaly into a local warming of 7.5 ± 1.8 °C. After accounting for ice sheet elevation changes and upstream effects, this resulted in a reconstruction of a 8 ± 4 °C warming compared to the last millennium (NEEM community members, 2013). Using an alternative method based on measurements of the ice core air isotopic composition ($\delta^{15}N$), Landais *et al.* (2016) deduce a similar surface temperature warming at NEEM of 8 ± 2.5 °C at 126 ka. Note that this latter estimate does not account for ice sheet altitude changes.

3.3.3.2 Sea surface temperature observations

Syntheses of maximum LIG surface temperature based on ice, marine and terrestrial archives (Turney and Jones, 2010; McKay *et al.*, 2011) have been until recently used for model evaluation (e.g., Lunt *et al.*, 2013; Sime *et al.*, 2013). However given that the warming was not synchronous globally (e.g., Govin *et al.*, 2012; Bauch and Erlenkeuser, 2008), these syntheses do not provide a realistic representation of the LIG climate nor a specific time slice.

More recent compilations by Capron *et al.* (2014) and Hoffman *et al.* (2017) have developed harmonized chronologies for paleoclimatic records to produce a spatio-temporal representation of the LIG climate. Capron *et al.* (2014, 2017) produced five 2000 year long time slices of high-latitude (above 60°N and 60°S) air and sea surface temperature anomalies centred on 115, 120, 125, 127 and 130 ka. Hoffman *et al.* (2017) provide time slices of global extent of SST anomalies at 120, 125 and 129 ka. While Capron *et al.* (2014) gather mainly summer high-latitude SST records, Hoffman *et al.* (2017) provide annual and summer SST records extending down to the tropics. These two datasets use different reference chronologies and distinct methodologies to deduce temporal surface temperature changes and associated uncertainties. Therefore, the two compilations should be used as independent data benchmarks (Capron *et al.*, 2017).

Here, we compare our model results with the LIG SST datasets compiled for the time interval 125 ka by Capron *et al.* (2014) and Hoffman *et al.* (2017) in the high latitude regions. In order to determine the degree of agreement between model results and data, we calculate the root mean square error (RMSE). We do not consider this analysis as an ideal skill score owing to uneven data coverage. Nevertheless, it provides a first-order estimate of the ability of the model to replicate the observations.

3.4 Isotopic simulation results

We present results from 22 sea ice scenarios here; In each case climatological averages are determined considering the last 50 years of the simulations and a two-sided Student's t-test is used to assess the statistical significant of changes (e.g., von Storch and Zwiers, 2001). In addition we focus on three example scenarios which depict low, medium and high sea ice loss. The example experiments show a winter sea ice reduction (hereafter WSIR) compared to the PI simulation of 7% (WSIR-7), 35% (WSIR-35), and 94% (WSIR-94) (experiments marked in red in Supplementary Table 3.6).

3.4.1 Model performance

We start the results section by reviewing the model sea ice output over the Arctic Ocean. Fig. 3.1 shows the comparison of the PI simulation to gridded observational sea ice data (Meier *et al.*, 2017; Peng *et al.*, 2013). HadCM3 simulates too little summer sea ice under PI conditions (Fig. 3.1f). Over the Labrador, Norwegian, Barents and Bering seas, the comparison reveals too much winter sea ice under PI conditions (Fig. 3.1c). The model-data mismatch may partly be attributed to the model sea ice physics. Although HadCM3 produces a fairly realistic simulation of sea ice (as previously described by Gordon *et al.* (2000)), the ice pack is represented by a single ice-thickness category and sea ice dynamics are modelled in a rather simple manner (e.g., sea ice is advected via the ocean surface currents) compared to more recent sea ice models (e.g. CICE sea-ice model). Furthermore, the difference between the modern reference (1979–1989 AD) used for the data and the PI reference used for the model may also contribute to the discrepancies between model output and data. For example, during the preindustrial era, the lower GHG emissions relative to the period 1979–1989 (IPCC, 2013), may have allowed more extensive winter sea ice cover.

3.4.2 Sea ice extent

For this analysis, we use the standard definition of sea ice extent: the ocean area where sea ice concentration (sic) is at least 15%. Plots of the September and March Arctic sea ice concentrations are presented in Fig. 3.2.

For the PI simulation, the mean annual sea ice extent is 12.77 x $10^6 km^2$, with a March mean of 18.90 x $10^6 km^2$ and a September mean of 5.43 x $10^6 km^2$ (Table 3.2). The 125ka control simulation (no sea ice forcing) show a lower September mean (4.05 x $10^6 km^2$ - Table 3.2) compared to the PI experiment. This is expected because, during the LIG, larger seasonal and latitudinal insolation variations at the top of the atmosphere (linked to the orbital forcing) resulted in melting of the Arctic sea ice during summer/spring (e.g., Otto-Bliesner *et al.*, 2006).

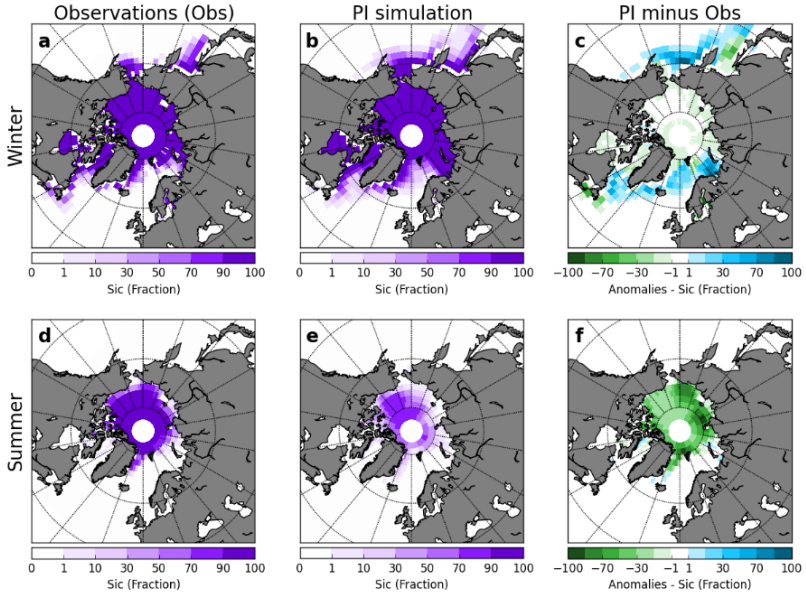

FIGURE 3.1: Comparison of the PI simulation to gridded observational sea ice data. Observational data for: (a) winter (March) and (d) summer (September) sea ice concentration (Meier *et al.*, 2017; Peng *et al.*, 2013). In particular, we use the Goddard Merged sea ice record from 1979 to 1989 (see Meier *et al.* (2017); Peng *et al.* (2013) for more information about the sea ice data). Simulated sea ice concentration for: (b) winter (March) and (e) summer (September) under PI conditions. (c) and (f) show anomalies (PI minus observations) for winter and summer respectively.

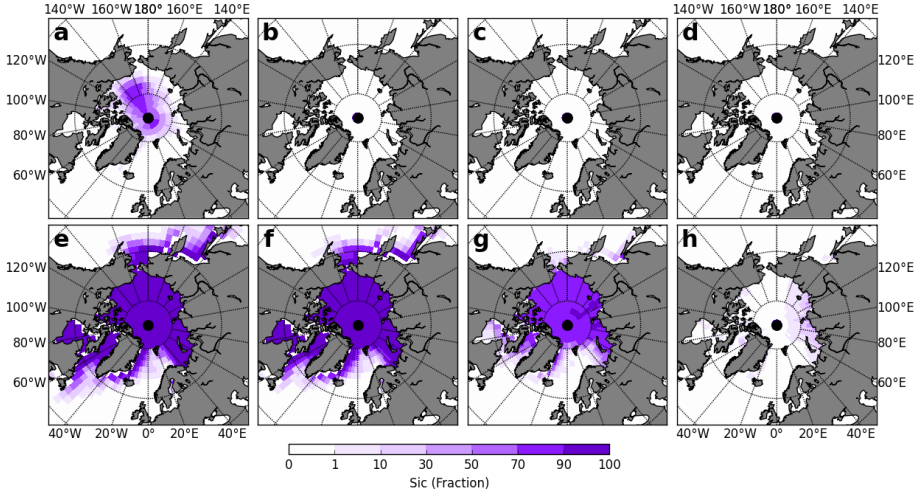

FIGURE 3.2: Mean sea ice concentrations (sic - %) for September (first row) and March (second row) for the experiments: 125-ka control (a and e), WSIR-7 (b and f), WSIR-35 (c and g) and WSIR-94 (d and h).

TABLE 3.2: Monthly and annual mean sea ice extent and amplitude of sea ice extent (maximum minus minimum annual sea ice extent) for the PI and selected LIG simulations. Values expressed in $10^6 km^2$.

	PI	**125ka-control**	**WSIR-7**	**WSIR-35**	**WSIR-94**
jan	15.76	16.03	14.60	8.87	2.30
feb	18.00	18.18	16.59	11.94	3.37
mar	18.90	19.46	17.62	12.25	1.18
apr	18.88	19.22	17.35	6.74	0.00
may	16.62	16.87	15.07	0.00	0.00
jun	13.85	13.70	9.93	0.00	0.00
jul	9.54	8.06	1.71	0.00	0.00
aug	6.08	4.59	0.00	0.00	0.00
sep	5.43	4.05	0.00	0.00	0.00
oct	6.53	5.67	0.00	0.00	0.00
nov	10.47	10.25	5.82	0.10	0.06
dec	13.20	13.30	11.58	1.41	0.68
Mean annual extent	**12.77**	**12.45**	**9.19**	**3.44**	**0.63**
Extent amplitude	**13.47**	**15.41**	**17.62**	**12.25**	**3.37**

The 125 ka control simulation with no additional sea ice forcing shows a mean annual sea ice extent of 12.45 x $10^6 km^2$. For the LIG sea ice retreat experiments, the annual mean sea ice extent ranges from 9.19 x $10^6 km^2$ to 0.63 x $10^6 km^2$ depending on the prescribed sea ice forcing (Table 1). The lowest March extent (1.18 x $10^6 km^2$) is shown by the experiment with the highest sea ice forcing (WSIR-94) (Table 3.2). To calculate the number of ice free days per year, we consider "nearly ice-free conditions" when the extent of sea ice is less than $10^6 km^2$ (IPCC AR5 definition; IPCC (2013)). While the sea ice sensitivity experiments show approximately 83 (WSIR-7), 205 (WSIR-35), 271 (WSIR-94) ice-free days per year, the PI and 125ka control simulations have none. Supplementary figure 3.14d shows the annual cycle of Arctic sea ice extent in the LIG simulations. The sea ice extent amplitude is 13.47 x $10^6 km^2$ and 15.41 x $10^6 km^2$ for the PI simulation and 125 ka control simulation respectively (Table 3.2). When simulating the response to a strong sea ice loss (WSIR-94), we obtain a much lower seasonal amplitude of 3.37 x $10^6 km^2$ (Table 3.2). WSIR-7 and WSIR-35 experiments show sea ice extent amplitudes of 17.62 x $10^6 km^2$ and 12.25 x $10^6 km^2$ respectively (Table 3.2).

3.4.3 Sea surface and surface air temperatures

For the 125 ka control simulation with no additional sea ice forcing, there is an increase of NH summer (June-July-August - JJA) temperatures compared to the PI simulation (local increases exceed 3 °C - Supplementary Fig. 3.15c). All sea ice loss experiments reveal an Arctic warming all year round despite reduced winter insolation (Supplementary Fig. 3.15d to 3.15l). The Arctic warming, which peaks during the winter months (December-January-February - DJF) (Supplementary Fig. 3.15e, 3.15h and 3.15k), is associated with sea ice retreat, through warmer, expanded ocean waters leading to a warmer atmosphere. This warming impacts the entire circumpolar region, including Greenland.

The large precipitation-weighted surface air temperature signal reconstructed for the NEEM depositional site of +7.5 ± 1.8 °C (8 ± 4 °C when accounting for GIS elevation changes) is not reproduced by any of our LIG simulations. At the NEEM deposition

site, the experiments WSIR-7, WSIR-35 and WSIR-94 show precipitation-weighted SAT anomalies of 2.5 °C, 3.5 °C, 3.0 °C respectively, whereas the 125 ka control simulation reveals a more modest warming of 2.1 °C relative to the PI control experiment. This underestimation in models of the LIG warming has already been extensively discussed in previous studies (e.g., Lunt *et al.*, 2013; Sime *et al.*, 2013; Landais *et al.*, 2016).

Fig. 3.3 shows results from the 125 ka simulations compared with the 125 ka time slice of Capron *et al.* (2014). Simulated summer SST anomalies are defined as July-August-September (JAS) for coherence with the dataset from Capron *et al.* (2014). Considering the uncertainties on SST estimates (±2.6 °C on average, see Capron *et al.* (2014, 2017) for 2σ uncertainty estimates of individual records), the match between the model simulation with no additional sea ice forcing and data is reasonable (Fig. 3.3a, RMSE = 3.0 °C). We obtain similar values of RMSE for NH SSTs for all simulations regardless of the sea ice forcing (Fig. 3.3). All simulations fail to reproduce the reconstructed SST anomalies at the sites characterised by cooler-than-present-day conditions irrespective of the sea ice forcing (Fig. 3.3). These are located in the Norwegian Sea and in the region south of Greenland. Previous modelling studies (e.g., Capron *et al.*, 2014; Pedersen *et al.*, 2016b) have also difficulties to capture this cooling trend over these regions. Bauch *et al.* (2012) propose a reduced Atlantic Ocean heat transfer to the LIG Arctic which could explain the regional cooling over the Nordic Seas. And, Langebroek and Nisancioglu (2014) simulate (with the Norwegian Earth System Model - NorESM) cooling conditions over central North Atlantic and Nordic Seas for the LIG, suggesting the simulated climate over these areas may be model dependent.

In addition, the model results are compared with the 125 time slice from the Hoffman *et al.* (2017) synthesis. All LIG simulations are generally in good agreement with both summer and annual SST data, considering the uncertainty range related to SST estimates (see Hoffman *et al.* (2017) for 2σ uncertainty estimates of individual records) (Figs. 3.4 and 3.5). While the experiments with medium and strong sea ice forcing (WSIR-35 and WSIR-94) show the lowest RMSE values ("best" model-data agreement) for both summer (RMSE = 1.5 °C and 1.4 °C respectively) and

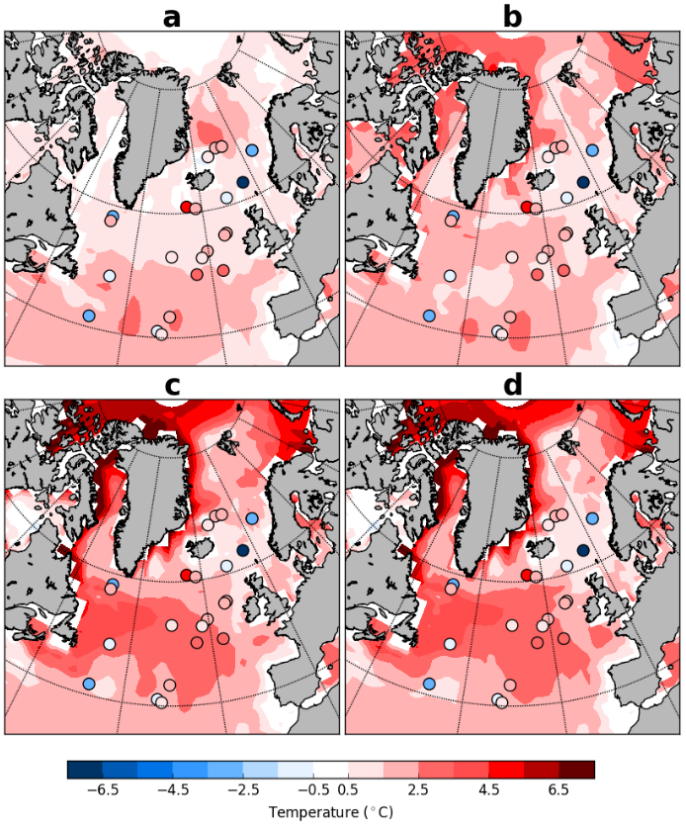

FIGURE 3.3: The 125 ka data-based time slice (dots) provided by Capron *et al.* (2014) superimposed onto modelled summer (JAS) SST anomalies relative to the PI simulation for: (a) 125ka-control (RMSE = 3.0), (b) WSIR-7 (RMSE = 3.0), (c) WSIR-35 (RMSE = 3.2) and (d) WSIR-94 (RMSE = 3.2).

annual (RMSE = 1.5 °C and 1.4 °C respectively) SSTs, the 125ka control simulation reveals the highest RMSE values (2.3 °C and 1.9 °C for summer and annual SSTs respectively) (Figs. 3.4 and 3.5).

3.4.4 Response of the hydrological cycle to the sea ice retreat

Annual, winter (DJF) and summer (JJA) averages of Arctic evaporation are shown in Fig. 3.6. Directly over areas of reduced Arctic sea ice cover, simulations show an increase in evaporation. Over the Arctic Ocean, all sea ice reduction experiments show an increase in evaporation during both summer and winter compared to the PI simulation (Fig. 3.6). When sea ice melts, the replacement of ice at temperatures below zero by open waters, results in a significant increase in evaporation, particularly during the winter months (Fig. 3.6h and k).

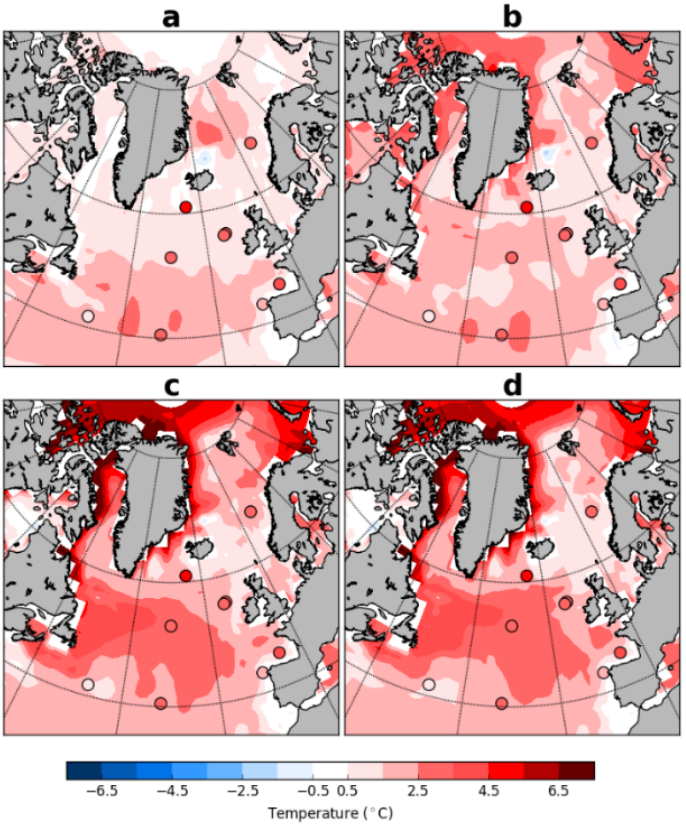

FIGURE 3.4: The 125 ka data-based time slice (dots) provided by Hoffman *et al.* (2017) superimposed onto modelled summer (JAS) SST anomalies relative to PI simulation for: (a) 125ka-control (RMSE = 2.3), (b) WSIR-7 (RMSE = 1.9), (c) WSIR-35 (RMSE = 1.5) and (d) WSIR-94 (RMSE = 1.4). Due to its coastal proximity we exclude MD95-2040 site from our model-data analysis. See Hoffman *et al.* (2017) for additional information.

Over the Arctic Basin, local increases in winter evaporation rate exceed 1 mm/day in WSIR-35 and 1.3 mm/day in WSIR-94, while in the low sea ice retreat scenario, WSIR-7, local increases are closer to 0.4 mm/day (Fig. 3.6e, h, k).

The increase in evaporation rate during both summer and winter leads to an increase in precipitation (Supplementary Fig. 3.16). The ice retreat experiments display similar spatial anomalies, particularly the rise in precipitation in the Arctic Ocean (Supplementary Fig. 3.16). The increases are more widespread and larger in WSIR-35 and WSIR-94 than in WSIR-7, which is expected considering the larger sea ice loss (Supplementary Fig. 3.16d-l). The increase in precipitation is greater during the winter months than during summer when precipitation is highest in the Arctic (Supplementary Fig. 3.16). A direct atmospheric reaction to sea ice loss and warmer SATs is a decrease in mean sea level pressure (MSLP). The less stable and warmer

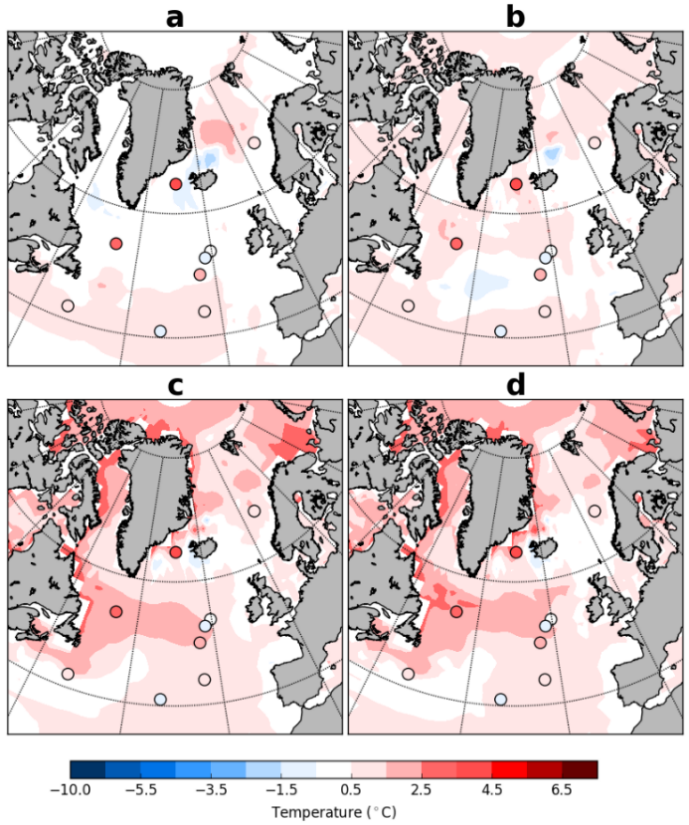

FIGURE 3.5: The 125 ka data-based time slice (dots) provided by Hoffman *et al.* (2017) superimposed onto modelled annual SST anomalies relative to PI simulation for: (a) 125ka-control (RMSE = 1.9), (b) WSIR-7 (RMSE = 1.5), (c) WSIR-35 (RMSE = 1.5) and (d) WSIR-94 (RMSE = 1.4). Due to its coastal proximity we exclude MD95-2040 site from our model-data analysis. See Hoffman *et al.* (2017) for additional information.

atmosphere leads to a widespread reduction in winter MSLP over the Arctic Ocean, North Pacific and Bering Sea (Supplementary Figs. 3.17b-d). Over the Arctic Ocean, local decreases in winter MSLP exceed 200 Pa, 650 Pa and 800 Pa in WSIR-7,WSIR-35 and WSIR-94 respectively (Supplementary Figs. 3.17b-d).

3.4.5 Decomposition of $\delta^{18}O$ changes

Ice core records reflect the deposition of snow on the surface, and therefore tend to record climatic information during snow deposition events (e.g., Steig *et al.*, 1994). Hence, precipitation seasonality can cause a recording bias towards those seasons with more snowfall events. Indeed, stable water isotopes in Greenland ice core records have

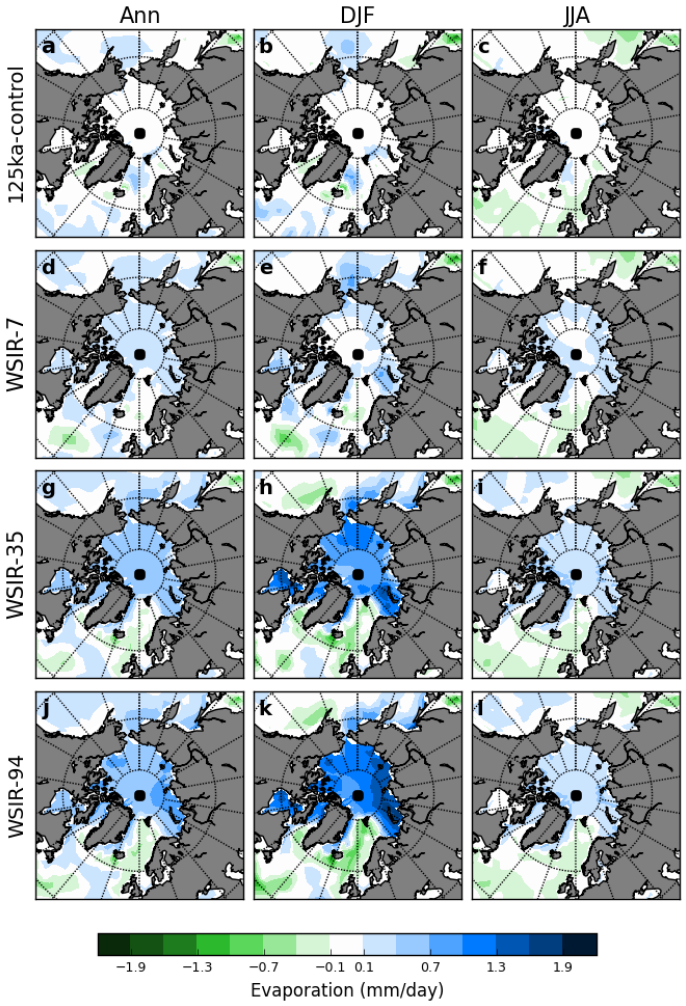

FIGURE 3.6: Modelled annual (ann), summer (JJA) and winter (DJF) evaporation anomalies for the 125ka-control simulation (a to c), WSIR-7 (d to f), WSIR-35 (g to i) and WSIR-94 (j to l) compared to the PI simulation. Only the anomalies statistically significant at the 95% confidence level are displayed.

been traditionally compared with precipitation isotopic composition reproduced by isotope-enabled models (e.g., Sime *et al.*, 2013).

In this section, we study how changes in both the monthly isotopic composition of precipitation and the amount of monthly precipitation contribute to the simulated positive $\delta^{18}O$ anomalies at the different Greenland ice core sites (Holloway *et al.*, 2016a; Liu and Battisti, 2015).

To isolate the importance of variations in the seasonal cycle of precipitation (ΔP_{seas}) to the changes in $\delta^{18}O$, we use the following decomposition:

$$\Delta P_{seas} = \frac{\Sigma_j \delta^{18}O_j^{CONT} * P_j}{\Sigma_j P_j} - \frac{\Sigma_j \delta^{18}O_j^{CONT} * P_j^{CONT}}{\Sigma_j P_j^{CONT}} \tag{3.1}$$

Superscript CONT denotes values from the 125 ka control simulation with no additional sea ice forcing and no superscript denote values from the sea ice sensitivity experiments. The relative impact of other factors (variations in the isotopic composition of precipitate and in the vapor source) contributing to the changes in $\delta^{18}O$ is quantified by:

$$\Delta\delta = \frac{\Sigma_j \delta^{18}O_j * P_j^{CONT}}{\Sigma_j P_j^{CONT}} - \frac{\Sigma_j \delta^{18}O_j^{CONT} * P_j^{CONT}}{\Sigma_j P_j^{CONT}} \tag{3.2}$$

Using the monthly $\delta^{18}O$ from the 125 ka control simulation and the monthly precipitation of the different sea ice forcing experiments (WSIR-7, WSIR-35 and WSIR-94) (Equation 3.1), we determine the differences in $\delta^{18}O$ due to variations in the seasonal cycle of precipitation (Fig. 3.7d-f). In the same way, using the monthly $\delta^{18}O$ from the sea ice retreat experiments (WSIR-7, WSIR-35 and WSIR-94) and the monthly precipitation of the 125 ka control simulation (Equation 3.2), we isolate the effect of the variations in the isotopic composition of precipitation to the total $\delta^{18}O$ changes (Fig. 3.7g-i).

For all sea ice sensitivity experiments (WSIR-7, WSIR-35 and WSIR-94), over the Arctic Ocean and Greenland, ΔP_{seas} is negative (Fig. 3.7d-f) and $\Delta\delta$ is generally strongly positive (Fig. 3.7g-i). Thus whilst more precipitation falls in the colder months under the sea ice loss scenarios, the increases in $\delta^{18}O$ related to the sea ice loss generally outweigh this impact over Greenland.

3.4.6 Mean annual $\delta^{18}O$ changes at the NEEM deposition site

At the NEEM deposition site, the 125-ka control simulation shows a precipitation-weighted $\delta^{18}O$ (hereafter $\delta^{18}O$p) anomaly of 1.7‰ compared to the PI control simulation (Fig. 3.8a). This is too low compared to the 3.6 ‰ increase measured in the NEEM ice core. When the response to a forced retreat of sea ice is simulated, $\delta^{18}O$p

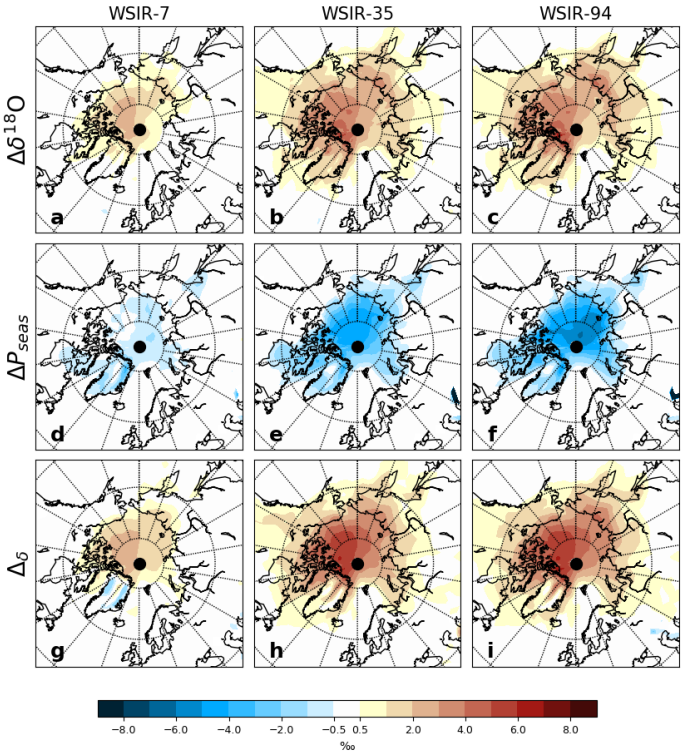

FIGURE 3.7: Decomposition of $\delta^{18}O$ changes from 125 ka sea ice retreat experiments. (a,d,g) WSIR-7; (b,e,h) WSIR-35; (c,f,i) WSIR-94. (a-c) The total change in $\delta^{18}O$ ($\Delta\delta^{18}O$). (d-f) The change due to variations in the seasonality of precipitation (ΔP_{seas}). (g-i) The change caused by variations in the $\delta^{18}O$ of precipitation ($\Delta\delta$). Anomalies are calculated compared to the 125 ka control simulation with no additional sea ice forcing.

anomalies rise to between 2.4‰ and 3.9‰ depending on the sea ice forcing prescribed (Fig. 3.8b-d and Table 3.3). Simulations with greater than a 17% reduction in winter sea ice best fit the NEEM ice core data (considering the ±1s uncertainty on the best fit curve - Fig. 3.9a).

3.4.7 Mean annual $\delta^{18}O$ changes at other Greenland ice core sites

The 125-ka control simulation with no additional sea ice forcing shows $\delta^{18}O$p anomalies of 1.4‰ at NGRIP and 1.1‰ at GISP2 compared to the PI control simulation (Fig. 3.8a). When forcing a sea ice reduction, simulated $\delta^{18}O$p anomalies rise to between 2.0‰ and 3.4‰ at NGRIP and between 1.6‰ and 2.9‰ at GISP2 depending on the sea ice forcing prescribed (Fig. 3.8b-d). At NGRIP and GISP2 sites,

TABLE 3.3: Modelled annual means of precipitation-weighted $\delta^{18}O$, precipitation-weighted SAT and non-weighted SAT anomalies compared to the PI simulation at the NEEM deposition site. Anomalies are listed for each of the 125 ka simulations. The experiments marked in red are the ones mainly discussed in the text.

Exp ID	Precipitation weighted $\delta^{18}O$ (‰)	Precipitation weighted SAT anomalies (°C)	Non-weighted SAT anomalies (°C)
125ka-control	1.7	2.1	0.5
WSIR-7	**2.6**	**2.5**	**0.7**
WSIR-11	2.5	2.9	1.1
WSIR-10	2.4	2.5	1.3
WSIR-15	3.0	3.1	1.6
WSIR-17	3.3	3.5	1.8
WSIR-17b	3.1	3.1	1.7
WSIR-19	2.9	2.6	1.6
WSIR-21	3.2	3.1	1.7
WSIR-22	3.2	3.2	1.7
WSIR-26	3.4	3.0	1.7
WSIR-35	**3.6**	**3.5**	**2.1**
WSIR-41	3.7	3.1	2.2
WSIR-54	3.9	3.5	2.4
WSIR-65	3.5	2.8	2.3
WSIR-72	3.9	3.2	2.2
WSIR-78	3.6	2.9	2.2
WSIR-81	3.6	2.7	1.9
WSIR-89	3.6	2.8	2.1
WSIR-94	**3.7**	**3.0**	**2.3**
WSIR-99	3.5	2.9	2.1
WSIR-100	3.8	3.2	2.1

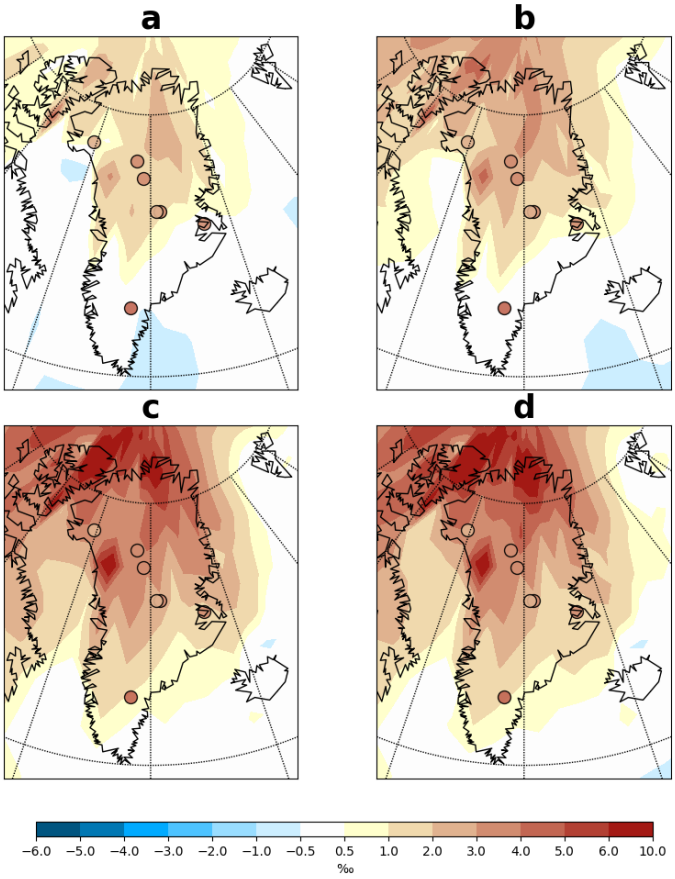

FIGURE 3.8: Observed $\delta^{18}O$ anomalies at seven Greenland ice core sites (dots) Johnsen and Vinther (2007); NEEM community members (2013) superimposed onto simulated annual mean precipitation-weighted $\delta^{18}O$ anomalies for: (a) 125ka-control, (b) WSIR-7, (c) WSIR-35 and (d) WSIR-94 compared to the PI simulation.

LIG $\delta^{18}O$ values were reported to be 3.1‰ and 2.7‰ higher than present day values respectively (Johnsen and Vinther, 2007). We find that simulations with a winter sea ice retreat higher than 14% and 16% may explain the NGRIP and GISP2 data respectively (considering the 1σ uncertainty on the best fit curves - Fig. 3.9b and g).

At Camp Century site, the sea ice retreat experiments show $\delta^{18}O$p anomalies ranging from 1.6‰ to 3.8‰ depending on the sea ice forcing, while the 125ka control simulation reveals a more modest increase in $\delta^{18}O$p of 0.5‰ (Fig. 3.8). Simulations with a winter sea ice reduction between 12% and 28% best fit the $\delta^{18}O$ anomaly of 2.5‰ observed at this location (considering the 1σ uncertainty on the best fit curve - Fig. 3.9e).

At GRIP, Renland and DYE3 sites, LIG $\delta^{18}O$ values were determined to be 3.5‰, 3.5‰, and 4.7‰ higher than present day values respectively (Johnsen and Vinther,

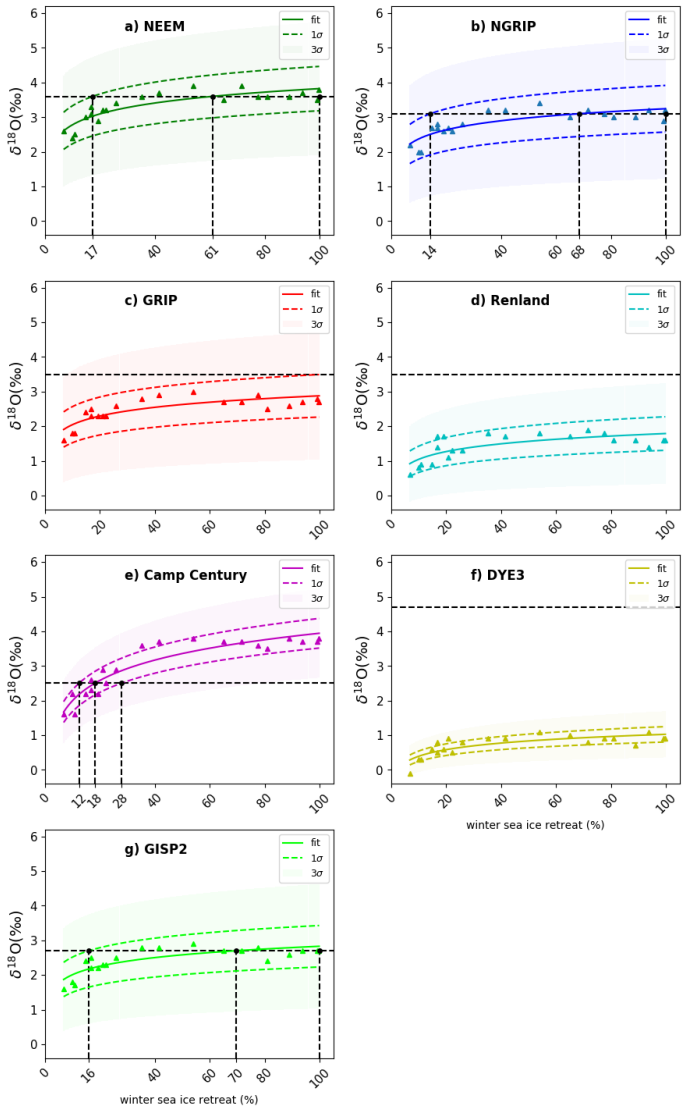

FIGURE 3.9: Simulated $\delta^{18}O$ anomalies as a function of winter (March) sea ice retreat. Ice core sites shown: (a) NEEM, (b) NGRIP, (c) GRIP, (d) Renland, (e) Camp Century, (f) DYE3, (g) GISP2. The retreat of sea ice is calculated as the percentage change in winter (March) sea ice extent compared to the PI experiment. Results for each of the 21 sea ice sensitivity experiments are represented by triangles. Solid lines signify best fit lines (fit = b * (log(x) – a)). Also shown 1σ (lines with dashes) and 3σ uncertainty (shade envelopes) on the best fit curve. The observed $\delta^{18}O$ anomalies at each ice core site are marked with a black horizontal line with dashes. Black vertical lines with dashes represent the intersections with best fit line and 1σ uncertainty lines.

2007). Depending on the sea ice forcing, simulated $\delta^{18}O$p anomalies vary between 1.6‰ and 3.0‰ at GRIP, between 0.6‰ and 1.9‰ at Renland and between -0.1‰ and 1.1‰ at DYE3 (Fig. 3.8). Thus, none of our LIG sea ice sensitivity experiments are able to capture the strong $\delta^{18}O$ enrichment reported at these three locations. The underestimated anomalies may be explained by the missing GIS elevation changes in the model runs, or other boundary condition changes not implemented in our simulations, or the uncertainty on both modelled $\delta^{18}O$ values (see section 3.7.2) and ice core measurements. This will be discussed in more detail in section 3.5.

3.5 Discussion

3.5.1 Estimating the Arctic LIG sea ice retreat from Greenland ice core $\delta^{18}O$

Loss of NH sea ice, alongside increased Arctic SSTs, enhances evaporation over the Arctic Ocean and consequently enriches $\delta^{18}O$ values over Greenland. This is a result of isotopically heavy water vapour and a shorter distillation path between the Arctic and Greenland. Thus, in line with previous studies, these results confirm that variations in sea ice and sea surface conditions lead to polar impacts on $\delta^{18}O$ (Holloway *et al.*, 2016a; Sime *et al.*, 2013; Sjolte *et al.*, 2014). However, all ice core sites indicate that Greenland $\delta^{18}O$ has a lower sensitivity to sea ice changes as the LIG winter sea ice loss becomes greater than 40-50% (Fig. 3.9). This behaviour is likely related to the higher sensitivity of Greenland $\delta^{18}O$ to GIS proximal sea ice. Thus, when winter sea ice proximal to Greenland has been lost, $\delta^{18}O$ in Greenland has almost no sensitivity to further sea ice loss. For this reason, whilst Greenland ice core data allows determination of sea ice change near Greenland, it may not allow insight into the possibility of near complete Arctic LIG sea ice loss.

The seven ice core records, which contain LIG ice, all indicate an increase in $\delta^{18}O$ across Greenland between the present and LIG (Johnsen and Vinther, 2007). HadCM3 simulations with greater than a 14%, 17% and 16% reduction in winter sea ice extent

(compared to the PI simulation) best fit the NGRIP, NEEM and GISP2 LIG $\delta^{18}O$ ice core data. For Camp Century core site, a winter sea ice reduction between 12% and 28% best fits the observed $\delta^{18}O$ anomaly. Our HadCM3 simulations of the response to sea ice retreat underestimate the observed $\delta^{18}O$ anomalies at Renland, DYE3 and GRIP. Thus we cannot simulate the LIG ice core $\delta^{18}O$ at these sites solely via a forced retreat of Arctic sea ice; the model used here may not adequately capture the features at Renland due to its coarse spatial resolution, relative to the size of the coastal Renland icecap. Although, that said, the summertime sea ice pack is too small in the PI simulation; a larger PI summer sea ice pack would increase the potential size of the LIG $\delta^{18}O$ anomaly, likely improving the model-data match at Renland, DYE3, and GRIP.

The existing observations of LIG Arctic sea ice cover are sparse and not quantitative. Moreover, there is not a current consensus on the presence of perennial (Stein *et al.*, 2017) or seasonal sea ice cover (e.g., Adler *et al.*, 2009; Brigham-Grette and Hopkins, 1995; Spielhagen *et al.*, 2004) over the central LIG Arctic Ocean in the marine core literature. Thus going beyond a qualitative agreement on sea ice retreat between our LIG sea ice results and current marine data is difficult. Additional marine core data, which helps establish the maximum extent of the LIG sea ice retreat, would be particularly valuable to further evaluate our quantitative sea ice retreat reconstruction.

3.5.2 What caused this LIG Arctic sea ice retreat?

Proxy data indicate that both winter and summer sea ice extent was likely reduced during the LIG compared to present day (e.g., Brigham-Grette and Hopkins, 1995; Stein *et al.*, 2017). However, our 125 ka control simulation, forced by GHG and orbital changes, actually shows a 3% increase in winter sea ice extent and only a small reduction in summer sea ice. Many GCMs also have difficulty in accurately capturing recent changes in Arctic sea ice that have occurred during the past decades (e.g., Stroeve *et al.*, 2007, 2012). Thus, factors causing the inaccurate representation of historical sea ice variations by GCMs could indicate deficiencies in model physics, for example, in the simulation of ocean circulation and heat changes, and/or possible

over-simplifications of sea ice model physics e.g. schemes of sea-ice albedo parameterization (e.g., Stroeve *et al.*, 2012). These issues can all affect the simulation of sea ice loss (or increase). However, we believe that it is more likely that the LIG retreat of Arctic sea ice was caused by long term changes in meltwater influences over the course of Termination II and early LIG, and subsequent changes in oceanic heat transport into the North Atlantic and Arctic (Capron *et al.*, 2014; Stone *et al.*, 2016).

Capron *et al.* (2014) suggest that it is necessary to account for freshwater input into the North Atlantic resulting from the NH ice sheet melting during the preceding deglaciation in order to better simulate marine core SST values at the beginning of the LIG. A subsequent build-up of heat in the rest of the global ocean, that was a likely consequence of this early LIG NH meltwater (Stone *et al.*, 2016), and later advection of excess heat to the North Atlantic, could then have caused Arctic sea ice retreat at 125 ka. However few, if any, sufficiently long GCM simulations with NH meltwater have been attempted for the LIG. In addition to a lack meltwater forcing, and sufficient duration simulations, there may also be a lack of possible other relevant forcing changes, such as changes in the Bering Strait flow during Termination II.

3.5.3 Uncertainties on LIG $\delta^{18}O$ from Greenland ice cores

The sea ice retreat insights provided by our study are dependent on the uncertainties attached to Greenland LIG $\delta^{18}O$ ice core data. Apart for the analytical uncertainty (of about 0.1‰), it is not straightforward to quantify the additional uncertainties on the $\delta^{18}O$ values that originate from the dating of the LIG layers, the possibility of missing LIG layers and also the lack of constraints on elevation changes at some sites, especially such as DYE3.

NEEM is the only Greenland ice core where the bottom ice has been relatively well-dated between 114.5 and 128.5 ka (NEEM community members, 2013). Absolute dating uncertainties on this record are estimated to be of at least 2000 years (Govin *et al.*, 2015). For the LIG ice at the bottom of other Greenland cores, the dating uncertainties are probably significantly larger. While tentative reconstructions of the chronology of the bottom of the GRIP and GISP2 ice cores have been made using

CH_4 gas record synchronization with Antarctic ice cores (Landais *et al.*, 2003; Suwa *et al.*, 2006a), dating the bottom of DYE3 and Camp Century is limited due to the poor preservation of the deep samples. In contrast, the stratigraphy in the NGRIP ice core is continuous all the way down to the bedrock, making the dating of the bottom ice layers less challenging. Still, only a few data constraints are available over this interval and the older LIG ice was likely removed due to basal melting. Hence, uncertainties of at least 2000 years are attached to the chronology deduced for the bottom section of the NGRIP ice core based on glaciological flow modelling (NGRIP Project Members, 2004).

In addition to the dating uncertainties, ice flow can significantly affect ice core $\delta^{18}O$. At some sites the bottom ice has flowed down to the drill site from higher elevation. Thus elevation change between deposition site and drill site adds to the uncertainty of the observed differences between LIG to present day $\delta^{18}O$. Based on total air content analysis it is, believed however that central Greenland elevation was likely unchanged during the LIG (Raynaud *et al.*, 1977), and the Renland LIG ice also very likely originated from elevations close to present (Johnsen and Vinther, 2007).

3.5.4 Ice sheet, temperature, and wider atmospheric circulation changes

This study focusses on examining the $\delta^{18}O$ signal of Arctic sea ice changes across Greenland, and does not simulate any ice sheet changes, or attempt to reconstruct temperature changes at ice core sites. Nevertheless, we make some comments on GIS, temperature, and wider atmospheric circulation LIG changes.

It has been postulated that the GIS experienced significant changes in volume and morphology between the present and LIG (e.g., IPCC, 2013; Dutton *et al.*, 2015). Thus, in addition to sea ice effects, LIG $\delta^{18}O$ signals in Greenland ice cores may also reflect changes in GIS topography. GIS elevation would also affect temperatures at the ice core sites, since lapse rate effects must have occurred, alongside atmospheric circulation and precipitation changes (Merz *et al.*, 2014b). Since most previous studies have suggested that the LIG GIS was smaller than present (e.g., IPCC, 2013; Dutton

et al., 2015), this also suggests that larger LIG temperature rises occurred at ice core sites than shown in our simulations, which feature no GIS change.

Previous modelling studies (e.g., Merz *et al.*, 2016; Pedersen *et al.*, 2016a; Lunt *et al.*, 2013), all show a smaller warming at NEEM compared to the published values of 8 ± 4 °C warming (based on ice $\delta^{18}O$ data; NEEM community members (2013)) and 8 ± 2.5 °C warming (based on air $\delta^{15}N$ data; Landais *et al.* (2016). Our medium sea ice loss (WSIR-35) simulation shows a warming of 3.5 °C at the NEEM deposition site. If an additional moderate reduction of NEEM's surface elevation, of 130 ± 300m lower than present (as proposed by the NEEM community members (2013)), were incorporated, an extra warming of around 1.3-4.3 °C (assuming an approximate lapse rate of 1 °C warming per 100m height decrease) would occur. This would lead to a possible core site warming of between 4.8 °C and 7.8 °C. Thus further studies examining the joint impacts of GIS change and sea ice change on Greenland, alongside long meltwater influence simulations, would all be most helpful in aiding a better understanding of what drove the LIG Greenland warming and $\delta^{18}O$ change.

Note also that the sea ice loss simulations (including WSIR-35) probably underestimate NEEM warming due to 125 ka sea surface condition changes. This is because the simulations exhibit somewhat less Northern Atlantic warming than would be expected due to our method of forcing the model to lose sea ice. In terms of atmospheric circulation changes over the wider North Atlantic region, it is also worth noting that sea ice loss and increased temperatures induce a significant drop in MSLP that extends well into the North Pacific. These variations also modify precipitation patterns over the whole Arctic region.

3.6 Conclusions

Our study is a useful complement to previous LIG modelling studies. It highlights the importance of understanding the impact of NH sea ice changes on the LIG Greenland isotopic maximum. Our results show, for the first time, that variations in NH sea ice conditions can lead to substantial LIG Greenland $\delta^{18}O$ increases which are

commensurate with $\delta^{18}O$ anomalies observed at NEEM, NGRIP, GISP2 and Camp Century sites. Further modelling studies looking at the combined impact of a smaller GIS and NH sea ice variations, together with additional LIG Arctic sea ice proxies, may help in understanding outstanding model-data mismatches and in evaluating whether Arctic sea ice retreat is indeed a major factor responsible for the high LIG $\delta^{18}O$ measured in Greenland ice cores.

3.7 Supplementary information

3.7.1 Model evaluation

In this section, we provide an evaluation of two control (PI and present-day experiments) HadCM3 isotope simulations over Greenland. Previous work by Sime *et al.* (2013), using the atmosphere only component of this model (HadAM3), has shown that annual Greenland means of both isotopic values and surface temperatures are on average 8.6‰ too heavy and 1.9°C too warm respectively, compared with present-day observations compiled by Vinther *et al.* (2010) and Sjolte *et al.* (2011). Following on from this, HadCM3 surface temperatures and isotopic values are compared with the observational data provided by Vinther *et al.* (2010) and Sjolte *et al.* (2011) (see Sime *et al.* (2013) for estimates and locations of individual records).

Comparison with observations indicates an annual warm bias over Greenland of 2.2°C for the PI simulation and 3.7°C for the present-day simulation (Fig. 3.10b). Note, most observational sites are located in central Greenland, providing an unequal representation of the whole of Greenland. Hence, the comparison can be considered more representative of the cold central Greenland region (see Fig. 3.10b for the position of the observational sites). The $\delta^{18}O$ results follow a similar pattern (Fig. 3.10b). Comparison with the observations suggests that both the PI and present-day simulations are on average 5.8‰ and 7.1‰ (Fig. 3.10a) too heavy, respectively. Some other models show similar heavy $\delta^{18}O$ biases (e.g., Hoffmann *et al.*, 1998; Sjolte *et al.*, 2011; Sime *et al.*, 2013). Sime *et al.* (2013) point to the inaccurate seasonal representation of the isotopes in precipitation as a possible reason for the model-data isotopic offset.

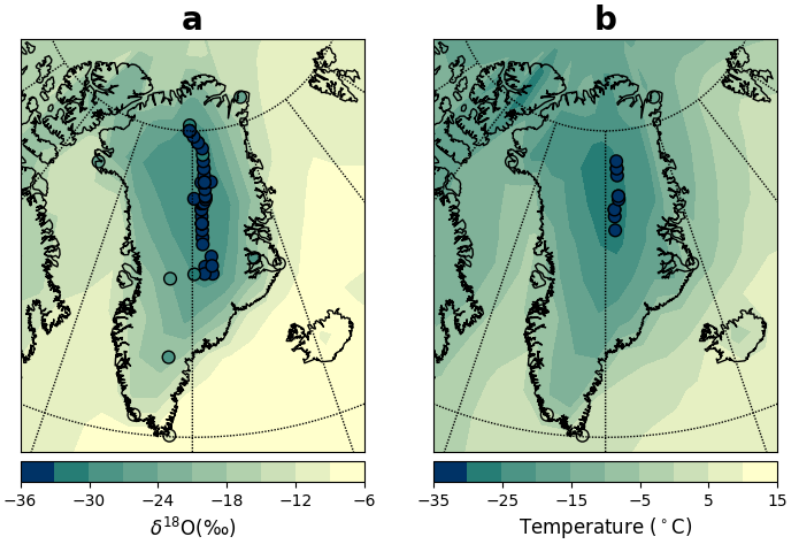

FIGURE 3.10: Present-day observations of $\delta^{18}O$ and temperature (Vinther *et al.*, 2010; Sjolte *et al.*, 2011) superimposed onto modelled present-day (1950-2000) values. (a) Annual $\delta^{18}O$ (‰) and (b) annual surface temperatures (°C). Seven transient present-day simulations covering the period 1850-2004 are considered for this analysis. In particular, the shading on each plot shows the mean of these seven present-day simulations for the period 1950-2000.

3.7.2 Modelled uncertainty on $\delta^{18}O$

Figure 3.11 shows the simulated annual to decadal variability of annual mean $\delta^{18}O$p for a low, medium and high sea ice forcing. $\delta^{18}O$p variability is larger near the coast at both annual and decadal time scales (Fig. 3.11). For the sea ice forcing ensemble, at all ice core sites, decadal isotope variability (ranging from standard deviations of 0.36‰ up to 0.62‰ depending on the site) is lower relative to the annual variability (ranging from standard deviations of 0.88‰ up to 1.6‰ depending on the site) (Table 3.4).

To complement this model uncertainty analysis on annual mean $\delta^{18}O$p values, the standard deviation of 50-year averages are also estimated as this is the time-window used to report all isotope averages in this study. Fig. 3.11 shows the modelled variability of 50-year averages for a low, medium and high sea ice forcing. For the sea ice forcing ensemble, the standard deviation at this 50-year time scale does not exceed; 0.19‰ at DYE3; 0.23‰ at GRIP and GISP2; 0.24‰ at NEEM and NGRIP; 0.28‰ at Renland; and 0.35‰ at Camp Century (Table 3.4).

TABLE 3.4: Modelled variability of annual mean $\delta^{18}O$p at seven ice cores sites at 50-year average, decadal and annual time scales. We list standard deviations (‰) for the sea ice retreat experiments ensemble and a present-day scenario. For the present-day scenario, the standard deviation between seven present-day experiments covering the period 1850-2000 is presented.

	Sea ice forcing ensemble			**Present-day forcing scenario**		
	Standard deviation (‰)			**Standard deviation (‰)**		
Ice core sites	**50-year average**	**Decadal**	**Annual**	**50-year average**	**Decadal**	**Annual**
NEEM	0.24	0.47	1.3	0.22	0.50	1.4
NGRIP	0.24	0.45	1.3	0.19	0.46	1.3
GRIP	0.23	0.36	1.0	0.15	0.34	1.0
Renland	0.28	0.45	1.1	0.33	0.51	1.3
Camp Century	0.35	0.62	1.6	0.30	0.65	1.7
DYE3	0.19	0.37	0.88	0.19	0.36	1.0
GISP2	0.23	0.37	1.1	0.17	0.36	1.1

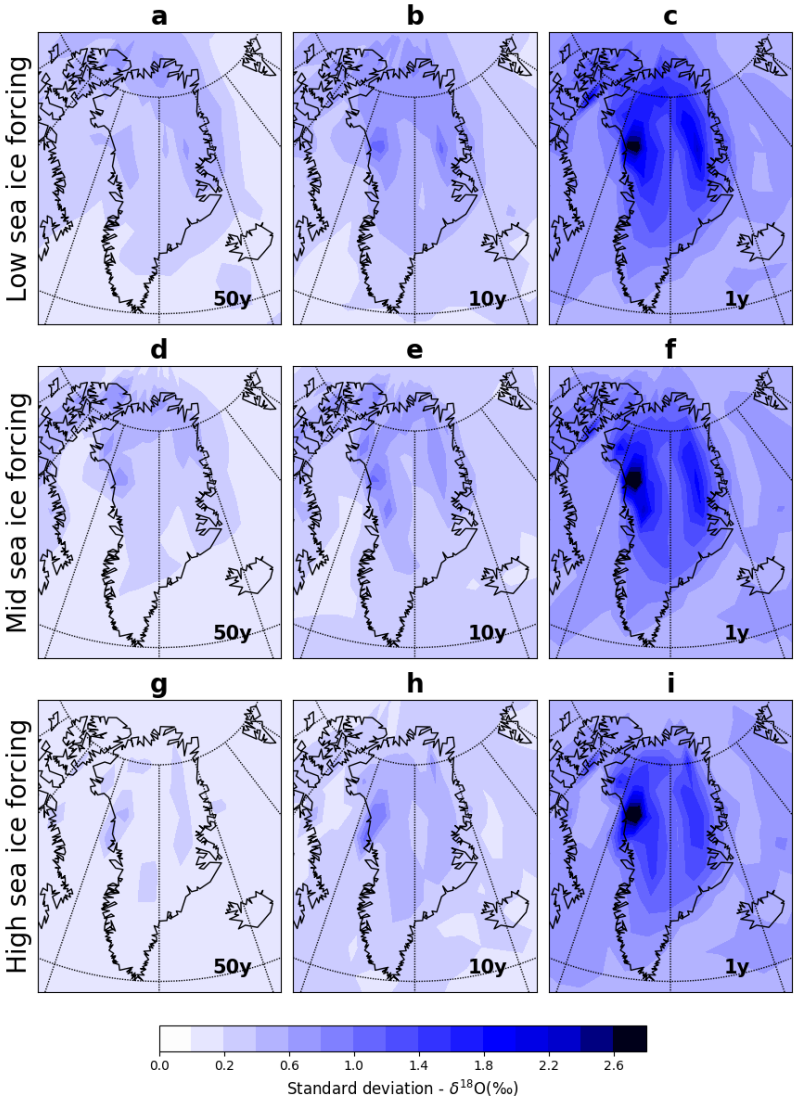

FIGURE 3.11: Variability of annual mean $\delta^{18}O$p for a low (a-c), medium (d-f) and high (g-i) sea ice forcing, at 50-year average (a, d, g), decadal (b, e, h) and annual (c, f, i) time scales. The shading in each plot shows the standard deviation calculated using sea ice retreat experiments with a low (between 7% and 19%), medium (between 21% and 65%) and high (between 72% and 100%) winter sea ice loss compared to the PI simulation.

For comparison, we also calculated the variability of annual mean $\delta^{18}O$p for a present-day scenario at annual, decadal and 50-year average time scales (Fig. 3.12). At all ice core sites, the simulated annual, decadal and 50-year average variability of $\delta^{18}O$p for the present-day forcing scenario is very similar relative to the sea ice forcing ensemble (Table 3.4).

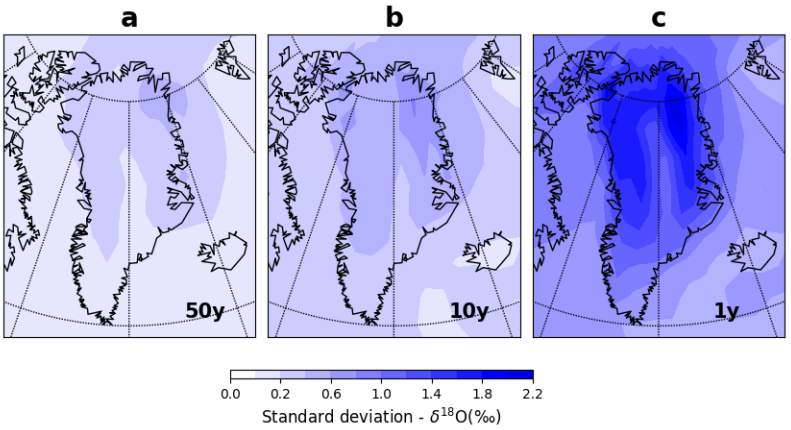

FIGURE 3.12: Variability of annual mean $\delta^{18}Op$ for a present-day scenario at (a) 50-year average, (b) decadal and (c) annual time scales. The shading in each plot shows the standard deviation calculated using seven present-day experiments covering the period 1850-2000.

3.7.3 Annual deuterium excess changes

Deuterium excess (hereafter d-excess) has been used as a proxy for source area conditions (e.g., Masson-Delmotte *et al.*, 2005; Steffensen *et al.*, 2008). Figure 3.13 shows results from the selected 125 ka simulations compared with d-excess data compiled by Landais *et al.* (2016). We obtain similar values of RMSE for d-excess for the 125ka control simulation (1.1‰), WSIR-7 (1.0‰) and WSIR-35 (1.1‰). The experiment WSIR-7 has the lowest ("best") RMSE (1.0‰), whereas the WSIR-94 experiment shows the highest RMSE (3.4‰). The modelled d-excess results should however be interpreted with caution. The representation of micro-scale cloud physics in HadCM3 does not have a discernible impact on first order $\delta^{18}O$ or δD, but does permit for some tuning of the d-excess (e.g., Tindall *et al.*, 2009; Schmidt *et al.*, 2007; Werner *et al.*, 2011). Better knowledge and improved model representation of micro-scale cloud physics could permit a more insightful analysis of the d-excess data (Landais *et al.*, 2016).

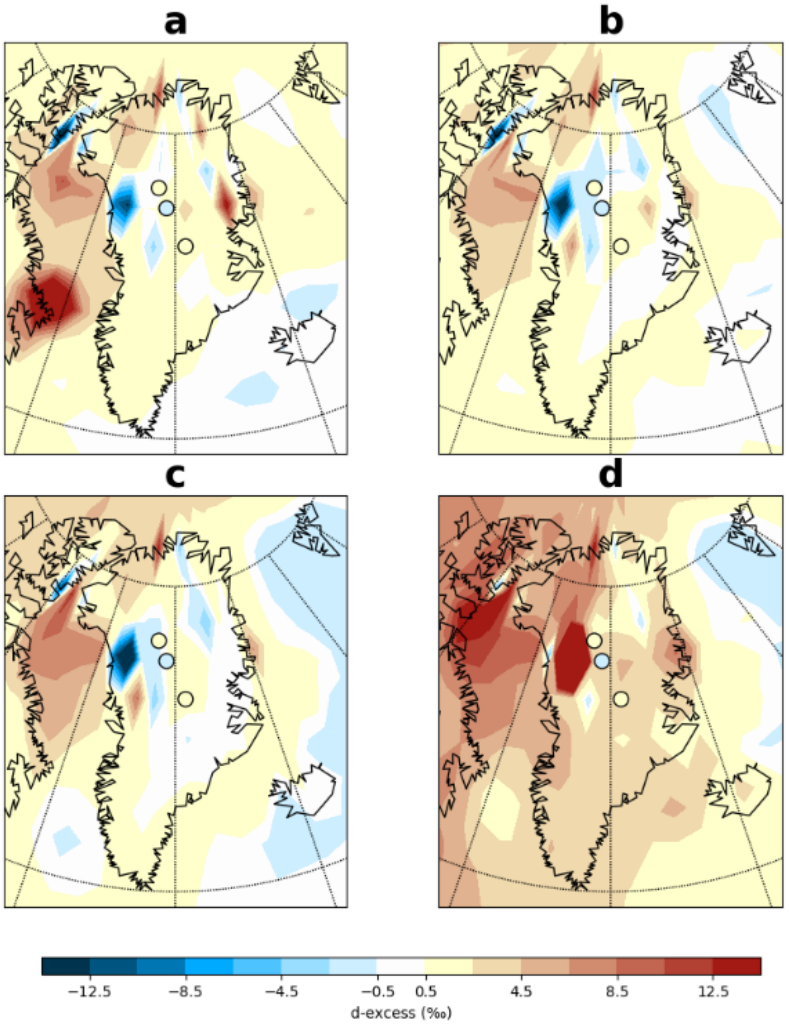

FIGURE 3.13: The d-excess data compiled by Landais *et al.* (2016) superimposed onto modelled annual d-excess anomalies relative to the PI simulation for: (a) 125ka control (RMSE = 1.1‰), (b) WSIR-7 (RMSE = 1.0‰), (c) WSIR-35 (RMSE = 1.1‰) and (d) WSIR-94 (RMSE = 3.4‰).

TABLE 3.5: Compilation of observations of NH sea ice changes for the LIG.

Site	Proxy	Comments	Reference
GreenICE (core 11)	Subpolar foraminifers	The presence of subpolar planktonic foraminifers in MIS 5e zone interpreted to indicate reduced sea ice cover compared to present.	Nørgaard-Pedersen et al., 2007
HLY0503-8JPC	Subpolar foraminifers	Subpolar planktonic foraminifers found in MIS 5e zone suggest reduced sea-ice cover, perhaps seasonally ice-free conditions.	Adler et al., 2009
Nome, St. Lawrence Island and Beaufort Sea shelf	Mollusc and ostracode faunas	Fossil assemblages suggest that the winter sea-ice limit did not expand south of Bering Strait, that the Bering Sea was annually ice-free and that the sea ice cover in the Arctic ocean was not perennial for some period.	Brigham-Grette and Hopkins. (1995)
NP26-5/32	Ostracode faunas	Ostracode *Acetabulastoma arcticum,* which inhabits exclusively in areas of perennial Artic sea ice, occurs during late MIS 5e but it is absent during peak interglacial.	Cronin et al., (2010)
Oden96/12-1pc	Ostracode faunas	Ostracode *Acetabulastoma arcticum,* which inhabits exclusively in areas of perennial Artic sea ice, occurs during late MIS 5e but it is absent during peak interglacial.	Cronin et al., (2010)
PS2200-5	Ostracode faunas	Ostracode *Acetabulastoma arcticum,* which inhabits exclusively in areas of perennial Artic sea ice, occurs during late MIS 5e but it is absent during peak interglacial.	Cronin et al., (2010)
	Biomarker proxy IP25, terrestrial biomarkers and open-water phytoplankton biomarkers	Biomarker proxies suggest perennial sea ice cover in the central part of Arctic Ocean during MIS 5e.	Stein et al. (2017)
PS51/038-3	Biomarker proxy IP25, terrestrial biomarkers and open-water phytoplankton biomarkers	Biomarker proxies suggest perennial sea ice cover in the central part of Arctic Ocean during MIS 5e.	Stein et al. (2017)
PS2138-2	Biomarker proxy IP25, terrestrial biomarkers and open-water phytoplankton biomarkers	Biomarker proxies suggest seasonal open-water conditions over the Barents Sea continental margin.	Stein et al. (2017)
PS2757-8	Biomarker proxy IP25, terrestrial biomarkers and open-water phytoplankton biomarkers	Biomarker proxies suggest relatively closed sea ice cover conditions during MIS 5e.	Stein et al. (2017)

TABLE 3.6: Full list of simulations. The experiments marked in red are those focussed upon in the text.

Exp ID	Eccentricity	Obliquity (°)	Perihelion (day of yr)	Prescribed heat flux (W m^{-2})	CO_2 (ppmv)	CH_4 (ppbv)	N_2O (ppbv)	Percentage change in March Arctic sea ice extent relative to PI simulation (%)
PI	0.0167	23.45	1.7	0	280	760	270	0
125ka-control	0.04001	23.80	201.3	0	276	640	263	+3
WSIR-7	0.04001	23.80	201.3	15	276	640	263	-7
WSIR-11	0.04001	23.80	201.3	20	276	640	263	-11
WSIR-10	0.04001	23.80	201.3	25	276	640	263	-10
WSIR-15	0.04001	23.80	201.3	30	276	640	263	-15
WSIR-17	0.04001	23.80	201.3	35	276	640	263	-17
WSIR-17b	0.04001	23.80	201.3	40	276	640	263	-17
WSIR-19	0.04001	23.80	201.3	50	276	640	263	-19
WSIR-21	0.04001	23.80	201.3	55	276	640	263	-21
WSIR-22	0.04001	23.80	201.3	60	276	640	263	-22
WSIR-26	0.04001	23.80	201.3	80	276	640	263	-26
WSIR-35	0.04001	23.80	201.3	100	276	640	263	-35
WSIR-41	0.04001	23.80	201.3	120	276	640	263	-41
WSIR-54	0.04001	23.80	201.3	140	276	640	263	-54
WSIR-65	0.04001	23.80	201.3	145	276	640	263	-65
WSIR-72	0.04001	23.80	201.3	150	276	640	263	-72
WSIR-78	0.04001	23.80	201.3	155	276	640	263	-78
WSIR-81	0.04001	23.80	201.3	160	276	640	263	-81
WSIR-89	0.04001	23.80	201.3	180	276	640	263	-89
WSIR-94	0.04001	23.80	201.3	200	276	640	263	-94
WSIR-99	0.04001	23.80	201.3	250	276	640	263	-99
WSIR-100	0.04001	23.80	201.3	300	276	640	263	-100

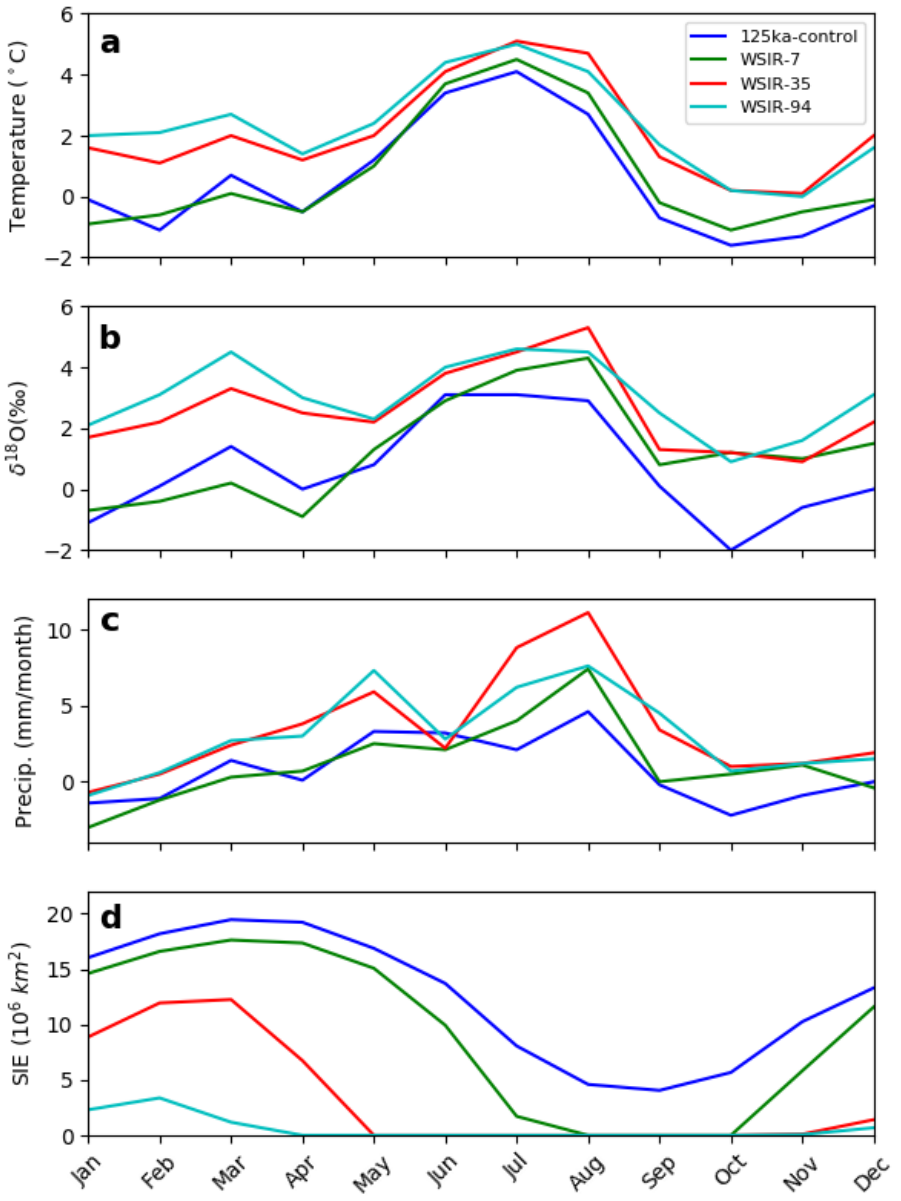

FIGURE 3.14: Change in the seasonal cycle of (a) temperature (°C), (b) $\delta^{18}O$ (‰), and (c) precipitation (mm/month) at the NEEM deposition site. Anomalies are calculated between the 125 ka simulations using heat fluxes of 0 W m-2 (125ka-control, dark blue), 15 W m-2 (WSIR-7, green), 100 W m-2 (WSIR-35, red) and 200 W m-2 (WSIR-94, cyan) compared to the PI simulation. Also shown the annual cycle of Arctic sea ice extent (SIE – 10^6 km^2) in the LIG simulations.

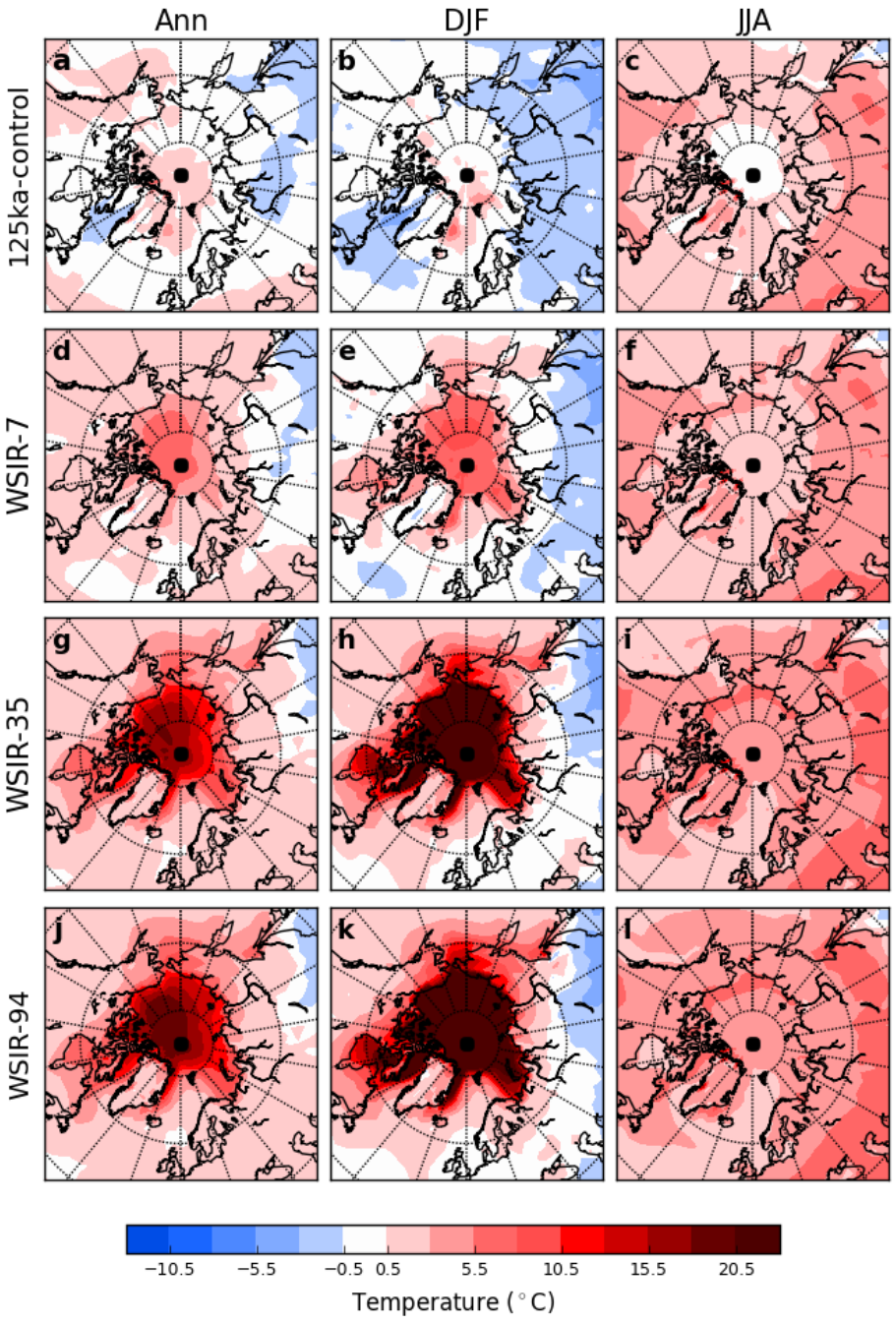

FIGURE 3.15: Modelled annual (ann), summer (JJA) and winter (DJF) surface air temperature anomalies for the 125ka-control simulation (a to c), WSIR-7 (d to f), WSIR-35 (g to i) and WSIR-94 (j to l) compared to the PI simulation. Only the anomalies statistically significant at the 95% confidence level are displayed.

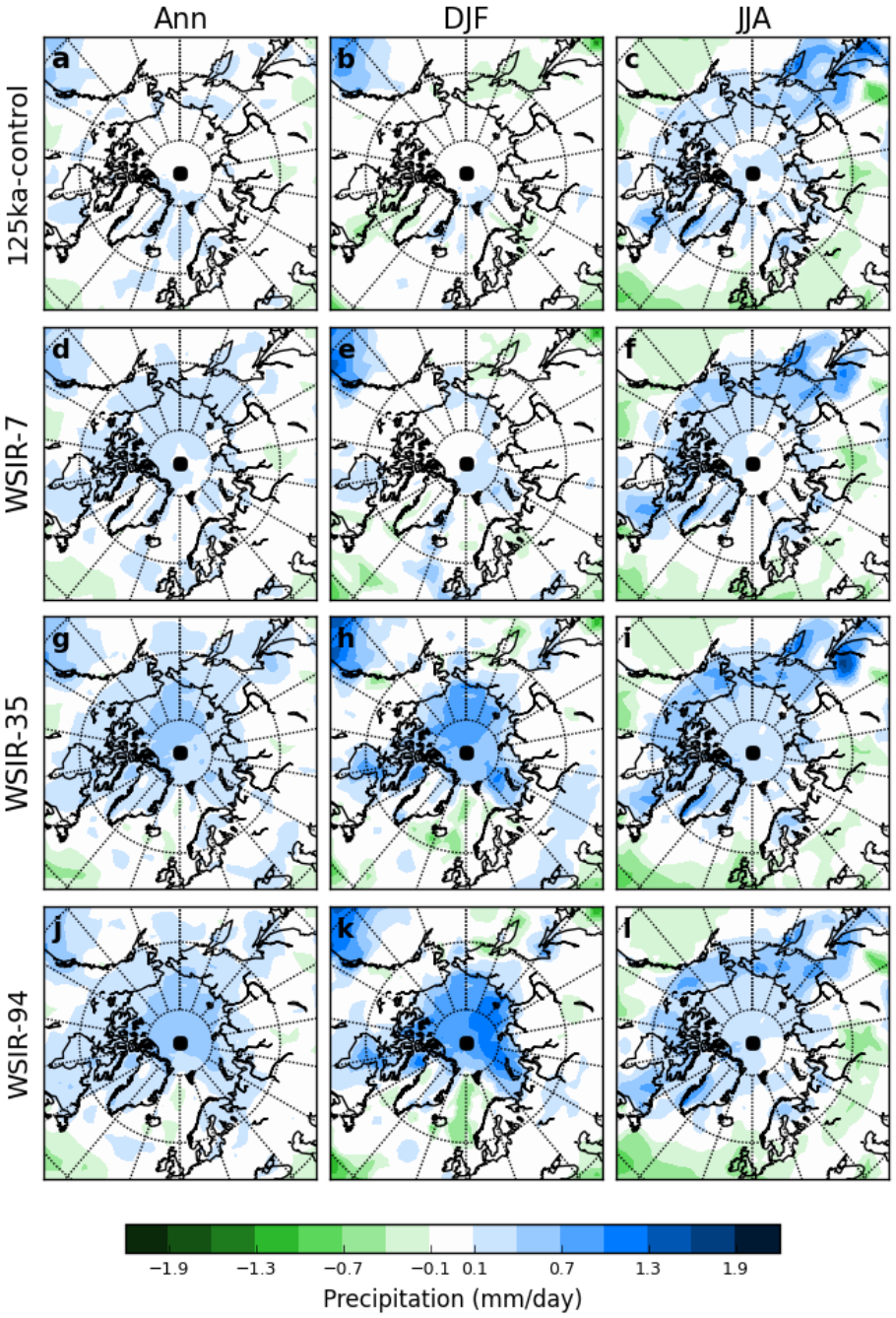

FIGURE 3.16: Modelled annual (ann), summer (JJA) and winter (DJF) precipitation anomalies for the 125ka-control simulation (a to c), WSIR-7 (d to f), WSIR-35 (g to i) and WSIR-94 (j to l) compared to the PI simulation. Only the anomalies statistically significant at the 95% confidence level are displayed.

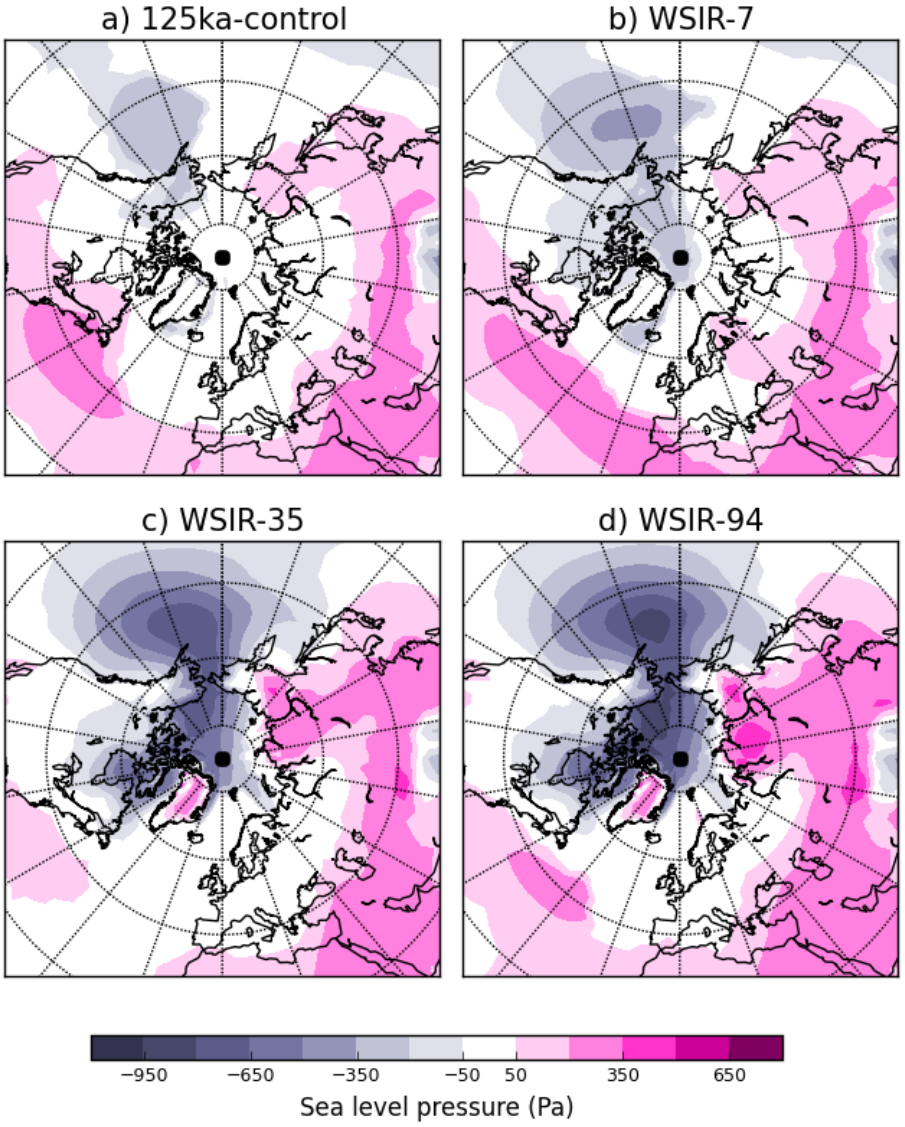

FIGURE 3.17: Modelled winter sea level pressure anomalies (Pa) for: a) 125ka-control, b) WSIR-7, c) WSIR-35 and d) WSIR-94 compared to the PI simulation. Only the anomalies statistically significant at the 95% confidence level are displayed.

Chapter 4

Using ice cores and Gaussian Process emulation to recover changes in the GIS during the LIG

This chapter is published in Journal of Geophysical Research as; Domingo, D., Malmierca-Vallet, I., Sime, L.C., Voss, J., and Capron, E. 2020. Using ice cores and Gaussian Process emulation to recover changes in the Greenland Ice Sheet during the Last Interglacial. Journal of Geophysical Research: Earth Surface, 125, 1-19, doi:10.1029/2019JF005237.

I.M.V and D.D are joint first authors of this article. I.M.V. performed the isotope-enabled climate model experiments and wrote the following sections of the article: Introduction, Methodology (sections 4.3 and 4.4.3), Results (section 4.5.4) and Conclusions. D.D. and J.V. developed the statistical methods. D.D. built the emulator of the climate simulator HadCM3. L.C.S. and J.V. provided feedback throughout the writing and analysis and L.C.S. also provided the initial motivation. E.C. provided additional advice related to interpreting $\delta^{18}O$ ice core records. All authors discussed the model results and commented on the manuscript.

4.1 Abstract

The shape and extent of the Greenland Ice Sheet (GIS) during the Last Interglacial (LIG) is a matter of controversy, with different studies proposing a wide range of reconstructions. Here, for the first time, we combine stable water isotopic information from ice cores with isotope-enabled climate model outputs to investigate the problem. Exploring the space of possible ice-sheet geometries by simulation is prohibitively expensive. We address this problem by using a Gaussian process emulator as a statistical surrogate of the full climate model. The emulator is calibrated using the results of a small number of carefully chosen simulations, and then permits fast, probabilistic predictions of the simulator outputs at untried inputs. The inputs are GIS morphologies, parameterised through a dimension-reduction technique adapted to the spherical geometry of the setting. Based on the emulator predictions, the characteristics of morphologies compatible with the available ice-core measurements are explored, leading to a reduction in uncertainty on the LIG GIS morphology. Moreover, a scenario-based approach allows to assess the gains in uncertainty reduction which would result from the availability of better dated LIG measurements in Greenland ice cores.

4.2 Introduction

The extent and shape of the Greenland ice sheet (GIS) during the Last Interglacial (LIG; 129 to 116 ka) is a matter of some controversy. Mean global sea level is thought to have been increased by between 6 to 9 meters compared to present-day level during this time period (*e.g.*Dutton *et al.*, 2015; Kopp *et al.*, 2009), with a likely contribution from both the Antarctic (*e.g.*DeConto and Pollard, 2016; Sutter *et al.*, 2016) and the Greenland ice sheets (*e.g.*Fyke *et al.*, 2011; Helsen *et al.*, 2013; Lhomme *et al.*, 2005; Tarasov and Peltier, 2003). The GIS contribution to the LIG highstand has however been difficult to pin down: studies suggest it may have contributed anywhere between +0.3 to +5.5 meters to global mean sea level (Born and Nisancioglu, 2012; Cuffey and Marshall, 2000; Helsen *et al.*, 2013; Otto-Bliesner *et al.*, 2006; Quiquet *et al.*,

2013; Robinson *et al.*, 2011; Stone *et al.*, 2013; Tarasov and Peltier, 2003; Yau *et al.*, 2016; NEEM community members, 2013). Possible drivers for these changes include stronger summertime insolation at high northern latitudes, and Arctic land summer temperatures 4-5°C higher than those that occurred during the pre-industrial (PI) (*e.g.*CAPE Last Interglacial Project Members, 2006).

Evidence proximal to Greenland about the LIG comes from sediment discharged from Greenland and from deep ice cores (*e.g.*Colville *et al.*, 2011; NGRIP Project Members, 2004; NEEM community members, 2013). From the sedimentary evidence from cores drilled off the Greenland coast it is difficult to produce an assessment of the extent and shape of the LIG GIS (Colville *et al.*, 2011). Ice sections corresponding to the LIG have been found, near the bed, at up to seven Greenland ice sites: NEEM, NGRIP, GRIP, Renland, DYE3, GISP2 and Camp Century (Johnsen and Vinther, 2007) (see Figure 4.1 for location of the sites). The suggestion of LIG ice in every one of these cores hinges on the occurrence of high stable water isotope ($\delta^{18}O$) measurements of the ice in the deepest parts of each core. At each of these sites, measurements from near the bottom show $\delta^{18}O$ that are above the range which occurred during the better dated most recent 120 ka (*e.g.*Johnsen and Vinther, 2007; NEEM community members, 2013). Climate model simulations of the LIG, forced by appropriate greenhouse gas (GHG) and orbital changes alone, have tended to fail to capture these observed $\delta^{18}O$ (and temperature) changes (*e.g.*Gierz *et al.*, 2017; Malmierca-Vallet *et al.*, 2018; Masson-Delmotte *et al.*, 2011; Sime *et al.*, 2013; Sjolte *et al.*, 2014).

If the LIG age interpretation of the near-bed ice at these ice core sites is correct, there must have been an extensive LIG GIS, with only a modest retreat during this period. However, this ice is difficult to date at several of the sites due to basal melting and complex flow interfering with age-depth modelling (NGRIP Project Members, 2004; NEEM community members, 2013; Landais *et al.*, 2003). This LIG-age uncertainty contributes to a wide range of possible LIG GIS scenarios. Some studies suggest DYE3 was ice covered during the LIG (*e.g.*Colville *et al.*, 2011; Willerslev *et al.*, 2007), whilst others imply a complete absence of ice in southern Greenland (*e.g.*Koerner and Fischer, 2002; MacGregor *et al.*, 2015). Some studies suggest strong melting

in the south (*e.g.*Otto-Bliesner *et al.*, 2006; Tarasov and Peltier, 2003), some in the north (*e.g.*Quiquet *et al.*, 2013; Stone *et al.*, 2013), and some in both (*e.g.*Born and Nisancioglu, 2012; Calov *et al.*, 2015; Helsen *et al.*, 2013; Robinson *et al.*, 2011). Some studies even propose a two-dome structure with a small ice dome in south Greenland and a large ice dome in north Greenland (*e.g.*Calov *et al.*, 2015; Langebroek and Nisancioglu, 2016).

Here we build on these studies with a new comprehensive investigation of the response of $\delta^{18}O$ to changes in the shape and extent of the GIS at 125 ka. We combine a synthesis of all available $\delta^{18}O$ data from deep Greenland ice cores, with simulation outputs from the Hadley Centre Coupled Model, version 3 (HadCM3, (Gordon *et al.*, 2000; Tindall *et al.*, 2009), referred to as simulator in the following). Since each simulation is computationally expensive and time consuming, the approach we follow is to use a Gaussian Process (GP) emulator: a fast and efficient statistical model providing probabilistic predictions of the simulator response to any GIS configuration, on the basis of the actual response on a selected set of GIS morphologies. Thanks to the emulator predictions, we inspect the properties of the GIS morphologies that are compatible with the available $\delta^{18}O$ records, reducing the uncertainty with respect to the previous studies.

The work is structured as follows. In Section 4.3 we summarise the available information from the current LIG $\delta^{18}O$ measurements in Greenland. In Section 4.4 the methodology is discussed. We describe the approach used to parameterise the range of possible GIS morphologies, Section 4.4.1, and to select the ones used as input to the HadCM3 simulation runs, Section 4.4.2. After a brief overview of the simulation setting, Section 4.4.3, Gaussian Process (GP) emulation is discussed in Section 4.4.4: in Section 4.4.4.1 a summary of the main steps and formulas needed to construct a GP emulator is provided, with the aim of providing a concise and self-contained reference of practical use; the specific choices and considerations to construct our GP emulators are detailed in Sections 4.4.4.2 and 4.4.4.3. Section 4.4.5 illustrates the way in which the emulator predictions are compared to the ice-core data, in order to identify record-compatible morphologies. In Section 4.5 (Results), we discuss the emulator fit and show the results of the comparison between emulator predictions

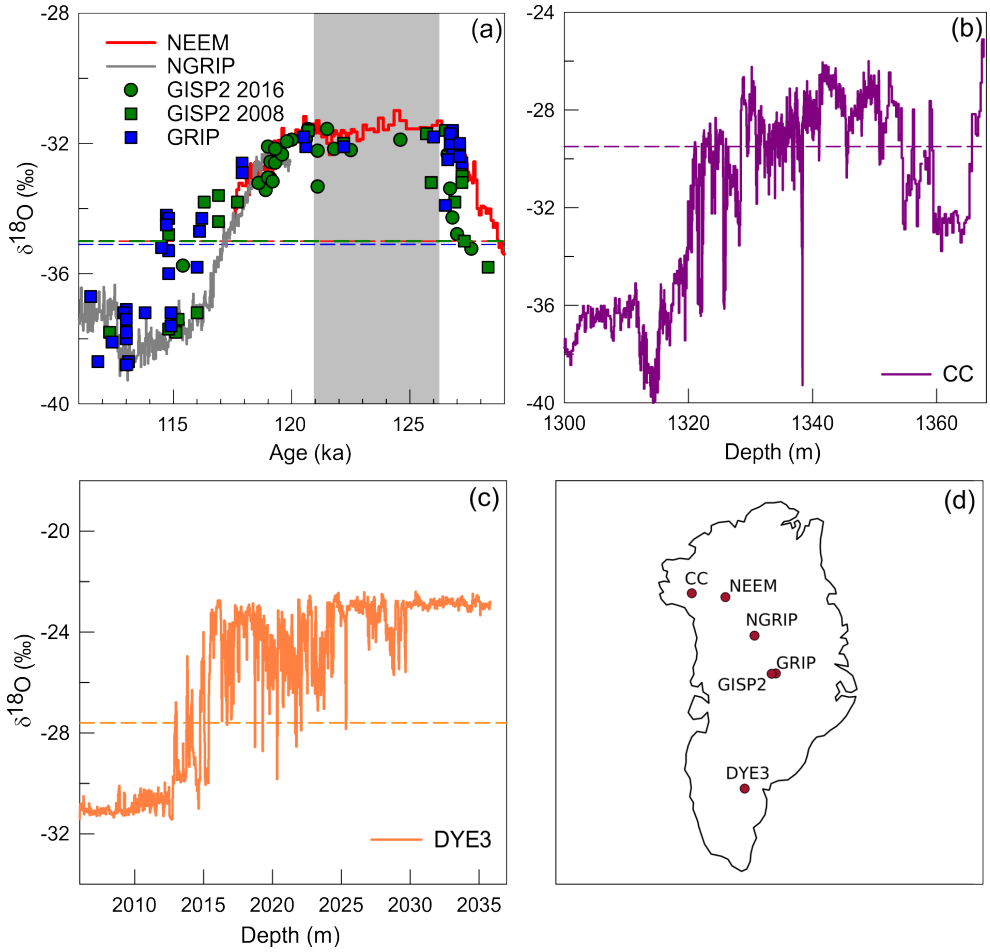

FIGURE 4.1: Summary of the data used. (a) $\delta^{18}O$ records from: NEEM (red line, NEEM community members (2013)) and NGRIP (grey line, NGRIP Project Members (2004)), both displayed on the AICC2012 chronology (Govin *et al.* (2015); Bazin *et al.* (2013); Veres *et al.* (2013); E. Capron, personal communication); GRIP (blue squares, dated by Landais *et al.* (2003)); GISP2 (green squares dated by Suwa and Bender (2008) and green circles dated by Yau *et al.* (2016)). (b) Camp Century, $\delta^{18}O$ on a depth scale (Johnsen *et al.*, 2001). (c) DYE3, $\delta^{18}O$ on a depth scale (Johnsen *et al.*, 2001). Panels (a) to (c): present-day $\delta^{18}O$ values are indicated with horizontal dashed lines. (d) Locations of Greenland ice cores: NEEM (77.45°N, 51.06°W), NGRIP (75.1°N, 42.3°W), GRIP (72.6°N, 37.6°W), GISP2 (72.6°N, 38.5°W), Camp Century (77.2°N, 61.1°W), DYE3 (65.2°N, 43.8°W).

and ice-core measurements, in terms of both mathematical properties and ice morphologies. Finally, implications for the GIS morphology during the LIG and for the ice core drilling community are discussed in Section 4.6.

4.3 Data

We compile LIG stable water isotopic ($\delta^{18}O$) information from six Greenland deep ice cores: NEEM, NGRIP, GRIP, GISP2, Camp Century and DYE3, see Figure 4.1 for references and illustration of the data, and also Johnsen and Vinther (2007), Suwa *et al.* (2006a). While LIG ice layers have been found in numerous Greenland deep ice cores, it is not straightforward to infer the LIG peak $\delta^{18}O$ and the associated uncertainty range because of the difficulties attached to the dating of the LIG layers and the possibility of missing LIG layers.

NEEM is the only Greenland ice core depicting a continuous LIG climatic record, *i.e.* it covers the time interval ∼114.5 to ∼128.5 ka (NEEM community members, 2013)). Absolute dating uncertainties for NEEM are estimated to be of at least two thousand years (Govin *et al.*, 2015). Dating uncertainty at the bottom for the other Greenland ice cores are likely larger. The ice stratigraphy at NGRIP is undisturbed but basal melting possibly removed the older LIG section. Hence, dating uncertainties are attached to the lack of data available to constrain the glaciological flow model used to establish the age model (NGRIP Project Members, 2004). While tentative reconstructions of the chronology of the bottom of the GRIP and GISP2 ice cores have been made using CH_4 gas record synchronisation with Antarctic ice cores (Landais *et al.*, 2003; Suwa *et al.*, 2006a), the accuracy of dating the bottom of Camp Century (CC) and DYE3 is limited by the poor preservation of deep ice samples. See Section 1 of the Supporting Information for full details.

In Table 4.1, we summarise the previous information by providing a most likely, minimum, and maximum value of $\delta^{18}O$ at each site. All values are provided as anomalies with respect to the present day. At NEEM, GRIP and GISP2, the LIG values are computed by considering the maximum and minimum $\delta^{18}O$ values measured across the time interval 120-126 ka (Figure 4.1). At NGRIP, we take the maximum/minimum value from near the bed, as the ice core does not reach back to 126 ka. We acknowledge that inferred uncertainties attached to the NGRIP $\delta^{18}O$ minimum anomaly might be underestimated due to dating uncertainties as well as elevation-related assumptions (see Supporting Information for details). For Camp Century and DYE3 sites, we use

TABLE 4.1: Stable water isotopic ($\delta^{18}O$) information from six Greenland deep ice cores: NEEM, NGRIP, GRIP, GISP2, Camp Century and DYE3. Most likely, maximum, and minimum values between 120 and 126 ka. All values are anomalies with respect to the present day. See Section 1 of the Supporting Information for full details.

	Anomaly values at each ice core site					
	NEEM	**NGRIP**	**GRIP**	**GISP2**	**CC**	**DYE3**
	$\delta^{18}O$ ‰	$\delta^{18}O$ ‰	$\delta^{18}O$ ‰	$\delta^{18}O$ ‰	$\delta^{18}O$ ‰	$\delta^{18}O$ ‰
Most likely[a]	+3.6	+3.1	+3.2	+2.7	+2.5	+4.7
Minimum[b]	+2.7	+2.5	+2.2	+1.7	+0.0	+0.0
Maximum[b]	+4.0	+3.8	+3.5	+3.4	+4.0	+5.2

[a]For NEEM, we take the value at the age 126 ka. For the other ice cores, this is the value provided by Johnsen and Vinther (2007). [b] We take the maximum/minimum value within 120-126 ka along the dated NEEM, GRIP and GISP2 ice cores. For NGRIP, we take the maximum/minimum value from near the bed, as the ice core does not reach back to 126 ka. For CC and DYE3, we use the maximum value from near the bed as a maximum, and the present-day value as the minimum. Details are provided in the Supporting Information.

the maximum value from near the bed as the maximum, and the present-day value as the minimum (see Supporting Information for details). The last choice is due to the fact that, at both sites, it is not possible to confidently identify ice from the 120-126 ka time interval. In Section 4.5, we investigate a series of scenarios which help to estimate how much information would be gained from recovering better dated LIG ice from the Camp Century and DYE3 core locations.

4.4 Methods

To tackle the problem of using ice core data to help constrain the morphology of the GIS at 125 ka, we develop a methodology using climate simulations and Gaussian process emulation to assess the response of $\delta^{18}O$ in Greenland ice cores to changes in the shape and extent of the GIS. This requires a mathematical parameterisation of the set of GIS morphologies (Section 4.4.1), and the selection of a small number of design morphologies on which to run the $\delta^{18}O$ climate simulator (Section 4.4.2). Based on the $\delta^{18}O$ simulated responses (Section 4.4.3) on the design morphologies, an emulator is built (Section 4.4.4) that allows almost instantaneous $\delta^{18}O$ predictions to any GIS morphology.

4.4.1 Parameterising the Set of Ice-Sheet Morphologies

We undertake the problem of parameterising the set of ice-sheet morphologies using a Principal Component Analysis (PCA) approach. This allows extrapolation of important morphology patterns from an initial set of LIG GIS reconstructions. A classical application of PCA to our ice-sheet data set, however, would be inappropriate due to the spherical geometry of the Earth. We therefore apply the PCA ideas while weighting the components of a real vector, in our case representing the surface height of an ice sheet at different grid cells, by the area of the grid cells. This represents a particular case of generalised PCA, described for example in Jolliffe (2002). The paper Salter *et al.* (2019) illustrates an application of the methodology within the uncertainty quantification literature. We provide full details of the approach applied to our case in the Supporting Information.

To represent the wide range of GIS morphologies proposed for the LIG, we gather 14 GIS data sets from across several studies, see Figure 4.2 for references and illustration (and Section 2 of the Supporting Information for full details). These ice-sheet morphologies are used as a starting point to generate a much wider set of synthetic, potential morphologies. Prior to this, the 14 original morphologies are regridded onto a common, rectangular grid with resolution of 0.2° in both directions, ranging over latitudes 59.7°N to 83.9°N and longitudes 73.6°W to 11°W. This results in a total of 122×314 grid cells for each morphology. The application of our PCA approach to this data set yields 13 Principal Components (PCs) $V_1, \ldots, V_{13}$, each in the form of a 122×314 matrix of surface height values (Figure 4.3). We can generate new morphologies by taking linear combinations of the PCs, and adding the morphology $\overline{M}$ obtained as the average of the original data set. That is, any synthetically generated morphology M in this work is of the form:

$$M = \overline{M} + \sum_{i=1}^{r} x_i V_i \ \in \mathbb{R}^{122 \times 314} \tag{4.1}$$

for some real-valued coefficients $x_1, \ldots, x_r$. We choose $r = 8$ in light of the two following observations. Table 4.2 shows that the first eight PCs already account

TABLE 4.2: Standard deviations σ_i associated with the Principal Components through PCA (first row), and corresponding percentages of variance explained (second and third row).

	PC 1	**PC 2**	**PC 3**	**PC 4**	**PC 5**	**PC 6**	**PC 7**	**PC 8**
σ_i	271.12	228.56	145.45	141.41	91.37	86.16	75.40	65.21
% of Explained Variance	36.37	25.85	10.47	9.90	4.13	3.67	2.81	2.10
Cumulative % of Expl. Var.	36.37	62.22	72.69	82.59	86.72	90.40	93.21	95.31

	PC 9	**PC 10**	**PC 11**	**PC 12**	**PC 13**
σ_i	56.62	47.80	44.45	36.72	25.71
% of Explained Variance	1.59	1.13	0.98	0.67	0.33
Cumulative % of Expl. Var.	96.90	98.03	99.01	99.67	100

for more than 95% of the data set variance, hence capturing most of the variability displayed by the 14 original morphologies. Moreover, we observe that clear patterns can be seen in the plots of the first PCs: for example, PC1 in Figure 4.3 reveals that a positive coefficient x_1 in equation (4.1) will mainly increase the surface height of the generated morphology in the north, and decrease it in the south. Patterns can also be seen in higher PCs, but the omitted (9th to 13th) PCs seem more challenging to interpret in a physical sense.

Associating a morphology M to the vector $\boldsymbol{x} = (x_1, \dots, x_8)$ of its coefficients in equation (4.1), and vice versa, allows us to parameterise morphologies using the Euclidean space $\mathbb{R}^8$. Within this parameterisation, we can canonically associate the 14 original morphologies to vectors $\widetilde{\boldsymbol{x}}^{(\mathbf{1})}, \dots, \widetilde{\boldsymbol{x}}^{(\mathbf{14})} \in \mathbb{R}^8$, obtained by projecting each morphology onto the space generated by the first eight PCs. Notice that equation (4.1) with coefficients $\boldsymbol{x} = \widetilde{\boldsymbol{x}}^{(\boldsymbol{j})}$ does not recover exactly the j^{th} original morphology, due to the truncation error. However, the differences are small, since the neglected components account for less than 5% of the original data set variance. By denoting with $\widetilde{x}_i^{(j)}$ the i^{th} component of the vector $\widetilde{\boldsymbol{x}}^{(\boldsymbol{j})}$, one can consider the sample variance

$$\sigma_i{}^2 = \mathrm{Var}\big\{\widetilde{x}_i^{(1)}, \dots, \widetilde{x}_i^{(14)}\big\}. \tag{4.2}$$

This provides a measure of the range covered by the original morphologies along the

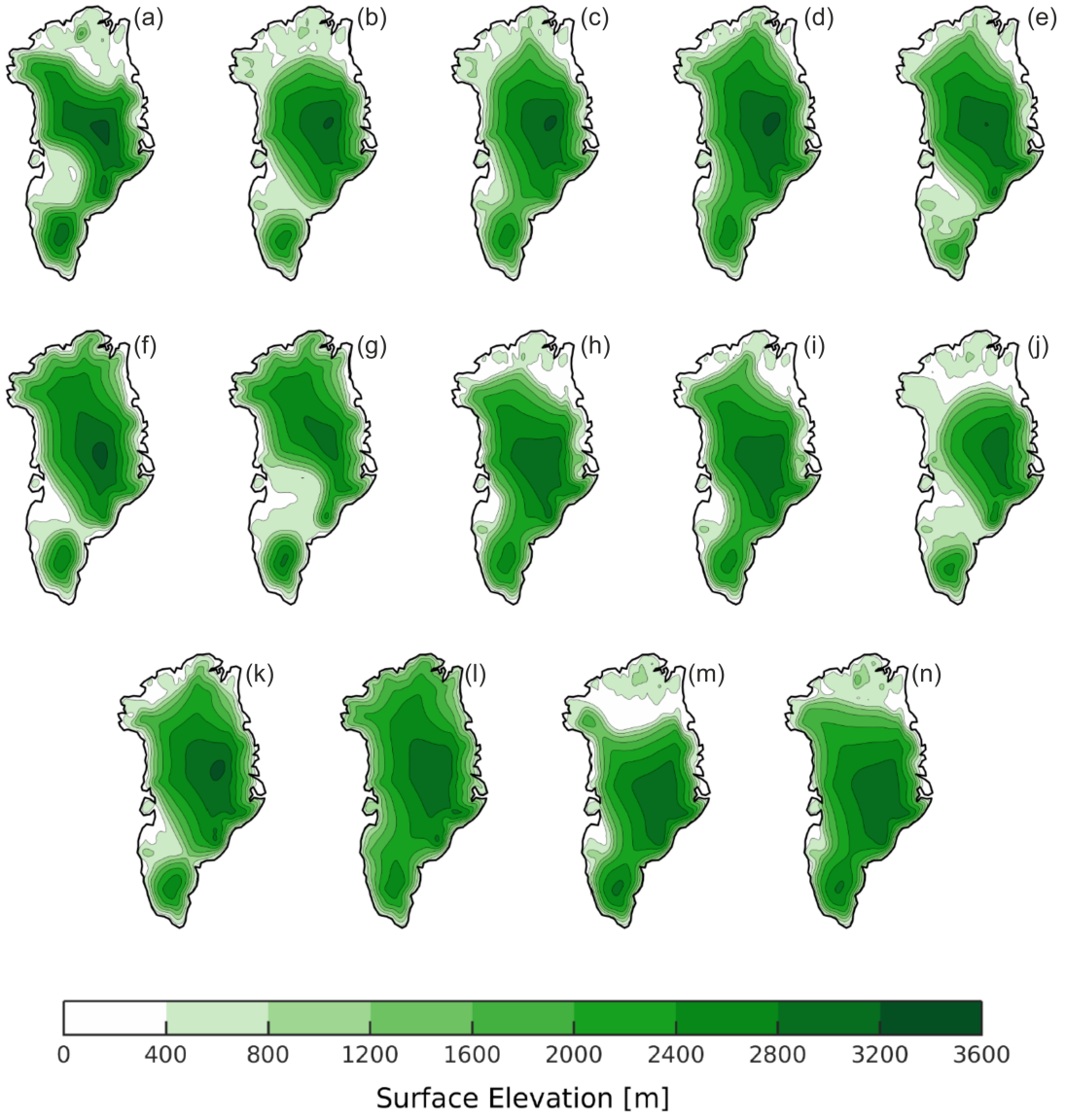

FIGURE 4.2: The surface height (meters) of LIG GIS morphologies used in this study. Panels contain data from: (a) Born and Nisancioglu (2012); (b) Calov *et al.* (2015) at 121.3 ka; (c) Calov *et al.* (2015) at 122.1 ka; (d) Calov *et al.* (2015) at 123.3 ka; (e) Helsen *et al.* (2013); (f) Langebroek and Nisancioglu (2016) (minimum GIS for temperature lapse rate of 6.5°C/km); (g) Langebroek and Nisancioglu (2016) (minimum GIS for temperature lapse rate of 8°C/km); (h) Quiquet *et al.* (2013) (CNRM anomaly experiment); (i) Quiquet *et al.* (2013) (IPSL anomaly experiment); (j) Robinson *et al.* (2011) (strongly retreated GIS); (k) Robinson *et al.* (2011) (moderately retreated GIS); (l) Robinson *et al.* (2011) (weakly retreated GIS);(m) Stone *et al.* (2013) (GIS extent for the maximum contribution to sea level rise, +3.8m); and (n) Stone *et al.* (2013) (GIS extent for the most likely contribution to sea level rise, +1.5m).

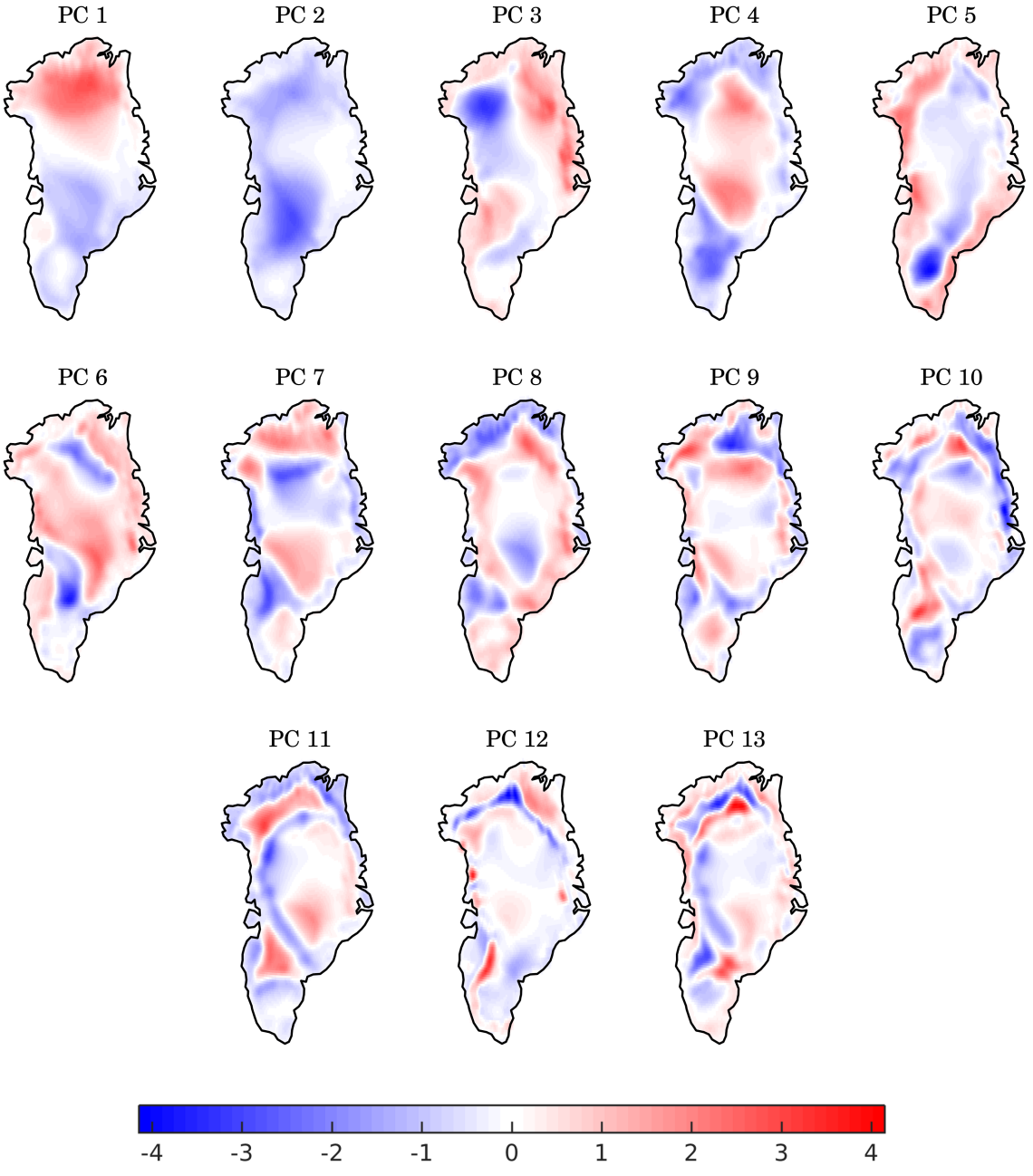

FIGURE 4.3: Plots of the PCs used to generate new synthetic morphologies in equation (4.1). Within each PC, areas of opposite sign yield opposite contributions to the surface height of the generated morphology. The values in the colour bar do not have a physical meaning: the PCs have norm equal to one with respect to the scalar product used to carry out the PCA.

i^{th} PC. The values of the standard deviation σ_i associated with the i^{th} PC are shown in Table 4.2.

For our analysis we consider a prior distribution on the shape of all ice sheets or, equivalently, on the parameter vectors $\boldsymbol{x} \in \mathbb{R}^8$. Since the prior distribution should be concentrated in a region of the parameter space informed by the 14 original morphologies, we use

$$x_i \sim N(0, {\sigma_i}^2) \tag{4.3}$$

independently, *i.e.* under the prior the parameters are independent, normally distributed with mean 0 and variance ${\sigma_i}^2$. We will use this prior distribution, when designing the simulation runs in the next section, and when the compatibility with the ice-core records is explored in Section 4.5.2.

Finally, in order to avoid generating a GIS morphology with unrealistically low surface heights, at each grid point we consider either the bedrock height (using Stone *et al.* (2013) at 1.5m of sea level rise) or the surface height from equation (4.1), whichever is greater. Once a morphology is generated, a corresponding land-ice mask is required to carry out a $\delta^{18}O$ climate simulation: at each grid-cell, this specifies whether the morphology is covered by ice or not. For the 14 original morphologies, the mask is provided. For a new morphology M, we generate the mask cell by cell, by comparing the cell height to the corresponding heights of the original morphologies, further considering which of them have ice in the cell in question. Full details are provided in Section 5 of the Supporting Information, where the mask-generation method is also validated.

4.4.2 Choosing Morphologies for the $\delta^{18}O$ Simulations

The isotope-enabled coupled atmosphere-ocean general circulation model employed in this work is HadCM3. The model has been used extensively, with $\delta^{18}O$ specific code, to examine a variety of climate, sea-ice, and ice-sheet problems (*e.g.*Holloway *et al.*, 2016a, 2017; Tindall *et al.*, 2010; Malmierca-Vallet *et al.*, 2018). In the present study,

HadCM3 is used to simulate $\delta^{18}O$ during the LIG, at the six Greenland locations introduced in Section 4.3.

In order to build an emulator of the climate simulator HadCM3, the simulated $\delta^{18}O$ response on some GIS morphologies is required. We call these design morphologies; the parameters $\boldsymbol{x}^{(j)} \in \mathbb{R}^8$ associated with them through equation (4.1) will be referred to as design points. Since each HadCM3 simulation is expensive, needing more than a week of real time to complete, only a few simulations can be performed. Careful selection of design morphologies is important to ensure a good calibration of the emulator (see Montgomery (2017)).

In this study, we perform simulations in two waves. For the first wave, our aim is to generate design morphologies which are well-scattered within the region of space that the emulator is required to explore. For this, we use a quasi-random sample from the prior distribution (4.3): we generate a Halton quasi-random sequence (Kocis and Whiten (1997)) of well-scattered vectors $\hat{\boldsymbol{x}}^{(j)}$ in the eight-dimensional unit cube, and we apply the inverse of a cumulative distribution function of $N(0, {\sigma_i}^2)$ to the i^{th} component of the vector $\hat{\boldsymbol{x}}^{(j)}$. This yields a sequence of design points $\boldsymbol{x}^{(j)}$ with the correct variance along each PC, and whose corresponding morphologies systematically cover different GIS scenarios for 125 ka. The GIS morphologies corresponding to the sequence of points $\boldsymbol{x}^{(j)}$ are generated, and the first 64 are selected that pass a basic plausibility test on their maximum height. The test consists in checking that the maximum surface height of a generated morphology is not greater than the mean plus four standard deviations of the set of maximum heights of the original morphologies. Two of the numerical simulations crashed for unknown reasons and were thus omitted from the analysis.

For the second wave, we use seven morphologies which are specially designed to assess how much small elevation changes in a morphology affect the simulator response. Each additional morphology is obtained upon perturbation of the parameter $\boldsymbol{x} \in \mathbb{R}^8$ associated with one of the first-wave morphologies (different in each case). In all seven cases, the induced difference on the surface elevation is order of only a few tens of meters. In two cases, differences of order of only few millimeters have been intentionally induced to test the chaoticity of the simulator response. This is also

discussed in Section 4.4.4.2, in relation to the use of a nugget term in equation (4.17). The total number of design morphologies that we use is therefore $n = 62 + 7 = 69$.

4.4.3 HadCM3 Simulation Runs

After the design morphologies are chosen, HadCM3 is used to reproduce the $\delta^{18}O$ response to these modified GIS morphologies at the ice-core sites. All LIG simulations are forced with GHG values and orbital forcing which are appropriate for 125 ka. Further details on the model and the simulations are provided in the Supporting Information, Section 3. In order to minimise the impact of climate biases of the simulator, anomalies with respect to a pre-industrial simulation are considered: more precisely, we use the difference between the time-averaged $\delta^{18}O$ output from the last 50 years of the modified GIS LIG simulations and the time-averaged $\delta^{18}O$ output from the last 50 years of the pre-industrial simulation.

A well-known limitation in comparing paleoclimate data with model results is the discrepancy in resolution. Model grid cells cover areas of hundreds of square kilometers, while the location where the ice core has been extracted corresponds to a single point on the globe. Here, we use bilinear interpolation over the different grid cells in order to compute the simulated $\delta^{18}O$ output at each of the ice-core locations of interest. We note further that the coarse HadCM3 spatial resolution makes it difficult to reliably simulate $\delta^{18}O$ values at the coastal margins. Accordingly, the small Renland ice dome (where LIG ice has been recovered) is not analysed in this study in that not adequately captured within the HadCM3 resolution.

In Figure 4.4, the outputs of the $n = 69$ simulation runs are shown for each ice-core site, together with bands highlighting the minimum and maximum $\delta^{18}O$ anomalies reconstructed from the ice-core records (Table 4.1). The figure shows that, for all pairs of locations, there are design morphologies whose simulated $\delta^{18}O$ anomalies are within the corresponding data ranges, illustrating that the model is able to reproduce the observed data in principle. Closer inspection shows that there are seven runs which match the data on five of the sites simultaneously. Due to the limited number of design morphologies, there is however no run which matches all six of the sites.

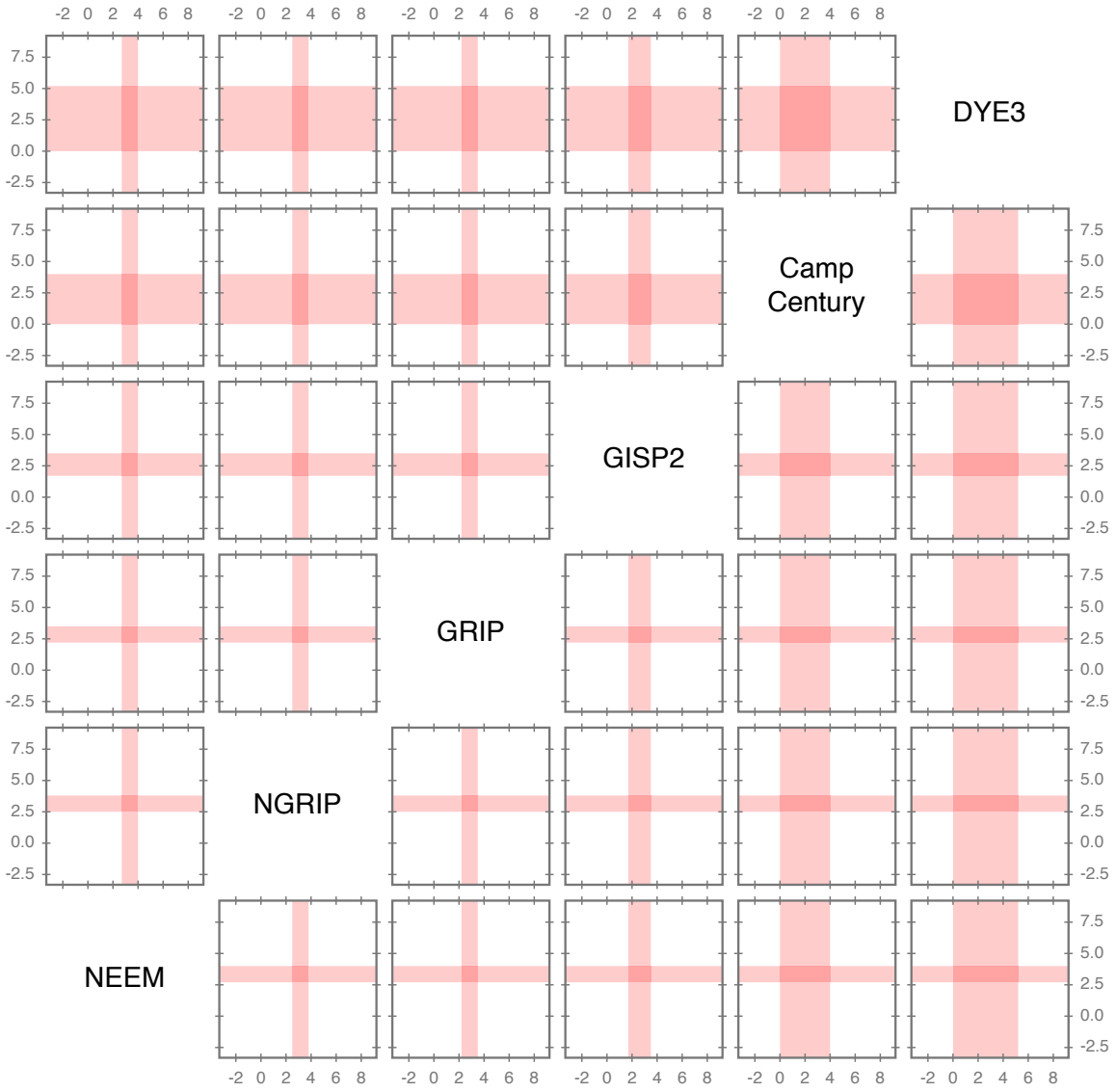

FIGURE 4.4: Simulated per-mille $\delta^{18}O$ anomalies for the design morphologies. Results are shown for pairs of locations. Shaded bands in red correspond to the ranges reconstructed using ice core records, using the minimum/maximum values shown in Table 4.1.

4.4.4 The Emulator

A GP emulator is a statistical model that effectively predicts the response of a complex simulator, on the basis of the actual simulator response at only a few inputs. In our case, we emulate the response of $\delta^{18}O$ anomalies to changes in the GIS morphology at 125 ka, starting from the climate simulator response on the design morphologies. For the convenience of the reader, in Section 4.4.4.1 we summarise the formulas needed to

build an emulator. In the subsequent sections, we explain and justify the particular choices undertaken in relation to the problem explored here.

4.4.4.1 General Setting

The Bayesian framework of GP emulation is investigated, among others, in O'Hagan (1978), Sacks *et al.* (1989), Kennedy and O'Hagan (2001). Further works address more specific questions, such as the use of appropriate covariance functions (Fricker *et al.*, 2012), the use of a nugget term (Andrianakis and Challenor, 2012), or methods to validate the emulator (Bastos and O'Hagan, 2009). In the following, we provide a concise summary of the main steps and formulas leading to the construction of a GP emulator: we refer the reader to the aforementioned literature for a more in-depth overview.

We use lowercase letters for numbers and vectors (plain and bold, respectively), and uppercase letters for matrices (plain). The general setting is the one where the simulator has been run on n design points $\boldsymbol{x^{(1)}}, \ldots, \boldsymbol{x^{(n)}} \in \mathbb{R}^p$, leading to outputs $y_1, \ldots, y_n \in \mathbb{R}$. The emulator is a stochastic process η providing probabilistic predictions of the simulator output at any point $\boldsymbol{x} \in \mathbb{R}^p$, and which interpolates the value y_j at the design point $\boldsymbol{x^{(j)}}$, $j = 1, \ldots, n$.

To build the emulator, a prior mean function $m(\cdot)$ and covariance function $v(\cdot, \cdot)$ must be chosen. Following O'Hagan (1992), we assume

$$m(\boldsymbol{x}) = \boldsymbol{h}(\boldsymbol{x})^\top \boldsymbol{\beta}, \quad \boldsymbol{x} \in \mathbb{R}^p \tag{4.4}$$

$$v(\boldsymbol{x}, \boldsymbol{x'}) = \sigma^2 \, c(\boldsymbol{x}, \boldsymbol{x'}), \quad \boldsymbol{x}, \boldsymbol{x'} \in \mathbb{R}^p \tag{4.5}$$

for some coefficients $\boldsymbol{\beta} \in \mathbb{R}^q$ and $\sigma^2 > 0$. Here, $\boldsymbol{h}(\boldsymbol{x})$ is a vector of q functions of the parameter $\boldsymbol{x}$, and $c(\boldsymbol{x}, \boldsymbol{x'})$ is a covariance function. The functions $\boldsymbol{h}$ and c must be chosen as part of the design of the emulator, while $\boldsymbol{\beta}$ and σ^2 can be estimated from data.

The GP $\eta(\cdot)$ with mean function $m(\cdot)$ and covariance function $v(\cdot, \cdot)$ is conditioned on the observations $\eta(\boldsymbol{x^{(j)}}) = y_j$ for $j \in \{1, \ldots, n\}$. Usually, a "flat" prior distribution

(O'Hagan (1992)) is chosen for the pair $(\boldsymbol{\beta}, \sigma^2)$. In this case, under the posterior distribution $\eta(\cdot)$ is a Student's t-process (Tracey and Wolpert (2018)) with $n - q$ degrees of freedom. To provide the expression of the posterior mean and covariance functions, we introduce some notation:

$$H = \begin{pmatrix} \boldsymbol{h}\left(\boldsymbol{x^{(1)}}\right)^\top \\ \vdots \\ \boldsymbol{h}\left(\boldsymbol{x^{(n)}}\right)^\top \end{pmatrix} \in \mathbb{R}^{n\times q}, \quad A = \begin{pmatrix} c\left(\boldsymbol{x^{(1)}}, \boldsymbol{x^{(1)}}\right) & \cdots & c\left(\boldsymbol{x^{(1)}}, \boldsymbol{x^{(n)}}\right) \\ \vdots & \ddots & \vdots \\ c\left(\boldsymbol{x^{(n)}}, \boldsymbol{x^{(1)}}\right) & \cdots & c\left(\boldsymbol{x^{(n)}}, \boldsymbol{x^{(n)}}\right) \end{pmatrix} \in \mathbb{R}^{n\times n}. \tag{4.6}$$

Set

$$B = H^\top A^{-1} H \in \mathbb{R}^{q\times q}, \tag{4.7}$$

$$\boldsymbol{b} = B^{-1} H^\top A^{-1} \boldsymbol{y} \in \mathbb{R}^q, \tag{4.8}$$

$$\boldsymbol{e} = \boldsymbol{y} - H\boldsymbol{b} \in \mathbb{R}^n, \tag{4.9}$$

where $\boldsymbol{y} = (y_1, \ldots, y_n)^\top$ and, for any input $\boldsymbol{x} \in \mathbb{R}^p$, define

$$\boldsymbol{t}(\boldsymbol{x}) = \left(c\big(\boldsymbol{x}, \boldsymbol{x^{(1)}}\big), \ldots, c\big(\boldsymbol{x}, \boldsymbol{x^{(n)}}\big)\right)^\top \in \mathbb{R}^n, \tag{4.10}$$

$$\boldsymbol{p}(\boldsymbol{x}) = \boldsymbol{h}(\boldsymbol{x}) - H^\top A^{-1} \boldsymbol{t}(\boldsymbol{x}) \in \mathbb{R}^q. \tag{4.11}$$

Using this notation, the posterior mean of σ^2 is

$$\hat{\sigma}^2 = \frac{\boldsymbol{e}^\top A^{-1} \boldsymbol{e}}{n - q - 2}. \tag{4.12}$$

The posterior mean and covariance function of the process $\eta(\cdot)$ are then given by

$$\hat{m}(\boldsymbol{x}) = \boldsymbol{h}(\boldsymbol{x})^\top \boldsymbol{b} + \boldsymbol{t}(\boldsymbol{x})^\top A^{-1} \boldsymbol{e} \tag{4.13}$$

and

$$\hat{v}(\boldsymbol{x}, \boldsymbol{x'}) = \hat{\sigma}^2 \left[c(\boldsymbol{x}, \boldsymbol{x'}) - \boldsymbol{t}(\boldsymbol{x})^\top A^{-1} \boldsymbol{t}(\boldsymbol{x'}) + \boldsymbol{p}(\boldsymbol{x})^\top B^{-1} \boldsymbol{p}(\boldsymbol{x'})\right], \tag{4.14}$$

respectively. In particular, the emulator prediction at a point $\boldsymbol{x} \in \mathbb{R}^p$ is a Student's t-distributed random variable with mean $\hat{m}(\boldsymbol{x})$, variance $\hat{v}(\boldsymbol{x}, \boldsymbol{x})$ and $\nu = n - q$ degrees

of freedom: this can be written as

$$\hat{m}(\boldsymbol{x}) + \sqrt{\frac{\nu-2}{\nu}\,\hat{v}(\boldsymbol{x},\boldsymbol{x})}\cdot T_\nu, \tag{4.15}$$

where T_ν denotes a standard t-distributed random variable with ν degrees of freedom.

4.4.4.2 Choosing the Mean and Covariance Functions

In the present application, we fit separate emulators for each ice-core site. For each site, the design points $\boldsymbol{x}^{(j)}$ are the eight-dimensional vectors associated with the design morphologies (Section 4.4.2), while the values y_j are the corresponding simulated $\delta^{18}O$ anomalies.

To help us decide on the form of the function $\boldsymbol{h}(\cdot)$ used in the prior mean (4.4), we perform a multiple linear regression, describing y_j as linear combination of $x_1^{(j)},\ldots,x_8^{(j)}$. For all the six locations, a linear model proves appropriate, showing unstructured residuals and adjusted coefficient of determination (adjusted R^2) greater than 0.89 for all sites. Given this very good fit, we choose

$$m(\boldsymbol{x}) = \beta_0 + \beta_1 x_1 + \ldots + \beta_8 x_8, \quad \boldsymbol{x}\in\mathbb{R}^8. \tag{4.16}$$

Using the notation in Section 4.4.4.1, we have $\boldsymbol{h}(\boldsymbol{x}) = \left(1,\boldsymbol{x}^\top\right)^\top$, $p=8$ and $q=p+1=9$.

For the covariance function $c(\cdot,\cdot)$ used in (4.5) we use the form

$$c(\boldsymbol{x},\boldsymbol{x'}) = \exp\left(-(\boldsymbol{x}-\boldsymbol{x'})^\top D^{-1}(\boldsymbol{x}-\boldsymbol{x'})\right) + \mu\,\delta_{\boldsymbol{x},\boldsymbol{x'}}, \quad \boldsymbol{x},\boldsymbol{x'}\in\mathbb{R}^8, \tag{4.17}$$

where D is the 8×8 diagonal matrix with diagonal elements ${d_1}^2,\ldots,{d_8}^2$, and $\delta_{x,y}$ equals 1 if $x=y$ and 0 otherwise. The parameters $d_1,\ldots,d_8$ and μ will be estimated from data (Section 4.4.4.3).

The first, squared-exponential term in the definition of $c(\cdot,\cdot)$ models the decay in correlation when the distance of inputs increases. The parameters d_i are known as "correlation lengths". In addition to the squared-exponential covariance function

used in (4.17), experiments with other covariance functions (Matérn with parameters $\nu = 3/2$ and $\nu = 5/2$, see Rasmussen and Williams (2006)) were carried out while training the emulator. The mean and variance of the emulator predictions, as well as cross-validated estimates of the emulation error, were remarkably similar in the three cases. Given the apparent smooth linear response of the vector $\boldsymbol{y}$ to the eight PC scores, we chose the smoothest of the three covariance functions, *i.e.* the squared exponential.

The second term in the definition of $c(\cdot, \cdot)$ takes observational variance into account. In the presence of this term, the emulator provides non-deterministic predictions (*i.e.* with non-zero variance) even at the design points. This term is often referred to as "the nugget term", see *e.g.* Andrianakis and Challenor (2012). In our case, its addition is necessary because the system simulated by HadCM3 is chaotic. Even after averaging the outputs over 50 years, GIS morphologies that are physically equivalent (*i.e.* with surface elevations differing only by millimetres) result in significantly different $\delta^{18}O$ simulated anomalies. A numerical benefit of using a nugget term is that it makes the matrix A in (4.6) better conditioned. It thus helps to achieve numerical stability when computing the emulator predictions, a step that involves the use of the matrix inverse A^{-1}.

4.4.4.3 Estimation of Correlation Lengths and Nugget Term

The correlation lengths d_i and the nugget term μ appearing in equation (4.17) can be estimated in different ways. A maximum likelihood approach is often used in the estimation of hyperparameters (see Berger *et al.* (2001); Andrianakis and Challenor (2012)): however, especially in higher dimensions, the maximisation algorithm is often trapped in either local maxima or flat regions. In this work, we use the alternative approach described in this section.

First we observe that all PCs are normalised and have therefore comparable size. Changes of similar magnitude in any two different components of an input parameter $\boldsymbol{x} \in \mathbb{R}^8$ therefore yield, overall, changes of similar magnitude in the corresponding ice morphologies. At a single-site level this becomes less true, with similar changes in

different PCs affecting differently the surface height at the site. We notice, however, that the simulated $\delta^{18}O$ response at a location does not depend only on the surface height at the location, but rather on the surface elevation within a larger area around it and, ultimately, on the whole morphology. In the light of this, assuming that similar changes in the components of a vector $\boldsymbol{x}$ have a comparable impact in the simulated $\delta^{18}O$ at a given location does not appear unreasonable.

Separately, we note that the number of parameters that have to be estimated to build each emulator includes the 9 mean regression coefficients $\beta_0, \ldots, \beta_8$, the variance σ^2, the nugget term μ and the 8 correlation lengths d_i. Given the limited number of training points ($n = 69$), an independent estimation of all the parameters presents a high risk of overfitting. In light of both this and the previous consideration, we assume $d_1 = \cdots = d_8 = d$. The parameter d and the nugget parameter μ are estimated simultaneously, by maximising a cross-validated estimate of the posterior density of the data, as explained below.

Starting from the data set $(\boldsymbol{x^{(j)}}, y_j)_{j=1,\ldots,n}$, consider the n emulators calibrated on the data sets where the j^{th} observation has been left out, respectively. Let $\rho^{(j)}_{d,\mu}(\cdot)$ be the posterior density function at $\boldsymbol{x^{(j)}}$ of such an emulator, where the parameters $\boldsymbol{d} = (d, \ldots, d)$ and μ are used as correlation lengths and nugget respectively. From Section 4.4.4.1 we know that $\rho^{(j)}_{d,\mu}$ is the density function of a t-distribution with mean and variance as in (4.13, 4.14). Now define

$$f(d, \mu) = \log\Big(\prod_{j=1}^{69} \rho^{(j)}_{d,\mu}(y_j)\Big) = \sum_{j=1}^{69} \log\big(\rho^{(j)}_{d,\mu}(y_j)\big). \tag{4.18}$$

The function $f(d, \mu)$ is a measure of the goodness of the emulator predictions, when correlation lengths d and nugget μ are used. The parameters d and μ used in our emulators are chosen to maximise $f(\cdot, \cdot)$. We use the Matlab nonlinear solver `fminunc`, and repeat the maximisation multiple times from different starting points, to reduce the risk of getting stuck in a local extremum.

4.4.5 Data-Model Comparison

In order to carry out the data-model comparison, we follow the idea of using an implausibility measure, as for example in Craig *et al.* (1997), Vernon *et al.* (2010), Williamson *et al.* (2015). Implausibility measures are used within the context of history matching: this last term, originally used in the oil industry (see the above-mentioned Craig *et al.* (1997)), is now employed in the emulation literature to refer to the process of finding the inputs of a model whose outputs match historical observations. In our case, to select the morphologies compatible with the observed ice-core records, we proceed as follows.

Let $\hat{m}_{L}(\boldsymbol{x})$ and $\hat{v}_{L}(\boldsymbol{x},\boldsymbol{x})$ be the mean and the variance of the $\delta^{18}O$ emulator prediction at a given location L, for the morphology represented by $\boldsymbol{x} \in \mathbb{R}^8$ (equations (4.13) and (4.14)). Let us further denote by R_{L} the most likely ice-core record $\delta^{18}O$ anomaly at that location, and by R_{L}^{-} and R_{L}^{+} the lower and upper bounds associated with it: values for $R_{L}^{-} < R_{L} < R_{L}^{+}$ are provided in Table 4.1. In order to quantify the mismatch, at the location L, between the emulator $\delta^{18}O$ prediction and the ice core record information, we define the following "implausibility function":

$$I_L(\boldsymbol{x}) = \frac{\left|\hat{m}_{L}(\boldsymbol{x}) - R_{L}\right|}{\sqrt{v_{L}(\boldsymbol{x},\boldsymbol{x}) + \mathrm{Var}(\mathrm{Rec}_{L})}}. \tag{4.19}$$

The quantity $\mathrm{Var}(\mathrm{Rec}_{L})$ is meant to provide a measure of the variability associated with the ice-core record. Based on the analogy that the variance of a uniform random variable on an interval of length l is $l^2/12$, we compute $\mathrm{Var}(\mathrm{Rec}_{L})$ as follows:

$$\mathrm{Var}(\mathrm{Rec}_{L}) = \begin{cases} \left(R_{L}^{+} - R_{L}\right)^2/3 & \text{if } \hat{m}_{L}(\boldsymbol{x}) > R_{L}, \\ \left(R_{L} - R_{L}^{-}\right)^2/3 & \text{if } \hat{m}_{L}(\boldsymbol{x}) < R_{L}. \end{cases} \tag{4.20}$$

Notice that, in equation (4.20), we deal with the two subintervals rather than the whole interval, hence the factor 1/3 rather than 1/12 appears. Finally, in order to obtain a quantitative measure of the mismatch between the emulator predictions for the morphology represented by $\boldsymbol{x} \in \mathbb{R}^8$ and the $\delta^{18}O$ information at all the six locations, we define

$$I(\boldsymbol{x}) = \max\{I_{L_1}(\boldsymbol{x}), \ldots, I_{L_6}(\boldsymbol{x})\}, \tag{4.21}$$

where $L_1, \ldots, L_6$ are the six locations in question.

We classify a morphology as Record-Compatible (RC), if the condition $I(\boldsymbol{x}) \leq 2$ holds, and at least 95% of the morphology cell heights are within 2 standard deviations of the average height of the 14 original morphologies at that cell. This ensures that RC morphologies pass a general physical plausibility test, in addition to being compatible with the data records. The possibility of relaxing the first criterion ($I_L(\boldsymbol{x}) \leq 2$ for $L = L_1, \ldots, L_6$) to the five sites with lowest implausibility measure has also been considered, but the choice leads to neglect in most cases the DYE3 constraint (in line with the high $\delta^{18}O$ anomaly recorded at the site). This is considered at odds with both the aim of the 3-scenario analysis and the fact that DYE3 is the only southern site available in this study.

We conclude with a comment. In the classical emulation literature, implausibility measures are generally used in combination with a several-wave simulation approach: the latter sequentially rules out the parts of the input space for which the condition $I(\boldsymbol{x}) > c$ holds true and builds a new emulator on the "Not Ruled Out Yet" (NROY) part of the space. The constant c is often chosen to be equal to 3 following Pukelsheim's 3σ rule (Pukelsheim (1994)). In this work, resource constraints prevented us from performing several iterations of the procedure. Hence, the implausibility measure $I(\boldsymbol{x})$, alongside the physical plausibility test described in the previous paragraph, is used to directly select morphologies, rather than rejecting them. For this reason we use a stricter criterion ($c = 2$) than the one more commonly found in the literature: the approach allows us to identify morphologies with a greater potential to match the ice-core data. Properties of these morphologies are explored in the next section.

TABLE 4.3: Location by location, the values of the correlation length (d) and the nugget term (μ) which are used to build the corresponding emulator. The estimation is carried out through the cross-validation procedure explained in Section 4.4.4.3. Higher values of d denote a stronger correlation between the $\delta^{18}O$ outputs associated with different morphologies. For a given d, higher values of μ indicate higher variance of the emulator predictions at the design points, alongside a generally smoother mean prediction.

	NEEM	**NGRIP**	**GRIP**	**GISP2**	**CC**	**DYE3**
d	208.14	309.40	397.58	322.93	3,117.3	513.40
μ	0.45	0.35	0.28	0.53	2.54×10^{-4}	0.09

4.5 Results

4.5.1 Fit of the Emulator

One emulator for each location is built according to the procedure described in Section 4.4.4. The estimated values of the correlation lengths and nugget are shown in Table 4.3. With the only exception of Camp Century, the estimated d are of comparable magnitude to the standard deviations σ_i of the first PCs, see Table 4.2. In the case of Camp Century, the estimation returns instead a relatively large d. After considerations, we decided to retain such value of d: indeed, it can be seen that for very large d the emulator converges to a simpler Bayesian linear regression model, which would still represent an appropriate limit case since the data at this site is well-described by a linear model, with an adjusted R^2 of 0.951.

To assess the quality of the fitted emulators we consider the cross-validated residuals for each site: that is, for each simulation, we fit an emulator leaving out this simulation, and use this emulator to predict the simulation output. This is done, in turn, for all n simulations. Figure 4.5 shows the differences between actual and predicted model outputs, at the six sites. The figure shows that nearly all simulation results lie within two emulator standard deviations of the prediction. Thus, both the values and the uncertainties predicted by the emulator seem appropriate. In particular, the emulator does not only make accurate predictions, but also can accurately assess the uncertainty of its predictions.

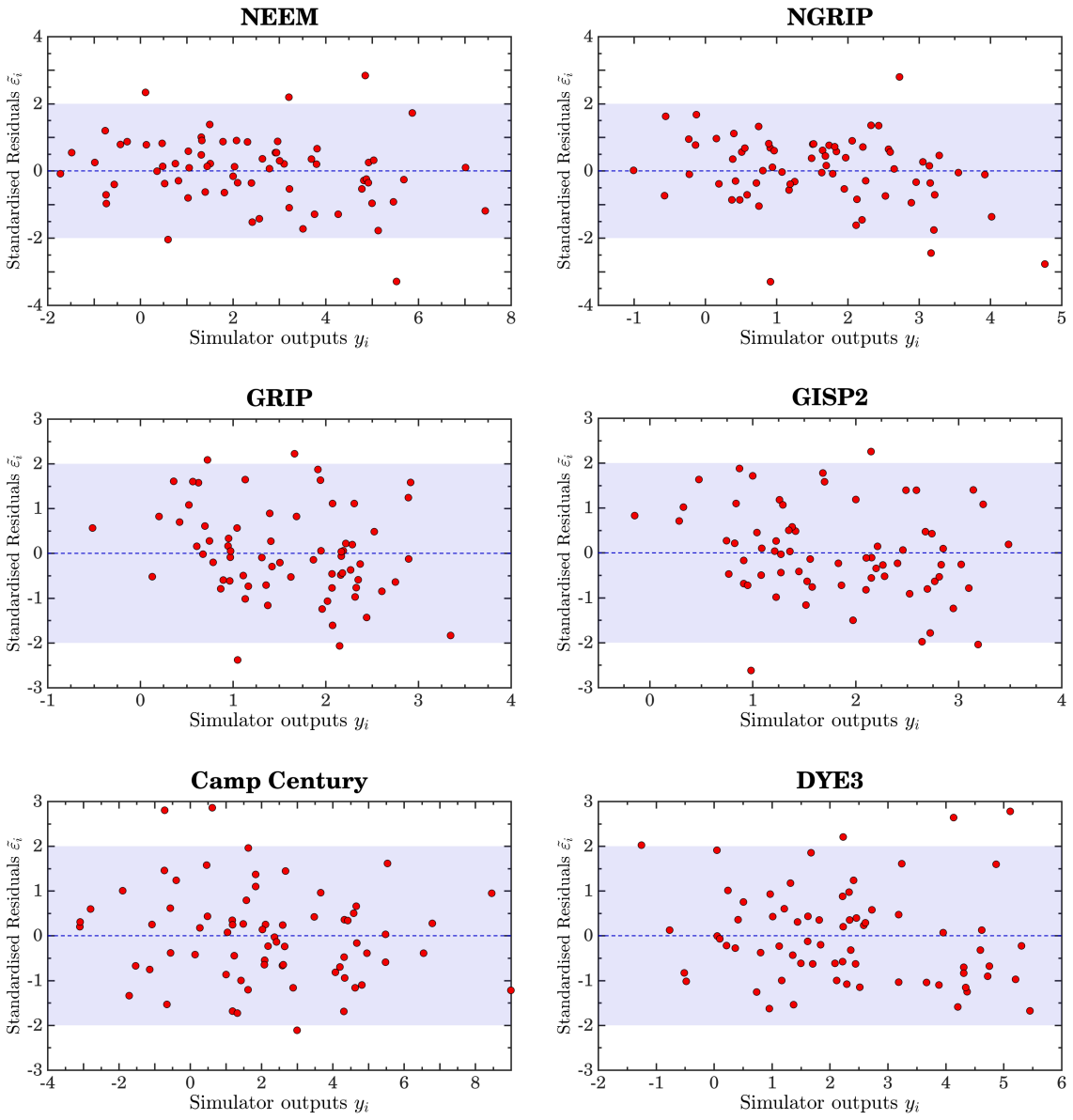

FIGURE 4.5: Cross-Validated residuals of the emulators at the different sites. Each red dot in a panel corresponds to one of the 69 simulations: the x component shows the simulator output; the y component shows the difference between the emulator prediction and the simulator output, measured in multiples of the standard deviation associated with the emulator prediction. The shaded bands highlight y values between -2 and 2, where around 95% of the standardised predictions are expected to lie. This is the case for all the six emulators used in this work.

4.5.2 Comparison Between Emulator Predictions and Ice Core Records

The six emulators allow us to efficiently predict, at the different locations, the $\delta^{18}O$ response of the climate simulator to any ice-sheet morphology. Using the methodology of Section 4.4.5, emulator outputs can be compared to the available $\delta^{18}O$ ice-core information to decide whether a given GIS morphology is record-compatible (RC).

In order to carry out the data-model comparison detailed in Section 4.4.5, values of R_{L}^{-}, R_{L} and R_{L}^{+} must be specified at all the locations where compatibility with records is to be imposed. We use the values in Table 4.1. However, as explained in Section 4.3, lower bounds for the $\delta^{18}O$ anomalies at Camp Century and DYE3 cannot be easily inferred from the records. In order to acknowledge this uncertainty, we carry out the analysis in the case of three different scenarios, according to how close these lower bounds are set to the most likely values $R_{\text{CC}} = +2.5‰$ and $R_{\text{DYE3}} = +4.7‰$. The scenarios we investigate are as follows:

1. Loose scenario (only imposing non-negative anomalies):

$$R_{\text{CC}}^{-} = 0‰, \quad R_{\text{DYE3}}^{-} = 0‰. \tag{4.22}$$

2. Middle scenario:

$$R_{\text{CC}}^{-} = 1‰, \quad R_{\text{DYE3}}^{-} = 2‰. \tag{4.23}$$

3. Tight scenario ($R_{L}^{-} = R_{L} - 1‰$):

$$R_{\text{CC}}^{-} = 1.5‰, \quad R_{\text{DYE3}}^{-} = 3.7‰. \tag{4.24}$$

For our analysis, we represent the prior distribution on all possible ice-sheet morphologies by a set of $N = 10^7$ morphologies, sampled randomly from the prior distribution described in Section 4.4.1. Each of these N morphologies is classified as either being RC or not, according to the criterion described in Section 4.4.5. The resulting RC morphologies then form a sample from the posterior distribution, incorporating

the constraints from the data. In the loose scenario case, where the imposition of the record compatibility at Camp Century and DYE3 has little effect, the RC morphologies represent 5.75% of the morphologies sampled from the prior distribution. This percentage approximately halves (2.86%) in the middle scenario, and further decreases to 0.73% in the tight scenario.

In each of the three scenarios, the percentage of morphologies that satisfy the condition $I(\boldsymbol{x}) < 2$ but do not pass the physical plausibility test (end of Section 4.4.5) is as follows: 16.5% (loose), 17.3% (middle), 27.0% (tight). Perhaps not surprisingly, this shows that the condition of matching the six ice-core records, as simulated by the HadCM3 model and later estimated via the emulator, is alone not sufficient to identify physical morphologies.

Figure 4.6 shows how the posterior distribution compares to the prior, in the two cases of the loose and tight scenarios. Two-dimensional cross-sections of the subspace spanned by the first three PCs are shown. The coloured lines represent contours of the posterior densities (red for the tight scenario, blue for the loose one), and the labels indicate the percentage of RC morphologies that are selected along the corresponding contour. The grey shaded background instead shows the Gaussian prior distribution.

From Figure 4.6, it can be appreciated that the posterior distribution of RC morphologies looks closer to the prior in the loose scenario than in the tight scenario, as expected. However, the particular directions in which the shifts happen, alongside the PC shapes, can provide insight on the patterns displayed by the RC morphologies. For example, especially in the tight scenario case, we can see that areas characterised by a higher density of RC morphologies tend to have a positive score in the first PC (more evident in the subplot of PC1 and PC3). In light of the "North-South" pattern shown by the first PC, this seems to suggest the following: imposing the compatibility with records leads to morphologies with lower surface height (*i.e.*, less or no ice) in the south and higher surface height in the north, compared to the average morphology generated through the prior.

Similarly, the two subplots in Figure 4.6 concerning the second and third PC reveal critical information. The RC morphology scores for the second PC are mostly negative

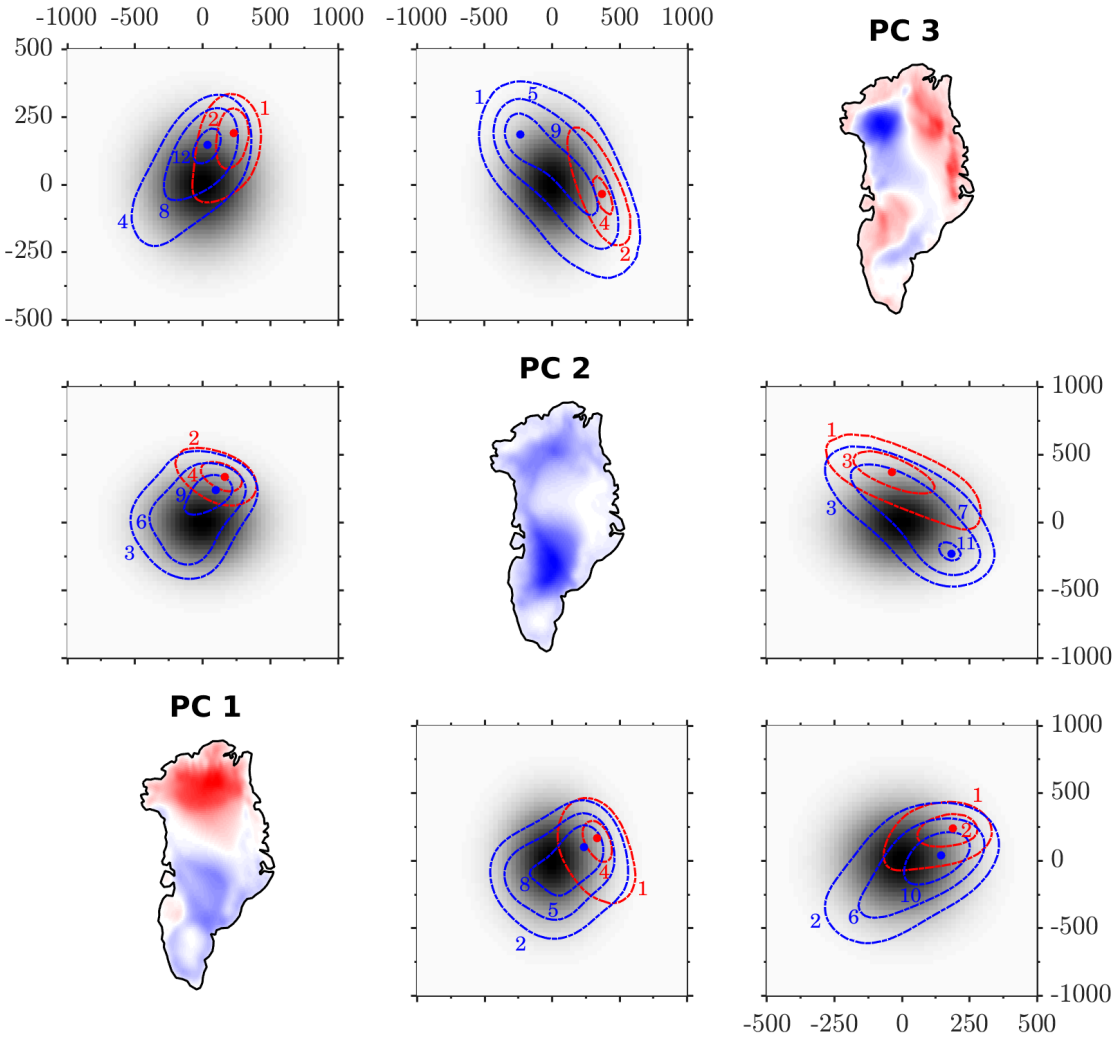

FIGURE 4.6: Two-dimensional sections of the space of PC scores, for the first three PCs. On the diagonal, illustration of the PCs. The shaded grey background in the off-diagonal plots represents the density of the prior Gaussian distribution on the morphologies. The contour lines represent contours of the posterior densities of RC morphologies, in the case of the loose (blue) and tight (red) scenarios. Labels indicate the percentage of morphologies that are compatible with the records along the specified contour. Different contours are shown in symmetric plots.

in the loose scenario (blue) and positive in the tight scenario (red). Notice that the second PC has negative values almost everywhere, particularly in the south-western block of Greenland. The strong constraint on DYE3 and Camp Century that is imposed in the tight scenario seems therefore to induce a clear loss of ice in the south-western block. However, when a loose constraint is imposed at the two locations, the typical surface elevation in the south would increase, reflecting the presence of more ice.

4.5.3 Shape and Uncertainty of Record-Compatible Morphologies

The main characteristics displayed by RC morphologies are illustrated in Figure 4.7. Mean and standard deviation are shown for the prior (left), and for the posterior in the three scenarios (right). Most of the variability, and thus of the uncertainty, is displayed within two regions, one in the north and one in the centre-south (top row). The uncertainty in surface elevation in these two areas is significantly reduced, once the constraints from the data are taken into account. However, whilst little difference is present in the north between the three scenarios, the imposition of a stronger constraint on the DYE3 and Camp Century records induces a clear reduction in the uncertainty of the southern surface elevation.

The prior and posterior mean morphologies are shown in the bottom row of Figure 4.7. To ease the interpretation, we show the prior mean on the left and the difference between posterior and prior means on the right. Progressively from left to right, a distinct decrease of surface height in the south appears. From the loose to the middle scenario, the increase of 2‰ on the lower bound of R^-_{DYE3} induces a decrease of the average surface height in the area surrounding DYE3 of up to 400 metres. Moreover, by further tightening the R^-_{DYE3} constraint of 1.7‰ (middle to tight scenario), we observe an additional decrease in the same area of up to 450–500 metres. The other area in Greenland where a similar phenomenon arises, albeit less prominently, is the one around Camp Century and in the immediate north of it, where the decrease is of approximately 150-200 meters in each of the two steps (loose to middle and middle to tight scenarios). Also observe that, in the case of the loose scenario, the areas displaying surface heights lower than the prior morphologies are concentrated around the four locations where record constraints play an active role (NEEM, NGRIP, GRIP, GISP2), leaving the DYE3 and Camp Century areas mostly unaffected.

We remark that our approach tightens simultaneously the DYE3 and Camp Century records, hence it does not allow us to ascribe with certainty a given posterior feature to the constraint imposed on one or the other location. The geographical position of the two sites and the size of the constraint on their R^-_{L} nonetheless favour

the interpretation that the DYE3 constraint is responsible for the southern surface elevation decrease of tighter scenarios, as implied above. Inspection of the land-ice masks for morphologies compatible with the tight scenario shows that most of these morphologies present a two-dome structure, with DYE3 sitting at the northern top of the southern dome.

We conclude with a note. The authors have carried out further experiments aiming to assess the sensitivity of the results to changes in the minimum NGRIP anomaly, whose value is also uncertain as acknowledged in Section 4.3. The experiments reveal that no tangible change to the shape of the RC morphologies can be appreciated when the minimum $\delta^{18}O$ NGRIP anomaly is decreased by 0.5‰, with Figures 4.6 and 4.7 remaining essentially unchanged. The percentage of morphologies which result record-compatible increases to approximately 7.5%, 4% and 1%, in the loose, middle and tight scenario respectively.

4.5.4 Record Compatibility in the Wider Sense

Within the ice-sheet modelling community, Greenland ice-age information from ice cores is used to attempt to constrain LIG GIS results. The presence of ice at NGRIP and at the Summit region through the (late) LIG period has previously been used to reject particular simulations (e.g., Robinson *et al.*, 2011; Stone *et al.*, 2013). Camp Century and DYE3 sites are not generally used in the same way because the age of the (possible) LIG-period ice is considerably more ambiguous. At DYE3, ice may or may not have covered the site during the LIG (Alley *et al.*, 2010; Willerslev *et al.*, 2007). At Camp Century some ice at the base occurs that has been interpreted as being pre-LIG in nature (Dansgaard *et al.*, 1982), however, as at DYE3, this is ambiguous. Without better ice-age information there will not be community agreement on whether DYE3, or Camp Century, was definitely ice-covered during the LIG.

As well as ice-age information, ice-core based elevation change reconstructions, based on $\delta^{18}O$, have been used to infer LIG GIS changes (*e.g.*Johnsen and Vinther, 2007). However this cannot be used as an additional constraint here, because this $\delta^{18}O$ information is already accounted for by our analytical approach. Beyond $\delta^{18}O$ elevation

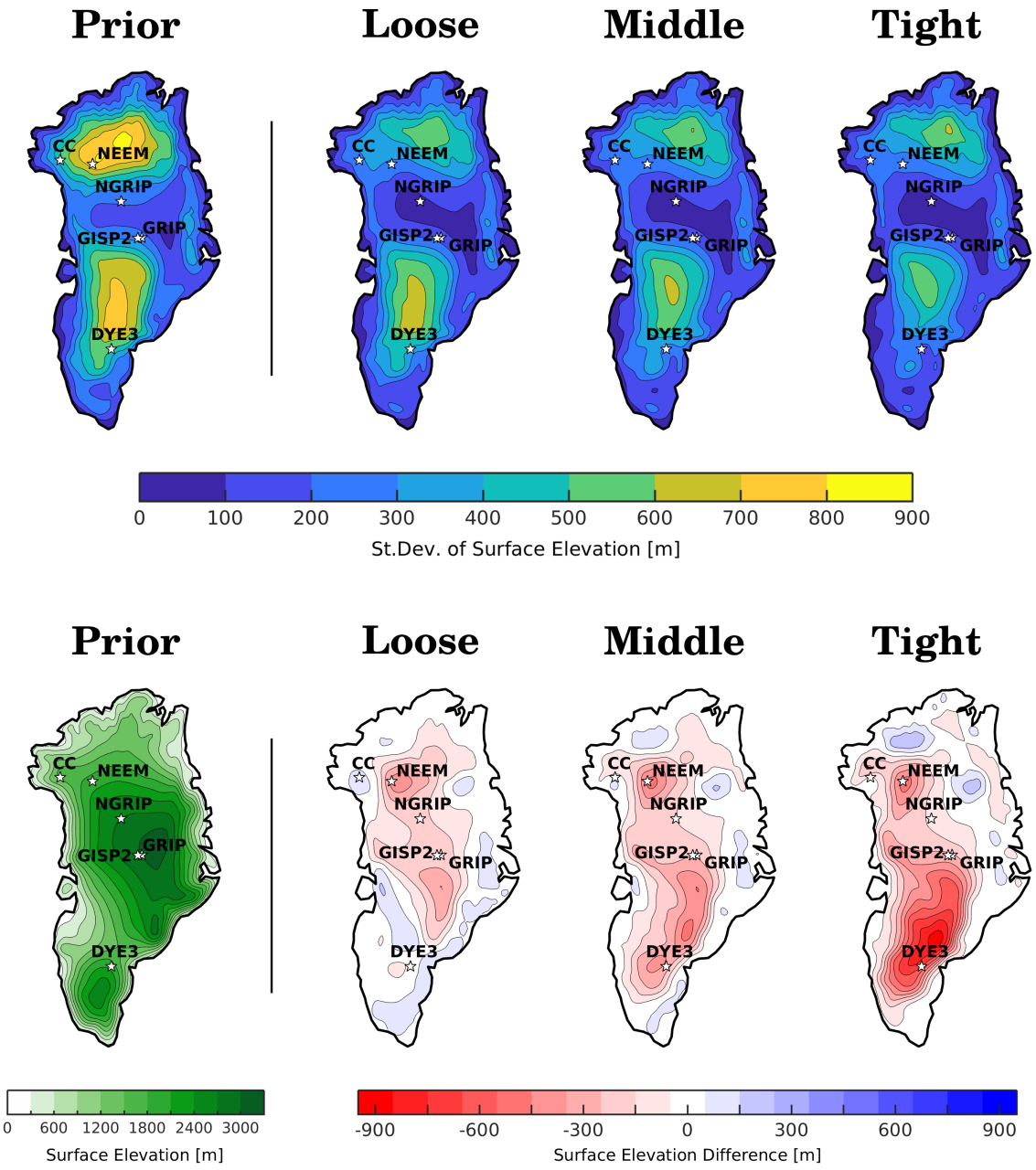

FIGURE 4.7: Plots represent the cell-wise standard deviation (top part) and average (bottom part) of the surface height of different sets of morphologies. $N = 10^7$ morphologies sampled from the prior distribution are used in the plots on the left; only RC morphologies are used for the posterior in the three scenarios on the right. To ease visual interpretation, in the bottom-right plots we show the difference between the posterior and prior mean. The "Loose" scenario corresponds to the best current data, the "Middle" and "Tight" scenarios illustrate results which could be achieved, if better constraints for DYE3 and Camp Century were available.

interpretations, air content measurements have also been used as an independent constraint. In particular, the NEEM elevation change reconstruction, which specifies a NEEM surface elevation difference of $+45 \pm 350$ m at 126 ka compared to present day, is derived from air content measurements (NEEM community members, 2013). This data is fully independent of our approach.

If we impose the NEEM elevation constraint on our resulting RC morphologies, in the loose and middle scenarios cases around 3.7% of the RC morphologies are compatible with this additional NEEM data. This percentage increases in the tight scenario, where 6.5% of our $\delta^{18}O$ compatible morphologies are in agreement. The relatively small overlap between air content and $\delta^{18}O$ compatible morphologies could possibly reflect uncertainties in the air content elevation reconstruction methodology. The method relies on calculating corrections to air content due to insolation and temperature (Raynaud *et al.*, 2007; Eicher *et al.*, 2016) alongside secular changes in surface pressure and winds (Martinerie *et al.*, 1994; Krinner *et al.*, 2000). Surface melting also affects NEEM air content measurements between 127 and 118.3 ka (NEEM community members, 2013). Thus the interpretation of elevation from air content measurements is rather uncertain. However, in spite of these uncertainties, results from the two independent approaches ($\delta^{18}O$ and air content) do overlap.

4.6 Conclusions

Malmierca-Vallet *et al.* (2018) demonstrated that an isotopic enabled climate model cannot correctly simulate the LIG $\delta^{18}O$ measurements at DYE3, GRIP and Renland sites via sea-ice changes alone. Here, our analysis using the emulator establishes that outputs from the isotope enabled HadCM3 model can be reconciled with the best current LIG $\delta^{18}O$ measurements from ice cores. We have shown that this requires a careful parameterisation of ice-sheet morphologies and a thorough approach to the characterisation of uncertainty.

The major source of uncertainty, tackled here via the construction of suitable emulators, arises from the impossibility of running the simulator on a high number of

morphologies. Additional uncertainties stem from the fact that, both in reality and in simulations, the isotopic response in the ice is not only dependent on the ice-sheet morphology, but also on other parameters such as evaporation conditions, transport pathway effects and Arctic sea-ice variations (Sime *et al.*, 2013). In this regard, we note that the nugget term used to model the prior emulator covariance, alongside reflecting the chaotic behaviour of the simulator, accounts as well for the variability in simulator outputs which is due to inputs not explicitly included in the emulator: this is referred to as residual variability in Kennedy and O'Hagan (2001). Last but not least, we stress once again that the available ice-core-based estimates of $\delta^{18}0$ anomalies are themselves uncertain. The case of DYE3 and Camp Century is a prototypical example of this.

In this work we aim to account for all the previous unavoidable sources of uncertainty within a unified framework, joining mathematical parameterisation of the space of morphologies, Gaussian process emulation and available ice-core records. The scenario-based approach we undertake demonstrates the importance of well-constrained records. In common with previous studies, we show that dated ice from around DYE3 is crucial for certain inferences about Greenland (Sime *et al.*, 2019). If more certain records at DYE3 and Camp Century confirmed that the high $\delta^{18}O$ values measured near the bottom of the ice cores were from the LIG, our results show that this would be compatible with morphologies characterised by low surface height in the south: roughly, a decrease of 200 metres has been observed corresponding to an increase of 1‰ in the minimal $\delta^{18}O$ anomaly. We have also shown that the variability in reconstructed surface elevation would decrease in such tighter scenarios, with glimpses that the data would then favour a two-dome structure of the LIG ice sheet.

Whilst this study's aims are to provide a methodology of wide applicability to infer LIG GIS changes and to stress the importance of statistical emulators in similar expensive tasks, we believe that further steps may be included to ensure wider data-model comparisons. In light of the above, we encourage the search of additional data at DYE3 and Camp Century and suggest that ice, sea ice, and isostatic changes are all accounted for within a joint framework. This may enable a useful quantitative

assessment of how Greenland ice-sheet changes affected global sea levels during the LIG.

4.7 Supplementary information

4.7.1 Ice-core Data

Compilation of stable water isotopic ($\delta^{18}O$) information for the LIG period from deep Greenland ice core sites requires us to consider the associated uncertainties for each ice core site. This section contains details on how we ascertained most likely, maximum, and minimum values for each site, from the interval from 120 to 126 ka. We discuss each ice core in turn. Note all values provided are LIG (120-126 ka) minus present-day values.

At the NEEM site, a 80 m segment of ice which covers the LIG interval, and which is in stratigraphic order, was found in between disturbed layers near the bottom of the NEEM ice core. The most likely peak LIG $\delta^{18}O$ value is +3.6‰. The maximum value is +4.0‰ and the minimum is +2.7‰ (NEEM community members, 2013). The LIG ice may originate from location about 205 km upstream from the NEEM site (NEEM community members, 2013). Note that for NEEM the present-day (average of the past millennium) value is obtained from this upstream (LIG deposition site) location. The maximum and minimum values are estimated using the maximum and minimum $\delta^{18}O$ values measured across the time interval from 120 to 126 ka along the ice core displayed on the AICC2012 chronology (Bazin *et al.*, 2013; Veres *et al.*, 2013; Govin *et al.*, 2015).

At the NGRIP site, we use a most likely LIG $\delta^{18}O$ peak of +3.1‰ relative to present-day, defined by (Johnsen and Vinther, 2007). The associated maximum is +3.8‰ and the minimum is +2.5‰. The NGRIP ice core is not affected by stratigraphic disturbances, but it only reaches back to 120-123 ka according to the defined chronologies (NGRIP Project Members, 2004; Wolff *et al.*, 2010; Bazin *et al.*, 2013; Veres *et al.*, 2013). Since we cannot preclude that the first part of the LIG, covering the climatic

optimum, is missing, we estimate the upper bound of the uncertainty range by taking the average maximum $\delta^{18}O$ value between NEEM and GISP2. This is because NGRIP is geographically located approximately equidistant from these two sites and following NGRIP Project Members (2004), we assume that the relative elevation differences during the LIG in Northern Greenland are not large. The minimum value is calculated considering the $\delta^{18}O$ value measured at the very bottom of the ice core (NGRIP Project Members, 2004). We proceed as such because when displayed on the AICC2012 chronology (Bazin *et al.*, 2013; Veres *et al.*, 2013), the oldest ice is only 120 ka. However, the dating of the NGRIP deep ice is uncertain by several thousands of years and it could possibly be older, as suggested by the original NGRIP chronology (NGRIP Project Members, 2004) giving to the oldest ice an age of 123 ka. Note that when considering this original chronology, the minimum $\delta^{18}O$ value over the interval 120-123 ka would lead to a minimum $\delta^{18}O$ anomaly of +0.4‰. Considering the dating uncertainties as well as the elevation-related assumptions, we acknowledge that the inferred uncertainties attached to the NGRIP $\delta^{18}O$ anomaly might be underestimated.

For the GISP2 and GRIP sites, the bottom part of both ice cores is affected by strong stratigraphic disturbances. Efforts have been made to propose a LIG climate reconstitution using globally homogeneous gas signals known from dated and undisturbed Antarctic ice core records (Landais *et al.*, 2003; Suwa *et al.*, 2006b; Yau *et al.*, 2016). Nevertheless, the LIG sections are not unambiguously datable. The most likely GISP2 LIG $\delta^{18}O$ value is +2.7‰ (Johnsen and Vinther, 2007). The associated maximum is estimated to be +3.4‰ and the minimum is +1.7‰. To calculate this uncertainty range we looked at the maximum and minimum LIG $\delta^{18}O$ values across the time interval 120-126 ka in the GISP2 LIG reconstructions from Suwa and Bender (2008) and Yau *et al.* (2016), and use here the larger range estimated from the Yau *et al.* (2016) data set.

At the GRIP site, the most likely LIG $\delta^{18}O$ anomaly is +3.2‰ (Landais *et al.*, 2003). The associated maximum value is +3.5‰ (Johnsen and Vinther, 2007) and the minimum is +2.2‰. Due to the proximity of GRIP and GISP2, we assume the same lower uncertainty band value of −1‰ for both sites. The maximum value is

based on the maximum $\delta^{18}O$ value reported by Johnsen and Vinther (2007) for the GRIP bottom section.

At the Camp Century (CC) and DYE3 sites, due to poor preservation of the deep ice core samples, it was not possible to date the LIG sections via synchronisation with global atmospheric records. Thus, these sites have the largest uncertainties. At Camp Century, the most likely LIG $\delta^{18}O$ value, taken from Johnsen and Vinther (2007), is +2.5‰ and we estimate a maximum value of +4.0‰, and a minimum value of +0‰. At DYE3, the most likely LIG $\delta^{18}O$ value, also taken from Johnsen and Vinther (2007), is +4.7‰, and we estimate a maximum of +5.2‰, and a minimum of +0‰. The maximum value from both Camp Century and DYE3 is the maximum $\delta^{18}O$ measured within each core.

4.7.2 The Selection of Greenland Ice Sheet Morphologies

To represent the range of GIS retreat scenarios proposed for the LIG (IPCC, 2013), we gather 14 GIS morphological data sets from several ice sheet modelling studies, see Figure 2 for references and morphologies. The ice sheet modelling approaches vary across the selected studies. Global climate models (GCMs) were used to drive the ice sheet models with (e.g., Quiquet *et al.*, 2013), or without (e.g., Born and Nisancioglu, 2012; Stone *et al.*, 2013) the use of additional proxy climate information. Some studies employed an intermediate downscaling method (e.g., Robinson *et al.*, 2011), and others a regional climate model (e.g., Helsen *et al.*, 2013). Since the margin position and minimum extent of the GIS during the LIG is not well constrained, especially around the north-east region (Fig 2), it is reasonable for our fourteen representative morphologies to show a strong variation in terms of volume and extent (e.g., Robinson *et al.*, 2011; Quiquet *et al.*, 2013; Stone *et al.*, 2013). Some of the LIG GIS morphologies show a rather moderate retreat of the ice (e.g. Fig 2 l; Robinson *et al.* (2011)), some show a possible division of the GIS into two domes (e.g. Fig 2 b and j; Robinson *et al.* (2011); Calov *et al.* (2015)), the majority display stronger ice loss in the south (e.g. Fig 2 e; Helsen *et al.* (2013)) though a few show substantial ice retreat in the north (e.g. Fig 2 m and n; Stone *et al.* (2013)). Some of the GIS

morphologies even show ice-free conditions at DYE3 and/or Camp Century ice core sites (Robinson *et al.*, 2011; Helsen *et al.*, 2013; Calov *et al.*, 2015).

In essence, whilst any given selection of original morphologies will be a somewhat subjective choice, a survey of the literature suggests that the fourteen morphologies that we settled on do seem to capture the wide range of possible shapes; which is the primary objective of this selection.

4.7.3 The $\delta^{18}O$ Climate Simulator

The HadCM3 simulator is a coupled atmosphere, ocean, and sea ice general circulation model. The dynamic vegetation model included in HadCM3 is TRIFFID (Cox *et al.*, 1998; Cox, 2001), which is coupled to the land surface scheme MOSES 2.1 (Braconnot *et al.*, 2007; Cox *et al.*, 2000). This model has been used extensively, with $\delta^{18}O$ specific code, to examine a variety of climate, sea ice, and ice sheet problems (*e.g.*Holloway *et al.*, 2016a, 2017; Tindall *et al.*, 2010; Malmierca-Vallet *et al.*, 2018). The horizontal resolution in the atmosphere is 3.75° longitude by 2.5° latitude; in the ocean it is 1.25° longitude by 1.25° latitude (Gordon *et al.*, 2000). The atmospheric and oceanic components have 19 and 20 vertical levels respectively.

Our pre-industrial simulation was set-up using guidelines from the Paleoclimate Model Intercomparison Project (PMIP), with atmospheric gas composition set to values for 1850 years BP - CO2 is 280 ppmv; CH4 is 760 ppbv; and N2O is 270 ppbv. See Holloway *et al.* (2016a) for full details.

All LIG simulations are forced with GHG values and orbital forcing which are appropriate for 125 ka. To reach a spun-up LIG climate, we use a 125 ka control simulation run with a modern-day GIS configuration (IceBridge BedMachine Greenland, Version 3 - Morlighem *et al.* (017b,a)). This spin-up simulation is run for 400 model years to allow quasi-equilibrium conditions to be reached between atmosphere and the upper ocean. After the 400 year LIG spin-up is completed, each subsequent LIG GIS change simulation is run on from the end of the spin-up for a further 70 model years, with averages from the last 50 years used in all calculations. For each of the LIG GIS

change simulations, we consider both changes in the elevation and extent of the ice sheet.

4.8 Weighted Principal Component Analysis

Here we provide details on the procedure used to generate the Principal Components forming a basis of the space of synthetically generated morphologies (see Section 3.1 in the main text). Recall that the morphologies corresponding to 14 different reconstructions of the Greenland Ice Sheet (GIS) at 125 ka are collected from different studies, and regridded into 122×314 matrices of surface height values. In the following, we denote by $p = 122 \cdot 314 = 38{,}308$ the total number of cells, and by

$$\boldsymbol{Y_1}, \ldots, \boldsymbol{Y_n} \in \mathbb{R}^p,$$

$n = 14$, the vectors whose j^{th} coordinate contains the surface height of these morphologies at the j^{th} grid cell, $j = 1, \ldots, p$.

The classical Principal Component Analysis (PCA) applied to a data set $\{\boldsymbol{Y_1}, \ldots, \boldsymbol{Y_n}\}$ of p-dimensional vectors, $p > n$, identifies a sequence of orthogonal directions $\boldsymbol{V_1}, \ldots, \boldsymbol{V_{n-1}} \in \mathbb{R}^p$ along which the data set displays the greatest variability: the $\boldsymbol{V_i}$ are called Principal Components (PCs). More precisely:

i) $\boldsymbol{V_1}$ maximises the function

$$F(\boldsymbol{v}) = \mathrm{Var}\Big\{\langle \boldsymbol{Y_1}, \boldsymbol{v}\rangle, \ldots, \langle \boldsymbol{Y_n}, \boldsymbol{v}\rangle\Big\}, \quad \boldsymbol{v} \in S^{p-1}, \tag{4.25}$$

where S^{p-1} represents the unit sphere in $\mathbb{R}^p$.

ii) Recursively, $\boldsymbol{V_{j+1}}$ maximises the function $F(\cdot)$ under the further constraint of being orthogonal to $\{\boldsymbol{V_1}, \ldots, \boldsymbol{V_j}\}$.

Both the norm used to define S^{p-1} and the scalar product $\langle \cdot, \cdot \rangle$ in equation (4.25) are the Euclidean ones on $\mathbb{R}^p$. It is a standard result that the $\boldsymbol{V_1}, \ldots, \boldsymbol{V_{n-1}}$ can be

found as the first $n-1$ eigenvectors of the $p \times p$ covariance matrix associated with $\boldsymbol{Y_1}, \ldots, \boldsymbol{Y_n}$.

In our case, a classical application of PCA to the $n = 14$ vectors $\boldsymbol{Y_i}$ ignores the following fact: coordinates corresponding to cells at higher latitudes account for significantly smaller areas than cells at lower latitudes. Hence, the variability displayed by the original morphologies in the north, where cells are more numerous, would be automatically overweighted by classical PCA in determining the PCs. To ensure a fair analysis, we replace the Euclidean scalar product on $\mathbb{R}^p$ with the following scalar product:

$$\langle \boldsymbol{x}, \boldsymbol{y} \rangle_W = \sum_{j=1}^{p} x_j \, w_j \, y_j = \boldsymbol{x}^\top \boldsymbol{W} \boldsymbol{y} \,, \quad \boldsymbol{x}, \boldsymbol{y} \in \mathbb{R}^p \,, \tag{4.26}$$

where $\boldsymbol{W}$ is the diagonal matrix whose diagonal positive elements w_j are proportional to the area of cell j. The condition

$$\sum_{j=1}^{p} w_j = 1$$

is imposed. Note that the scalar product in (4.26) represents a "discretisation" of the natural L^2 scalar product for functions f, g defined on the subset $G \subset S^2$ of the sphere whose spherical coordinates identify Greenland:

$$\langle f, g \rangle_G = \frac{1}{4\pi} \int_{G \subset S^2} f(z) \, g(z) \, dz \,. \tag{4.27}$$

By using the scalar product in (4.26), the solution to the maximisation problem defined in i) and ii) is given by the eigenvectors of the matrix

$$\boldsymbol{Q} = \boldsymbol{C}\boldsymbol{W} \in \mathbb{R}^{p \times p},$$

where $\boldsymbol{C}$ is the $p \times p$ covariance matrix associated with the vectors $\boldsymbol{Y_1}, \ldots, \boldsymbol{Y_n}$. The endomorphism associated with $\boldsymbol{Q}$ is symmetric with respect to the scalar product in (4.26), *i.e.*

$$\langle \boldsymbol{Q}\boldsymbol{x}, \boldsymbol{y} \rangle_W = \langle \boldsymbol{x}, \boldsymbol{Q}\boldsymbol{y} \rangle_W \quad \forall \, \boldsymbol{x}, \boldsymbol{y} \in \mathbb{R}^p \,,$$

hence the spectral theorem ensures that the eigenvectors of $\boldsymbol{Q}$ are orthogonal with respect to the scalar product $\langle \cdot, \cdot \rangle_W$, as requested. As a side note, notice that in the case of the Euclidean scalar product, where $\boldsymbol{W} = \boldsymbol{I_p}$ is the identity matrix of order p, one recovers the result of classical PCA.

The square matrix $\boldsymbol{Q}$ is a non-symmetric matrix, in our case of order $p = 38{,}308$. A straight computation of all its eigenvectors is therefore computationally unaffordable: storing its approximately 10^9 elements in double precision is already challenging. However, since the rank of the matrix is only $n - 1$ ($n = 14$ in our case), a suitable application of the Singular Value Decomposition (SVD) allows to compute the eigenvectors of interest. Define the matrix:

$$\overline{Y} = \Big[\boldsymbol{Y_1} - \boldsymbol{M} | \ldots | \boldsymbol{Y_n} - \boldsymbol{M}\Big]^\top \in \mathbb{R}^{n \times p}$$

where $\boldsymbol{M} = \sum_{i=1}^{n} \boldsymbol{Y_i}/n$ is the average of the vectors $\boldsymbol{Y_i}$. Further consider the SVD of $\overline{\boldsymbol{Y}}\boldsymbol{W}^{1/2}$:

$$\overline{\boldsymbol{Y}}\boldsymbol{W}^{1/2} = \boldsymbol{U}\boldsymbol{D}\widetilde{\boldsymbol{V}}^\top , \tag{4.28}$$

where $\boldsymbol{U}$ is an orthogonal matrix of order n, $\boldsymbol{D}$ is a diagonal matrix of order n with positive diagonal elements d_j, and $\widetilde{\boldsymbol{V}}$ is a $p \times n$ matrix satisfying $\widetilde{\boldsymbol{V}}^\top \widetilde{\boldsymbol{V}} = \boldsymbol{I_n}$.

The columns of $\widetilde{\boldsymbol{V}}$ are easily seen to be the eigenvectors of $\boldsymbol{W}^{1/2}\boldsymbol{C}\boldsymbol{W}^{-1/2}$ corresponding to the first n largest eigenvalues, the n^{th} of them being 0. Hence, the first $n - 1$ columns of $\boldsymbol{V} = \boldsymbol{W}^{-1/2}\widetilde{\boldsymbol{V}}$ are the sought eigenvectors of $\boldsymbol{Q} = \boldsymbol{C}\boldsymbol{W}$: these are the principal components, in the manuscript denoted by $\boldsymbol{V_1}, \ldots, \boldsymbol{V_{13}}$. Notice that the vectors $\boldsymbol{Y_i} - \boldsymbol{M}$ belong to the space generated by the PCs. More precisely, by rearranging equation (4.28), one can see that

$$\boldsymbol{Y_k} - \boldsymbol{M} = \sum_{i=1}^{n-1} d_i u_{ki} \boldsymbol{V_i} .$$

Through the SVD decomposition, the i^{th} eigenvalue of $\boldsymbol{Q}$ can be easily computed as $d_i^2/(n-1)$. These are denoted by ${\sigma_i}^2$ in the manuscript, and represent the sample

variance of the projections of $\boldsymbol{Y_1}, \ldots, \boldsymbol{Y_n}$, with respect to (4.26), onto the i^{th} PC: that is, ${\sigma_i}^2 = F(\boldsymbol{V_i})$.

4.9 Mask Generation for Synthetic Morphologies

In order to carry out a simulation, the $\delta^{18}O$ climate simulator requires as input not only a morphology of surface heights, but also an associated land-ice mask. At each grid cell, this specifies whether the morphology is covered by ice or not.

The land-ice mask is provided for the 14 original morphologies (see main text for the list of these) but it needs to be defined for any synthetically generated morphology M. Starting from the morphology heights, the idea to generate the mask is the following: first associate ice (respectively, land) with a cell, if its height is greater (respectively, lower) than a given threshold; then smooth the mask. The threshold is computed on the basis of the value of the masks and the heights of the 14 original morphologies on the cell in question. More precisely, at a grid cell:

1. Let $z_1^{(I)}, \ldots, z_r^{(I)}$ and $z_1^{(L)}, \ldots, z_s^{(L)}$ $(r + s = 14)$ be the surface heights of the original morphologies: the superscript I or L serves to distinguish between morphologies having ice or land at the grid cell, respectively.

2. Let a be the minimum of $z_1^{(I)}, \ldots, z_r^{(I)}$, and b be maximum of $z_1^{(L)}, \ldots, z_s^{(L)}$. Define $c = (a + b)/2$.

3. Associate ice to the grid cell in question if the corresponding surface height of M is greater than c, and land otherwise.

Finally, in order to smooth possible irregular patterns of the mask obtained through steps 1–3, we generate a new mask where ice (respectively, land) is associated with each grid cell, according to whether a majority of ice (respectively, land) cells are present in the original mask, within a circle of radius 35 km around the grid cell centre. This last process is repeated ten times, at which point changes become hardly detectable. In Figures 4.8 and 4.9, we compare the original masks of the 14 morphologies, to the synthetic masks generated for these by the procedure detailed above.

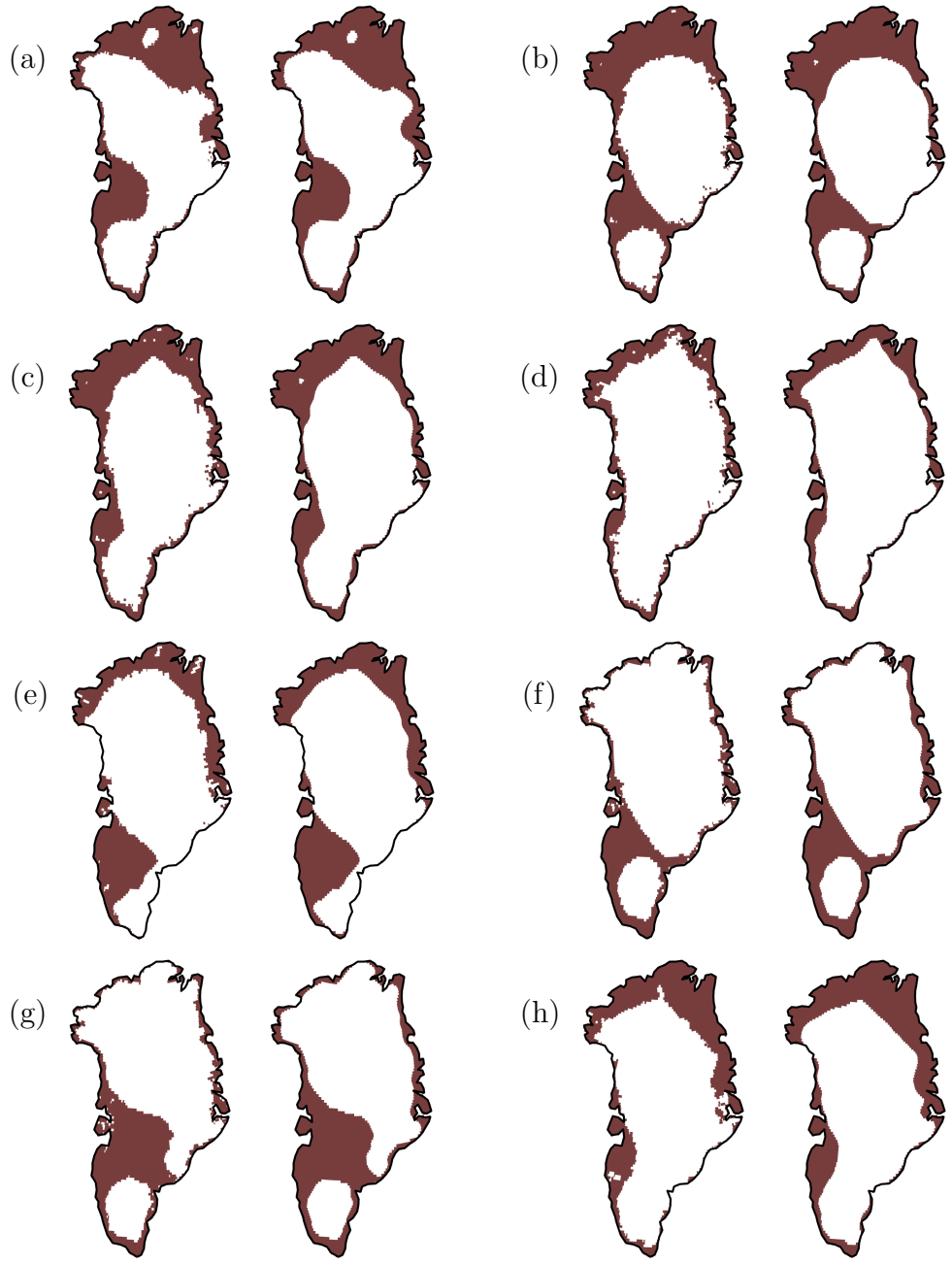

FIGURE 4.8: Masks associated with the reconstructed GIS morphologies of the studies listed below. In each panel: on the left the original mask provided by the corresponding study; on the right, the mask generated through the procedure described in Section 4.9, starting solely from the morphology surface height. It can be appreciated that differences are mostly negligible, supporting the validity of the mask-generation procedure employed. Panels show data from: (a) Born and Nisancioglu (2012); (b) Calov *et al.* (2015) at 121.3 ka; (c) Calov *et al.* (2015) at 122.1 ka; (d) Calov *et al.* (2015) at 123.3 ka; (e) Helsen *et al.* (2013); (f) Langebroek and Nisancioglu (2016) (minimum GIS for temperature lapse rate of 6.5°C/km); (g) Langebroek and Nisancioglu (2016) (minimum GIS for temperature lapse rate of 8°C/km); and (h) Quiquet *et al.* (2013) (CNRM anomaly experiment).

FIGURE 4.9: Continued from Figure 4.8, with data from the following studies: (a) Quiquet *et al.* (2013) (IPSL anomaly experiment); (b) Robinson *et al.* (2011) (strongly retreated GIS); (c) Robinson *et al.* (2011) (moderately retreated GIS); (d) Robinson *et al.* (2011) (weakly retreated GIS); (e) Stone *et al.* (2013) (GIS extent for the maximum contribution to sea level rise, +3.8m); and (f) Stone *et al.* (2013) (GIS extent for the most likely contribution to sea level rise, +1.5m).

Chapter 5

Sea-ice feedbacks influence the isotopic signature of GIS elevation changes: LIG HadCM3 simulations

This chapter is under review in Climate of the Past as; Malmierca-Vallet, I., Sime, L.C., Valdes, P.J., Tindall, J.C. 2020. Sea-ice feedbacks influence the isotopic signature of Greenland Ice Sheet elevation changes: Last Interglacial HadCM3 simulations. Climate of the Past, doi:10.5194/cp-2020-40.

I.M.V. performed the isotope-enabled climate model experiments, carried out the analysis and wrote the article. L.C.S. provided feedback throughout the writing and analysis and L.C.S. also provided the initial motivation. P.J.V., and J.C.T. provided technical advice about how to perform and interpret the climate model simulations. All authors discussed the model results and commented on the manuscript.

5.1 Abstract

Volumetric changes in the Greenland ice sheet (GIS) affect global sea level. Greenland stable water isotope ($\delta^{18}O$) records from ice cores offer information on past changes in the surface of the GIS. Here, we use the isotope-enabled HadCM3 climate model

to simulate a set of Last Interglacial (LIG) idealised GIS surface elevation change scenarios focusing on GIS ice core sites. We investigate how $\delta^{18}O$ depends on the magnitude and sign of GIS elevation change and evaluate how the response is altered by sea ice changes. We find that modifying GIS elevation induces changes in Northern Hemisphere atmospheric circulation, sea ice and precipitation patterns. These climate feedbacks lead to ice core-averaged isotopic lapse rates of 0.49‰ per 100 m for the lowered GIS states and 0.29‰ per 100 m for the enlarged GIS states. This is lower than the spatially derived Greenland lapse rates of 0.62-0.72 ‰ per 100 m. These results thus suggest non-linearities in the isotope-elevation relationship, and have consequences for the interpretation of past elevation and climate changes across Greenland. In particular, our results suggest that winter sea ice changes may significantly influence isotopic-elevation gradients: winter sea ice effect can decrease (increase) modelled core-averaged isotopic lapse rate values by about -19% (and +28%) for the lowered (enlarged) GIS states respectively. The largest influence of sea ice on $\delta^{18}O$ changes is found in coastal regions like the Camp Century site.

5.2 Introduction

Ice core records of stable water isotopes ($\delta^{18}O$) yield useful information on past climate change over the last several glacial-interglacial cycles (e.g., Sime *et al.*, 2009). Alongside site elevation, ice core $\delta^{18}O$ is affected by variations in site temperature, sea ice, evaporation conditions, and transport pathway effects (Sime *et al.*, 2013; Werner *et al.*, 2018). Improving our understanding of the elevation signal captured in Greenland ice core isotopic records means we also need to consider these impacts.

The Last Interglacial period (LIG - between around 130,000 and 115,000 ka) was the last time when the volume of the GIS is believed to have been considerably reduced (Robinson *et al.*, 2011; Stone *et al.*, 2013). This period was characterised by warmer-than-present-day conditions in the high latitudes and stronger summer time insolation (Hoffman *et al.*, 2017; Capron *et al.*, 2017). Over Arctic land areas, LIG summer temperatures are estimated to have been around 4-5°C above present-day (e.g., CAPE Last Interglacial Project Members, 2006) and the NEEM ice core record

suggests surface temperatures 8 ± 4°C warmer compared to the last millennium (when accounting for elevation changes in the GIS) (NEEM community members, 2013).

LIG global mean sea level is believed to have been risen by between 6 to 9 m compared to present-day levels (Kopp *et al.*, 2009; Dutton *et al.*, 2015) which likely indicates both reduced Antarctic (DeConto and Pollard, 2016; Sutter *et al.*, 2016) and Greenland ice sheets (Tarasov and Peltier, 2003; Lhomme *et al.*, 2005; Helsen *et al.*, 2013; Calov *et al.*, 2015). The contribution of the GIS to this LIG high stand remains unclear: previous studies suggest a possible contribution anywhere between +0.3 to +5.5 m to global mean sea level (Cuffey and Marshall, 2000; Robinson *et al.*, 2011; Quiquet *et al.*, 2013; Stone *et al.*, 2013; Plach *et al.*, 2019). Interestingly though, some total air content measurements have been interpreted as indicative of the elevation over central Greenland remaining nearly unchanged (only few hundred meters lower than today) (Raynaud *et al.*, 1977) and the NEEM air content data have also been interpreted as indicative of a lowering of the surface elevation of only 130 ± 300 m relative to present (NEEM community members, 2013).

Seven deep ice cores, that likely contain some LIG ice, have been recovered from the GIS with stable water isotope records ($\delta^{18}O$ and δD): NEEM, NGRIP, GISP2, GRIP, DYE3, Camp Century and Renland (Johnsen and Vinther, 2007; NEEM community members, 2013). Isotope-elevation slopes derived from spatial data from central and northwest Greenland suggest that a change in elevation of 100 m may provide a 0.62‰ and 0.72‰ change in $\delta^{18}O$ respectively (Dansgaard, 1973; Johnsen *et al.*, 1989; Poage and Chamberlain, 2001). Though the suggested global average isotope lapse rate is 0.3‰ per 100m (Blisniuk and Stern, 2005), it is possible that isotope-elevation relationships vary more widely at high latitudes because of the higher temperature variability (Rowley and Garzione, 2007) or sea ice effects (Holloway *et al.*, 2016a, 2017; Malmierca-Vallet *et al.*, 2018).

While the LIG global average warming is in line with projections for the end of the century (Clark and Huybers, 2009; Hoffman *et al.*, 2017), there is considerable uncertainty on the timing of the sea level high stand during the LIG (Kopp *et al.*, 2009; Düsterhus *et al.*, 2016; Barlow *et al.*, 2018) and the magnitude considerably surpasses near (2100 - 2200) future projections (e.g., Fischer *et al.*, 2018). Thus,

the LIG represents a relevant period, when the implications of changes in ice sheet elevation are highly pertinent for mid to far future projections (DeConto and Pollard, 2016). An improved understanding of the isotopic response to GIS elevation changes may therefore help improve the interpretation of LIG Greenland isotope data and help constrain the GIS response to future sea level and temperature scenarios.

In this study, we investigate the impact of GIS elevation changes on Greenland $\delta^{18}O$ and the underlying processes. We perform a suite of idealised elevation change simulations with the isotope-enabled climate model HadCM3 to (1) analyse the response of Arctic sea ice and atmospheric circulation to these GIS elevation changes and, (2) test to what extent variations in the background climate state (Arctic sea ice extent) may influence the isotopic lapse rate values at different Greenland ice core sites.

5.3 Methods

5.3.1 Experimental setup

We use the isotope-enabled General Circulation Model (GCM) HadCM3 to simulate the isotopic response to idealised variations in the elevation of the GIS. This GCM has been widely used to examine present, past and future climates (IPCC, 2013, 2007) and consists of a coupled ocean, atmosphere and sea ice model. Tindall *et al.* (2009) presents the implementation of the water isotope code in HadCM3.

We run a first ensemble of 16 idealised elevation change HadCM3 simulations with greenhouse-gas and orbital forcing centred at 125,000 years BP (125ka) (See Table 5.1). A 125ka control experiment (hereafter, 125Control) is performed including a present-day GIS configuration (IceBridge BedMachine Greenland, Version 3 – Morlighem *et al.* (017b,a)). To generate the idealised elevation changes, we scale up and down the GIS height from ± 50 m up to ±1300 m; in particular, we scale elevations relative to the elevation at the NEEM ice core site, following

$$\beta = \Delta z / Z_{NEEM} \tag{5.1}$$

where Δz is the elevation change prescribed; Z_{NEEM} is the elevation at the NEEM ice core site in the present-day GIS configuration and β is the scaling percentage. GIS elevations are then decreased/increased by β;

$$Z_{new} = Z_{ini} \pm (\beta * Z_{ini}) \tag{5.2}$$

where Z_{ini} is the two-dimension array for the present-day GIS and Z_{new} is a new two-dimension array with modified elevations. Our simulations use Δz equal to ± 50, 100, 300, 500, 700, 900, 1000, 1300 m (see Table 5.1). To help isolate the impact of elevation changes, the present-day GIS extent is unmodified. Each elevation change simulation is time integrated for a total of 475-years which ensures appropriately spun-up atmosphere and upper ocean fields. In each case the final 50 years of the simulations are considered for averaging.

A second ensemble of 32 simulations with different GIS configurations and sea ice retreat scenarios is used to help explore the joint impacts of sea ice change and GIS change on Greenland (See Fig. 5.8 and Table 5.1). We follow the methodology of Holloway *et al.* (2016a, 2017) and Malmierca-Vallet *et al.* (2018) on sea ice forcing. This set of simulations help us explore both changes in the extent (land-ice fraction) and elevation of the GIS. The methodology outlined in Domingo *et al.* (2020) is used to generate these simulations. In summary, (1) GIS morphology modes are calculated from an initial ensemble of 14 LIG GIS reconstructions (Robinson *et al.*, 2011; Born and Nisancioglu, 2012; Helsen *et al.*, 2013; Quiquet *et al.*, 2013; Stone *et al.*, 2013; Calov *et al.*, 2015; Langebroek and Nisancioglu, 2016), and (2) associated relevant sea ice retreat scenarios are calculated from 22 Arctic sea ice change experiments performed by Malmierca-Vallet *et al.* (2018) (See Fig. 5.8 and Table 5.1).

5.4 Isotopic simulation results

We present results from (1) 16 GIS elevation change only scenarios and, (2) 32 experiments with combined Arctic sea ice forcing and modified GIS morphology (see Table

5.1). A two-sided Student's t-test is utilised to estimate the statistical significance of changes (von Storch and Zwiers, 2001). Hereafter, lapse rates are defined to be positive, if the analysed atmospheric variable decreases with elevation.

5.4.1 GIS elevation change scenarios

5.4.1.1 Mean annual $\delta^{18}O$ changes at ice core sites

At the NEEM deposition site (around 205 ± 20 km upstream of the NEEM drill site due to ice flow), the 125Control experiment simulates a precipitation-weighted $\delta^{18}O$ (hereafter $\delta^{18}O$p) anomaly of 1.9‰ compared to PI. The lowered GIS experiments have $\delta^{18}O$p anomalies which vary between 0.6‰ and 6.4‰ whilst the increased GIS elevation experiments act to decrease $\delta^{18}O$p anomalies by as much as -3.9‰ in the most extreme scenario p1300, relative to 125Control (Fig. 5.1a).

The 125Control experiment shows $\delta^{18}O$p anomalies of 1.5‰ at GRIP and GISP2 and 1.6‰ at NGRIP compared to PI. Depending on the prescribed reduction of the ice sheet elevation, $\delta^{18}O$p anomalies compared to 125Control vary between 0.5‰ and 6.5‰ at NGRIP (Fig. 5.1f), between 0.3‰ and 6.8‰ at GISP2 (Fig. 5.1p) and between 0.2‰ and 6.6‰ at GRIP (Fig. 5.1k). In contrast, the increased elevation scenarios show a decline in $\delta^{18}O$p anomalies of up to -3.6‰ at NGRIP and GRIP and -4.0‰ at GISP2 in the most extreme scenario p1300 relative to 125Control (Fig. 5.1f,k and p).

With respect to the PI simulation, the 125Control simulation shows a $\delta^{18}O$p rise of 1.0‰ at DYE3 and 1.8‰ at Camp Century. The decreased elevation scenarios present $\delta^{18}O$p anomalies ranging from 0.4‰ to 5.7‰ at DYE3 and from 0.7‰ to 4.6‰ at Camp Century compared to 125Control (Fig. 5.1u and z). $\delta^{18}O$p anomalies decrease up to -3.9‰ at DYE3 and -3.3‰ at Camp Century in p1300 compared to 125Control (Fig. 5.1u and z).

We find a non-linearity for $\delta^{18}O$ changes over Greenland; $\delta^{18}O$p anomalies are weaker for increases in GIS elevation than for decreases (Fig. 5.1). Core-averaged $\delta^{18}O$p anomalies are -3.7‰ compared to 6.1‰ for a 1300m increase/decrease in relative

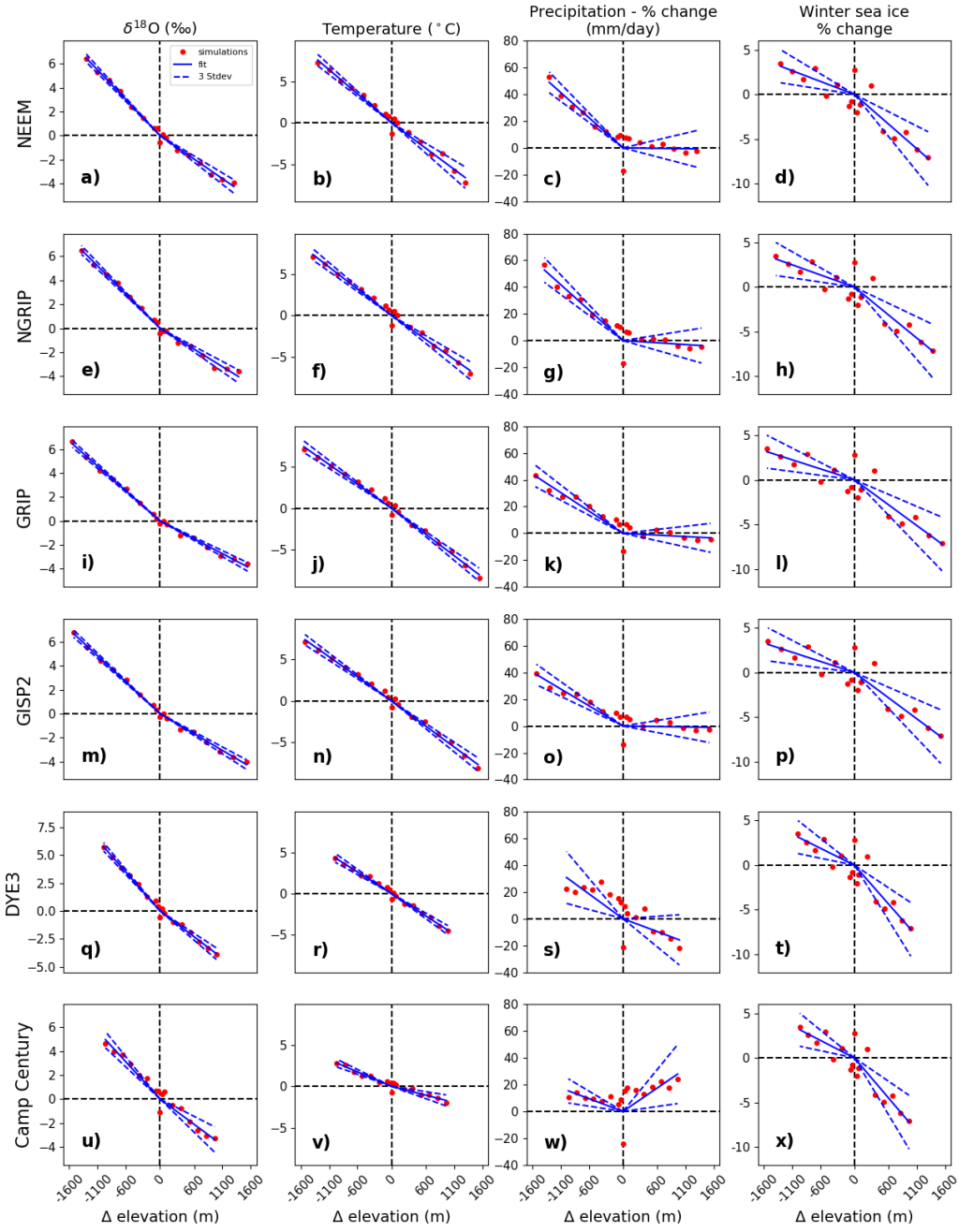

FIGURE 5.1: Change in $\delta^{18}Op$, temperature, precipitation flux and winter (March) sea ice extent as a function of GIS elevation changes (m - absolute change in meters compared to 125 ka control at each ice core site location). Changes are calculated as anomalies compared to 125 ka control experiment. Ice core sites displayed: (a-d) NEEM, (e-h) NGRIP, (i-l) GRIP, (m-p) GISP2, (q-t) DYE3, (u-x) Camp Century. Results for each of the 16 GIS elevation change scenarios are represented by red dots. Solid lines signify best fit curves (y = ax). Also shown ±3 Stdev (lines with dashes) on the best fit lines.

elevation respectively. This results in a non-linear isotopic lapse rate across the elevation change scenarios (Fig. 5.1), which will be discussed in the following sections.

For the rest of the results section, for clarity, we focus particularly on two example scenarios which depict medium-high GIS elevation changes (experiments marked in blue in Table 5.1).

5.4.1.2 Surface air temperatures

Orbital forcing dominates the climate in the 125Control simulation. In Greenland, summer local temperature increases exceed 3.5°C due to the large increase in summertime insolation (Fig. 5.2c).

The local surface climate over Greenland is noticeably affected by local changes in GIS surface elevation. Decreases in GIS elevation act to increase surface air temperatures (SATs) across Greenland, and vice versa (Fig. 5.1 and Fig. 5.2). In Greenland, the scenario with decreased elevation (m900) simulates positive SAT anomalies all year round compared with 125Control (Fig. 5.2d-f). Annual local temperature increases exceed 4.5°C in m900 relative to 125Control. As expected, the increased elevation scenario p900 shows negative SAT anomalies throughout the year relative to 125Control experiment (Fig. 5.2g-i). In central regions over Greenland, local temperature decreases exceed -4.5°C during both summer and winter seasons.

Averaging across six ice core sites (Camp Century, NEEM, NGRIP, GRIP, GISP2 and DYE3), temperature lapse rates vary from 0.47°C per 100 m for the lowered GIS states to 0.44°C per 100 m for the enlarged GIS states (Fig. 5.1).

5.4.1.3 Atmospheric circulation

To better understand the variations in atmospheric circulation that occur in response to changes in surface elevation we show changes in the low-level wind pattern (at 850 hPa) and mean sea level pressure (MSLP) field. The 125Control simulation exhibits a widespread decrease in summer (JJA) MSLP compared to PI (Fig. 5.3c); the warmer SATs and Arctic sea ice loss in 125Control result in a warmer and less

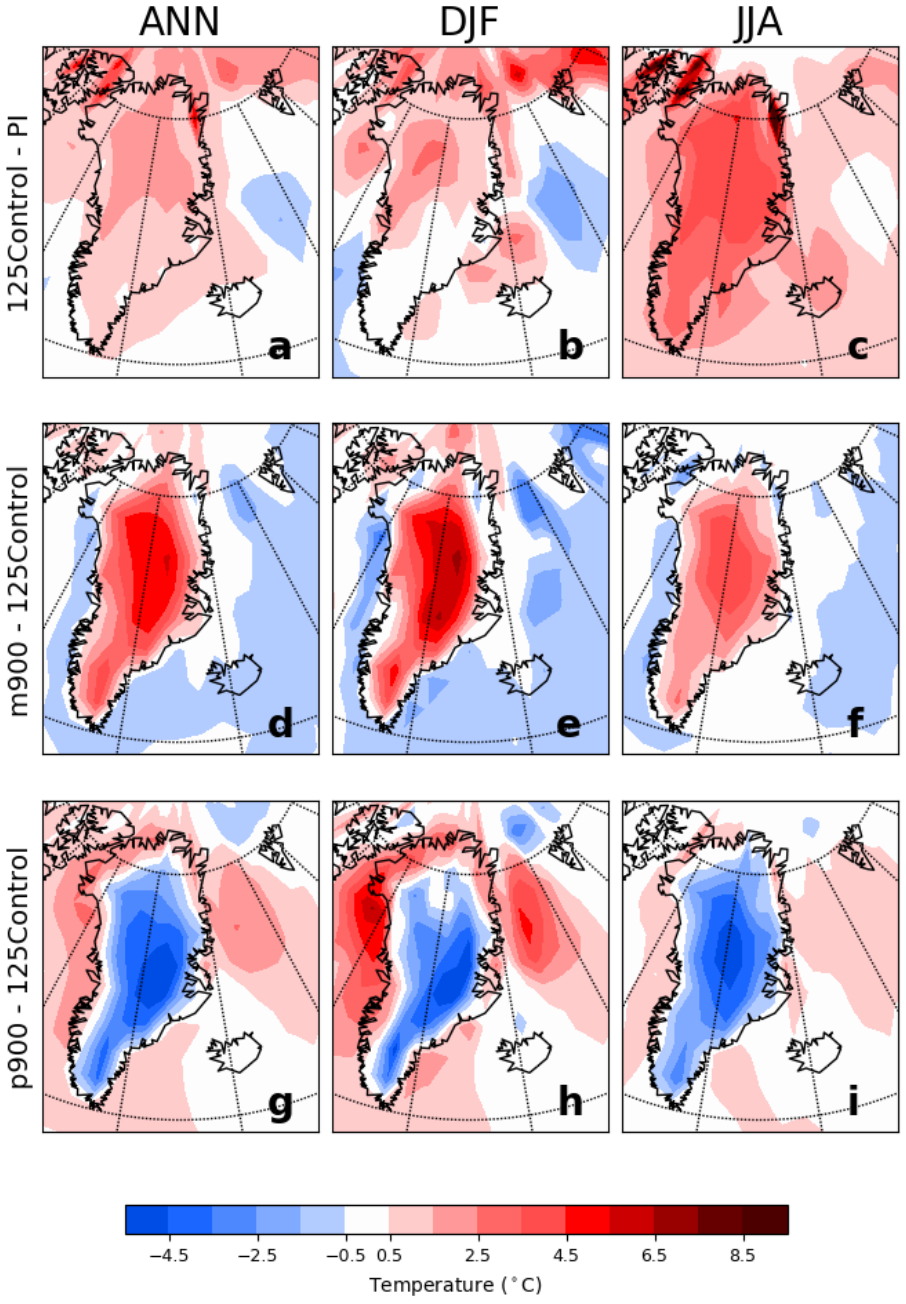

FIGURE 5.2: Modelled annual (ANN), winter (DJF) and summer (JJA) surface air temperature anomalies for m900 (d to f), and p900 (g to i) compared to the 125Control simulation. Also shown temperature anomalies for the 125Control compared to the PI simulation (a to c). Only the anomalies statistically significant at the 95% confidence level are displayed.

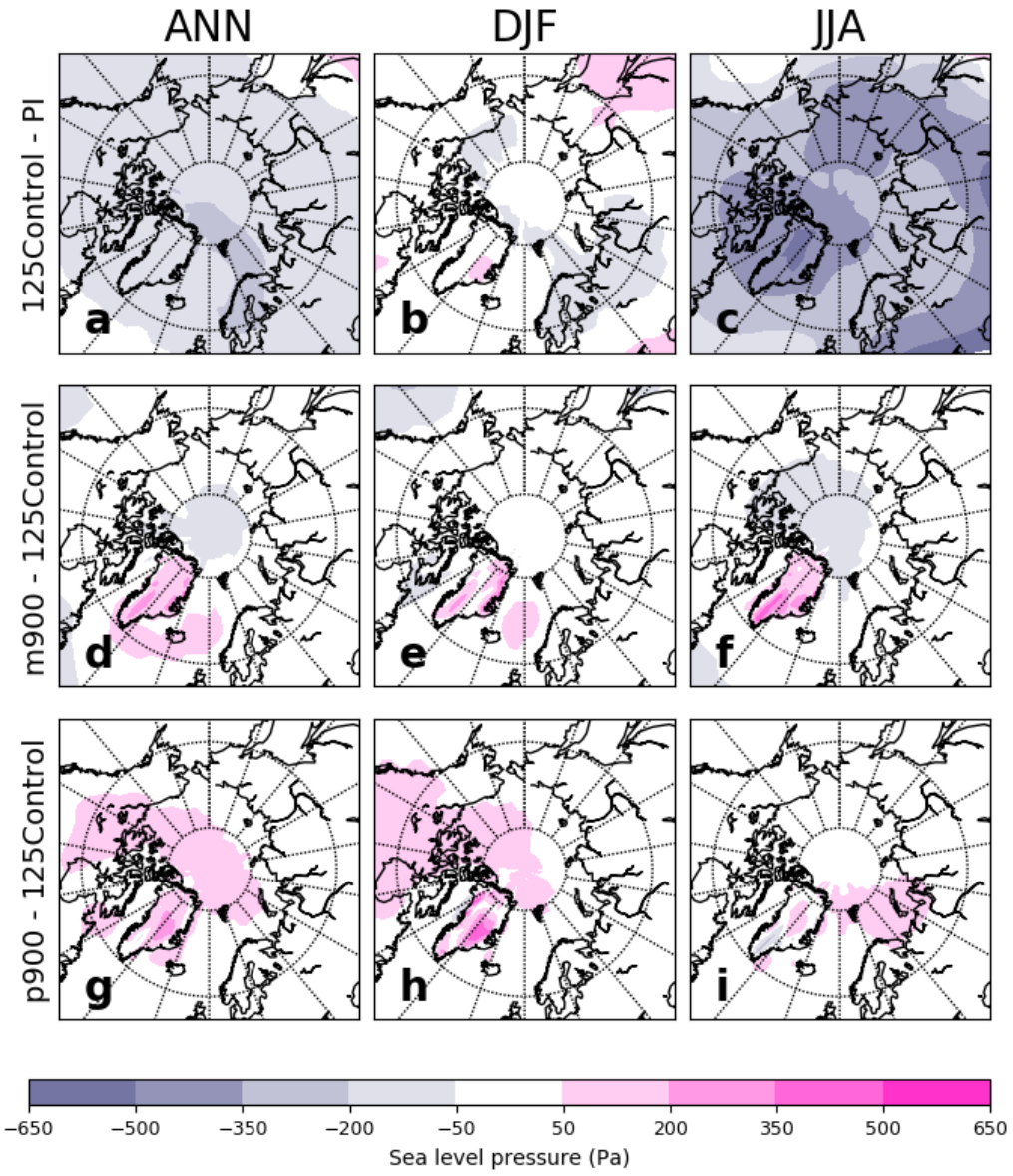

FIGURE 5.3: ANN, DJF and JJA mean sea level pressure anomalies (Pa) for: m900 (d to f) and p900 (g to i) compared to the 125Control simulation. Also shown sea level pressure anomalies for the 125Control compared to the PI simulation (a to c). Only the anomalies statistically significant at the 95% confidence level are displayed.

stable atmosphere at northern high latitudes during summer. During both winter and summer, the 125Control experiment shows no major differences in wind direction or strength relative to PI (Fig. 5.4a-d and Fig. 5.9a-b).

Over the Norwegian Sea, there is a increase in winter MSLP (local increases exceed +50 Pa) in m900 relative to 125Control (Fig. 5.3e). This increase is coincident with a sea ice increase (Fig. 5.5d) and cooler SATs (Fig. 5.2e) over the same region

compared to 125Control. Around northern Greenland, the scenario m900 shows a decrease in summer MSLP relative to 125Control (local decreases exceed -50 Pa; Fig. 5.3f); this is coincident with a decline in sea ice concentration (Fig. 5.5a). The scenario p900 shows and increase in annual MSLP over central Arctic Ocean (Fig. 5.3g).

Over Greenland, the surface winds respond to variations in the GIS surface elevation. Strong anticyclonic flow centred over Greenland is characteristic of the PI and 125Control simulations (Fig. 5.4 and Fig. 5.9). In the decreased elevation experiment (m900), the Greenland anticyclone becomes smaller (especially during the winter months compared to 125Control; Fig. 5.4c-f and Fig. 5.9c) and, over north-east Greenland, local wind vectors suggest air masses inflow from the Arctic Ocean contrary to the common outflow observed in the PI and 125Control (Fig. 5.4 and Fig. 5.9c). In contrast, the scenario with increases in the GIS elevation (p900) display an enhanced anticyclonic flow particularly during winter (Fig. 5.4g-h and Fig. 5.9e).

5.4.1.4 Changes in precipitation pattern

During summer, the 125Control shows an enhanced precipitation rate compared to PI mainly across southwestern and central Greenland (Fig. 5.6c). This is in line with results from other climate models (e.g., Otto-Bliesner *et al.*, 2006; Merz *et al.*, 2014b).

There is a rise in precipitation rate over much of Greenland throughout the year in m900 compared to 125Control (Fig. 5.6d to f). This is expected as the lowering of the orography leads to a wider spread of precipitation across Greenland from the east and west which is blocked by the higher and steeper elevation of the present-day GIS. Local increases over south-east Greenland exceed 0.8 mm/day in m900 during winter (Fig. 5.6e). This increase in precipitation accords with a reduction in winter sea ice concentration along the east coast of Greenland relative to 125Control (Fig. 5.5d).

For the increased elevation scenarios, local changes in precipitation rate relative to 125Control are less widespread and smaller than for the decreased elevation scenarios during both seasons (Fig. 5.6 d-i). Over south-east Greenland, p900 is up to 0.6 mm/day drier than the 125Control simulation during winter (Fig. 5.6 h).

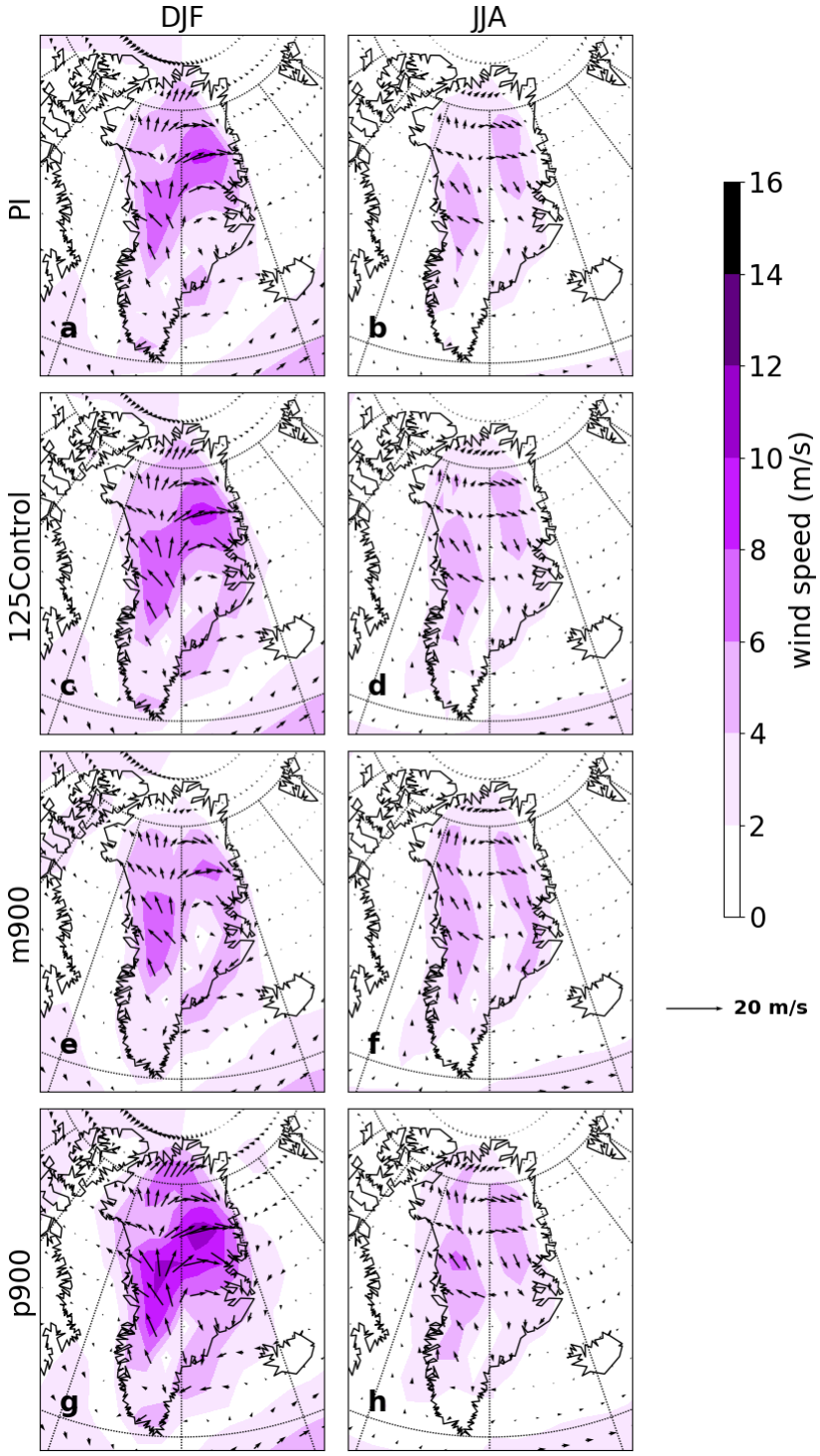

FIGURE 5.4: Absolute DJF and JJA low-level winds (at 850hPa) for PI (a-b), 125Control (c-d), m900 (e-f) and p900 (g-h). Shading displays wind speed (m/s).

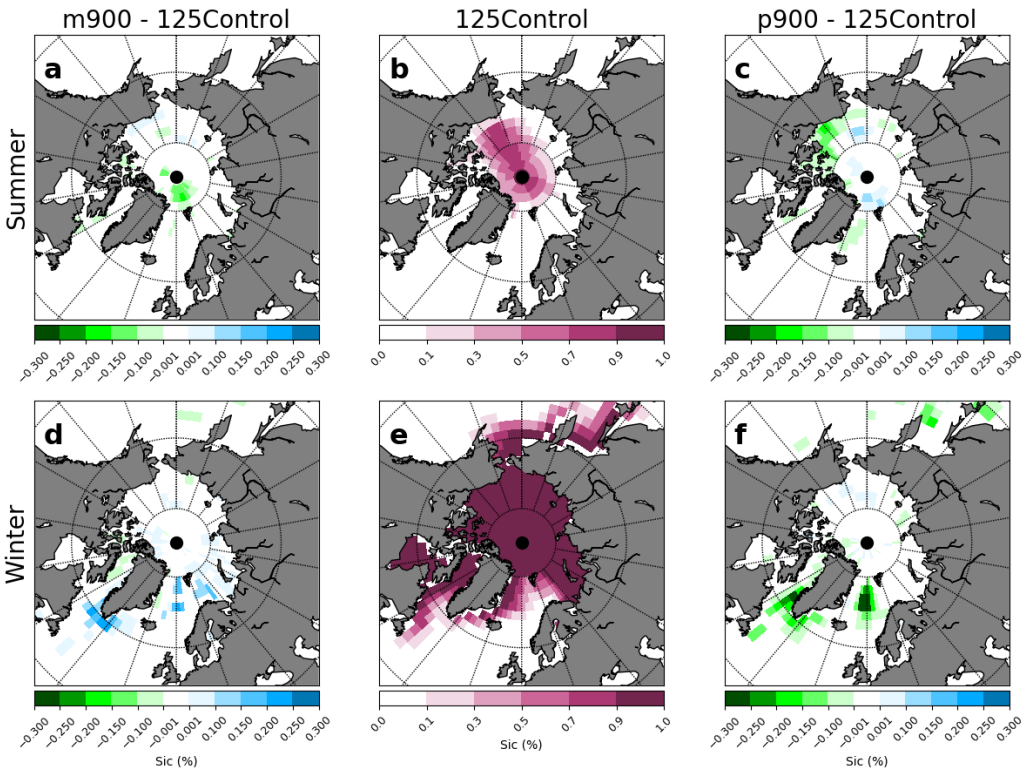

FIGURE 5.5: Sea ice concentration anomalies (%) for summer (September) and winter (March) for the scenarios m900 (a and d) and p900 (c and f) compared to the 125Control simulation. Also shown absolute sea ice concentration for the 125Control simulation for summer (b) and winter (e). Only the anomalies statistically significant at the 95% confidence level are displayed.

Precipitation increases linked to elevation decreases are much larger than the drying linked to elevation increases, implying non-linearities in the climate response to GIS elevation change (Fig. 5.1 and Fig. 5.6). The core-average precipitation lapse rate varies from 0.097 mm/year per 100 m for the decreased GIS elevation states to 0.009 mm/year per 100 m for the increased GIS elevation states. Nevertheless, this is considerably influenced by the DYE3 and Camp Century ice core sites (Fig. 5.1 w and ab). The DYE3 ice core site shows a much steeper relationship than the other ice core sites, 0.26 mm/year per 100 m for the decreased elevation scenarios and 0.134 mm/year per 100 m for the increased elevation scenarios (Fig. 5.1 w). At Camp Century site, precipitation tends to increase with both increases and decreases in the GIS elevation at a rate of 0.05 mm/year per 100 m for the decreased elevation scenarios and -0.091 mm/year per 100 m for the increased elevation scenarios (Fig. 5.1 ab). The different behaviour found at Camp Century site is likely linked to the reduced winter sea ice concentration over the Baffin Bay on both decreased and

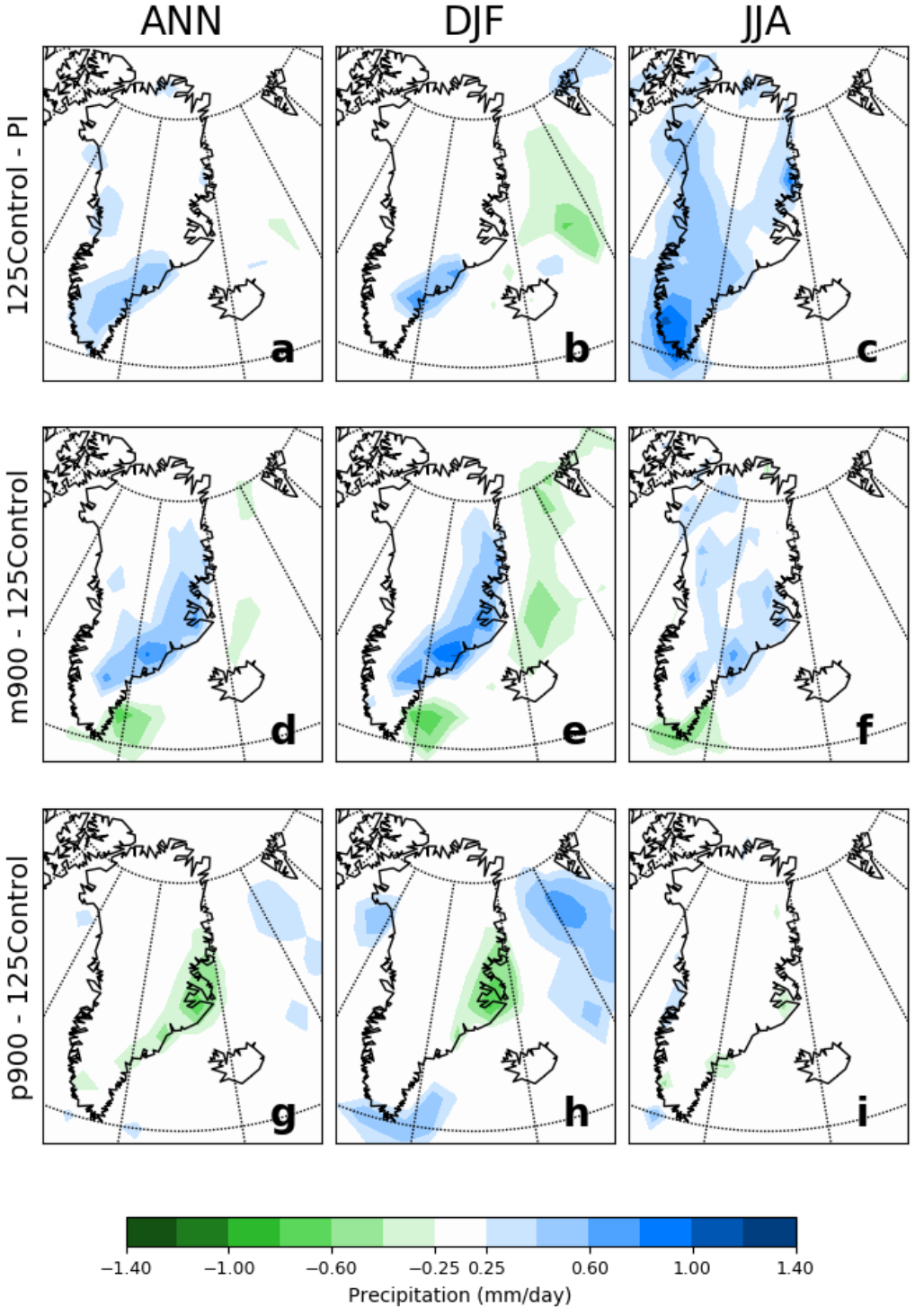

FIGURE 5.6: Annual (ANN), Winter (DJF) and summer (JJA) precipitation anomalies for m900 (d to f) and p900 (g to i) compared to the 125Control simulation. Also shown precipitation anomalies for the 125Control compared to the PI simulation (a to c). Only the anomalies statistically significant at the 95% confidence level are displayed.

increased elevation change scenarios (Fig. 5.5 d and f); reduced sea ice concentration permits more moisture to penetrate inland Greenland (Malmierca-Vallet *et al.*, 2018; Sime *et al.*, 2013).

5.4.1.5 Changes in sea ice

For the PI simulation, the September mean sea ice extent is $5.8 \times 10^6 km^2$. The 125Control simulation shows a reduced September mean of $4.4 \times 10^6 km^2$ relative to PI; larger seasonal and latitudinal insolation variations (linked to the orbital forcing) lead to Arctic sea ice loss during summer/spring (e.g., Otto-Bliesner *et al.*, 2006).

GIS elevation reductions lead to an increase in winter sea ice extent, whereas increases in the GIS elevation result in winter sea ice retreat (Fig. 5.1). In contrast to $\delta^{18}O$ and SAT, variations in winter sea ice extent are smaller for decreases in GIS elevation compared to increase elevation scenarios. For example, the March sea ice extent is reduced by -4.2% in p900 and increased by $+1.7\%$ in m900 compared to the 125Control simulation.

The decreased elevation scenario (m900) displays an increase of winter sea ice concentration on the Norwegian Seas and on the southern-eastern coast of Greenland compared to 125Control simulation (Fig. 5.5 d). The reduced cyclogenesis off the south-east coast of Greenland (Fig. 5.11), results in growth of winter sea ice over these regions (Fig. 5.5 d). This is probably associated with a decrease in wind-driven ocean heat transport (e.g., Pausata *et al.*, 2011; Stone and Lunt, 2013; Davini *et al.*, 2015). The increased elevation scenario (p900) experience the same forcing but in opposite direction (Fig. 5.5 f and Fig. 5.11).

We also find some local changes in summer sea ice concentration; while p900 shows decreases of summer sea ice over the Beaufort Sea, it shows increases over the Fram Strait area. Similar patterns are found in m900 but in opposite direction and of lower magnitude (Fig. 5.5 a,c).

We ascribe these changes in summer sea ice to variations in ocean salinity caused by anomalous downwelling or upwelling, induced by anomalously low or high sea level

pressure over the Arctic (Jackson and Vellinga, 2012). In HadCM3, the geostrophic balance of the Beaufort gyre can be altered ageostrophically by wind stresses linked to low-frequency sea level pressure variability (Jackson and Vellinga, 2012). Our increased elevation scenario (p900) show high sea level pressure anomalies over the Arctic basin (Fig. 5.3) which lead to downwelling in the center of the Arctic basin and upwelling along the coasts respectively (Fig. 5.10). Since the surface water is fresher and colder than the subsurface water, this results in salinification near the coasts and freshening in the center of basin. The same mechanisms apply to the decreased elevation scenario (m900) but in opposite direction (Fig. 5.10).

The increase in wind speed along the Fram Strait in p900 compared to 125Control and vice versa for m900 (Fig. 5.11) also affects the advection of sea ice from the Arctic to the Atlantic ocean (Davini *et al.* (2015)).

5.4.2 The response of the isotopic lapse rate to changes in the background climate state

Malmierca-Vallet *et al.* (2018) demonstrate the importance of Arctic sea ice changes as a control on LIG Greenland ice core $\delta^{18}O$ because of its impact on both the regional temperature increase and the moisture source. Thus, we also study 32 simulations that examine the joint impact of modified Arctic sea ice retreat and modified GIS morphology (considering both changes in the extent and elevation of the GIS - see Table 5.1 and section 2.1).

We use the sea ice retreat simulations of Malmierca-Vallet *et al.* (2018) to isolate the impacts of $\delta^{18}O$ due to sea ice variation. This allows to test to which extent Arctic sea ice changes may influence isotopic lapse rate values. Fig 5.12 shows the change in $\delta^{18}O$ as a function of winter (March) sea ice retreat. We (1) remove the orbital forcing effect by calculating $\delta^{18}O$ anomalies compared to the 125 ka control simulation, and (2) we only analyse scenarios with winter sea ice retreats lower than 55%, due to the almost no sensitivity of Greenland $\delta^{18}O$ to sea ice losses greater than 50% (for more detail see Malmierca-Vallet *et al.* (2018)).

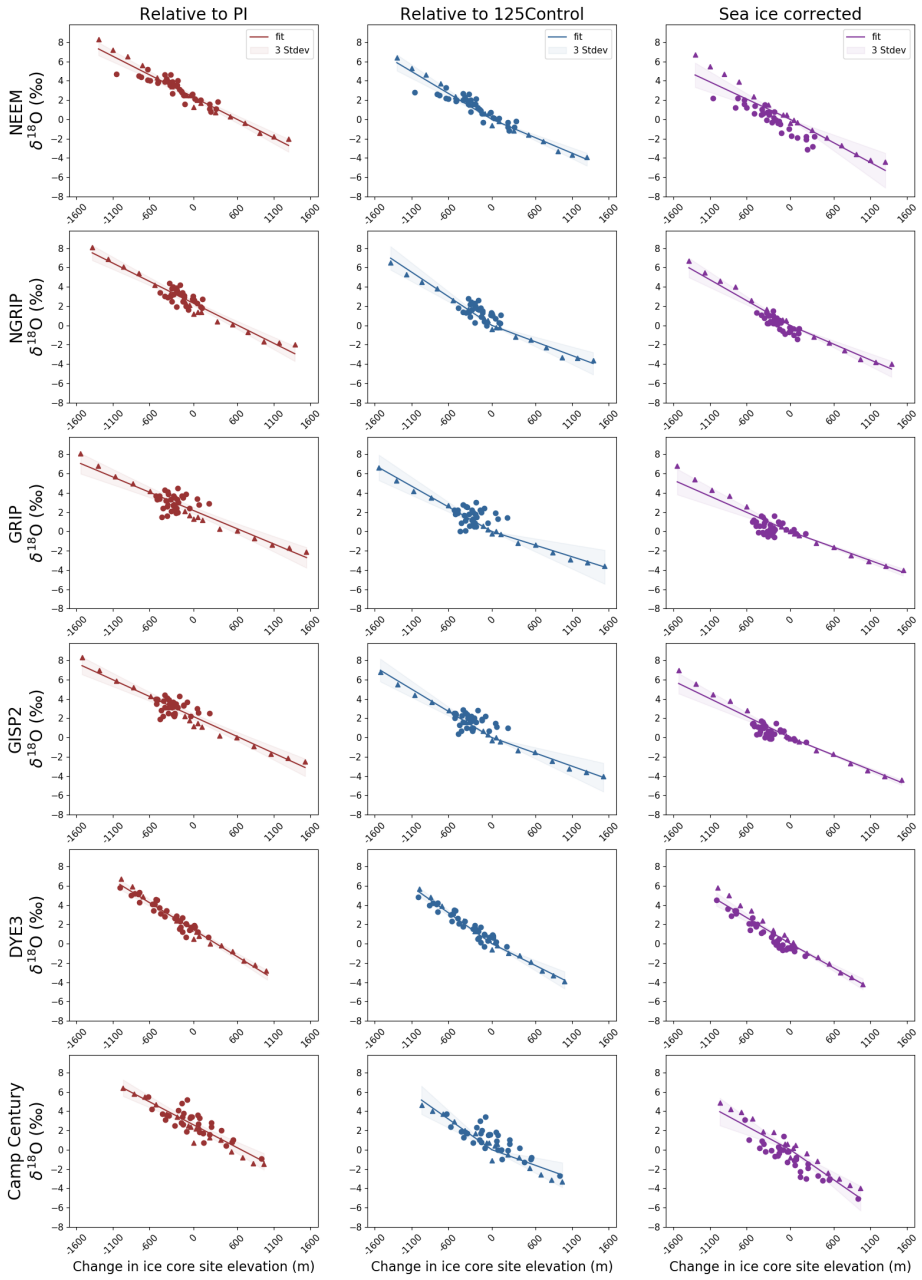

FIGURE 5.7: $\delta^{18}Op$ anomalies as a function of ice core site elevation change (m) relative to PI (first column) and 125Control (second column). Also shown sea-ice-corrected $\delta^{18}Op$ anomalies compared to 125Control (third row). Ice core sites displayed: NEEM (first row), NGRIP (second row), GRIP (third row), GISP2 (fourth row), DYE3 (fifth row) and Camp Century (sixth row). Triangles represent results for the 16 elevation change experiments. Dots represent results for the 32 simulations that examine the joined impact of Arctic sea ice retreat and modified GIS shape. Solid lines signify best fit curves (first column, y = a + bx; second and third columns, y = ax) and shade envelopes represent ±3s uncertainty on the best fit lines.

To calculate the sea-ice-corrected $\delta^{18}O$ anomalies we deduct the sea-ice-associated $\delta^{18}O$ effect from the total $\delta^{18}O$ anomalies. Fig 5.7 shows the resulting sea-ice-corrected $\delta^{18}O$ anomalies (Fig 5.7 – purple curve fits) as well as total $\delta^{18}O$p anomalies (compared to both the PI and 125Control simulations) not corrected for sea ice changes (Fig 5.7 – red and blue curve fits respectively) for both sets of simulations (Fig 5.7 - triangles for elevation change simulations and dots for simulations looking at the combined impact of sea ice retreat and GIS changes).

When considering total $\delta^{18}O$p anomalies (relative to 125Control) not corrected for sea ice changes, a non-linear $\delta^{18}O$ lapse rate is observed over Greenland (Fig 5.7 - second column); The core-average $\delta^{18}O$ lapse rate varies from 0.29‰ per 100 m for the enlarged GIS states to 0.49‰ per 100 m for the lowered GIS states (Fig 5.7 – second column). These results thus strongly suggest a non-linearity in the isotope-elevation relationship, with higher $\delta^{18}O$-elevation gradients for lowered GIS states and vice versa.

When further deducting the winter sea ice effect, we find an almost stationary core-average $\delta^{18}O$ lapse rate, slightly varying from 0.38‰ per 100m for the enlarged GIS scenarios to 0.39‰ per 100m for the lowered GIS scenarios (Fig 5.7 - third column). The sea ice effect increases $\delta^{18}O$-elevation gradients by 28% in the enlarged GIS states and decreases $\delta^{18}O$-elevation gradients by -19% in the lowered GIS states. Indeed, this suggests that sea ice changes may strongly influence linearity in the isotope-elevation relationship.

The dependence of the $\delta^{18}O$ variable on elevation variations occurs in response to variations in winter sea ice extent. GIS elevation reductions lead to an increase in winter sea ice extent, whereas increases in the GIS elevation result in winter sea ice retreat (Fig. 5.1). Thus, the loss/increase of winter sea ice extent act as a positive/negative feedback on $\delta^{18}O$.

5.5 Discussion

5.5.1 Response of Arctic sea ice and atmospheric circulation to GIS elevation changes

Our lowered GIS experiments show similar climate behaviour to previous studies where GIS is removed (Toniazzo *et al.*, 2004; Stone and Lunt, 2013; Davini *et al.*, 2015). During summer warming over the GIS is enhanced due to its lower elevation and Arctic sea ice retreat (Lunt *et al.*, 2004). During winter warm anomalies extend over the Arctic Ocean. These anomalies are related to a smaller anticyclone over Greenland (Fig. 5.4h) (Stone and Lunt, 2013; Davini *et al.*, 2015). The lowering of the elevation also leads to a weakened ice sheet barrier effect, permitting cyclonic systems to get into more central and northern areas of Greenland. The reduction in cyclogenesis over the Norwegian Sea and off the south-east coast of Greenland due to lowering of the GIS elevation leads to the growth of further sea ice, especially during the winter months (Fig. 5.5g and h). Reduced ocean heat transport, due to weakened wind-driven currents (Stone and Lunt, 2013) may also contribute to decreased surface temperatures over the Norwegian and Barents Seas and on the south-east coast of Greenland (Fig. 5.2 e and h).

When elevation is increased, colder GIS temperatures occur, but a compensating warming occurs around Greenland (Fig. 5.2). Mechanisms causing this surface temperature pattern were discussed in previous studies which investigated changes in northern hemisphere ice sheets during the last glacial period (e.g., Felzer *et al.*, 1996; Singarayer and Valdes, 2010; Pausata *et al.*, 2011). Fennoscandian and North American ice sheets cause warming south of the ice sheets and east of Greenland. This localized warming has been attributed to glacial anticyclones which are linked to subsidence, decreased cloud cover and soil moisture during summer, generally deeper Icelandic low and increased ocean and atmosphere heat transport into the North Atlantic (Felzer *et al.*, 1996; Pausata *et al.*, 2011). In our experiments, the glacial anticyclone over Greenland intensify as elevation increases, especially during the winter months (Fig. 5.4i). This leads to enhanced cyclogenesis over the Barents Seas and

south-east coast of Greenland which result in winter sea ice retreat over the same regions (Fig. 5.5f).

5.5.2 Lapse rates in response to GIS elevation changes

The combined changes explained above lead to non-linearities in the climate response to Greenland elevation change (Fig. 5.1). Averaging across the six ice core sites, we find temperature lapse rates of 0.47°C and 0.44°C per 100m for the decreased/increased elevation change scenarios respectively (Fig. 5.1). We also find that the wetting related to decreases in GIS elevation are higher than the drying related to increases in elevation.

Our temperature lapse rates compare well with previous estimates which show that the near-surface temperature lapse rate can generally differ from the free-air lapse rate (gradient of moist adiabatic cooling of 0.65°C per 100m) (Marshall *et al.*, 2007; Fausto *et al.*, 2009; Gardner *et al.*, 2009; Erokhina *et al.*, 2017). Marshall *et al.* (2007) monitored 25 sites with altitudes between 130 to 2010 m across the Prince of Wales Icefield and observed a mean daily temperature lapse rate of 0.41°C per 100 m. Furthermore, Gardner *et al.* (2009) showed temperature lapse rates near four glacier surfaces, in the Canadian high Arctic, of 0.49°C per 100 m (ablation season mean). Gardner *et al.* (2009) also suggested that lower temperature lapse rates are expected under a warming climate and linked this to the negative relationship found between lower-troposphere temperatures and slope lapse rates.

Our results are also in agreement with Erokhina *et al.* (2017), who point to a non-stationarity response of the climate to GIS elevation changes during the Holocene and Last Glacial Maximum (LGM). Erokhina *et al.* (2017) propose that following the transition from the LGM to the Holocene, mean annual temperature lapse rates over the GIS decreased by almost 20%.

5.5.3 The response of the isotopic lapse rate to the background climate state

Isotope-elevation gradients have tended to be calculated from modern surface data (e.g., Dansgaard, 1973): a present-day spatial relationship is presumed to apply to temporal changes. This disregards any impact that variations in the ice sheet elevation may have on the atmospheric circulation, precipitation patterns and eventually the isotopic composition.

Our idealized elevation change simulations with HadCM3 allow a fuller calculation. We find a smaller core-average $\delta^{18}O$ lapse rate for enlarged GIS states (0.29‰ per 100 m) than for the lowered GIS states (0.49‰ per 100 m) (Fig 5.7). Hence, $\delta^{18}O$-elevation gradients do not remain constant across the parameter space of elevation changes. This strongly suggest non-linearities in the isotopic response to Greenland elevation change.

We also find that winter sea ice variations can increase/decrease modelled core-averaged isotopic lapse rate values by about +28% and −19% for the enlarged/lowered GIS states respectively (Fig. 5.7). These results thus suggest that sea ice variations may have a strong influence on $\delta^{18}O$-elevation gradients, especially at coastal areas such as the Camp century ice core site (Fig. 5.13). In particular, at this location, we find that the winter sea ice effect decreases the $\delta^{18}O$-elevation gradient by −24% in the lowered GIS states and increases the $\delta^{18}O$-elevation gradient by as much as 92% in the enlarged GIS states (Fig. 5.13 e). While the largest influence of sea ice on $\delta^{18}O$ changes is found at Camp Century site, DYE3 site shows the smallest (Fig. 5.13 e-f). These results point to elevation changes as a likely driver (together with GHGs and orbital forcing) on LIG $\delta^{18}O$ changes at DYE3 ice core site. This is in agreement with previous LIG GIS modelling studies which propose a significant LIG lowering around the DYE3 area, even the total loss of ice (Robinson *et al.*, 2011; Helsen *et al.*, 2013).

Interestingly, modelled isotopic lapse rates are lower than the calculated spatially derived gradients of 0.62‰ per 100 m and 0.72‰ per 100 m in central and northwest Greenland respectively (Dansgaard, 1973; Johnsen *et al.*, 1989; Vinther *et al.*, 2009).

Furthermore, our core-average $\delta^{18}O$ lapse rates are also somewhat lower than the lapse rate of 0.56‰ per 100 m modelled (with the isotope enabled version of the European Centre Hamburg Model version 4) over Greenland for the LIG period by Sjolte *et al.* (2014). Note our modelled isotopic lapse rates contemplate the dynamical response of atmospheric circulation to GIS elevation changes and Arctic sea ice variations, whereas previous studies disregard these effects.

These elevation change simulation results thus suggest possible non-linearity in isotope-elevation gradients. It would be useful if this was checked with other models to assess model-dependence in the results.

5.6 Conclusions

The results of this study are relevant for the interpretation of past climates from Greenland ice core records. Changing GIS elevation in HadCM3 alters the NH atmospheric circulation circulation, sea ice and precipitation patterns over Greenland and further afield. These climate feedbacks result in lower isotopic-elevation gradients for enlarged GIS states, and vice versa. Our results thus point to non-linear $\delta^{18}O$-elevation gradients over Greenland. We further show that isotopic lapse rate values may be significantly influenced by the background climate, in particular, winter sea ice changes.

These model results highlight the importance of the dynamical response of atmospheric circulation to GIS elevation changes when using isotopic measurements to derive past elevation changes: there may be non-linearities in isotope-elevation relationships. Although the underlying mechanism need further investigation, our finding has important implications for paleoclimate studies, in which stationary lapse rates are assumed and are normally based on present-day observations. Inter-model comparison studies would be helpful in further developing our understating of the isotope-elevation gradient over Greenland and how it varies with the background climate state.

5.7 Supplementary information

TABLE 5.1: Full list of scenarios. Third and fourth columns show the sea ice forcing (SIF) implemented and the winter sea ice extent (SIE) respectively. The simulations highlighted in blue are the ones primarily discussed in the text. All LIG simulations are performed with greenhouse-gas and orbital forcing centred at 125ka (Eccentricity - 0.04001; Obliquity - 23.80°; Perihelion - 201.3 day of yr; CO_2 - 276 ppmv; CH_4 - 640 ppbv; N_2O - 263 ppbv). The boundary conditions for the PI simulation are the following: Eccentricity - 0.0167; Obliquity - 23.45°; Perihelion - 1.7 day of yr; CO_2 - 280 ppmv; CH_4 - 760 ppbv; N_2O - 270 ppbv. Note (*): To account for the modelled climate variability for a 125 ka control scenario, we use an average of three 125 ka simulations which feature very minor GIS elevation changes between them (maximum scaling percentage of ±1.8 in Eq. 1) as our 125 ka control.

Exp ID	**NEEM Δz** (m)	**SIF** (W/m^2)	**March SIE** ($10^6 km^2$)
PI	0	0	18.77
125Control *	0	0	19.87
p50	50	0	19.46
p100	100	0	19.65
p300	300	0	20.07
p500	500	0	19.06
p700	700	0	18.88
p900	900	0	19.02
p1100	1100	0	18.63
p1300	1300	0	18.46
m50	-50	0	19.71
m100	-100	0	19.61
m300	-300	0	20.09
m500	-500	0	19.82
m700	-700	0	20.45
m900	-900	0	20.20
m1100	-1100	0	20.39

Continued on next page

Table 5.1 – continued from previous page

Exp ID	**NEEM Δz** (m)	**SIF** (W/m^2)	**March SIE** ($10^6 km^2$)
m1300	-1300	0	20.56
GIS1-SIE-11.49	99	119.3	11.49
GIS2-SIE-11.52	-316	116	11.52
GIS3-SIE-11.67	14	114.6	11.67
GIS4-SIE-11.72	303	111.9	11.72
GIS5-SIE-12.25	231	109.6	12.25
GIS6-SIE-12.63	-246	97.6	12.63
GIS7-SIE-13.45	-19	91.2	13.45
GIS8-SIE-13.77	-371	83.5	13.77
GIS9-SIE-13.77	-322	85.1	13.77
GIS10-SIE-14.05	-391	77.8	14.05
GIS11-SIE-14.15	328	77.4	14.15
GIS12-SIE-14.93	-391	60.2	14.93
GIS13-SIE-14.98	216	55	14.98
GIS14-SIE-15.33	-288	55.3	15.33
GIS15-SIE-15.37	-228	63	15.37
GIS16-SIE-15.46	-167	51	15.46
GIS17-SIE-15.59	-749	54.4	15.59
GIS18-SIE-15.77	-190	45.1	15.77
GIS19-SIE-16.02	-493	35.5	16.02
GIS20-SIE-16.08	-632	40	16.08
GIS21-SIE-16.24	-217	39.5	16.24
GIS22-SIE-16.25	221	31.2	16.25
GIS23-SIE-16.58	-117	28.4	16.58
GIS24-SIE-16.75	-156	22.6	16.75
GIS25-SIE-17.21	-140	18.9	17.21
GIS26-SIE-17.54	-592	16.7	17.54
GIS27-SIE-18.15	-631	9.4	18.15
GIS28-SIE-18.18	-482	12.2	18.18

Continued on next page

Table 5.1 – continued from previous page

Exp ID	**NEEM Δz** (m)	**SIF** (W/m^2)	**March SIE** $(10^6 km^2)$
GIS29-SIE-18.29	-1053	7.5	18.29
GIS30-SIE-18.65	-343	8.4	18.65
GIS31-SIE-19	-719	0.9	19.00
GIS32-SIE-19.48	-292	1.3	19.48

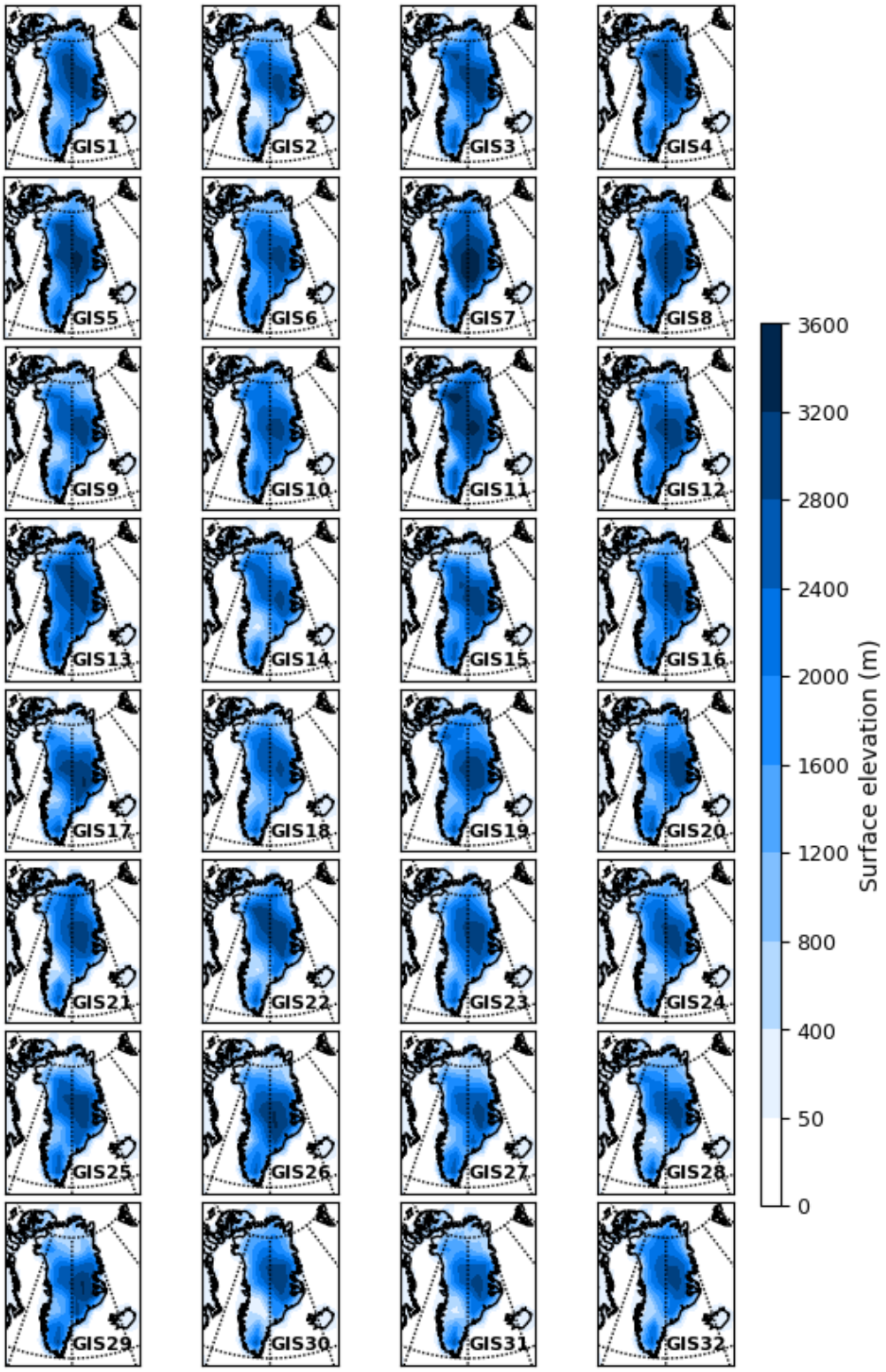

FIGURE 5.8: Surface elevation (meters) of LIG GIS morphologies used in the 32 simulations that examine the joint impact of modified Arctic sea ice retreat and modified GIS morphology. See Table. 5.1 for more details.

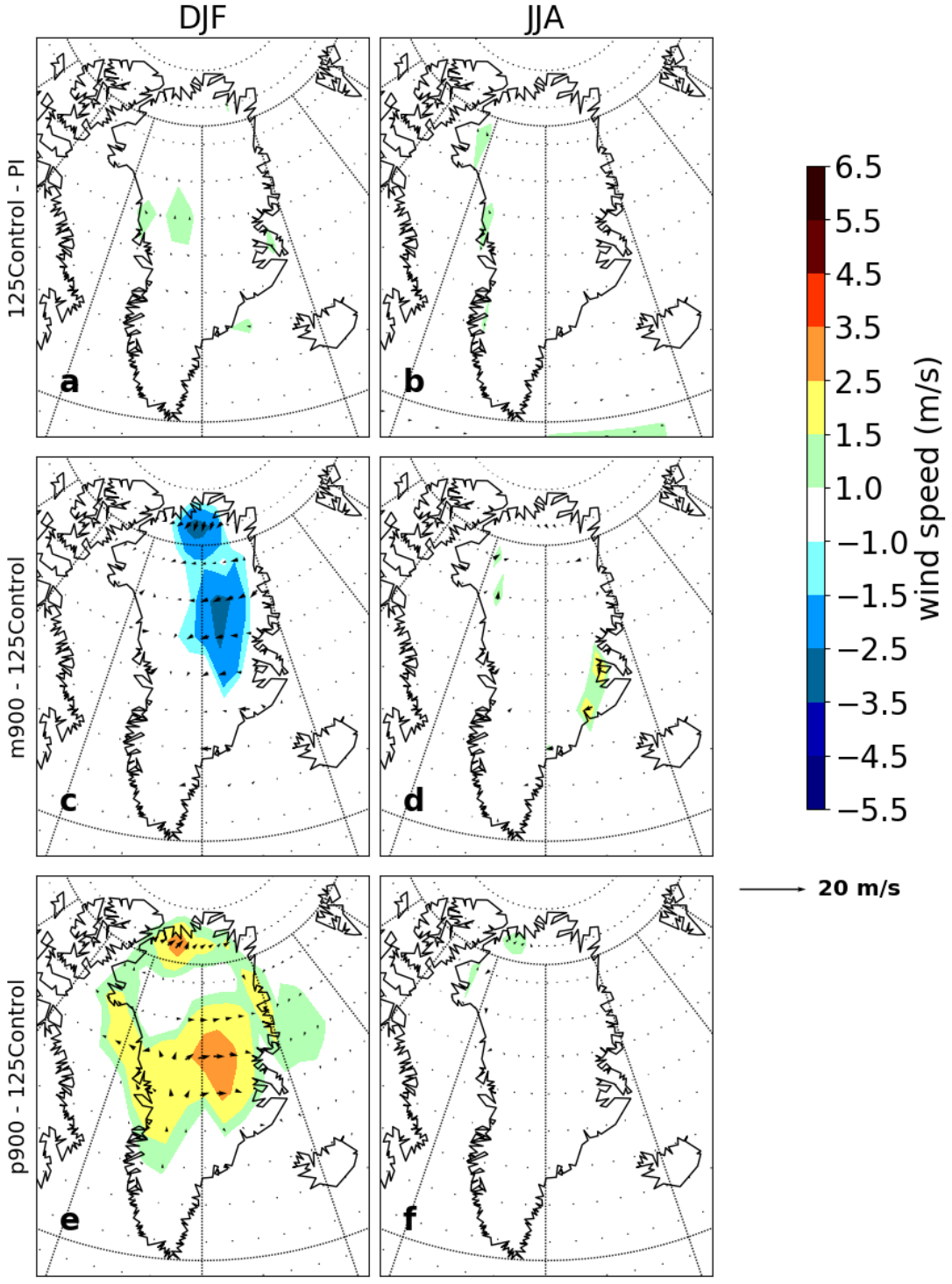

FIGURE 5.9: Winter (DJF) and summer (JJA) low-level winds (at 850 hPa) anomalies for m900 (c-d) and p900 (e-f) compared to the 125Control simulation. Also shown low-level wind anomalies for the 125Control compared to the PI simulation (a-b). Only the anomalies statistically significant at the 95% confidence level are displayed. Shading displays wind speed (m/s).

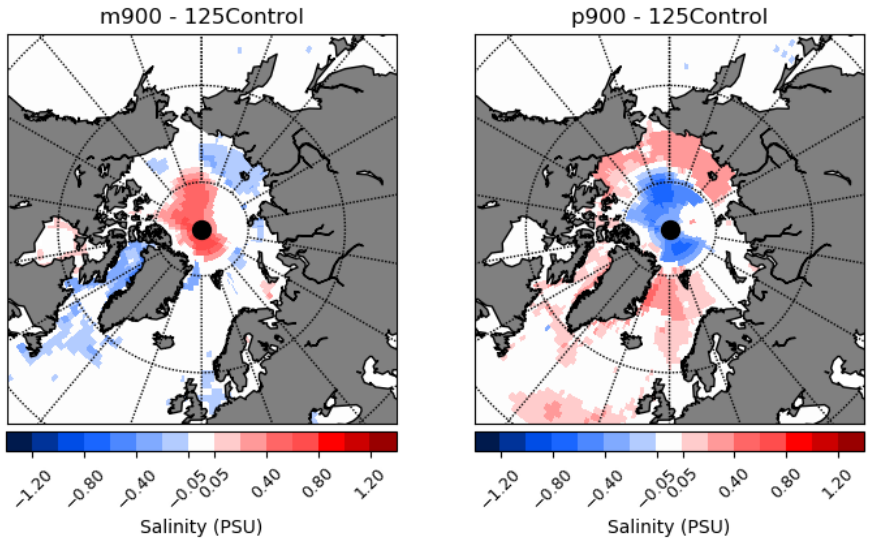

FIGURE 5.10: Annual salinity (PSU; averaged over the top 535 m) anomalies for m900 (a) and p900 (b) compared to 125Control simulation. Only the anomalies statistically significant at the 95% confidence level are displayed. Shading displays wind speed (m/s).

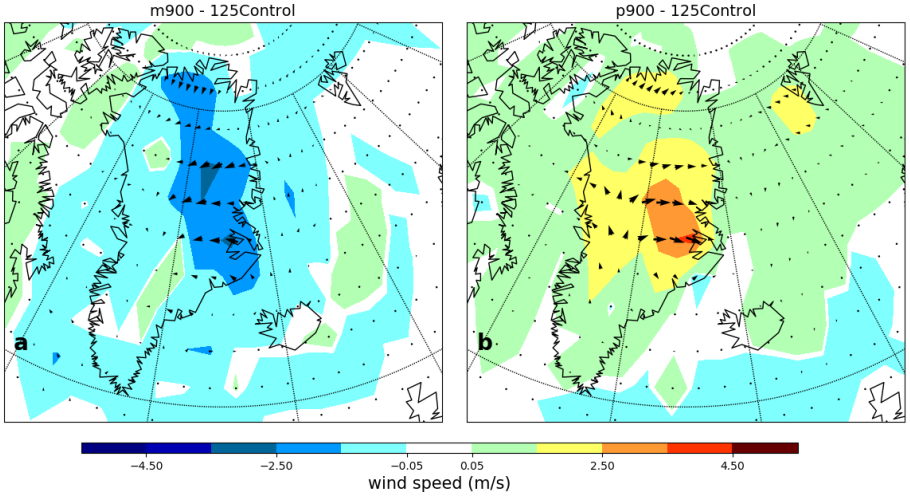

FIGURE 5.11: Change in 10 m winter (DJF) wind speed (in m/s) for (a) m900 and (b) p900 compared to 125Control. Only the anomalies statistically significant at the 95% confidence level are displayed.

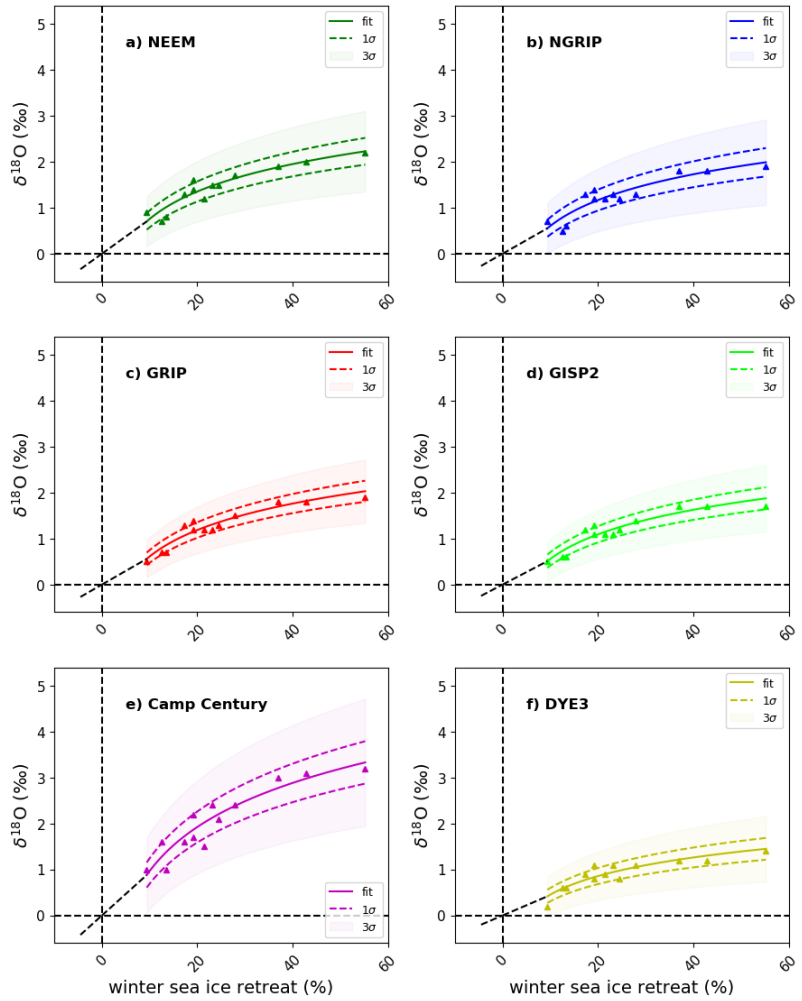

FIGURE 5.12: Simulated $\delta^{18}Op$ anomalies as a function of winter (March) sea ice retreat. The retreat of sea ice is calculated as the percentage change in winter sea ice extent compared to the 125 ka control simulation. Ice core sites shown: (a) NEEM, (b) NGRIP, (c) GRIP, (d) GISP2, (e) Camp Century, (f) DYE3. Triangles represent results from the sea ice sensitivity experiments performed by Malmierca-Vallet et al. (2018). Solid lines signify best fit lines (fit = b*(log(x) – a)). Also shown 1σ (lines with dashes) and 3σ uncertainty (shade envelopes) on the best fit curve. We assume a straight line regression (fit = a+bx) for winter sea ice losses between 0% and 9% and increases up to −4.5%. This figure is an adaptation of figure 10 shown in Malmierca-Vallet et al. (2018).

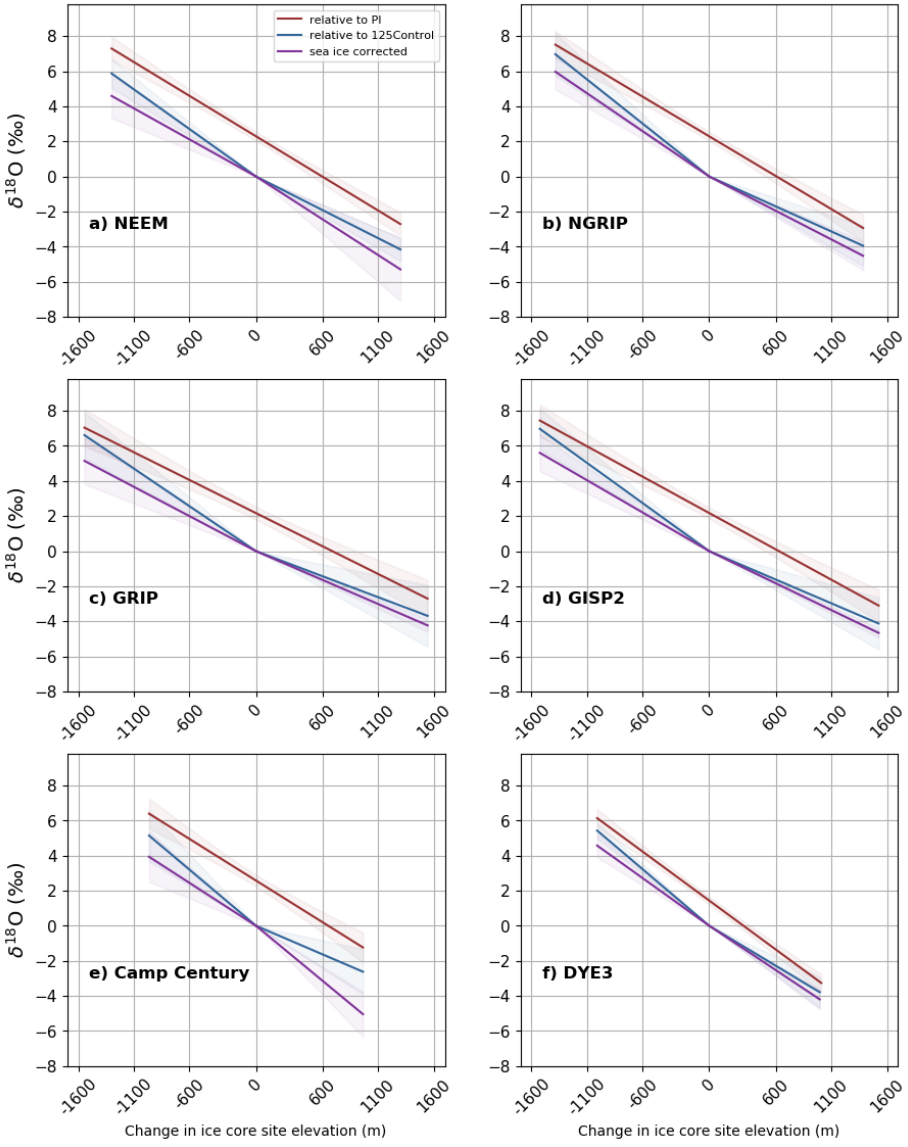

FIGURE 5.13: $\delta^{18}Op$ anomalies as a function of the ice core site elevation change (m) relative to (1) PI (red), and (2) 125Control (blue). Also shown sea-ice-corrected $\delta^{18}Op$ anomalies relative to 125Control (purple). Ice core sites shown: (a) NEEM, (b) NGRIP, (c) GRIP, (d) GISP2, (e) Camp Century, (f) DYE3. Solid lines signify best fit curves and shade envelopes represent ±3 Stdev on the best fit lines.

Chapter 6

The role of Greenland iceberg discharge on the ice $\delta^{18}O$ signal across Greenland: LIG HadCM3 simulations

6.1 Introduction

Mass reduction from the Greenland ice sheet (GIS) is now seen as the largest source of sea level rise (IPCC, 2013; Box and Sharp, 2017), contributing around 1 mm per year of global water equivalent during the 2010-2015 period (van den Broeke *et al.*, 2016). Iceberg meltwater fluxes are a main element of the total GIS mass balance (Bigg *et al.*, 2014). The GIS discharges approximately 550 Gt of icebergs yearly (Enderlin *et al.*, 2014), which explains up to half of the freshwater flux from the GIS to the surrounding ocean basins and fjords (Bamber *et al.*, 2012; Enderlin *et al.*, 2014; van den Broeke *et al.*, 2016). Since the late twentieth century, the overall iceberg frequencies from the GIS are much higher compared to earlier periods (Bigg *et al.*, 2014; Zhao *et al.*, 2016). To comprehend the future role of the Greenland iceberg calving process, it is instructive to investigate iceberg meltwater flux changes during past warm climate states.

The Last Interglacial (LIG; approximately 130,000 to 115,000 ka), one of the warmest periods through the last 800,000 years (Past Interglacials Working Group of PAGES, 2016), was the last time in Earth's history when the GIS is thought to have been substantially smaller (e.g., Stone *et al.*, 2013; IPCC, 2013; Calov *et al.*, 2015; Dutton *et al.*, 2015; Plach *et al.*, 2019). Compare to pre-industrial (PI), the LIG is believed to have had 4-5°C higher Arctic summer temperatures (CAPE Last Interglacial Project Members, 2006), reduced Arctic and Antarctic sea ice extent (Sime *et al.*, 2013; Malmierca-Vallet *et al.*, 2018; Holloway *et al.*, 2016a), and up to 2°C warmer global annual average temperatures (Turney and Jones, 2010; McKay *et al.*, 2011; Hoffman *et al.*, 2017).

Our knowledge of the rates and magnitudes of mass loss in today's ice sheets (GIS and Antarctic ice sheet) in response to (future and past) warming beyond PI levels remains limited. With global mean sea levels 6 to 9 meters higher than present (Kopp *et al.*, 2009; Dutton and Lambeck, 2012; Dutton *et al.*, 2015), the LIG is an ideal case study for improving this knowledge.

Layers of LIG ice have been retrieved from numerous Greenland deep ice cores: NEEM, NGRIP, GRIP, GISP2, Camp Century, DYE3 and Renland (e.g., NEEM community members, 2013; Landais *et al.*, 2016). Previous isotopic climate simulations of the LIG in response solely to GHG and orbital forcing have failed to reproduce the observed Greenland $\delta^{18}O$ increases of at least 2.5‰ compared to present-day (e.g., Masson-Delmotte *et al.*, 2011; Sime *et al.*, 2013; Sjolte *et al.*, 2014). Later studies have been able to reduce the disagreement between models and data when contemplating changes in both the GIS topography and Arctic sea ice extent (Malmierca-Vallet *et al.*, 2018; Domingo *et al.*, 2020).

This paper investigates the stable water isotope ($\delta^{18}O$) response to variations in the Greenland iceberg calving flux values in the UK Met Office coupled atmosphere-ocean general circulation model (HadCM3). Since iceberg calving values in HadCM3 are tuned with regard to a modern ice sheet distribution, they may not remain adequate for simulating past climates like the LIG, characterised by a reduced GIS (e.g., Robinson *et al.*, 2011; Stone *et al.*, 2013; Dutton *et al.*, 2015). We perform an ensemble of idealised meltwater forcing experiments to investigate the role of freshwater from the

retreating GIS on the LIG Greenland ice core isotope record. We focus only on the Greenland iceberg calving process in order to better isolate and quantify the impacts of this mechanism on the climate of the LIG.

6.2 Methods

6.2.1 Model Description

The isotope-enabled version of HadCM3 is used to simulate the climate response to idealised variations in the discharge of icebergs from Greenland. This General Circulation Model (GCM) is made of a coupled ocean, atmosphere and sea ice model (Gordon *et al.*, 2000) and has been extensively employed to explore past, present and future climate states (IPCC, 2007, 2013). We use the MOSES 2.1 land surface scheme (Cox *et al.*, 1999; Essery *et al.*, 2001) fully coupled to the TRIFFID (Top-down Representation of Interactive Foliage and Flora Including Dynamics) dynamic global vegetation model (Cox, 2001).

6.2.1.1 Water conservation in HadCM3

In HadCM3, the river runoff is instantly transferred into the ocean by means of a prescribed runoff map; nevertheless, the area-average water flux is not zero (Gordon *et al.*, 2000). The majority of the imbalance derives from snow accumulation on both ice sheets (Gordon *et al.*, 2000). In the real world, this fresh water is reverted to the ocean through the iceberg calving process. Ice sheets in HadCM3 are not modelled dynamically; thus snow accumulation on land ice points is assumed to be balanced by the loss through a theoretical iceberg calving process which is represented as a fixed time-invariant freshwater flux (Gordon *et al.*, 2000). The rigid lid of the ocean model implies that the freshwater flux over the ocean surface do not result in variations in the volume of water in the column (Gordon *et al.*, 2000). Thus, the freshwater (W) is converted into an equivalent virtual salinity flux (Fs) which is distributed all around

the edge of the Greenland Ice Sheet (GIS) and Antarctica Ice Sheet (AIS) and polar oceans (Gordon *et al.*, 2000). The global salinity budget is closed following:

$$Fs = -WS_0/p_0 \tag{6.1}$$

Where S_0 is a constant salinity (35‰) and p_0 a constant reference density (Gordon *et al.*, 2000).

The isotope budget is conserved following a similar method; $H_2^{18}O$ and $H_2^{16}O$ in precipitation, evaporation and run-off lead to isotope and water fluxes into the ocean respectively (Tindall *et al.*, 2009). These are converted into a virtual isotope flux, similar to the virtual salinity flux, which modifies the $H_2^{18}O/H_2^{16}O$ ratio of the ocean top level by an amount accord with the isotope and water fluxes from the land surface and atmosphere (Tindall *et al.*, 2009). As for the case of salinity, the lack of iceberg calving in HadCM3 also leads to a small isotope flux being needed to characterise the reintroduction of $H_2^{18}O$ into the ocean, with a prescribed value of $\delta^{18}O$ equal to -30‰ relative to the flux of water. This is a "sensible estimate" of $\delta^{18}O$ for high latitude sea ice (Tindall *et al.*, 2009).

6.2.2 Experimental Setup

HadCM3 is used to explore the climate response to different Greenland iceberg discharge scenarios. We perform LIG snapshot simulations, all driven with appropriate GHG values and orbital forcing for 125 ka and compared to a 600-year long PI simulation centred at 1850-years before present (hereafter, PI-Cnt). The LIG simulations are driven by greenhouse-gas and orbital forcing centred at 125ka (Eccentricity - 0.04001; Obliquity - °23.80; Perihelion - 201.3 day of yr; CO_2 - 276 ppmv; CH_4 - 640 ppbv; N_2O - 263 ppbv). For the PI simulations, the boundary conditions are: Eccentricity - 0.0167; Obliquity - °23.45; Perihelion - 1.7 day of yr; CO_2 - 280 ppmv; CH_4 - 760 ppbv; N_2O - 270 ppbv. All simulations are run with a present-day GIS distribution (IceBridge BedMachine Greenland, Version 3 – Morlighem *et al.* (017a,b).

Each of the 200-year long LIG sensitivity simulations are continued from a 125 ka control simulation run for over 600 model years (hereafter, 125-Cnt).

To generate the idealised changes in the discharge of icebergs from Greenland, we modify the Greenland iceberg freshwater flux (W in Eq. 6.1) by between -80% and +80% in 10% intervals between latitudes 85-40°N and longitudes 80°W–0°E. The isotope fluxes are also rescaled using the same percentages and over the same region. A total of 14 simulations had been conducted each forced by a different iceberg calving flux, ranging from 0.003 to 0.024 Sv (1 Sv = 10^6 m^3/s) (see Table 6.1).

We investigate the $\delta^{18}O$ response to both increases and decreases in the Greenland iceberg freshwater flux of between ±20% and ±80% relative to the PI control (see Table 6.1). It is sensible to assume that the Greenland iceberg discharge rate would not have remained constant through time (Otto-Bliesner *et al.*, 2006; Bakker *et al.*, 2012; Irvali *et al.*, 2012; Nicholl *et al.*, 2012), and could have been larger at the beginning and mid LIG than during late LIG.

6.3 Results

We present results from 14 Greenland iceberg discharge scenarios here; In each case the last 100 years of the simulations are used to determine climatological averages. A two-sided Student's t-test is utilised to estimate the statistical significance of changes von Storch and Zwiers (2001). For this section, for clarity, we mainly focus on the two scenarios which depict the highest Greenland iceberg freshwater fluxes (FWinc80 and FWred80; Table. 6.1).

6.3.1 Model performance

We start the results section by reviewing the model total accumulation (Precipitation minus Evaporation) output over Greenland. The Program for Arctic Regional Climate Assessment (PARCA) dataset provides an estimate of total accumulation (P-E) over Greenland of 300 mm/yr for the period 1950-2000 (Bales *et al.*, 2009).

Kiilsholm *et al.* (2003) simulate total accumulation values of 421 mm/yr using the coupled ocean atmosphere GCM ECHAM4/OPYC model for a present-day scenario. In addition, Sjolte *et al.* (2011) using the global model ECHAM4 fitted with stable water isotopes, simulate a mean accumulation of 336 mm/yr for Greenland for the period 1971-1990. At 302 mm/yr, our PI HadCM3 simulation has a similar total accumulation (P-E) over Greenland to that indicated by previous modelling studies and published estimates.

6.3.2 Climate response to variations in Greenland iceberg discharge

The simulations with modified iceberg fluxes from the GIS display a clear impact on the surface climate over the North Atlantic area.

The increase in Greenland iceberg input into the North Atlantic results in cooling over most of the North Atlantic area and a significant warming north of $\sim 70°$N, especially over the Barents Seas (Fig. 6.1 e-f). Local increases in SSTs exceed 0.5°C over the Barents Sea in FWinc80 compared to 125-Cnt (Fig. 6.1 f). Similar patterns but in opposition direction are found when reducing Greenland iceberg fluxes; Cooling conditions north of $\sim 70°$N, especially over the Greenland–Iceland–Norwegian (GIN) Sea (local decreases in SSTs exceed 1.5°C in FWred80), and widespread warming over Europe relative to 125-Cnt (Fig. 6.1 c-d).

In addition, the prescribed freshwater fluxes lead to distinctive sea surface salinity anomalies. In FWinc80, we find an overall freshening over most of the North Atlantic induced by the increased Greenland iceberg discharge, while salinity increases in the Barents Seas (local increases exceed +0.5 psu) relative to 125-Cnt (Fig. 6.2 e-f). In contrast, in FWred80 scenario, salinity generally increases south of Iceland and decreases over the GIN and Barents Seas (local decreases exceed -1 psu) compared to 125-Cnt (Fig. 6.2 c-d).

Increases in freshwater forcing into the North Atlantic result in decreases in sea ice concentration over the Nordic Seas and increases over the Labrador Sea. In FWinc80

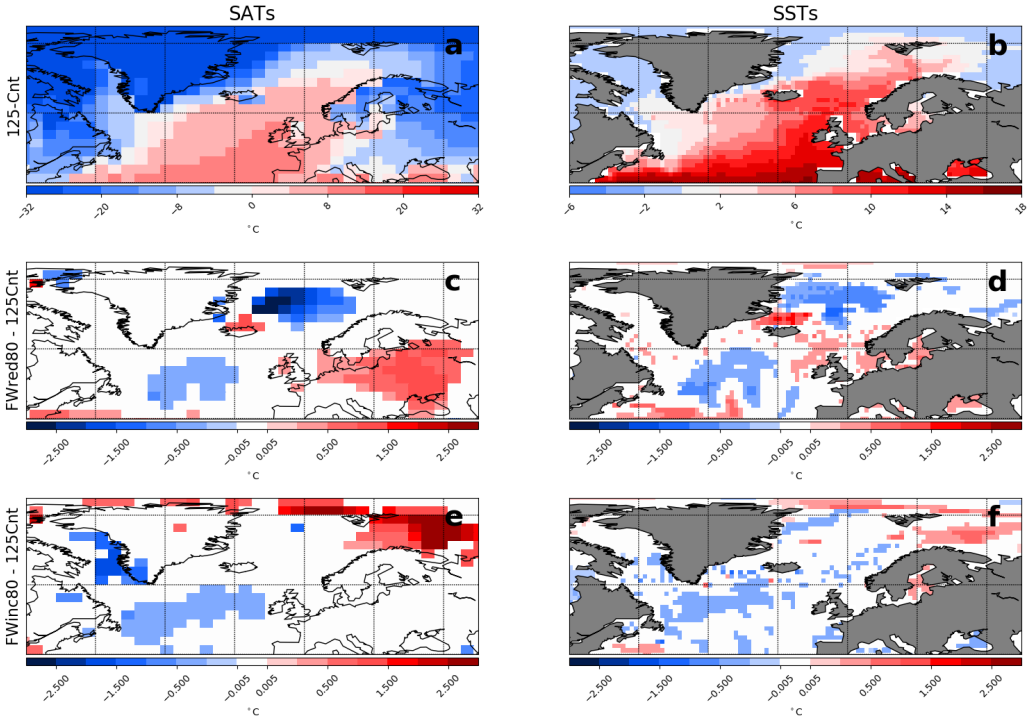

FIGURE 6.1: Mean climatologies for 125-Cnt (a-b) and anomalies for FWred80 (c-d) and FWinc80 (e-f) relative to 125-Cnt for winter (December-January-February) SATs and SSTs. Only anomalies considered 95% confident are displayed.

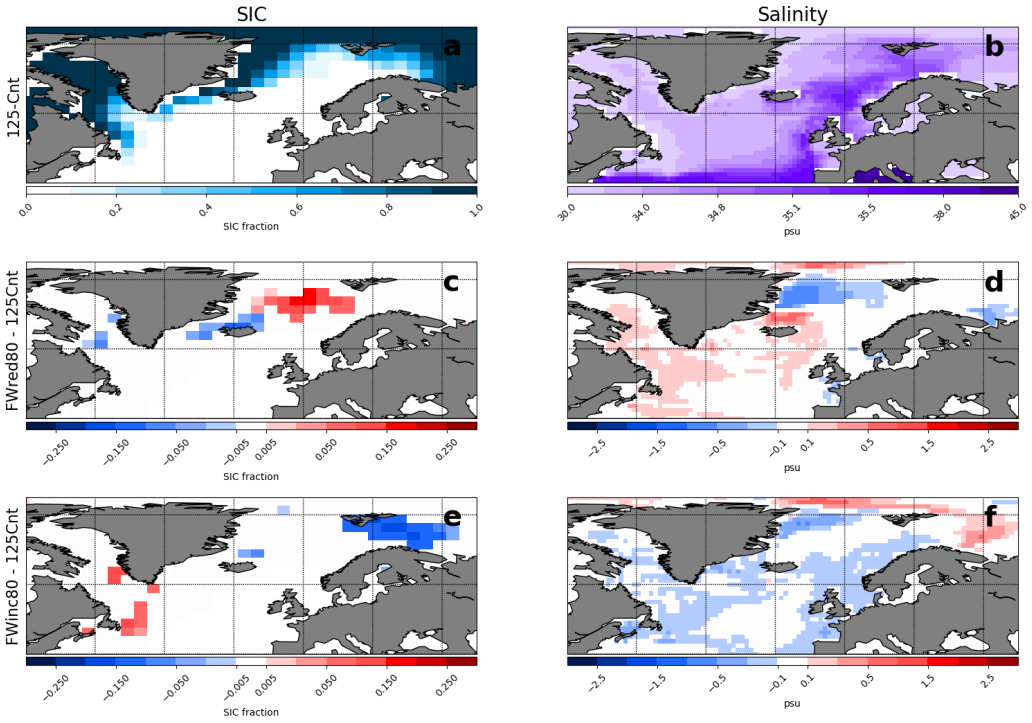

FIGURE 6.2: Mean climatologies for 125-Cnt (a-b) and anomalies for FWred80 (c-d) and FWinc80 (e-f) relative to 125-Cnt for March sea ice concentration (SIC) and annual salinity. Only anomalies considered 95% confident are displayed.

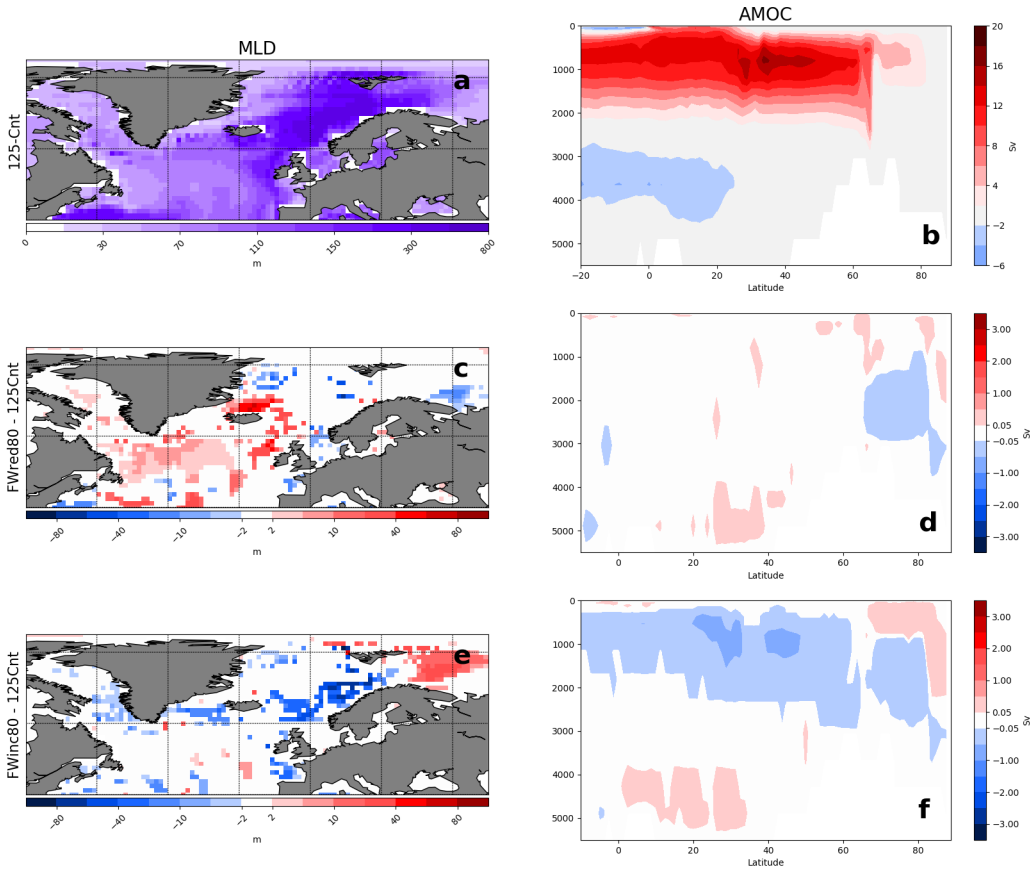

FIGURE 6.3: Mean climatologies for 125-Cnt (a-b) and anomalies for FWred80 (c-d) and FWinc80 (e-f) relative to 125-Cnt for DJF Mixed Layer Depth (MLD) and AMOC. Only anomalies considered 95% confident are displayed.

local increases (decreases) exceed 15% (5%) over the Nordic Seas and Labrador Sea respectively (Fig. 6.2 e-f). Similar changes are found in FWred80 but in opposite direction (Fig. 6.2 c-d). Sea ice changes in the Labrador Sea are decoupled from the sea ice changes in the Nordic Seas. There is an anticorrelation between the response of the high-latitude North Atlantic climate and the climate response south of Iceland.

Convection depth, shown in Fig. 6.3 by the mixed layer depth, increases over the Barents Sea (local increases exceed 20 m) and decreases over the Labrador and Irminger Seas (local decreases exceed 20 m) in FWred80 compared to 125-Cnt (Fig 6.3 c-d). FWinc80 shows similar patterns but it opposite direction (Fig. 6.3 e-f). Such an anticorrelated behaviour between the main convection sites was also found by Bakker *et al.* (2012), Kleinen *et al.* (2009) and Stouffer *et al.* (2006).

6.3.3 Overturning circulation

Fig 6.4 shows the differences in Atlantic Meridional Overturning Circulation (AMOC), here defined as the maximum annual strength of the overturning stream function over the North Atlantic (between latitudes 30-50°N and between depth of 500-2000 m), for each sensitivity experiment compared to the 125-Cnt.

In our 125-Cnt experiment, deep convection occurs in both the Nordic and Labrador Seas, and the modelled AMOC strength of 16.6 sverdrup (Sv) is similar to the PI strength of 16.2 Sv (in agreement with observations; Cunningham *et al.* (2007)). The increase (decrease) in Greenland freshwater forcing injected into the North Atlantic leads to a maximum decrease (increase) of the AMOC strength of up to -4% (+3%) relative to 125-Cnt (Fig. 6.4). There seem to be a tendency: increases in Greenland iceberg fluxes act to decrease AMOC strength and vice versa (Fig. 6.4). Having said that, changes in the AMOC strength are relatively small, (ranging between -0.6 Sv to +0.5 Sv compared to 125 ka), which could be considered within the AMOC model internal variability (Armstrong *et al.*, 2019; Jackson and Vellinga, 2012; Roberts *et al.*, 2014), and only half of the sensitivity simulations show significance changes (at the 95% confidence level) relative to the 125-Cnt (Fig. 6.3d,f and 6.4).

Previous LIG modelling studies showed a rather strong decrease in the AMOC strength because of freshwater input inserted into the North Atlantic (Ritz *et al.*, 2011; Loutre *et al.*, 2014; Goelzer *et al.*, 2016). Govin *et al.* (2012) investigated the GIS melting (injecting a freshwater flux of 0.17 Sv in the North Atlantic) and its impact on North Atlantic Deep Water (NADW) formation and surface temperatures at 126ka and showed decreased SSTs over the North Atlantic together with a $\sim$ 38% reduction of the AMOC strength. Similar work by Otto-Bliesner *et al.* (2006) showed that melting of the GIS (freshwater flux of 0.1 Sv) led to cooling around the Labrador Sea and a 25% slowdown of the AMOC. Using an ensemble of LIG sensitivity experiments, Bakker *et al.* (2012) showed that GIS meltwater fluxes, ranging between 0.052 and 0.13 Sv, led to reduced AMOC strength (a 39% reduction for a freshwater forcing of 0.052 Sv), and decreases in both temperatures and deep convection over the Labrador Seas and North Atlantic.

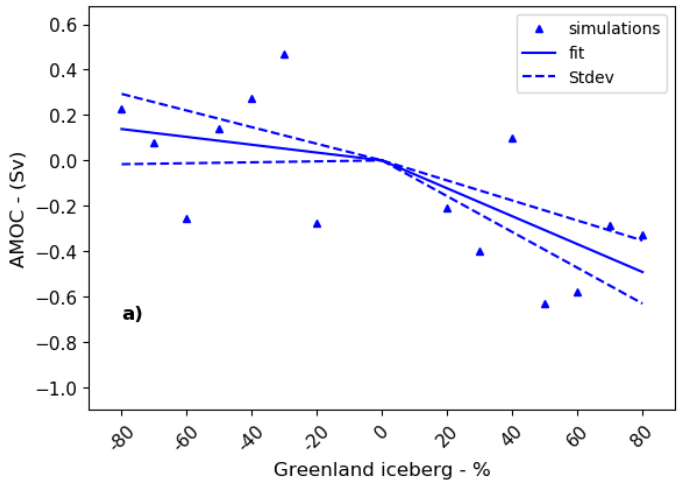

FIGURE 6.4: Change in the maximum AMOC strength (Sv) as a function of Greenland iceberg flux changes (Sv). Changes are calculated as anomalies compared to 125-Cnt. Results for each of the 14 sensitivity simulations are represented by blue triangles. Solid lines signify best fit curves (y = bx). Also shown ± 1 Stdev (lines with dashes) on the best fit lines.

The changes of up to ± 3-4% in the AMOC strength found in HadCM3 in response to changes in Greenland iceberg fluxes are significantly lower than those found in the above-mentioned studies. This is not surprising and is closely related to the much lower freshwater fluxes (ranging between 0.003 to 0.024 Sv; Table. 6.1) used in this study compare to previous ones. Note, our freshwater fluxes represent exclusively changes in the iceberg calving process and do not include the effects of other freshwater sources such as the GIS meltwater runoff.

6.3.4 Constraints on LIG Greenland iceberg fluxes

In HadCM3, snow accumulation over Greenland is assumed to be balanced by the loss through a time-invariant iceberg calving flux which is tuned with regard to a present-day ice sheet distribution (Gordon *et al.*, 2000). An ensemble of 32 simulations with different LIG GIS morphologies, previously examined in Chapter 5 (Fig. 5.8 and Table 5.1; Malmierca-Vallet *et al.* (2020)), show different surface elevations, and consequently different cumulative mass balances over Greenland compared to the PI simulation performed with a present-day ice sheet distribution (Fig. 6.5). In particular, Greenland net snow accumulation values are reduced by 38% up to 58% in the 32 LIG GIS configurations compared to PI (Fig. 6.5).

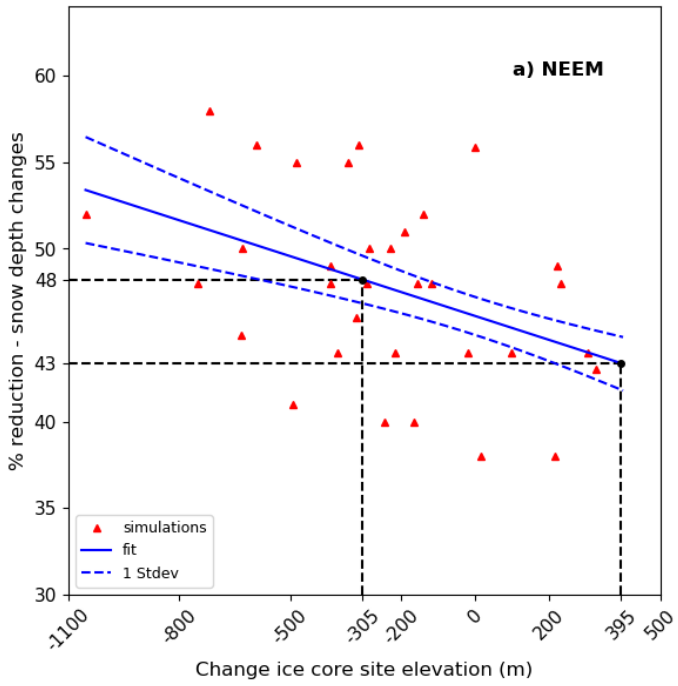

FIGURE 6.5: Percentage reduction (%) in cumulative mass balance over the whole Greenland area as a function of NEEM ice core site elevation change (m) relative to PI. Triangles represent results for the 32 simulations with different LIG GIS shapes previously examined in Chapter 5 (Malmierca-Vallet *et al.*, 2020). Solid lines signify best fit curves (y = a + bx) and dash lines represent ±1s uncertainty on the best fit lines. Note: To estimate cumulative mass balance over Greenland, we calculate snow depth changes over 10 year non-overlapping periods during the course of each run. That is snow depth at the end of 10 years minus snow depth at the beginning of the 10 years. We then average the last 3 estimates (last 30 years of each run) to give a most definitive estimate for each run. In the model the net snow accumulation can be seen somehow as a result of doing the surface mass balance (SMB) at the scale of the GCM grid box. Note, these numbers are not used in this paper as a true SMB values because we know that true snow melt happens in a much narrow region associated with the elevation and this is not well represented at the HadCM3 grid.

Considering the NEEM elevation reconstruction, which indicates NEEM elevation differences of +45±350 at 126 ka relative to present-day (NEEM community members, 2013), we find a most likely reduction in snow accumulation values of 43% - 48% (Fig. 6.5) over Greenland for our LIG HadCM3 simulations relative to PI. Thus, according to the NEEM elevation reconstruction, we find that Greenland iceberg discharge fluxes of between 0.007 and 0.008 Sv (experiments FWred40 and FWred50, Table. 6.1) represent the most likely LIG scenario according to the NEEM elevation reconstruction.

6.3.5 Model-Data comparisons

6.3.5.1 $\delta^{18}O$ changes over Greenland

Fig. 6.6 shows the results of the 125 ka simulations compared with the Domingo *et al.* (2020) compilation of LIG stable water isotopic information ($\delta^{18}O$) from Greenland deep ice cores. Compared to the PI, we find a weak isotopic response to 125-ka greenhouse gas and orbital forcing alone. Averaging across the six ice core locations (NEEM, NGRIP, GISP2, GRIP, DYE3 and Camp Century), we find a $\delta^{18}O$ anomaly of +0.7‰. This does not compare well with the observed Greenland ice core isotope peak of +3.3‰ (Domingo *et al.*, 2020).

Our most likely scenarios according to the NEEM elevation reconstruction, FWred40 and FWred50, show lower Root Mean Square Error (RMSE) values for $\delta^{18}O$p (RMSE= 2.4‰ and 2.6‰ respectively), compared to the 125-Cnt (RMSE=2.8‰) (Fig. 6.6). Thus, FWred40 and FWred50 display a $\delta^{18}O$ model-data discrepancy improvement compared to the 125-Cnt; the variations represent reductions in model-data disagreement of 9-12%.

There seems to be a tendency, decreases in Greenland iceberg calving fluxes act to increase $\delta^{18}O$ across Greenland (Fig. 6.7). The effect of increases in Greenland iceberg fluxes seems to vary between ice core locations. While at NEEM and DYE3, $\delta^{18}O$ appears to decrease with increased iceberg discharge, the opposite behaviour seem to act at the rest of the ice core sites (Fig. 6.7). Having said that, changes in $\delta^{18}O$ are rather small, ranging between 0.1‰ to 0.5‰ in most cases (with only one simulation showing $\delta^{18}O$ changes of up to 0.8‰) (Fig. 6.7). This is within the model uncertainty of annual mean $\delta^{18}O$p (Malmierca-Vallet *et al.*, 2018). Therefore it is complicated to draw firm conclusions.

6.3.5.2 Sea surface temperatures changes

Modelled annual NH SSTs are compared with the time slice centred at 125 ka of Hoffman *et al.* (2017). The match between LIG simulations and annual SST data is

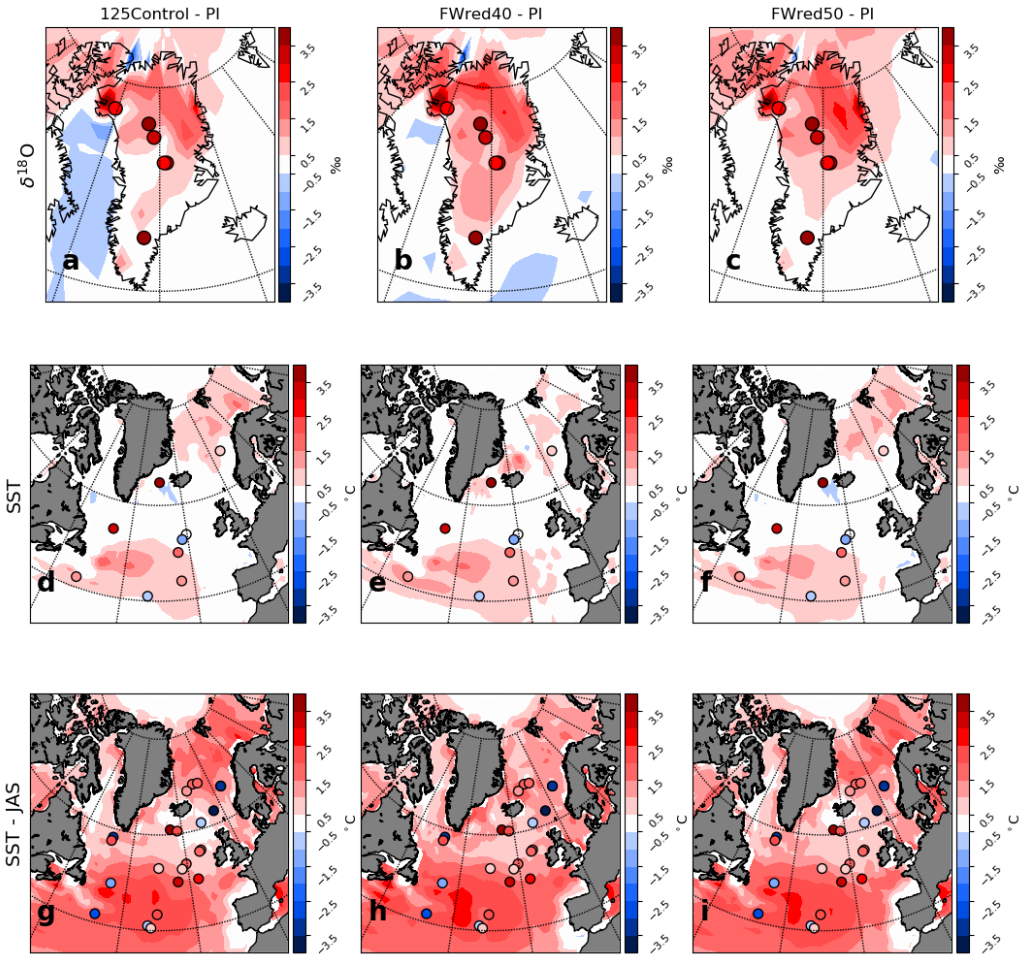

FIGURE 6.6: Modelled annual $\delta^{18}O$ (first row), annual SSTs (second row) and summer (JAS) SSTs (third row) anomalies compared to PI for: 125-Cnt (first column), FWred40 (second column) and FWred50 (third column). Model results are compared to: (a-c) the Domingo *et al.* (2020) compilation of LIG stable water isotopic information ($\delta^{18}O$), (d-f) the 125 ka data-based time slice provided by Hoffman *et al.* (2017), and (g-i) the 125 ka data-based time slice provided by Capron *et al.* (2014).

reasonable, considering the reported $\pm 2\sigma$ uncertainty estimates for individual records (see Hoffman *et al.* (2017)). We find comparable values of RMSE for annual SSTs for the 125-Cnt (RMSE=1.9°C) and sensitivity experiments FWred40 (RMSE=1.8°C) and FWred50 (RMSE=1.9°C) in spite of the freshwater forcing (Fig 6.6g-i).

In addition, Fig. 6.6 displays results of the 125 ka simulations relative to the time slice centred at 125 ka of Capron *et al.* (2014). For coherence with the SST data from Capron *et al.* (2014), modelled summer SST anomalies are classified as July-August-September (JAS). The agreement between the 125-Cnt simulation and JAS SST data is reasonable, taking into consideration the reported uncertainties on SST

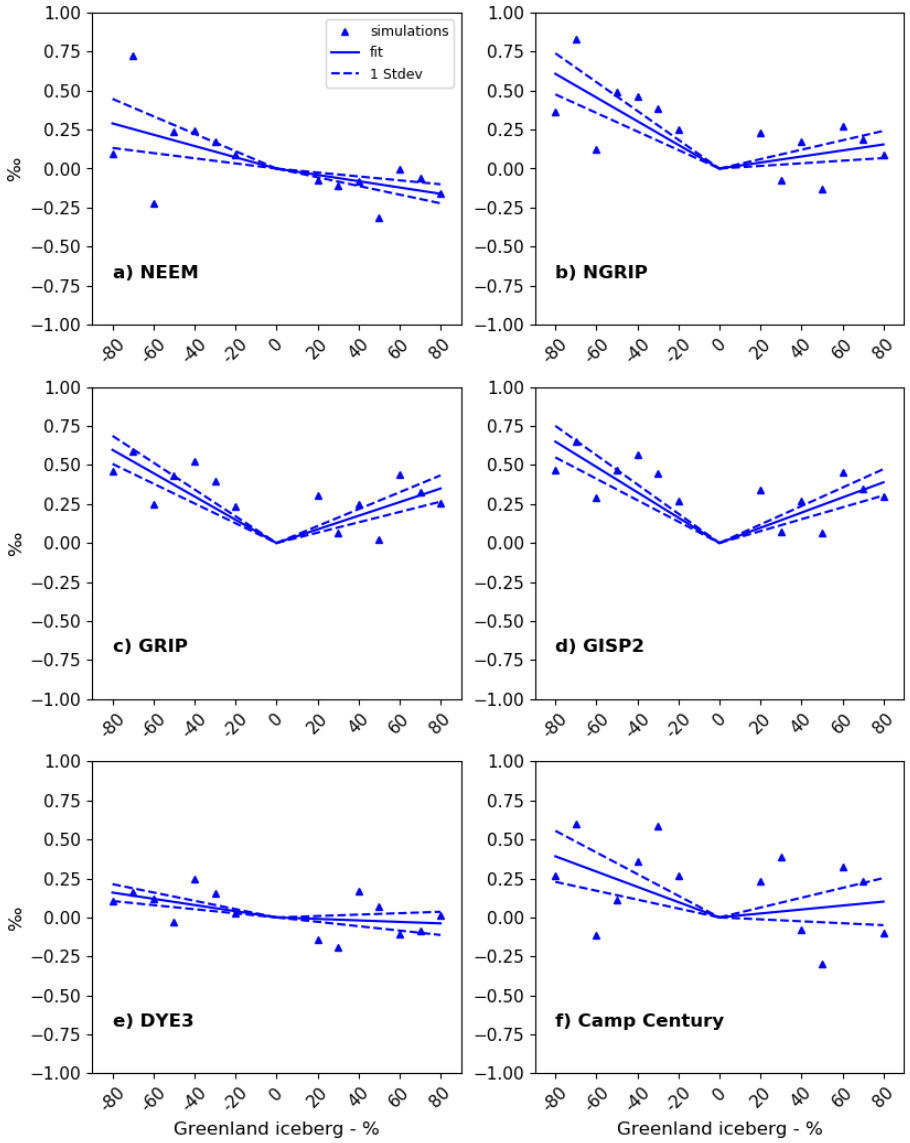

FIGURE 6.7: Change in $\delta^{18}Op$ as a function of Greenland iceberg flux changes (Sv). Changes are calculated as anomalies compared to 125-Cnt. Ice core sites displayed: (a) NEEM, (b) NGRIP, (c) GRIP, (d) GISP2, (e) DYE3 and, (f) Camp Century. Results for each of the 14 sensitivity simulations are represented by blue triangles. Solid lines signify best fit curves (y = bx). Also shown ±1 Stdev (lines with dashes) on the best fit lines.

estimates (on average ±2.6°C; Capron *et al.* (2014, 2017)) (Fig. 6.6, RMSE=3.0°C). Comparable values of RMSE for NH SSTs are obtained for the sensitivity simulations FWred40 (RMSE=3.0°C) and FWred50 (RMSE=3.1°C) regardless of the freshwater forcing (Fig. 6.6j-l).

6.4 Discussion

6.4.0.1 $\delta^{18}O$ response to variations in Greenland iceberg discharge

The HadCM3 response to increases in Greenland iceberg discharge fluxes is an overall cooling south of Iceland, while SSTs and SATs in the high-latitude North Atlantic increase (Fig. 6.1 e-f). In addition, the climate response consists of increases in MLD over those regions where warming is largest, and a rise in salinity, in spite of the overall freshening over the North Atlantic driven by the increased freshwater fluxes (Fig. 6.3 e and 6.2 f). This leads to sea ice decreases over the Nordic Seas and increases over the Labrador Sea (Fig. 6.2 e). Reductions in the Greenland iceberg calving fluxes in HadCM3 results in similar climatic patterns, but in opposite direction (Fig. 6.1 and 6.2 and 6.3).

The climatic patterns explained above match with the classical North Atlantic climate response simulated in freshwater forcing experiments by coupled models (e.g., Stouffer *et al.*, 2006; Bakker *et al.*, 2012; Kleinen *et al.*, 2009).

6.4.0.2 Estimating LIG Greenland iceberg discharge rates

At the start of the LIG (about 129 ka), a strong AMOC is recorded; nevertheless, there is significant proxy evidence of a slowdown at around 127-126 ka, with a number of studies suggesting concurrent iceberg discharge rates (Nicholl *et al.*, 2012; Irvali *et al.*, 2012). Rapid centennial-scale decreases in deep water formation in the North Atlantic have been recorded, suggesting periods of enhanced ice rafting and the expansion of polar waters southwards throughout the LIG (Galaasen *et al.*, 2014).

Here, we use the NEEM elevation reconstruction (+45±350 m at 126 ka) to constrain 32 LIG simulations performed with different GIS morphologies (Malmierca-Vallet *et al.*, 2020), and show most likely LIG Greenland iceberg discharge rates of between 0.007 Sv and 0.008 Sv (experiments FWred40 and FWred50, Table6.1). These are smaller than previously published LIG GIS meltwater rates, ranging from 0.013 to 0.1 Sv (Otto-Bliesner *et al.*, 2006; Bakker *et al.*, 2012; Kopp *et al.*, 2009; Van de Berg *et al.*, 2011).

As a considerable ice sheet melt (as shown in the 32 LIG simulations performed with different GIS shapes in Chapter 5) requires interglacial climate conditions during several millennia, we believe that Greenland iceberg discharge changes similar to the ones shown in our most likely scenarios (FWred40, FWred50; Table. 6.1) may have occurred during later stages of the LIG. Note also that our rates exclusively represent freshwater originated from iceberg discharge and do not include other freshwater sources such as meltwater runoff from the GIS.

In addition, modelled Greenland iceberg discharge rates are strongly model-dependent and in part limited by the setup of initial conditions of our experiments. It is thus essential to compare these results with similar simulations run with other climate models.

Our findings are also strongly dependent on the uncertainties attached to the air content NEEM elevation reconstruction method. The methodology depends on making corrections to air content measurements related to insolation and temperature in conjunction with secular variations in surface pressure and winds (Raynaud *et al.*, 2007; Martinerie *et al.*, 1994; Krinner *et al.*, 2000). In addition, NEEM air content measurements between 127 and 118.3 ka are known to be affected by surface melting (NEEM community members, 2013). This results in a relatively smooth 128-118 ka transition of NEEM's elevation from +201±350 m above present to -130±310m below present (NEEM community members, 2013). The consequence is rather little melting of the GIS but comparatively very strong LIG warming (+8±4°C) remaining after lapse rate corrections carried out by the NEEM community members (2013).

The implementation of our most likely Greenland iceberg discharge rates of between 0.007 Sv and 0.008 Sv in HadCM3, more in accordance with the reduced GIS characteristic of the LIG period (e.g., Robinson *et al.*, 2011; Stone *et al.*, 2013; Dutton *et al.*, 2015), help reduce the $\delta^{18}O$ data-model mismatches. The variations represent increases in the model-data improvement of 9-12%. Previous studies have demonstrated that Arctic sea ice changes and GIS changes need to be accounted for to ensure an optimised model-data solution (Malmierca-Vallet *et al.*, 2018; Merz *et al.*, 2016). Future modelling studies considering in a joint framework, sea ice changes together with GIS changes and appropriate Greenland meltwater rates would be most helpful in understanding remaining model-data mismatches.

6.5 Conclusions

Changing the Greenland iceberg discharge fluxes in HadCM3 has a clear impact on the LIG North Atlantic surface climate, altering SSTs, salinity, MLD and sea ice patterns. We further show that Greenland iceberg discharge rates of between 0.007 Sv and 0.008 Sv best fit the NEEM elevation reconstruction ($+45 \pm 350$ m at 126 ka) in HadCM3, and help increase the LIG Greenland $\delta^{18}O$ data-model improvement by 9-12%.

Our modelled Greenland iceberg discharge rates are smaller than previously published LIG GIS meltwater rates, ranging from 0.013 to 0.1 Sv (Otto-Bliesner *et al.*, 2006; Bakker *et al.*, 2012; Kopp *et al.*, 2009; Van de Berg *et al.*, 2011). Note our rates focus only on the Greenland iceberg calving process and do not account for other freshwater sources such as the meltwater runoff from the GIS. Our findings are strongly model-dependent and in part limited by the uncertainties attached to ice core measurements and air content elevation reconstructions. Inter-model comparison studies may be very helpful in further developing our understating of the importance of the GIS melting during the LIG.

TABLE 6.1: Full list of scenarios. First column shows percentage changes in the Greenland iceberg freshwater flux (W in Eq. 1) for each sensitivity experiment relative to PI. Second column displays Greenland iceberg discharge rates between latitudes 85-40°N and longitudes 80°W–0°E.

Expt ID	% reduction in W	Rates (Sv)	GHGs and orbital parameters
PI-Cnt	-	0.013	PI
125-Cnt	-	0.013	125 ka
FWred80	-80%	0.003	125 ka
FWred70	-70%	0.004	125 ka
FWred60	-60%	0.005	125 ka
FWred50	-50%	0.007	125 ka
FWred40	-40%	0.008	125 ka
FWred30	-30%	0.009	125 ka
FWred20	-20%	0.011	125 ka
FWinc20	+20%	0.016	125 ka
FWinc30	+30%	0.017	125 ka
FWinc40	+40%	0.019	125 ka
FWinc50	+50%	0.020	125 ka
FWinc60	+60%	0.021	125 ka
FWinc70	+70%	0.023	125 ka
FWinc80	+80%	0.024	125 ka

6.6 Supplementary Information

Chapter 7

Conclusions

This final chapter synthesises the main findings and achievements of the thesis regarding the aims outlined in Section 1.4.1. Since each Chapter includes a discussion-conclusions section, only the key results are summarised here. This final Chapter also outlines where further improvements and development can be made for this research project and how this may be achieved.

7.1 Summary of principal findings

7.1.1 Simulating the LIG Greenland stable isotope peak: The role of Arctic sea ice changes

There are seven deep ice cores recovered from Greenland, with stable water isotope records ($\delta^{18}O$ and δD), that likely contain LIG ice: Camp Century, NEEM, NGRIP, GRIP, GISP2, Renland and DYE3. Ice core isotope records yield important information on past climate variations over the last several cycles of glacial-interglacial conditions (e.g., Sime *et al.*, 2009). Ice core $\delta^{18}O$ is affected by changes in site temperature and elevation, alongside changes in evaporation conditions, sea ice and transport pathway effects (Sime *et al.*, 2013; Werner *et al.*, 2018).

Chapter 3 focuses on investigating the isotopic signal of Arctic sea ice variations across Greenland. It is shown, for the first time, that changes in Arctic sea ice conditions can result in significant LIG $\delta^{18}O$ increases over Greenland which are commensurate with observed $\delta^{18}O$ anomalies at Camp Century, NEEM, NGRIP and GISP2 sites. Loss of Arctic sea ice, together with increased SSTs, result in increased evaporation rates across the Arctic Ocean and enhanced $\delta^{18}O$ values over the GIS. This is a consequence of isotopically heavy water vapor and the short distillation path between the Arctic Ocean and the GIS (Sime *et al.*, 2013; Holloway *et al.*, 2016a; Sjolte *et al.*, 2014).

Although records of sea ice for the LIG are sparse and liable to large uncertainties in chronology, evidence form both ice cores and marine sediment cores proposes significantly reduced sea ice extent (Otto-Bliesner *et al.*, 2006; CAPE Last Interglacial Project Members, 2006; Nørgaard-Pedersen *et al.*, 2007). LIG Arctic sea ice loss may have been one of the first elements in the Earth System to have tipped during the LIG, predating other large-scale variations in the Arctic region (Adler *et al.*, 2009; Zöe *et al.*, 2020).

HadCM3 simulations of the response to solely Arctic sea ice loss underestimate the reported $\delta^{18}O$ anomalies at DYE3, GRIP and Renland core sites. The sea ice loss insights provided in Chapter 3 are reliant on the uncertainties associated with both LIG Greenland $\delta^{18}O$ ice core data and modelled $\delta^{18}O$ values (see sections 3.7.2 and 4.3). Since underestimated anomalies may be also related to missing GIS elevation changes, Chapter 4 and 5 examine the $\delta^{18}O$ signal of GIS changes to help in understanding outstanding model-data mismatches.

7.1.2 Using ice cores and GP emulation to recover changes in the GIS during the LIG

Current evidences of LIG peak global mean sea level have agreed on a range of about 6-9 m higher than PI (Kopp *et al.*, 2009; Grant *et al.*, 2014; Dutton *et al.*, 2015). Both the GIS and AIS must have been considerably smaller than at present, but there is considerable debate concerning the exact contribution of each ice sheet to the LIG global mean sea level (Helsen *et al.*, 2013; Stone *et al.*, 2013; Yau *et al.*, 2016).

The shape and extent of the LIG GIS is a matter of controversy, with previous studies proposing a wide range of GIS reconstructions (see Fig. 4.2). Chapter 4, for the first time, combines stable water isotopic information from Greenland deep ice cores with isotope-enabled modelling to study this problem. Investigating the space of possible GIS geometries by simulation is excessively expensive. This problem is tackled using a Gaussian process emulator that is a statistical surrogate of the full HadCM3 climate model.

Chapter 4 highlights the significance of understanding the effect of GIS changes on the LIG Greenland isotopic maximum. If more certain records at Camp Century and DYE3 were available, results from the emulator show that: (1) this would be in agreement with GIS morphologies characterised by lower surface elevation in the south compared to present-day, and (2) data would be compatible with a two-dome structure of the LIG GIS. This is in line with previous studies that point to strong melting in south Greenland (e.g., Otto-Bliesner *et al.*, 2006; Tarasov and Peltier, 2003) or even a two-dome structure with a small ice dome in south Greenland and a large ice dome in north Greenland (e.g., Calov *et al.*, 2015; Langebroek and Nisancioglu, 2016).

7.1.3 Sea-ice feedbacks influence the isotopic signature of GIS elevation changes: LIG HadCM3 simulations

Whereas the LIG global average warming corresponds with projections for the end of the century (Clark and Huybers, 2009; Hoffman *et al.*, 2017), there are considerable uncertainties surrounding the timing of the LIG peak sea level (Kopp *et al.*, 2009; Düsterhus *et al.*, 2016; Barlow *et al.*, 2018) and the magnitude substantially surpasses near future (2100-2200) predictions (e.g., Fischer *et al.*, 2018). The LIG is therefore a pertinent period, when the consequences of variations in the GIS elevation are very relevant for future projections (DeConto and Pollard, 2016). Increasing our knowledge of the isotopic signature of GIS elevation variations may therefore assist in improving the interpretation of LIG Greenland $\delta^{18}O$ data and help constraint the response of the GIS to future sea level and temperature scenarios.

Chapter 5 examines how Greenland $\delta^{18}O$ is affected by GIS elevation changes. An ensemble of idealised LIG GIS surface elevation change scenarios is used to examine how $\delta^{18}O$ is determined by the magnitude and sign of GIS elevation variations and investigate how the response is modified by changes in sea ice. Chapter 5 shows that altering GIS elevation induces changes in the NH atmospheric circulation, precipitation and sea ice patterns. Together these climate feedbacks result in ice core-averaged isotopic lapse rates of 0.29 ‰ per 100 m for the enlarged GIS states and 0.49‰ per 100 m for the lowered GIS states. This is lower than the isotope-elevation relationships obtained from spatial data from northwest and central Greenland which propose that an elevation change of 100 m may provide a 0.72‰ - 0.62‰ variation in $\delta^{18}O$ (Dansgaard, 1973; Johnsen *et al.*, 1989; Poage and Chamberlain, 2001). Thus, one of the main conclusions of Chapter 5 is that there are non-linearities in the isotope-elevation relationship. This has important consequences for the interpretation of past changes in elevation and climate over Greenland.

In addition, Chapter 5 suggests that changes in winter sea ice may considerably influence isotope-elevation slopes. Whereas the largest sea ice influence on $\delta^{18}O$ variations is observed at Camp Century site, DYE3 site displays the smallest. This suggests elevation changes as a possible driver (in combination with orbital and GHG forcing) on LIG $\delta^{18}O$ variations at the DYE3 ice core site. This is in line with the results from Chapter 4 which propose LIG GIS morphologies characterised by lower surface elevation in the south compared to present-day.

7.1.4 The role of Greenland iceberg discharge on the ice $\delta^{18}O$ signal across Greenland: LIG HadCM3 simulations

Chapter 6 studies the role of freshwater from the retreating GIS on the LIG Greenland ice core isotope record. In particular, Chapter 6 focus on the Greenland iceberg calving process to better isolate the impacts of this mechanism on the ice $\delta^{18}O$ signal across Greenland. Changing the Greenland iceberg discharge fluxes in HadCM3 has a clear impact on the LIG North Atlantic surface climate, altering salinity, SSTs, sea ice and MLD and sea ice patterns. These climate feedbacks affect Greenland stable

water isotope; $\delta^{18}O$ tends to increase at a rate of 0.15‰ per 0.01 Sv decrease in the Greenland iceberg fluxes in HadCM3.

Chapter 6 further shows that Greenland iceberg discharge rates of between 0.007 Sv and 0.008 Sv best fit the NEEM elevation reconstruction ($+45 \pm 350$ m at 126 ka; NEEM community members (2013)) in HadCM3, and help increase the LIG Greenland $\delta^{18}O$ data-model improvement by 9-12%.

The HadCM3 rates of 0.007-0.008 Sv are smaller than previously published LIG GIS meltwater rates, ranging from 0.013 to 0.1 Sv (Otto-Bliesner *et al.*, 2006; Bakker *et al.*, 2012; Kopp *et al.*, 2009; Van de Berg *et al.*, 2011). Note that the HadCM3 rates exclusively represent freshwater originated from iceberg discharge and do not include other freshwater sources such as meltwater runoff from the GIS. The results of Chapter 6 are strongly model-dependent and in part limited by the setup of initial conditions of the HadCM3 experiments. It is thus essential to compare these results with similar simulations run with other climate models. The findings of Chapter 6 are also strongly dependent on the uncertainties attached to ice core measurements (e.g., Domingo *et al.*, 2020) and air content elevation reconstructions (Raynaud *et al.*, 2007; Martinerie *et al.*, 1994; Krinner *et al.*, 2000).

7.2 Future work

An important contribution of the thesis concentrates on explaining the LIG $\delta^{18}O$ maximum, at around 125 ka. Chapters 3 to 6 further the existing literature and demonstrate that Arctic sea ice changes together with GIS changes, and associated appropriate Greenland meltwater rates need to be accounted for to ensure an optimised model-data solution. The next steps are to: obtain additional (DYE3 and Camp Century) data; consider sea ice and ice changes in a joint framework following a Gaussian Process emulation approach; take also account of isostatic change. This may permit a valuable quantitative assessment of how changes in the GIS affected LIG global sea levels.

In addition, the results of this thesis are relevant for the interpretation of past climates from Greenland ice core records. Changing the GIS elevation in HadCM3 modifies the NH atmospheric circulation, sea ice and precipitation patterns over the GIS and further afield. This results in lower isotopic-elevation slopes for enlarged GIS states, and vice versa. These results thus suggest non-linearity $\delta^{18}O$-elevation slopes over Greenland and further show that isotopic lapse rate values may be significantly influenced by winter sea ice changes. Inter-model comparison studies would be useful in further improving our understanding of the isotope-elevation relationship over Greenland and how it varies with the background climate state.

A direction for further development lays on the proxy model themselves. It appears sensible to ask whether better LIG model-data agreement could be obtained using higher resolution models. More complex models with higher resolution would permit a better representation of the topography and consequently, a more realistic representation especially during periods characterised by smaller ice sheets.

Isotope-enabled climate models are the best tool available to asses past climate records. Nevertheless, the "state of the art" climate models with isotope diagnostics lag behind climate models with no isotope diagnostics. The initial cost of incorporating isotope physics into the models' architecture is exacerbated by the higher computational time cost due to the added complexity. In the wider climate and weather modelling community in the UK, the HadGEM model family has replaced HadCM3. Yet, after two decades HadCM3 is still a useful tool for paleoclimate and water isotope modelling.

The incorporation of isotope diagnostics in more complex climate models would permit the isotope modelling community to take advantage of the benefits of higher complexity and resolution. Nevertheless, it is not surprising the lack of consistency between the paleoclimate and climate model development. The "state of the art" climate models with their near real time running cost, are not practical tools for paleoclimate studies which require running simulations for many hundreds of years to obtain an equilibrium with considerably different boundary conditions. Nevertheless, there are many other applications for water isotopes in advancing our knowledge of today's climate system. Recent developments in satellite observation have made

available widespread observational constraints on large scale isotope budgets, cloud vapor isotopic composition and isotopic transport pathways (e.g., Risi *et al.*, 2012; Worden *et al.*, 2007). Thus, the incorporation of isotope diagnostics into the most advanced climate models could improve our knowledge of those processes which are at present most limiting within the climate modelling community, like cloud-related processes (e.g., Worden *et al.*, 2007).

Bibliography

Adler, R. E., Polyak, L., Ortiz, J. D., Kaufman, D. S., Channell, J. E. T., Xuan, C., Grottoli, A. G., Selln, E., and Crawford, K. A. (2009). Sediment record from the western Arctic Ocean with an improved Late Quaternary age resolution: HOTRAX core HLY0503-8JPC, Mendeleev Ridge. *Global and Planetary Change*, **68**, 18–29.

Alley, R. B., Andrews, J. T., Brigham-Grette, J., Clarke, G. K. C., Cuffey, K. M., Fitzpatrick, J. J., Funder, S., Marshall, S. J., Miller, G. H., Mitrovica, J. X., Muhs, D. R., Otto-Bliesner, B. L., Polyak, L., and White, J. W. C. (2010). History of the Greenland Ice Sheet: paleoclimatic insights. *Quaternary Science Reviews*, **29**, 1728–1756.

Andrianakis, I. and Challenor, P. G. (2012). The effect of the nugget on Gaussian process emulators of computer models. *Computational Statistics and Data Analysis*, **56**(12), 4215–4228.

Armstrong, E., Valdes, P., House, J., and Singarayer, J. (2019). Investigating the feedbacks between CO_2, vegetation and the AMOC in a coupled climate model. *Climate Dynamics*, **53**, 2485–2500.

Bakker, P., Van Meerbeeck, C. J., and Renssen, H. (2012). Sensitivity of the North Atlantic climate to Greenland Ice Sheet melting during the Last Interglacial. *Clim. Past*, **8**, 995–1009.

Bales, R. C., Guo, Q., Shen, D., McConnell, J. R., Du, G., Burkhart, J. F., Spikes, V. B., Hanna, E., and Cappelen, J. (2009). Annual accumulation for Greenland updated using ice core data developed during 2000–2006 and analysis of daily coastal meteorological data. *J. of Geophys. Res.*, **114**.

Bamber, J., van den Broeke, M., Ettema, J., Lenaerts, J., and Rignot, E. (2012). Recent large increases in freshwater fluxes from Greenland in the North Atlantic. *Geophys. Res. Lett.*, **39**.

Barlow, N. L. M., McClymont, E. L., Whitehouse, P. L., Stokes, C. R., Jamieson, S. S. R., Woodroffe, S. A., Bentley, M. J., Callard, S. L., Cofaigh, C. Ó., Evans, D. J. A., Horrocks, J. R., Lloyd, J. M., Long, A. J., Margold, M., Roberts, D. H., and Sanchez-Montes, M. L. (2018). Lack of evidence for a substantial sea-level fluctuation within the last interglacial. *Nature Geoscience*, **11**, 627–634.

Bastos, L. S. and O'Hagan, A. (2009). Diagnostics for Gaussian process emulators. *Technometrics*, **51**(4), 425–438.

Bauch, H. A. and Erlenkeuser, H. (2008). A "critical" climatic evaluation of last interglacial (MIS 5e) records from the Norwegian Sea. *Polar Res.*, **27**, 135–151.

Bauch, H. A., Kandiano, E. S., and Helmke, J. P. (2012). Contrasting ocean changes between the subpolar and polar North Atlantic during the past 135 ka. *Geophys. Res. Lett.*, **39**.

Bazin, L., Landais, A., Lemieux-Dudon, B., Toyé Mahamadou Kele, H., Veres, D., Parrenin, F., Martinerie, P., Ritz, C., Capron, E., Lipenkov, V., Loutre, M. F., Raynaud, D., Vinther, B., Svensson, A., Rasmussen, S. O., Severi, M., Blunier, T., Leuenberger, M., Fischer, H., Masson-Delmotte, V., Chappellaz, J., and Wolff, E. W. (2013). An optimized multi-proxy, multi-site Antarctic ice and gas orbital chronology (AICC2012): 120–800 ka. *Clim. Past*, **9**, 1715–1731.

Berger, A. and Loutre, M. F. (1991). Insolation values for the climate of the last 10 million years. *Quaternary Science Reviews*, **10**, 297–317.

Berger, J. O., de Oliveira, V., and Sansó, B. (2001). Objective Bayesian analysis of spatially correlated data. *Journal of the American Statistical Association*, **96**(456), 1361–1374.

Bigg, G. R., Wei, H. L., Wilton, D. J., Zhao, Y., Billings, S. A., Hanna, E., and Kadirkamanathan, V. (2014). A century of variation in the dependence of Greenland iceberg calving on ice sheet surface mass balance and regional climate change. *Proc. R. Soc. A*, **470**.

Blisniuk, P. M. and Stern, L. A. (2005). Stable isotope paleoaltimetry: A critical review. *American Journal of Science*, **305**, 1033–1074.

Böhm, E., Lippold, J., Gutjahr, M., Frank, M., Blaser, P., Antz, B., Fohlmeister, J., Frank, N., Andersen, M. B., and Deininger, M. (2015). Strong and deep Atlantic meridional overturning circulation during the last glacial cycle. *Nature*, **517**, 73–76.

Born, A. and Nisancioglu, K. H. (2012). Melting of Northern Greenland during the last interglaciation. *The Cryosphere*, **6**, 1239–1250.

Box, J. and Sharp, M. (2017). Changes to Arctic land ice. In: Snow, Water, Ice and Permafrost in the Arctic (SWIPA). Technical report, Arctic Monitoring and Assessment Programme (AMAP).

Braconnot, P., Otto-Bliesner, B., Harrison, S., Joussaume, S., Peterchmitt, J. Y., Abe-Ouchi, A., Crucifix, M., Driesschaert, E., Fichefet, T., Hewitt, C. D., Kageyama, M., Kitoh, A., Laîné, A., Loutre, M. F., Marti, O., Merkel, U., Ramstein, G., Valdes, P., Weber, S. L., Yu, Y., and Zhao, Y. (2007). Results of PMIP2 coupled simulations of the Mid-Holocene and Last Glacial Maximum – part 1: experiments and large-scale features. *Clim. Past*, **3**, 261–277.

Braconnot, P., Harrison, S. P., Kageyama, M., Bartlein, P. J., Masson-delmotte, V., Abe-ouchi, A., Otto-Bliesner, B., and Zhao, Y. (2012). Evaluation of climate models using palaeoclimatic data. *Nature Climate Change*, **2**, 417–424.

Brigham-Grette, J. and Hopkins, D. M. (1995). Emergent marine record and paleoclimate of the last interglaciation along the northwest Alaskan coast. *Quaternary Research*, **43**, 159–173.

Brigham-Grette, J., Hopkins, D. M., Ivanov, V. F., Basilyan, A., Benson, S. L., Heiser, P., and Pushkar, V. (2001). Last interglacial (Isotope stage 5) glacial and

sea level history of coastal Chukotka Peninsula and St. Lawrence Island, western Beringia. *Quaternary Science Reviews*, **20**, 419–439.

Calov, R., Robinson, A., Perrette, M., and Ganopolski, A. (2015). Simulating the Greenland ice sheet under present-day and palaeo constraints including a new discharge parameterization. *The Cryosphere*, **9**, 179–196.

CAPE Last Interglacial Project Members (2006). Last Interglacial Arctic warmth confirms polar amplification of climate change. *Quaternary Science Reviews*, **25**, 1382–1400.

Cappa, C. D., Hendricks, M. B., DePaolo, D. J., and Cohen, R. C. (2003). Isotopic fractionation of water during evaporation. *J. of Geophys. Res.*, **108**.

Capron, E., Govin, A., Stone, E. J., Masson-Delmotte, V., Mulitza, S., Otto-Bliesner, B., Rasmussen, T. L., Sime, L. C., Waelbroeck, C., and Wolff, E. (2014). Temporal and spatial structure of multi-millennial temperature changes at high latitudes during the Last Interglacial. *Quaternary Science Reviews*, **103**, 116–133.

Capron, E., Govin, A., Feng, R., Otto-Bliesner, B. L., and Wolff, E. W. (2017). Critical evaluation of climate syntheses to benchmark CMIP6/PMIP4 127 ka Last Interglacial simulations in the high-latitude regions. *Quaternary Science Reviews*, **168**, 137–150.

Carlson, A. E. (2008). Why there was not a Younger Dryas-like event during the Penultimate Deglaciation. *Quaternary Science Reviews*, **27**, 882–887.

Cattle, H. and Crossley, J. (1995). Modeling Arctic Climate-Change. *Philosophical Transactions of the Royal Society of London Series A-Mathematical Physical and Engineering Sciences*, **352**, 201–213.

Clark, I. and Fritz, P. (1997). *Environmental Isotopes in Hydrogeology*. Taylor and Francis. 312 pp.

Clark, P. U. and Huybers, P. (2009). Interglacial and future sea level. *Nature*, **462**, 856–857.

Colville, E. J., Carlson, A. E., Beard, B. L., Hatfield, R. G., Stoner, J. S., Reyes, A. V., and Ullman, D. J. (2011). Sr-Nd-Pb isotope evidence for ice-sheet presence on southern Greenland during the last interglacial. *Science*, **333**, 620–623.

Cooper, C. and Gordon, C. (2002). North Atlantic Oceanic Decadal Variability in the Hadley Centre Coupled Model. *J. Climate*, **15**, 45–72.

Cox, M. D. (1984). A primitive equation, three dimensional model of the ocean. Technical report, Issue 1 of GFDL Ocean Group technical report.

Cox, P. M. (2001). Description of the TRIFFID dynamic global vegetation model. Technical report, Met Office Hadley Centre, Exeter, UK.

Cox, P. M., Huntingford, C., and Harding, R. J. (1998). A canopy conductance and photosynthesis model for use in a GCM land surface scheme. *Journal of Hydrology*, **212–213**, 79–94.

Cox, P. M., Betts, R. A., Bunton, C. B., Essery, R. L. H., Rowntree, P. R., and Smith, J. (1999). The impact of new land surface physics on the GCM simulation of climate and climate sensitivity. *Climate Dynamics*, **15**, 183–203.

Cox, P. M., Betts, R. A., Jones, C. D., Spall, S. A., and Totterdell, I. J. (2000). Acceleration of global warming due to carbon-cycle feedbacks in a coupled climate model. *Nature*, **408**, 184–187.

Craig, P. S., Goldstein, M., Seheult, A. H., and Smith, J. A. (1997). Pressure matching for hydrocarbon reservoirs: A case study in the use of bayes linear strategies for large computer experiments. In *Case Studies in Bayesian Statistics*, pages 37–93, New York, NY. Springer New York.

Cronin, T. M., Gemery, L., Jr., B., M., W., Jakobsson, M., Polyak, L., and Brouwers, E. M. (2010). Quaternary Sea-ice history in the Arctic Ocean based on a new ostracode sea-ice proxy. *Quaternary Science Reviews*, **29**, 3415–3429.

Cuffey, K. M. and Marshall, S. J. (2000). Substantial contribution to sea-level rise during the last interglacial from the Greenland ice sheet. *Nature*, **404**, 591–594.

Cuffey, K. M. and Paterson, W. S. B. (2010). *The physics of glaciers*. Academic Press. 704 pp.

Cunningham, S. A. *et al.* (2007). Temporal variability of the Atlantic Meridional Overturning Circulation at 26.5°N. *Science*, **317**, 935–938.

Dansgaard, W. (1953). The abundance of ^{18}O in atmospheric water and water vapor. *Tellus*, **5**, 461–469.

Dansgaard, W. (1964). Stable isotopes in precipitation. *Tellus*, **16**, 436–468.

Dansgaard, W. (1973). *Stable Isotope Glaciology*. Meddelelser om Grønland. Reitzel, C.A., København.

Dansgaard, W., Johnsen, S. J., Möller, J., and Langway, C. C. (1968). Oxygen isotope analysis of an ice core representing a complete vertical profile of a polar ice sheet.

Dansgaard, W., Johnsen, S. J., Moller, J., and Langway, C. C. (1969). One thousand centuries of climatic record from Camp Century on the Greenland ice sheet. *Science*, **166**, 377–381.

Dansgaard, W., Clausen, H. B., Gundestrup, N., Hammer, C. U., Johnsen, S. J., Kristinsdottir, M., and Reeh, N. (1982). A new Greenland deep ice core. *Science*, **218**, 1273–1277.

Davini, P., von Hardenberg, J., Filippi, L., and Provenzale, A. (2015). Impact of Greenland orography on the Atlantic Meridional Overturning Circulation. *Geophys. Res. Lett.*, **42**, 871–879.

DeConto, R. M. and Pollard, D. (2016). Contribution of Antarctica to past and future sea-level rise. *Nature*, **531**, 591–597.

Dessler, A. E., Zhang, Z., and Yang, P. (2008). Water-vapor climate feedback inferred from climate fluctuations, 2003-2008. *Geophys. Res. Lett.*, **35**.

Domingo, D., Malmierca-Vallet, I., Sime, L. C., Voss, J., and Capron, E. (2020). Using ice cores and gaussian process emulation to recover changes in the Greenland Ice Sheet during the Last Interglacial. *J. of Geophys. Res.: Earth Surface*, **125**.

Dong, B. and Sutton, R. T. (2002). Variability in north atlantic heat content and heat transport in a coupled ocean-atmosphere gcm. *Climate Dynamics*, **19**, 485–497.

Düsterhus, A., Tamisiea, M. E., and Jevrejeva, S. (2016). Estimating the sea level highstand during the last interglacial: a probabilistic massive ensemble approach. *Geophysical Journal International*, **206**, 900–920.

Dutton, A. and Lambeck, K. (2012). Ice Volume and Sea Level During the Last Interglacial. *Science*, **337**, 216–219.

Dutton, A., Carlson, A. E., Long, A. J., Milne, G. A., Clark, P. U., DeConto, R., Horton, B. P., Rahmstorf, S., and Raymo, M. E. (2015). Sea-level rise due to polar ice-sheet mass loss during past warm periods. *Science*, **349**(6244).

Edwards, J. M. and Slingo, A. (1996). Studies with a flexible new radiation code .1. Choosing a configuration for a large-scale model. *Quarterly Journal of the Royal Meteorological Society*, **122**, 689–719.

Eicher, O., Baumgartner, M., Schilt, A., Schmitt, J., Schwander, J., Stocker, T., and Fischer, H. (2016). Climatic and insolation control on the high-resolution total air content in the NGRIP ice core. *Clim. Past*, **12**, 1979–1993.

Enderlin, E. M., Howat, I. M., Jeong, S., Noh, M. J., van Angelen, J., and van den Broeke, M. R. (2014). An improved mass budget for the Greenland Ice Sheet. *Geophys. Res. Lett.*, **41**, 866–872.

EPICA community members (2004). Eight glacial cycles from an Antarctic ice core. *Nature*, **429**, 623–628.

Erokhina, O., Rogozhina, I., Prange, M., Bakker, P., Bernales, J., André, P., and Schulz, M. (2017). Dependence of slope lapse rate over the greenland ice sheet on background climate. *J. of Glaciology*, **63**, 568–572.

Essery, R., Best, M., and Cox, P. (2001). Moses 2.2 Technical Documentation. Hadley Centre technical note 30. Technical report.

Fausto, R. S., Ahlstrøm, A. P., Van As D, Bøggild, C. E., and Johnsen, S. J. (2009). A new present-day temperature parameterization for greenland. *J. of Glaciology*, **55**, 95–105.

Felzer, B., Oglesby, R. J., Webb, T., and Hyman, D. E. (1996). Sensitivity of a general circulation model to changes in northern hemisphere ice sheets. *J. of Geophys. Res.*, **101**, 19077–19092.

Fischer, H., Meissner, K. J., Mix, A. C., Abram, N. J., Austermann, J., Brovkin, V., Capron, E., Colombaroli, D., Daniau, A. L., Dyez, K. A., Felis, T., Finkelstein, S. A., Jaccard, S. L., McClymont, E. L., Rovere, A., Sutter, J., Wolff, E. W., Affolter, S., Bakker, P., Ballesteros-Cánovas, J. A., Barbante, C., Caley, T., Carlson, A. E., Churakova, O., Cortese, G., Cumming, B. F., Davis, B. A., De Vernal, A., Emile-Geay, J., Fritz, S. C., Gierz, P., Gottschalk, J., Holloway, M. D., Joos, F., Kucera, M., Loutre, M. F., Lunt, D. J., Marcisz, K., Marlon, J. R., Martinez, P., Masson-Delmotte, V., Nehrbass-Ahles, C., Otto-Bliesner, B. L., Raible, C. C., Risebrobakken, B., Sánchez Goñi, M. F., Arrigo, J. S., Sarnthein, M., Sjolte, J., Stocker, T. F., Velasquez Alvárez, P. A., Tinner, W., Valdes, P. J., Vogel, H., Wanner, H., Yan, Q., Yu, Z., Ziegler, M., and Zhou, L. (2018). Palaeoclimate constraints on the impact of 2°C anthropogenic warming and beyond. *Nature Geoscience*, **11**, 474–485.

Folland, C. K., Karl, T. R., and Vinnikov, K. Y. (1990). *Observed climate variations and change, in: Climate Change: The IPCC Scientific Assessment*, pages 195–238. Cambridge University Press, New York, NY, USA.

Fricker, T. E., Oakley, J. E., and Urban, N. M. (2012). Multivariate Gaussian process emulators with nonseparable covariance structures. *Technometrics*, **55**, 47–56.

Fyke, J. G., Weaver, A. J., Pollard, D., Eby, M., Carter, L., and Mackintosh, A. (2011). A new coupled ice sheet/climate model: description and sensitivity to model physics under Eemian, Last Glacial Maximum, late Holocene and modern climate conditions. *Geoscientific Model Development*, **4**, 117–136.

Galaasen, E. V. *et al.* (2014). Rapid reductions in north atlantic deep water during the peak of the last interglaical period. *Science*, **343**, 1129–1132.

Gardner, A. S., Sharp, M. J., Koerner, R. M., Labine, C., Boon, S., Marshall, S. J., Burgess, D. O., and Lewis, D. (2009). Near-Surface Temperature Lapse Rates over Arctic Glaciers and Their Implications for Temperature Downscaling. *J. Climate*, **22**, 4281–4298.

Gierz, P., Werner, M., and Lohmann, G. (2017). Simulating climate and stable water isotopes during the Last Interglacial using a coupled climate-isotope model. *Journal of Advances in Modeling Earth Systems*, **9**, 2027–2045.

Goelzer, H., Huybrechts, P., Loutre, M. F., and Fichefet, T. (2016). Impact of ice sheet meltwater fluxes on the climate evolution at the onset of the Last Interglacial. *Clim. Past*, **12**, 1721–1737.

Gonantine, R. *et al.* (2001). The altitude effect on the isotopic composition of tropical rains. *Chemical Geology*, **181**, 147–167.

Gordon, C., Cooper, C., Senior, C. A., Banks, H., Gregory, J. M., Johns, T. C., Mitchell, J. F. B., and Wood, R. A. (2000). The simulation of SST, sea ice extents and ocean heat transports in a version of the Hadley Centre coupled model without flux adjustments. *Climate Dynamics*, **16**, 147–168.

Govin, A., Braconnot, P., Capron, E., Cortijo, E., Duplessy, J. C., Jansen, E., Labeyrie, L., Landais, A., Marti, O., Michel, E., Mosquet, E., Risebrobakken, B., Swingedouw, D., and Waelbroeck, C. (2012). Persistent influence of ice sheet melting on high northern latitude climate during the early Last Interglacial. *Clim. Past*, **8**, 483–507.

Govin, A., Capron, E., Tzedakis, P. C., Verheyden, S., Ghaleb, B., Hillaire-Marcel, C., St-Onge, G., Stoner, J. S., Bassinot, F., Bazin, L., Blunier, T., Combourieu-Nebout, N., Ouahabi, A. E., Genty, D., Gersonde, R., Jimenez-Amat, P., Landais, A., Martrat, B., Masson-Delmotte, V., Parrenin, F., Seidenkrantz, M. S., Veres, D., Waelbroeck, C., and Zahn, R. (2015). Sequence of events from the onset to the demise of the last interglacial: Evaluating strengths and limitations of chronologies used in climatic archives. *Quaternary Science Reviews*, **129**, 1 – 36.

Grachev, A. M. and Severinghaus, J. P. (2005). A revised +10±4°C magnitude of the abrupt change in greenland temperature at the younger dryas termination using published GISP2 gas isotope data and air thermal diffusion constants. *Quaternary Science Reviews*, **24**, 513–519.

Grant, K. M., Rohling, E. J., Bar-Matthews, M., Ayalon, A., Medina-Elizalde, M., Ramsey, C. B., Satow, C., and Roberts, A. P. (2012). Rapid coupling between ice volume and polar temperature over the past 150,000 years. *Nature*, **491**, 744–747.

Grant, K. M., Rohling, E. J., Ramsey, C. B., Cheng, H., Edwards, R. L., Florindo, F., Heslop, D., Marra, F., Roberts, A. P., Tamisiea, M. E., and Williams, F. (2014). Sea-level variability over five glacial cycles. *Nature Communications*, **5**.

Gregory, D. and Rowntree, P. R. (1190). A Mass Flux Convection Scheme with Representation of Cloud Ensemble Characteristics and Stability-Dependent Closure. *Monthly Weather Review*, **118**, 1483–1506.

GRIP members (1193). Climate instability during the last interglacial period recorded in the grip ice core. *Nature*, **364**, 203–207.

Grootes, P. M., Stuiver, M., White, J. W. C., Johnsen, S. J., and Jouzel, J. (1993). Comparison of oxygen isotope records from the GISP2 and GRIP Greenland ice cores. *Nature*, **366**, 552–554.

Hall, A. (2014). The role of surface albedo feedback in climate. *J. Climate*, **17**, 1550–1568.

Hansen, J., Sato, M., Hearty, P., Ruedy, R., Kelley, M., Masson-Delmotte, V., Russell, G., Tselioudis, G., Cao, J., Rignot, E., Velicogna, I., Tormey, B., Donovan, B., Kandiano1, E., von Schuckmann, K., Kharecha, P., Legrande, A. N., and Bauer, M. (2016). Ice melt, sea level rise and superstorms: Evidence from paleoclimate data, climate modeling, and modern observations that 2°c global warming could be dangerous. *Atmospheric Chemistry and Physics*, **16**, 3761–3812.

Helsen, M. M., Berg, W. J. v. d., Wal, R. S. W. v. d., Broeke, M. R. v. d., and Oerlemans, J. (2013). Coupled regional climate-ice-sheet simulation shows limited Greenland ice loss during the Eemian. *Clim. Past*, **9**, 1773–1788.

Hoffman, G., Jouzel, J., and Masson, V. (2000). Stable water isotopes in atmospheric general circulation models. *Hydrological Processes*, **14**, 1385–1406.

Hoffman, J. S., Clark, P. U., Parnell, A. C., and He, F. (2017). Regional and global sea-surface temperatures during the last interglaciation. *Science*, **355**, 276–279.

Hoffmann, G., Werner, M., and Heimann, M. (1998). The water isotope module of the ECHAM atmospheric general circulation model – a study on time scales from days to several years. *J. of Geophys. Res.*, **103**, 16871–16896.

Holloway, M. D., Sime, L. C., Singarayer, J. S., Tindall, J. C., Bunch, P., and Valdes, P. J. (2016a). Antarctic last interglacial isotope peak in response to sea ice retreat not ice sheet collapse. *Nature Communications*, **7**.

Holloway, M. D., Sime, L. C., Singarayer, J. S., Tindall, J. C., and Valdes, P. J. (2016b). Reconstructing paleosalinity from $\delta^{18}O$: Coupled model simulations of the Last Glacial Maximum, Last Interglacial and Late Holocene. *Quaternary Science Reviews*, **131**, 350–364.

Holloway, M. D., Sime, L. C., Allen, C. S., Hillenbr, C., Bunch, P., Wolff, E., and Valdes, P. J. (2017). The spatial structure of the 128 ka Antarctic sea ice minimum. *Geophys. Res. Lett.*, **44**, 11129–11139.

IPCC (2001). *Climate Change 2001: The physical science basis. Contribution of Working Group I to the Third Assessment Report of the Intergovernmental Panel on Climate Change. 881 pp*. Cambridge University Press, Cambridge, United Kingdom and New York, NY, USA.

IPCC (2007). *Climate Change 2007: The physical science basis. Contribution of Working Group I to the fourth assessment report of the Intergovernmental Panel on Climate Change. 996 pp*. Cambridge University Press, Cambridge, United Kingdom and New York, NY, USA.

IPCC (2013). *Climate Change 2013: The Physical Science Basis. Contribution of Working Group I to the Fifth Assessment Report of the Intergovernmental Panel on Climate Change. 1535 pp*. Cambridge University Press, Cambridge, United Kingdom and New York, NY, USA.

Irvali, N., Ninnemann, U. S., Galaasen, E. V., Rosenthal, Y., Kroon, D., Oppo, D. W., Kleiven, H. F., Darling, K. F., and Kissel, C. (2012). Rapid switches in subpolar North Atlantic hydrography and climate during the Last Interglacial (MIS 5e). *Paleoceanography and Paleoclimatology*, **27**, 1–16.

Jackson, L. and Vellinga, M. (2012). Multidecadal to Centennial Variability of the amoc: Hadcm3 and a Perturbed Physics Ensemble. *J. Climate*, **26**, 2390–2407.

Johnsen, S. and Vinther, B. (2007). Ice core records — Greenland stable isotopes. In S. A. Elias, editor, *Encyclopedia of Quaternary Science*, pages 1250–1258. Elsevier, Oxford.

Johnsen, S. J., Dansgaard, D., and White, J. W. C. (1989). The origin of Arctic precipitation under present and glacial conditions. *Tellus*, **41**, 452–469.

Johnsen, S. J., Dahl-Jensen, D., Gundestrup, N., Steffensen, J. P., Clausen, H. B., Miller, H., Masson-Delmotte, V., Sveinbjörnsdottir, A. E., and White, J. (2001). Oxygen isotope and palaeotemperature records from six greenland ice-core stations: Camp century, dye-3, grip, gisp2, renland and northgrip. *Journal of Quaternary Science*, **16**(4), 299–307.

Jolliffe, I. T. (2002). *Principal Component Analysis*. Springer Series in Statistics. Springer, second edition.

Jones, C. P. (1995). Unified Model Documentation Paper no 70. Specification of Ancillary fields. version 4. Technical report.

Jouzel, J., Koster, R. D., Suozzo, R. J., and Russell, G. L. (1994). Stable water isotope behaviour during the last glacial maximum: a general circulation model analysis. *J. Geophys. Res.*, **99**, 25791–25801.

Jouzel, J., Alley, R. B., Cuffey, K. M., Dansgaard, W., Grootes, P., Hoffmann, G., Johnsen, S. J., Koster, R. D., Peel, D., Shuman, C., Stievenard, M., Stuiver, M., and White, J. (1997). Validity of the temperature reconstruction from water isotopes in ice cores. *J. Geophys. Res.*, **102**, 26471–26487.

Jouzel, J., Masson-Delmotte1, V., Cattani, O., Dreyfus, G., Falourd, S., Hoffmann, G., Minster, B., Nouet, J., Barnola, J. M., Chappellaz, J., Fischer, H., Gallet, J. C., Johnsen, S., Leuenberger, M., Loulergue, L., Luethi, D., Oerter, H., F., P., Raisbeck, G., Raynaud, D., Schilt, A., Schwander, J., Selmo, E., Souchez, R., Spahni, R., Stauffer, B., Steffensen, J. P., Stenni, B., Stocker, T. F., Tison, J. L., Werner, M., and Wolff, E. W. (2007). Orbital and millennial Antarctic climate variability over the past 800,000 years. *Science*, **317**, 793–796.

Kennedy, M. C. and O'Hagan, A. (2001). Bayesian calibration of computer models. *Journal of the Royal Statistical Society, B*, **63**, 425–464.

Kiilsholm, S. J., Dethloff, C. K., and Rinke, A. (2003). Net accumulation of the greenland ice sheet: High resolution modeling of climate changes. *Geophys. Res. Lett.*, **30**.

Kleinen, T., Osborn, T. J., and Briffa, K. R. (2009). Sensitivity of climate response to variations in freshwater hosing location. *Ocean Dynamics*, **59**, 509–521.

Kleppin, H., Jochum, M., Otto-Bliesner, B., Shields, C. A., and Yeager, S. (2015). Stochastic atmospheric forcing as a cause of Greenland climate transitions. *J. Clim.*, **28**, 7741–7763.

Kocis, L. and Whiten, W. J. (1997). Computational investigations of low-discrepancy sequences. *ACM Transactions on Mathematical Software*, **23**(2), 266–294.

Koerner, R. M. and Fischer, H. (2002). Ice-core evidence for widespread Arctic glacier retreat in the Last Interglacial and the early holocene. *Annals of Glaciology*, **35**, 19–24.

Kopp, R. E., Simons, F. J., Mitrovica, J. X., Maloof, A. C., and Oppenheimer, M. (2009). Probabilistic assessment of sea level during the last interglacial stage. *Nature*, **462**, 863–867.

Krinner, G., Raynaud, D., Doutriaux, C., and Dang, H. (2000). Simulations of the Last Glacial Maximum ice sheet surface climate: Implications for the interpretation of ice core air content. *J.Geophys.Res.Atmos.*, **105**, 2059–2070.

Lachniet, M. S. (2009). Climatic and environmental controls on speleothem oxygen-isotope values. *Quaternary Science Reviews*, **58**, 412–432.

Landais, A., Chappellaz, J., Delmotte, M. Jouzel, J., Blunier, T., Bourg, C., Caillon, N., Cherrier, S., Malaizé, B., Masson-Delmotte, V., Raynaud, D., Schwander, J., and Steffensen, J. P. (2003). A tentative reconstruction of the last interglacial and glacial inception in greenland based on new gas measurements in the Greenland Ice Core Project (GRIP) ice core. *Geophys. Res. Lett.*, **108**(D18).

Landais, A., Steffensen, J. P., Caillon, N., Jouzel, J., MassonDelmotte, V., and Schwander, J. (2004a). Evidence for stratigraphic distortion in the Greenland Ice Core Project (GRIP) ice core during Event 5e1 (120 kyr BP) from gas isotopes. *J. Geophys. Res.*, **109**(D06103).

Landais, A., Caillon, N., Goujon, C., Grachev, A. M., Barnola, J., Chappellaz, J., Jouzel, J., Masson-Delmotte, V., and Leuenberger, M. (2004b). Quanti
cation of rapid temperature change during do event 12 and phasing with methane inferred from air isotopic measurements. *Earth and Planetary Science Letters*, **225**, 221–232.

Landais, A., Masson-Delmotte, V., Capron, E., Langebroek, P. M., Bakker, P., Stone, E. J., Merz, N., Raible, C. C., Fischer, H., Orsi, A., Prié, F., Vinther, B., and Dahl-Jensen, D. (2016). How warm was Greenland during the last interglacial period? *Clim. Past.*, **12**, 1933–1948.

Langebroek, P. M. and Nisancioglu, K. H. (2014). Simulating last interglacial climate with NorESM: role of insolation and greenhouse gases in the timing of peak warmth. *Clim. Past*, **10**, 1305–1318.

Langebroek, P. M. and Nisancioglu, K. H. (2016). Moderate Greenland ice sheet melt during the last interglacial constrained by present-day observations and paleo ice core reconstructions. *The Cryosphere Discussions*.

Laskar, J., Robutel, P., Joutel, F., Gastineau, M., Correia, A. C. M., and Levrard, B. (2004). A long-term numerical solution for the insolation quantities of the earth. *Earth Astronomy and Astrophysics*, pages 261–285.

Lhomme, N., Clarke, G. K. C., and Marshall, S. J. (2005). Tracer transport in the Greenland ice sheet: constraints on ice cores and glacial history. *Quaternary Science Reviews*, **24**, 173–194.

Liu, X. and Battisti, D. S. (2015). The influence of orbital forcing of tropical insolation on the climate and isotopic composition of precipitation in South America. *J. Clim.*, **28**, 4841–4862.

Lototskaya, A. and Ganssen, G. M. (1999). The structure of Termination II (penultimate deglaciation and Eemian) in the North Atlantic. *Quaternary Science Reviews*, pages 1641–1654.

Loutre, M. F., Fichefet, T., Goosse, H., Huybrechts, P., Goelzer, H., and Capron, E. (2014). Factors controlling the last interglacial climate as simulated by LOVECLIM1.3. *Clim. Past*, pages 1541–1565.

Lunt, D. J., de Noblet-Ducoudré, N., and Charbit, S. (2004). Effects of a melted greenland ice sheet on climate, vegetation, and the cryosphere. *Climate Dynamics*, **23**, 679–694.

Lunt, D. J., Abe-Ouchi, A., Bakker, P., Berger, A., Braconnot, P., Charbit, S., Fischer, N., Herold, N., Jungclaus, J. H., Khon, V. C., Krebs-Kanzow, U., Langebroek, P. M., Lohmann, G., Nisancioglu, K. H., Otto-Bliesner, B. L., Park, W., Pfeiffer, M., Phipps, S. J., Prange, M., Rachmayani, R., Renssen, H., Rosenbloom, N., Schneider, B., Stone, E. J., Takahashi, K., Wei, W., Yin, Q., and Zhang, Z. S. (2013). A multi-model assessment of last interglacial temperatures. *Clim. Past*, **9**, 699–717.

Lüthi, D., Le Floch, M., Bereiter, B., Blunier, T., Barnola, J. M., Siegenthaler, U., Raynaud, D., Jouzel, J., Fischer, H., Kawamura, K., and Stocker, T. F. (2008). High-resolution carbon dioxide concentration record 650,000-800,000 years before present. *Nature*, **435**, 379–382.

MacGregor, J. A., Fahnestock, M. A., Catania, G. A., Paden, J. D., Gogineni, S. P., Young, S. K., Rybarski, S. C., Mabrey, A. N., Wagman, B. M., and Morlighem,

M. (2015). Radiostratigraphy and age structure of the Greenland Ice Sheet. *J. of Geophys. Res.*, **120**(2), 212–241.

Malmierca-Vallet, I., Sime, L. C., Tindall, J., Valdes, P. J., Capron, E., Vinther, B. M., and Holloway, M. D. (2018). Simulating the Last Interglacial Greenland stable water isotope peak: The role of Arctic sea ice changes. *Quaternary Science Reviews*, **198**, 1–14.

Malmierca-Vallet, I., Sime, L. C., Tindall, J., and Valdes, P. J. (2020). Sea-ice feedbacks influence the isotopic signature of Greenland Ice Sheet elevation changes: Last Interglacial HadCM3 simulations. *Clim. Past. In review.*

Marshall, S. J., Sharp, M. J., Burgess, D. O., and Anslow, F. S. (2007). Nearsurface-temperature lapse rates on the prince of wales icefield, ellesmere island, canada: implications for regional downscaling of temperature. *Int. J. Climatol.*, **27**, 385–398.

Martinerie, P., Lipenkov, V., Raynaud, D., Chappellaz, J., Barkov, N., and Lorius, C. (1994). Air content paleo record in the Vostok ice core (Antarctica): A mixed record of climatic and glaciological parameters. *Geophys.Res.*, **99**, 565–576.

Masson-Delmotte, V. *et al.* (2008). A Review of Antarctic Surface Snow Isotopic Composition: Observations, Atmospheric Circulation, and Isotopic Modeling. *J. Climate*, **21**, 3359–3387.

Masson-Delmotte, V. *et al.* (2015). Recent changes in north-west Greenland climate documented by NEEM shallow ice core data and simulations, and implications for past-temperature reconstructions. *The Cryosphere*, **9**, 1481–1504.

Masson-Delmotte, V., Jouzel, J., Landais, A., Stievenard, M., Johnsen, S. J., White, J. W. C., Werner, M., Sveinbjornsdottir, A., and Fuhrer, K. (2005). Grip deuterium excess reveals rapid and orbital-scale changes in Greenland moisture origin. *Science*, **309**, 118–121.

Masson-Delmotte, V., Stenni, B., Blunier, T., Cattani, O., Chappellaz, J., Cheng, H., Dreyfus, G., Edwards, R. L., Falourd, S., Govin, A., Kawamura, K., Johnsen,

S. J., Jouzel, J., Landais, A., Lemieux-Dudon, B., Lourantou, A., Marshall, G., Minster, B., Mudelsee, M., Pol, K., Rothlisberger, R., Selmo, E., and Waelbroeck, C. (2010). Abrupt change of Antarctic moisture origin at the end of Termination II. *PNAS*, **107**, 12091–12094.

Masson-Delmotte, V., Braconnot, P., Hoffmann, G., Jouzel, J., Kageyama, M., L, A., Lejeune, a. Q., Risi, C., Sime, L. C., Sjolte, J., Swingedouw, D., and Vinther, B. M. (2011). Sensitivity of interglacial Greenland temperature and $\delta^{18}o$: ice core data, orbital and increased co_2 climate simulations. *Clim. Past*, **7**, 1041–1059.

McKay, N. P., Overpeck, J. T., and Otto-Bliesner, B. L. (2011). The role of ocean thermal expansion in Last Interglacial sea level rise. *Geophys. Res. Lett.*, **38**.

Meier, W., Fetterer, F., Savoie, M., Mallory, S., Duerr, R., and Stroeve, J. (2017). NOAA/NSIDC climate Data Record of Passive Microwave Sea Ice Concentration, Version 3. Goddard Merged Sea Ice Record from 1979 to 1989.

Merlivat, L. and Jouzel, J. (1979). Global Climate Interpretation of the Deuterium-Oxygen 18 Relationship for Precipitation. *J. of Geophys. Res.*, **84**, 5029–5033.

Merz, N., Born, A., Raible, C. C., Fischer, H., and Stocker, T. F. (2014a). Dependence of Eemian Greenland temperature reconstructions on the ice sheet topography. *Clim. Past*, **10**, 1221–1238.

Merz, N., Gfeller, G., Born, A., Raible, C. C., Stocker, T. F., and Fischer, H. (2014b). Influence of ice sheet topography on Greenland precipitation during the Eemian interglacial. *J. Geophys. Res.*, **119**, 10749–10768.

Merz, N., Born, A., Raible, C. C., and Stocker, T. F. (2016). Warm Greenland during the last interglacial: the role of regional changes in sea ice cover. *Clim. Past*, **12**, 2011–2031.

Monnin, E., Indermuhle, A., Dallenbach, A., Fluckiger, J., Stauffer, B., Stocker, T. F., Raynaud, D., and M, B. J. (2001). Atmospheric CO_2 concentrations over the last glacial termination. *Science*, **291**, 112–114.

Montgomery, D. C. (2017). *Design and Analysis of Experiments*. John Wiley & Sons, Inc., USA, ninth edition.

Morlighem, M. *et al.* (2017a). IceBridge BedMachine Greenland, Version 3. [Ice surface elevation and mask]. Boulder, Colorado USA. NASA National Snow and Ice Data Center Distributed Active Archive Center.

Morlighem, M., Williams, C., Rignot, E., An, L., Arndt, J. E., Bamber, J., Catania, G., Chauché, N., Dowdeswell, J. A., Dorschel, B., Fenty, I., Hogan, K., Howat, I., Hubbard, A., Jakobsson, M., Jordan, T. M., Kjeldsen, K. K., Millan, R., Mayer, L., Mouginot, J., Noël, B., O'Cofaigh, C., Palmer, S. J., Rysgaard, S., Seroussi, H., Siegert, M. J., Slabon, P., Straneo, F., Broeke, M. R. v. d., Weinrebe, W., Wood, M., and Zinglersen, K. (2017b). BedMachine v3: Complete bed topography and ocean bathymetry mapping of Greenland from multi-beam echo sounding combined with mass conservation. *Geophys. Res. Lett.*, **44**.

NEEM community members (2013). Eemian interglacial reconstructed from a Greenland folded ice core. *Nature*, **493**, 489–494.

NGRIP Project Members (2004). High-resolution record of northern hemisphere climate extending into the last interglacial period. *Nature*, **431**, 147–151.

Nicholl, J. A. L., Hodell, D. A., Naafs, B. D. A., Hillaire-Marcel, C., Channell, J. E. T., and Romero, O. E. (2012). A Laurentide outburst flooding event during the last interglacial period. *Nature Geoscience*, **5**, 901–904.

Noone, D. and Simmonds, I. (1998). Implications for the interpretation of ice-core isotope data from analysis of modelled Antarctic precipitation. *Annals of Glaciology*, **27**, 398–402.

Nørgaard-Pedersen, N., Mikkelsen, N., Lassen, S. J., Kristoffersena, Y., and Sheldon, E. (2007). Reduced sea ice concentrations in the Arctic Ocean during the last interglacial period revealed by sediment cores off northern Greenland. *Paleoceanography*, **22**(1), PA1218.

O'Hagan, A. (1978). Curve fitting and optimal design for prediction. *Journal of the Royal Statistical Society, B*, **40**(1), 1–42.

O'Hagan, A. (1992). Some Bayesian numerical analysis. In J. M. Bernardo, J. O. Berger, A. c. P. Dawid, and A. F. M. Smith, editors, *Bayesian Statistics 4*, pages 345–363. Proceedings of the Fourth Valencia International Meeting.

Oppo, D. W., Horowitz, M., and Lehman, S. J. (1997). Marine core evidence for reduced deep water production during Termination II followed by a relatively stable substage 5e (Eemian). *Paleoceanography*, **12**, 51–63.

Otto-Bliesner, B., Rosenbloom, N., Stone, E., McKay, N. P., Lunt, D. J., Brady, E. C., and Overpeck, J. T. (2013). How warm was the Last Interglacial? New model-data comparisons. *Philos. Trans. R. Soc. A*, **371**.

Otto-Bliesner, B. L., Marsha, S. J., Overpeck, J. T., Miller, G. H., Hu, A. X., and CAPE Last Interglacial Project members (2006). Simulating Arctic climate warmth and icefield retreat in the last interglaciation. *Science*, **311**(5768), 1751–1753.

Pardaens, A. K., Banks, H. T., Gregory, J. M., and Rowntree, P. R. (2003). Freshwater transports in HadCM3. *Climate Dynamics*, **21**, 177–195.

Past Interglacials Working Group of PAGES (2016). Interglacials of the last 800,000 years. *Rev. Geophys.*, **54**, 162–219.

Pausata, F. S. R., Li, C., Wettstein, J., Kageyama, M., and Nisancioglu, K. (2011). The key role of topography in altering North Atlantic atmospheric circulation during the last glacial period. *Clim. Past*, **7**, 1089–1101.

Pedersen, R. A., Langen, P. L., and Vinther, B. M. (2016a). Greenland during the last interglacial: the relative importance of insolation and oceanic changes. *Clim. Past*, **12**, 1907–1918.

Pedersen, R. A., Langen, P. L., and Vinther, B. M. (2016b). The last interglacial climate: comparing direct and indirect impacts of insolation changes. *Climate Dynamics*, **48**, 3391–3407.

Peltier, W. R. and Vettoretti, G. (2014). Dansgaard-Oeschger oscillations predicted in a comprehensive model of glacial climate: A "kicked" salt oscillator in the Atlantic. *Geophys. Res. Lett.*, **41**, 7306–7313.

Peng, G., Meier, W. N., Scott, D. J., and Savoie, M. H. (2013). A long-term and reproducible passive microwave sea ice concentration data record for climate studies and monitoring. *Earth Syst. Sci.*, pages 311–318.

Plach, A., Nisancioglu, K. H., Langebroek, P. M., Born, A., and Le clec'h, S. (2019). Eemian greenland ice sheet simulated with a higher-order model shows strong sensitivity to surface mass balance forcing. *The Cryosphere*, **13**(8), 2133–2019.

Poage, M. A. and Chamberlain, C. P. (2001). Empirical relationships between elevation and the stable isotope composition of precipitation and surface waters: Considerations for studies of paleoelevation change. *American Journal of Science*, **301**(1), 1–15.

Pope, V. D., Gallani, M. L., Rowntree, P. R., and Stratton, R. A. (2000). The impact of new physical parametrizations in the hadley centre climate model: Hadam3. *Climate Dynamics*, **16**, 123–146.

Pukelsheim, F. (1994). The three sigma rule. *The American Statistician*, **48**(2), 88–91.

Quiquet, A., Ritz, C., Punge, H. J., and Melia, D. S. y. (2013). Greenland ice sheet contribution to sea level rise during the last interglacial period: a modelling study driven and constrained by ice core data. *Clim. Past*, **9**, 353–366.

Rasmussen, C. E. and Williams, C. K. I. (2006). Covariance Functions. In *Gaussian Processes for Machine Learning.*, Adaptive computation and machine learning. MIT Press.

Raynaud, D., Chappellaz, J., Ritz, C., and Martinerie, P. (1977). Air content along the Greenland Ice Core Project core: a record of surface climatic parameters and elevation in central greenland. *J. Geophys. Res.*, **102**, 26607–26613.

Raynaud, D., Lipenkov, V., Lemieux-Dudon, B., Duval, P., Loutre, M. F., and Lhomme, N. (2007). The local insolation signature of air content in Antarctic ice. a new step toward an absolute dating of ice records. *Earth Planet. Sci. Lett.*, **261**, 337–349.

Rehfeld, K., Münch, T., Ho, S., and Laepple, T. (2018). Global patterns of declining temperature variability from the last glacial maximum to the Holocene. *Nature*, **554**, 356–359.

Risi, C. *et al.* (2012). Process-evaluation of tropospheric humidity simulated by general circulation models using water vapor isotopologues: 1. comparison between models and observations. *J. of Geophys. Res.*, **117**, 1–26.

Ritz, S. P., Stocker, T. F., and Joos, F. (2011). A Coupled Dynamical Ocean Energy Balance Atmosphere Model for Paleoclimate Studies. *J. Clim.*, **24**, 349–375.

Roberts, C. D., Jackson, L., and McNeall, D. (2014). Is the 2004–2012 reduction of the Atlantic meridional overturning circulation significant? *Geophys. Res. Lett.*, **41**, 3204–3210.

Robinson, A., Calov, R., and Ganopolski, A. (2011). Greenland ice sheet model parameters constrained using simulations of the Eemian interglacial. *Clim. Past*, **7**, 381–396.

Rowley, D. B. and Garzione, C. N. (2007). Stable Isotope-Based Paleoaltimetry. *Annual Review of Earth and Planetary Sciences*, **35**, 463–508.

Rozanski, K. *et al.* (1993). Isotopic Patterns in Modern Global Precipitation. *Geophysical Monograph Series*, **78**.

Sacks, J., Welch, W. J., Mitchell, T. J., and Wynn, H. P. (1989). Design and analysis of computer experiments. *Statistical Science*, **4**(4), 409–435.

Salter, J. M., Williamson, D. B., Scinocca, J., and Kharin, V. (2019). Uncertainty Quantification for Computer Models With Spatial Output Using Calibration-Optimal Bases. *Journal of the American Statistical Association*, **114**, 1800–1814.

Schmidt, G. A., LeGrande, A. N., and Hoffmann, G. (2007). Water isotope expressions of intrinsic and forced variability in a coupled ocean-atmosphere model. *J. Geophys. Res.*, **112**.

Schmidt, G. A., Annan, J. D., Bartlein, P. J., Cook, B. I., Guilyardi, E., Hargreaves, J. C., Harrison, S. P., Kageyama, M., LeGrande, A. N., Konecky, B., Lovejoy,

S., Mann, M. E., Masson-Delmotte, V., Risi, C., Thompson, D., Timmermann, A., Tremblay, L. B., and Yiou, P. (2014). Using palaeo-climate comparisons to constrain future projections in CMIP5. *Clim. Past*, **10**, 221–250.

Semtner, A. J. (1976). A Model for Thermodynamic Growth of Sea Ice in Numerical Investigations of Climate. *Journal of Physical Oceanography*, **6**, 379–389.

Sime, L. C., Stevens, D. P., Heywood, K. J., and Oliver, K. I. C. (2006). A decomposition of the Atlantic Meridional Overturning. *Journal of Physical Oceanography*, **36**, 2253–2270.

Sime, L. C., Tindall, J. C., Wolff, E. W., Connolley, W. M., and Valdes, P. J. (2008). Antarctic isotopic thermometer during a CO_2 forced warming event. *Journal of Physical Oceanography*, **113**, 2253–2270.

Sime, L. C., Wolff, E. W., Oliver, K. I. C., and Tindall, J. C. (2009). Evidence for warmer interglacials in East Antarctic ice cores. *Nature*, **462**, 342–346.

Sime, L. C., Risi, C., Tindall, J. C., Sjolte, J., Wolff, E. W., Masson-Delmotte, V., and Capron, E. (2013). Warm climate isotopic simulations: what do we learn about interglacial signals in Greenland ice cores? *Quaternary Science Reviews*, **67**, 59–80.

Sime, L. C., Hopcroft, P. O., and Rhodes, R. H. (2019). Impact of abrupt sea ice loss on Greenland water isotopes during the last glacial period. *Proceedings of the National Academy of Sciences*, **116**(10), 4099–4104.

Singarayer, J. and Valdes, P. J. (2010). High-latitude climate sensitivity to ice-sheet forcing over the last 120 kyr. *Quaternary Science Reviews*, **29**, 43–55.

Sjolte, J., Hofmann, G., Johnsen, S. J., Vinther, B., Masson-Delmotte, V., and Sturm, C. (2011). Modeling the water isotopes in greenland precipitation 1959–2001 with the meso-scale model REMO-iso. *J. Geophys. Res.*, **116**(D18105).

Sjolte, J., Hofmann, G., and Johnsen, S. J. (2014). Modelling the response of stable water isotopes in Greenland precipitation to orbital configurations of the previous interglacial. *Tellus B: Chemical and Physical Meteorology*, **66**(22872).

Smith, S. J., Edmonds, J., Hartin, C. A., Mundra, A., and Calvin, K. (2015). Near-term acceleration in the rate of temperature change. *Nature Climate Change*, **5**, 333–336.

Spielhagen, R. F., Baumann, K., Erlenkeuser, H., Nowaczyk, N. R., Nørgaard-Pedersen, N., Vogt, C., and Weiel, D. (2004). Arctic Ocean deep-sea record of Northern Eurasian ice sheet history. *Quaternary Science Reviews*, **23**, 1455–1483.

Steffensen, J. P., Andersen, K. K., Bigler, M., Clausen, H. B., Dahl-Jensen, D., *et al.* (2008). High-resolution Greenland ice core data show abrupt climate change happens in few years. *Science*, **321**, 680–684.

Steig, E. J., Grootes, P. M., and Stuiver, M. (1994). Seasonal precipitation timing and ice core records. *Science*, **266**, 1885–1886.

Stein, R., Fahl, K., Gierz, P., Niessen, F., and Lohmann, G. (2017). Arctic Ocean sea ice cover during the penultimate glacial and the last interglacial. *Nature communications*, **8**(373).

Stenni, B. *et al.* (2003). A late-glacial high-resolution site and source temperature record derived from the EPICA Dome C isotope records (East Antarctica). *Earth and Planetary Science Letters*, **217**, 183–195.

Stone, E. J. and Lunt, D. J. (2013). The role of vegetation feedbacks on Greenland glaciation. *Climate Dynamics*, **40**, 2671–2686.

Stone, E. J., Lunt, D. J., Annan, J. D., and Hargreaves, J. C. (2013). Quantification of the Greenland ice sheet contribution to Last Interglacial sea level rise. *Clim. Past*, **9**, 621–639.

Stone, E. J., Capron, E., Lunt, D. J., Payne, A., Singarayer, J. S., Valdes, P. J., and Wolff, E. W. (2016). Impact of meltwater on high-latitude early Last Interglacial climate. *Clim. Past*, **12**, 1919–1932.

Stouffer, R. J. *et al.* (2006). Investigating the Causes of the Response of the Thermohaline Circulation to Past and Future Climate Changes. *J. Climate*, **19**, 1365–1387.

Stroeve, J., Holland, M. M., Meier, W., Scambos, T., and Serreze, M. (2007). Arctic sea ice decline: faster than forecast. *Geophys. Res. Lett.*, **34**.

Stroeve, J. C., Kattsov, V., Barrett, A., Serreze, M., Pavlova, T., Holland, M., and Meier, W. N. (2012). Trends in Arctic sea ice extent from CMIP5, CMIP3 and observations. *Geophys. Res. Lett.*, **39**.

Sturm, C., Zhang, Q., and Noone, D. (2010). An introduction to stable water isotopes in climate models: benefits of forward proxy modelling for paleoclimatology. *Clim. Past*, **6**, 115–129.

Sutter, J., Gierz, P., Grosfeld, K., Thoma, M., and Lohmann, G. (2016). Ocean temperature thresholds for Last Interglacial West Antarctic Ice Sheet collapse. *Geophys. Res. Lett.*, **43**, 2675–2682.

Suwa, M. and Bender, M. L. (2008). O2/N2 ratios of occluded air in the gisp2 ice core. *J. of Geophys. Res.: Atmospheres*, **113**(D11).

Suwa, M., von Fischer, J. C., Bender, M. L., Landais, A., and Brook, E. J. (2006a). Chronology reconstruction for the disturbed bottom section of the GISP2 and the GRIP ice cores: Implications for Termination II in Greenland. *J. of Geophys. Res.: Atmospheres*, **111**(D2).

Suwa, M., von Fischer, J. C., Bender, M. L., Landais, A., and Brook, E. J. (2006b). Chronology reconstruction for the disturbed bottom section of the GISP2 and the GRIP ice cores: Implications for Termination II in Greenland. *J. of Geophys. Res.: Atmospheres*, **111**(D2).

Tarasov, L. and Peltier, W. R. (2003). Greenland glacial history, borehole constraints , and Eemian extent. *J. of Geophy. Res.*, **108**(2143).

Tett, S. F. B. *et al.* (2007). The impact of natural and anthropogenic forcings on climate and hydrology since 1550. *Climate Dynamics*, **28**(1), 3–34.

Tindall, J. and Haywood, A. (2015). Modeling Oxygen Isotopes in the Pliocene: Large Scale Features over the Land and Ocean. *Paleoceanography*, **30**, 1183–1201.

Tindall, J., Flecker, R., Valdes, P. J., Schimidt, D. N., Markwick, P., and Harris, J. (2010). Modelling the oxygen isotope distribution of ancient seawater using a coupled ocean-atmosphere GCM: Implications for reconstructing early Eocene climate. *Earth and Planetary Science Letters*, **292**, 265–273.

Tindall, J. C. and Valdes, P. J. (2011). Modeling the 8.2 ka event using a coupled atmosphere-ocean GCM. *Global and Planetary Change*, **79**, 312–321.

Tindall, J. C., Valdes, P. J., and Sime, L. C. (2009). Stable water isotopes in HadCM3: Isotopic signature of El Niño Southern Oscillation and the tropical amount effect. *J. of Geophys. Res.*, **114**(D4), D04111.

Toniazzo, T., Gregory, J., and P., H. (2004). Climatic impact of a Greenland deglaciation and its possible irreversibility. *J. Climate*, **17**, 21–33.

Tracey, B. D. and Wolpert, D. (2018). Upgrading from Gaussian Processes to Student's-T Processes. In *2018 AIAA Non-Deterministic Approaches Conference*, Kissimmee, Florida.

Turney, C. and Jones, R. T. (2010). Does the Agulhas Current amplify global temperatures during super-interglacials? *J. Quat. Sci.*, **25**, 839–843.

Van de Berg, W. J. *et al.* (2011). Significant contribution of insolation to Eemian melting of the Greenland ice sheet. *Nat Geosci*, **4**, 679–683.

van den Broeke, M. R., Enderlin, E., Howat, I., Kuipers Munneke, P., Noël, B., van de Berg, W. J., van Meijgaard, E., and Wouters, B. (2016). On the recent contribution of the Greenland ice sheet to sea level change. *The Cryosphere*, (10), 1933–1946.

Veres, D., Bazin, L., Landais, A., Toyé Mahamadou Kele, H., Lemieux-Dudon, B., Parrenin, F., Martinerie, P., Blayo, E., Blunier, T., Capron, E., Chappellaz, J., Rasmussen, S. O., Severi, M., Svensson, A., Vinther, B., and Wolff, E. W. (2013). The Antarctic ice core chronology (AICC2012): an optimized multi-parameter and multi-site dating approach for the last 120 thousand years. *Clim. Past*, **9**, 1733–1748.

Vernon, I., Goldstein, M., and Bower, R. G. (2010). Galaxy formation: a Bayesian uncertainty analysis. *Bayesian Analysis*, **5**(4), 619–669.

Vinther, B. M., Buchardt, S. L., Clausen, H. B., Dahl-Jensen, D., Johnsen, S. J., Fisher, D. A., Koerner, R. M., Raynaud, D., Lipenkov, V., Andersen, K. K., Blunier, T., Rasmussen, S. O., Steffensen, J. P., and Svensson, A. M. (2009). Holocene thinning of the Greenland ice sheet. *Nature*, **461**, 385–388.

Vinther, B. M., Jones, P. D., Briffa, K. R., Clausen, H. B., Andersen, K. K., Dahl-Jensen, D., and Johnsen, S. J. (2010). Climatic signals in multiple highly resolved stable isotope records from Greenland. *Quat. Sci. Rev.*, **29**, 522–538.

von Storch, H. and Zwiers, F. W. (2001). *Statistical Analysis in Climate Research*. Cambridge University Press, Cambridge, UK and New York, NY, USA.

Waelbroeck, C., Mulitza, S., Spero, H., Dokken, T., Kiefer, T., and Cortijo, E. (2005). A global compilation of late Holocene planktonic foraminiferal δ^{18}O: relationship between surface water temperature and δ^{18}O. *Quaternary Science Reviews*, **24**, 853–868.

WAIS Divide Project Members (2015). Precise interpolar phasing of abrupt climate change during the last ice age. *Nature*, **520**, 661–665.

Werner, M. and Heimann, M. (2002). Modeling Interannual Variability of Water Isotopes in Greenland and Antarctica. *J. of Geophys. Res.*, **107**.

Werner, M., Heimann, M., and Hoffmann, G. (2001). Isotopic Composition and Origin of Polar Precipitation in Present and Glacial Climate Simulations. *Tellus: Chemical and Phisical Meteorology*, **53**.

Werner, M., Langebroek, P. M., Carlsen, T., Herold, M., and Lohmann, G. (2011). Stable water isotopes in the ECHAM5 general circulation model: toward high-resolution isotope modeling on a global scale. *J. of Geophys. Res.*, **116**.

Werner, M., Jouzel, J., Masson-Delmotte, V., and Lohmann, G. (2018). Reconciling glacial antarctic water stable isotopes with ice sheet topography and the isotopic paleothermometer. *Nature Communications*, **9**.

Willerslev, E., Cappellini, E., Boomsma, W., Nielsen, R., Hebsgaard, M. B., Br, T. B., Hofreiter, M., Bunce, M., Poinar, H. N., Dahl-Jensen, D., Johnsen, S., Steffensen, J. P., Bennike, O., Schwenninger, J. L., Nathan, R., Armitage, S., Hoog, C. J. d., Alfimov, V., Christl, M., Beer, J., Muscheler, R., Barker, J., Sharp, M., Penkman, K. E. H., Haile, J., Taberlet, P., Gilbert, M. T. P., Casoli, A., Campani, E., and Collins, M. J. (2007). Ancient biomolecules from deep ice cores reveal a forested southern Greenland. *Science*, **317**, 111–114.

Williamson, D., Blaker, A. T., Hampton, C., and Salter, J. (2015). Identifying and removing structural biases in climate models with history matching. *Climate Dynamics*, **45**, 1299–1324.

Winnick, M. J., Chamberlain, C. P., Caves, J. K., and Welker, J. M. (2014). Quantifying the isotopic "continental effect". *Earth and Planetary Science Letters*, **406**, 123–133.

Wolff, E. W., Chappellaz, J., Blunier, T., Rasmussen, S. O., and Svensson, A. (2010). Millennial-scale variability during the last glacial: The ice core record. *Quaternary Science Reviews*, **29**, 2828–2838.

Worden, J., Noone, D., and Bowman, K. (2007). Importance of rain evaporation and continental convection in the tropical water cycle. *Nature*, **445**, 528–532.

Xi, X. (2014). A Review of Water Isotopes in Atmospheric General Circulation Models: Recent Advances and Future Prospects. *International Journal of Atmospheric Sciences*, **2014**.

Xinping, Z., Zhian, S., Huade, G., Xinzhu, Z., Huawu, W., and Yimin, H. (2012). Simulations of Stable Isotopes in the Water Cycle in Comparison with GNIP Observations over East Asia. *Acta Meteorologica Sinica*, **26**, 420–437.

Yau, A. M., Bender, M. L., Robinson, A., and Brook, E. J. (2016). Reconstructing the last interglacial at Summit, Greenland: Insights from GISP2. *PNAS*, **113**, 9710–9715.

Zhang, X., Prange, M., Merkel, U., and Schulz, M. (2014). Instability of the Atlantic overturning circulation during Marine Isotope Stage 3. *Geophys. Res. Lett.*, **41**, 4285–4293.

Zhao, Y., Bigg, G. R., Billings, S. A., Hanna, E., Sole, A. J., Wei, H. L., Kadirkamanathan, V., and Wilton, D. J. (2016). Inferring the variation of climatic and glaciological contributions to west Greenland iceberg discharge in the twentieth century. *Cold Reg Sci Technol.*, **121**, 167–178.

Zöe, A. T. *et al.* (2020). Tipping elements and amplified polar warming during the Last Interglacial. *Quaternary Science Reviews*, **233**.

Appendix A

Meetings, Presentations and Courses

A.1 Scientific Presentations

International Union for Quaternary Research (INQUA) conference. Dublin, Ireland, 2019. "Ice cores and isotopic climate emulation to reconstruct the Last Interglacial Greenland Ice Sheet". (Poster)

PALSEA-QUIGS workshop on "Climate, Ice Sheets and Sea level during past interglacials". Galloway, USA, 2018. "Ice cores and isotopic climate emulation to reconstruct the Last Interglacial Greenland Ice Sheet". (Poster)

INQUA-PAGES workshop, Impacts of sea-level rise from past to present. Utrecht University, Netherlands, 2018. "Ice cores and isotopic climate emulation to reconstruct the Last Interglacial Greenland Ice Sheet". (Poster)

Past Earth Network Conference. University of Leeds, UK, 2018. "Simulating the Last Interglacial Greenland stable water isotope peak: The role of Arctic sea ice changes". (Poster)

Wessex DTN Annual Congress. University of Southampton, UK, 2018. "Simulating the Last Interglacial Greenland stable water isotope peak: The role of Arctic sea ice changes". (Talk)

BAS annual student science symposium. British Antarctic Survey, UK, 2017. "Simulating the Last Interglacial Greenland stable water isotope peak: The role of Arctic sea ice changes". (Talk)

PMIP4 conference. Stockholm, Sweden, 2017. "Simulating the Last Interglacial Greenland stable water isotope peak: The role of Arctic sea ice changes". (Poster)

The 5th PAGES OSM. Zaragoza, Spain, 2017. "The impact of Arctic sea ice changes on the Last Interglacial Greenland isotopic maximum". (Poster)

Visiting speaker at the Centre for Ice and Climate. University of Copenhagen, Denmark, 2017. "The impact of Arctic sea ice changes on the Last Interglacial Greenland isotopic maximum". (Talk)

Physical Geography PhD Talks. University of Bristol, UK, 2016. "The impact of Arctic sea ice changes on the Last Interglacial Greenland isotopic maximum". (Talk)

Past Earth Network - ESS Workshop "Assessing Paleoclimate uncertainty". Cambridge, UK, 2016. "The impact of Arctic sea ice changes on the Last Interglacial Greenland isotopic maximum". (Poster)

Wessex DTN Annual Congress. University of Oxford, UK, 2016. "8°C of Greenland warming? Ice cores and ice sheet loss during the Last Interglacial". (Poster)

Cambridge Centre for Climate Science Student and postdoc symposium. University of Cambridge, UK, 2017. "8°C of Greenland warming? Ice cores and ice sheet loss during the Last Interglacial". (Poster)

A.2 Courses

National Centre for Atmospheric Science Climate Modelling Summer School (two week course). Cambridge, UK.

Urbino Summer School in Paleoclimatology (two-week course). Urbino, Italy.

Impact Training Course. Communicating your research to a non-academic audience. British Antarctic Survey, Cambridge, UK.

GW4+ DTP Training – Data Analysis with R Statistical Software (one-week course). Cardiff University, UK.

Software Carpentry Workshop. Three-day workshop on core computing skills. Leeds University, UK.

NCAS UM training course, University of Reading, UK

Appendix B

Published and Submitted Work

Published scientific paper in Quaternary Science Reviews - Malmierca-Vallet, I., Sime, L.C., Tindall, J.C., Capron, E., Valdes, P.J. Vinther, B.M., and Holloway, M.D. 2018. Simulating the Last Interglacial Greenland stable water isotope peak: The role of Arctic sea ice changes. **Quaternary Science Reviews 198**, 1-14, doi:10.1016/j.quascirev.2018.07.027.

Published scientific paper in Journal of Geophysical Research - Domingo, D., Malmierca-Vallet, I., Sime, L.C., Voss, J., Capron, E. 2020. Using Ice Cores and Gaussian Process Emulation to Recover Changes in the Greenland Ice Sheet During the Last Interglacial. **Journal of Geophysical Research**, doi:10.1029/2019JF005237.

In revision scientific paper in Climate of the Past - Malmierca-Vallet, I., Sime, L.C., Tindall, J.C., Valdes, P.J. 2020. Sea-ice feedbacks influence the isotopic signature of Greenland Ice Sheet elevation changes: Last Interglacial HadCM3 simulations. **Climate of the Past**, doi:10.5194/cp-2020-40.

B.1 Collaborative Publications

Work during this thesis has also contributed to a number of collaborative projects, including:

In revision scientific paper in Nature Climate Change - Guarino, M.V., Sime, L.C., Schroeder, D., Malmierca-Vallet, I., Rosenblum, E., Ringer, M., Ridley, J., Feltham, D., Bitz, C., Steig, E.j., Wolff, E., Stroeve, J., and Sellar, A. (in revision). A sea ice-free Arctic during the Last Interglacial supports fast future loss. **Nature Climate Change**.

In revision scientific paper in Climate of the Past - Kageyama, M., Sime, L.C., Sicard, M., Guarino, M.V., de Vernal, A., Schroeder, D., Stein, R., Malmierca-Vallet, I., Abe-Ouchi, A., Braconnot, P., Chamberlain, M.A., Lohmann, G., Menviel, L., Morozova, P., Nisancioglu, K., Otto-Bliesner, B., O'ishi, R., Sherriff-Tadano, S., Shi, X., Sun, B., Volodin, E., Yeung, N., Zhang, Q., Feltham, D., Bitz, C., Stroeve, J., and Ziehn, T. (in revision). A multi-model CMIP6 study of Arctic sea ice at 127 ka: Sea ice data compilation and model differences. **Climate of the Past**.

In revision scientific paper in Climate of the Past - Williams, C.J.R., Guarino, M.V., Capron, E., Malmierca-Vallet, I., Singarayer, J.S., Sime, L.C., Lunt D.J. and Valdes, P.J. (in revision). The UK contribution to CMIP6/PMIP4: mid-Holocene and Last Interglacial experiments with HadGEM3, and comparison to the pre-industrial era and proxy data. **Climate of the Past**.